5-2023

FABRICATION, MEASUREMENTS, AND MODELING OF SEMICONDUCTOR RADIATION DETECTORS FOR IMAGING AND DETECTOR RESPONSE FUNCTIONS

Corey David Ahl
University of Tennessee, Knoxville, cahl@vols.utk.edu

To the Graduate Council:

I am submitting herewith a dissertation written by Corey David Ahl entitled "FABRICATION, MEASUREMENTS, AND MODELING OF SEMICONDUCTOR RADIATION DETECTORS FOR IMAGING AND DETECTOR RESPONSE FUNCTIONS." I have examined the final electronic copy of this dissertation for form and content and recommend that it be accepted in partial fulfillment of the requirements for the degree of Doctor of Philosophy, with a major in Nuclear Engineering.

Erik Lukosi, Major Professor

We have read this dissertation and recommend its acceptance:

Madison Andrews, Jason Hayward, Eric Lukosi, Yuri Efremenko

Accepted for the Council:

Dixie L. Thompson

Vice Provost and Dean of the Graduate School

(Original signatures are on file with official student records.)

FABRICATION, MEASUREMENTS, AND MODELING OF SEMICONDUCTOR RADIATION DETECTORS FOR IMAGING AND DETECTOR RESPONSE FUNCTIONS

**A Dissertation Presented for the
Doctor of Philosophy
Degree
The University of Tennessee, Knoxville**

**Corey David Ahl
May 2023**

ACKNOWLEDGEMENTS

PREFACE

The format of this PhD proposal will come in two parts to cover two separate projects. These two parts are separates by Chapters I and II. While there is an abstract for the dissertation as a whole (see page *iv* above), each part (or chapter) has its own, and thus more dedicated abstract. The first part, "**Development of a diamond double-sided strip detector for alpha-tagging in associated particle imaging**," is the result of my first two years of graduate school. I was an NSSC fellow during this time, but this fellowship did not continue beyond the summer 2021 semester. With this, the work on the diamond double-sided strip detector also discontinued. However, during the summer 2020 semester, while still an NSSC fellow, the fellowship provided the opportunity to do an internship with Los Alamos National Laboratory. This relationship with Los Alamos National Laboratory continued when they decided to collaborate, beginning in the Fall of 2021. From here, my research efforts transitioned from the aforementioned diamond double-sided strip detector, to building an HPGe detector response function for Los Alamos National Laboratory Detector Response Function Toolkit. That leads us to the second part of this PhD proposal. The second part, "**A high purity germanium detector response function for the Los Alamos National Laboratory detector response function toolkit**," is the result of my work in collaboration with Los Alamos National Laboratory. While these two projects do have some technical overlap because they are based in radiation detection with semiconductors, they are separate enough to merit their own sections in this proposal. This two-part format will allow me to cover both projects clearly and thoroughly.

ABSTRACT

In the first part of this dissertation, we cover the development of a diamond semiconductor alpha-tagging sensor for associated particle imaging to solve challenges with currently employed scintillators. The alpha-tagging sensor is a double-sided strip detector made from polycrystalline CVD diamond. The performance goals of the alpha-tagging sensor are 700-picosecond timing resolution and 0.5 mm spatial resolution. A literature review summarizes the methodology, goals, and challenges in associated particle imaging. The history and current state of alpha-tagging sensors, followed by the properties of diamond semiconductors are discussed to close the literature review. The materials and methods used to calibrate the detector readout, fabricate the sensor, perform simulations, take measurements, and conduct data analysis are discussed. The results of our simulations and measurements are described with challenges and interpretations. The first part of the dissertation is concluded with potential solutions to challenges with our diamond alpha-tagging sensor design, recommendations of work to help further verify or refute diamonds viability for alpha tagging in associated particle imaging.

In the second part of this dissertation, we cover the development of a high-purity germanium detector response function for the Los Alamos National Laboratory Detector Response Function Toolkit. The goal is to accurately model the pulse-height spectra measured by semiconductor radiation detectors. The literature review provides information on high-purity germanium radiation detectors and semiconductor charge transport kinematics. The components of the electronic readout and their effect on radiation measurements are discussed. The literature review ends with a discussion on different methods for building detector response functions. In the methods section, we explain our methodology for building detector response functions. This includes models of radiation transport, electrostatics, charge transport, and electronic readout components. Within the methods section, there are results from individual components to demonstrate their functionality. The results section is reserved for demonstrating the use of the detector response function as a whole. We provide the modeled pulse-height spectra for different radiation sources and user input parameters. These are compared to experimentally measured datasets. The second part of the dissertation concludes with a discussion of the benefits, drawbacks, and future improvements that could be made.

TABLE OF CONTENTS

LIST OF TABLES

LIST OF FIGURES

CHAPTER I
DEVELOPMENT OF A DIAMOND DOUBLE-SIDED STRIP DETECTOR FOR ALPHA-TAGGING IN ASSOCIATED PARTICLE IMAGING

ABSTRACT

In neutron imaging, more specifically associated particle imaging, current alpha-tagging scintillators become overwhelmed by X-rays in the neutron generators. We developed and tested a double-sided strip detector made from polycrystalline chemical vapor deposition (CVD) diamond which may be a viable option to solve the current challenges. The performance goals of the alpha-tagging sensor are 700-picosecond timing resolution and 0.5 mm spatial resolution. In this project, we designed a printed circuit board (PCB) to test and calibrate the charge division readout without a radiation sensor attached. A second PCB was designed for radiation measurements, of which a polycrystalline CVD diamond was mounted and tested. The diamond was metallized with the strip design on both sides of the device. The device was mounted to the PCB while forming electrical contacts between the strips on the bottom of the device and the contacts on the PCB using an anisotropic conductive film. The strips on the top side of the diamond were electrically connected to the PCB by wire bonding. The position sensitivity of the finished device was tested by performing a knife-edge test with an alpha source, using the calibration data to determine each alpha particle interaction location. The timing resolution of CVD diamonds are well documented, but we measured the timing resolution of a single crystal CVD diamond with a Cividec C6 charge amplifier readout to confirm that the readout electronics could achieve the timing resolution goals. Geant4 and Cividec C6 pulse models were used to correct for energy straggling and time-walk in the timing resolution measurements. After time-walk and energy straggling corrections, the timing resolution met the 700-picosecond goal. The spatial resolution during the knife edge test met the 0.5 mm goal in one dimension.

INTRODUCTION AND GENERAL INFORMATION

A. Overview

Associated particle imaging (API) is a method of neutron imaging that can be applied to nuclear security, nonproliferation, and treaty verification [1-5]. In API, neutrons from deuterium-tritium fusion (DT fusion) neutron generators are used to interrogate objects of interest so that we may obtain information about their construction and composition. The products of DT fusion are the neutron used for interrogation, and its associated anti-coincident alpha particle. In API, the direction and birth time of the neutron is determined by detecting the direction and birth time of the alpha particle. This is referred to as alpha-tagging. Currently, Yttrium-aluminum-perovskite (YAP) scintillators are being employed as alpha-tagging detectors. The YAP scintillators are able to achieve the timing resolution demands to determine the birth time of the anti-coincident neutron, but their sensitivity to photons causes them to be overwhelmed by X-rays in the neutron generator. Diamond may be a good replacement alpha-tagging sensor to improve alpha-tagging capabilities at high neutron generation rates. Diamond has a low proton number (Z), large band gap, and high charge-carrier mobility, which provides a low sensitivity to X-rays, a high signal-to-noise ratio, and fast timing capabilities. Furthermore, diamond is radiation hard, prolonging its operation capability in a high flux environment.

We developed a double-sided strip detector out of polycrystalline CVD diamond as a potential solution to the challenges with YAP scintillators. The performance goals of the alpha-tagging sensor are 700 ps timing resolution and 0.5 mm spatial resolution. The double-sided strip design (or cross strip design) utilizes 11 strip electrodes on each side of the diamond with a charge-division readout. The strip electrodes are electrically connected with resistors between them, with the readouts being on the outermost lying strips. The four readouts (2 on each side of the detector) are connected to Cividec C6 fast charge amplifiers designed specifically for diamond. A bias is applied to the electrodes through the bias tee on the charge amplifiers. During a detection event, the ratio of the pulse-heights at the readouts provides information about where the alpha particle interaction occurred.

First, we designed a printed circuit board (PCB) with no sensor attached to calibrate the readout. This was done by using a pulse generator and a capacitor to inject charge into each strip position of the circuit. The charge is injected through pin connectors attached to the PCB, and each pin connector is analogous to a strip on a sensor. Injecting charge into a specific pin is analogous to a strip collecting the charge that would result from an alpha particle interaction. During calibration, each readout was connected to a Cividec C6 amplifier in the same way that it would be during alpha measurements. Each Cividec output was plugged into a CAEN DT5730 Digitizer and CAEN's CoMPASS software to collect the resulting pulses. After collecting pulses, the time-correlated pulses were used to calculate pulse-height-ratios. Injecting charge into each strip results in a unique pulse-height-ratio. We did this with a few different resistor impedances between each strip in the readout to tune the readout. A 2nd order fit on the pulse-height-ratio vs. strip of charge injection gives us a relationship that can be used later to convert a pulse-height-ratio to an alpha particle interaction location. For alpha particle measurements, we designed a separate PCB for mounting the diamond sensor. This PCB has the same readout design and trace

layout, but a diamond sensor can be attached instead of pin-connectors. First, a polycrystalline diamond wafer was metallized via sputtering. The strip electrode design was achieved using a shadow mask of the strip pattern. The diamond was mounted, and an electrical connection was formed between the strips on the bottom of the diamond and PCB using an anisotropic conductive film (ACF). A custom heat press was built to achieve the pressure and heat required to make the bond and cure the ACF. The strips on the top of the detector were connected to the PCB by wire bonding, which was outsourced.

To confirm that the diamond and Cividec C6 shaping amplifier readout was capable of achieving our timing resolution goals, we measured the timing resolution of a single-crystal CVD diamond with a Cividec C6 readout by measuring the time-of-flight of an alpha particle between a known thin plastic scintillator and the diamond. These measurements were taken in collaboration with Dr. Cordell Delzer and Dr. Xianfei Wen, both members of Dr. Jason Hayward's research group. Time-walk due to energy straggling and jitter in the system was corrected by modeling the system in Geant4. Time-walk was significant due to the Cividec C6 readout having a fixed risetime, and their being variations in pulse-heights from energy straggling of the alpha particles.

To test the position sensitivity of the diamond double-sided strip detector (DSSD), we conducted a knife-edge test using a piece of paper to cover roughly half of the strips. An edge spread function (ESF) was fit to the interaction position distribution measured during the knife edge test. The line spread function (LSF) was calculated from the ESF and used to measure the spatial resolution in one dimension.

The next chapters will continue as follows. In the Literature Review, I will summarize key features of API and the limitations resulting from challenges with alpha-tagging sensors. I will also summarize the potential solutions to these challenges, separate from our DSSD design. Since diamond is the sensor we propose, an overview of diamond as a semiconductor and its performance compared to other semiconductors is included. In Materials and Methods, I will discuss how we designed and fabricated the detector, how measurements were taken, how models were written, and the data analysis techniques used. I will also talk about some of the challenges and changes in design that were made throughout the process to provide a perspective on why certain design and fabrication choices were made. In Results and Discussion, I will present the specific findings of our models and measurements and provide interpretation and meaning to them. This includes an analysis on whether or not we met the performance goals, and how the design exceeded or fell short of each goal. Lastly, I will conclude part one with Conclusions and Future Work, providing quick summary of the results and recommend areas where the DSSD could be improved.

LITERATURE REVIEW

In this literature review, I will review the applications and mechanisms of active interrogation and associated particle imaging (API), as well as the factors and challenges associated with it. This will provide context for understanding the role of the alpha-tagging sensor and how it fits in the API system. I will follow the review on API with a review on diamond as a semiconductor. This will provide context to understand why diamond is being explored as an option for alpha-tagging in API. This will also provide a foundation for

understanding the design choices and the challenges with the alpha-tagging sensor we have fabricated.

A. Associated Particle Imaging

    1. Applications of Active Interrogation

Active interrogation with neutrons has usefulness in non-proliferation and treaty verification due to its capabilities in identifying and classifying special nuclear materials (SNM). For some SNM, such as plutonium, passive measurements can be used for detecting the presence of a material, but for other materials that do not have as easily detectable passive signatures, active interrogation is more effective. For example, the most easily accessible SNM is largely considered to be uranium, making it a notable proliferation risk as a consequence. Uranium does not undergo spontaneous fission and its characteristic gamma rays are low energy and easily shielded, so passive measurements might be ineffective for the most detailed classifications [6-8]. Active interrogation via induced fission can be used to detect and classify SNM that is otherwise difficult to detect. Since the energy distribution of fission neutrons follow the Watt spectrum, fission neutrons from SNM can be discriminated from DT neutrons being used to induce the fission events. In addition to energy, timing data may be used to discern between neutrons of different origins. This data can allow multiplicity counting and estimations of the fissile mass/enrichment in SNM. Using these capabilities, active interrogation vastly increases classification and verification capabilities when compared to passive measurements. Figure 1 shows an example of what an active interrogation setup may look like. It shows DT neutrons interrogating SNM inside of a container, and the array of detectors to measure neutrons and gamma rays (dual particle imager) for measurement of fission products [7]. Note the difference between the orientation of the detectors in Figure 1 in comparison to a transmission imaging setup (Figure 2). The method shown in Figure 1 is similar to API, but is actually known as dual particle imaging (DPI). Both methods utilize a DT neutron generator to actively interrogate an object of interest, however, in API, the detector array is placed in line with the neutron "beam" opposite of the object of interest for transmission imaging and relatively higher contrast image reconstruction and localization.

There are other drawbacks and challenges to certain passive measurement techniques that can be overcome by active interrogation. For example, fluctuating background and limiting false alarm rates in portal monitors. X-ray imaging systems can be used at ports of entry to get a look inside of cargo and containers, but the high energy X-ray sources needed to penetrate thick or high-Z material objects would require unacceptably large exclusion zones to achieve acceptable low doses. Furthermore, X-rays may differentiate between material density and atomic number (Z) via photofission, but require very high intensities to differentiate between isotopic differences and identify SNM. However, it is possible to take multiplicity measurements using photofission and pulse-shape-discrimination [6, 9]. Neutron imaging can be used complimentary to X-ray imaging to cover a wider range of cargo/container possibilities [8]. Not only can neutron based active interrogation systems induce fission, creating useful material signatures that are highly sensitive to isotopic differences, but they can also penetrate cargo with high-Z materials more easily than X-rays.
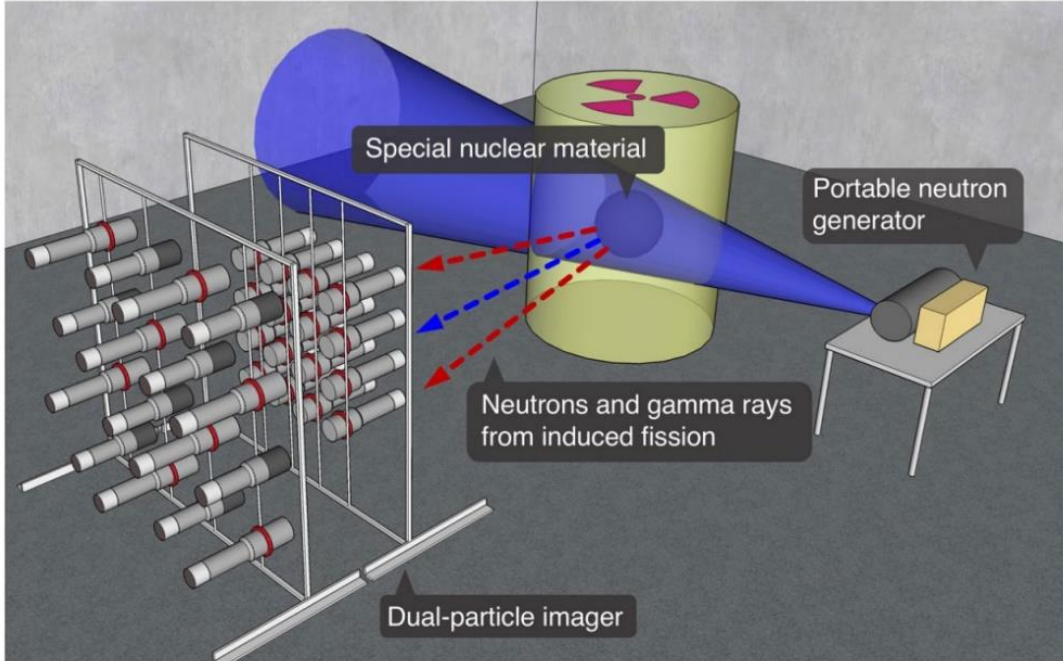
Figure 1: An example of an active interrogation scenario using dual particle imaging (DPI) [7].
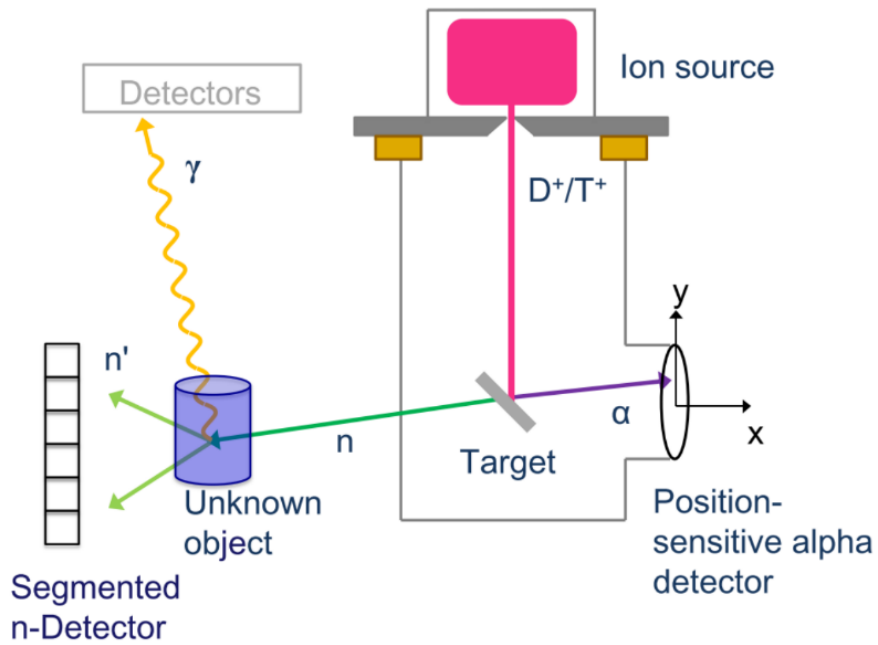
Figure 2: An example diagram of a DT neutron generator in an active interrogation scenario [10].

The need for detecting, localizing, and characterizing SNM is required for nuclear weapons non-proliferation. This is true not only for treaty verification with nuclear weapons states, but for ports of entry. Neutron imaging techniques can be used to detect materials including SNM, contraband, explosives, and other illegal items during smuggling attempts.

2. *Introduction to deuterium-tritium neutron generators*

In API, the neutrons used for interrogation are generated by DT-fusion within neutron generators. In the neutron generators, an ionized deuterium nucleus is accelerated into a target containing tritium. Upon collision, deuterium-tritium fusion results in a neutron and alpha-particle pair being produced. The 14.1 MeV neutron and 3.5 MeV alpha-particle pair are emitted anti-parallel, or anti-coincident from one another. The neutron can be used in active interrogation through a multitude of mechanisms. Given the high energy of the neutrons emitted, they are highly penetrating and especially useful for imaging thick and unknown objects, especially if made up of high-Z materials. The goals of a reconstructed image, as stated in the 2017 Oak Ridge National Laboratory (ORNL) report ORNL/TM-2017/187, are to identify the materials and their locations, perform dimensional analysis of simple shapes, and locate anomalous features in the reconstruction if a certain geometry is expected [11]. To successfully image an object with neutrons, the direction and birth time of the neutrons must be known, as well as the time and location of their arrival at an array of detectors. The emission directions for the neutrons are uniform around 4π, but the direction of a neutron may be determined if the alpha-particle direction is resolved with the alpha-tagging detector. This requires knowing where the alpha-particle was generated, and where it interacted in the alpha-tagging detector. Increased precision in the alpha-particle interaction position improves the angular resolution of the neutron direction. This is known as direction-tagging. The "spot size" of neutron production will limit the ability to determine directionality because it determines the uncertainty in knowing where DT fusion occurred. Spot sizes in DT-fusion neutron generators have been reduced to 1 mm or less in some cases [3]. The birth time of the neutron can also be determined by the alpha-particle, which is referred to as time-tagging. By measuring the time of arrival of the alpha-particle and using the distance between the neutron production spot and the alpha-tagging detector, the birth time of the neutron can be calculated. Knowing both the birth time and direction of the neutrons is necessary for discrimination between background and different neutron reactions, creating better contrast and image resolution. Figure 2 shows what an active interrogation scenario might look like [10]. It includes the DT neutron generator producing the alpha-particle and neutron in anti-parallel, along with an unknown object that the neutrons are being used to interrogate.

3. *Associated Particle Imaging Technology Developments*

The first fast-neutron imagers developed by Oak Ridge National Laboratory (ORNL) did not utilize associated particle imaging, but used a neutron source (^{252}Cf spontaneous fission) for active interrogation of fissile materials [12]. An object or container with fissile material would be placed between the neutron source and an array of detectors. Neutrons from the source would enter the container with fissile material and induce fission.

Both transmitted gamma rays and neutrons from the source, as well as fission induced neutrons and gamma rays from the object would interact in a detector array placed near the container. Gamma rays and neutrons directly from the ^{252}Cf source could be separated from those resulting from induced fission using timing data. Using time correlations, transmitted gamma rays from ^{252}Cf spontaneous fission could be separated from scattered gamma rays and ^{252}Cf source neutrons. Time separation to isolate transmitted gamma ray detections allowed imaging similar to X-ray imaging because the transmitted gamma rays are effectively collimated. After the arrival of transmitted gamma rays, scattered gamma rays and ^{252}Cf source neutrons arrive at the detectors. Last, is the arrival of neutrons and gamma rays from induced fission in the object of interest. Given adequate separation, the arrival of each is used for imaging and identification of fissile material in the object. In the late 1950s and 1960s, pulsed DT neutron sources were used for the first time for these measurements, as well as multiplicity measurements. The arrival times of neutrons were used to determine how many fission neutrons were striking the detector. The development of signal processing equipment with higher bandwidth improved the ability to time correlate neutrons and separate the arrival of transmitted gamma, transmitted neutrons, scattered gamma, scattered neutrons, and decay products. This increased the practicality of determining the fissile mass and configurations of plutonium and uranium systems, making it a useful tool for identifying fissile and nuclear weapons materials, and subcritical neutron multiplication measurements in criticality safety. Figure 3 shows a typical time response of DT neutrons traversing a Y-12 NSC standard 18 kg, annular 161 storage casting [4]. In this figure, you can see how products of different neutron interactions, as well as transmitted neutrons can be separated in time with an adequate timing resolution.

Later developments led to associated particle imaging, which allows users to better time correlate neutrons, while adding the ability to determine the direction of neutrons for better resolution imaging. Associated particle imaging also uses DT neutron generators, but specifically refers to the technique of using the alpha particle that is associated with the neutron to determine the birth times and directions of the neutrons that leave the DT neutron generator for interrogation [13].

These systems can be used for both transmission imaging with neutrons and induced-fission imaging to get 3D reconstructions, including reconstructions of the fissile materials. In these systems, the neutron generator must be designed specifically for API to include the alpha-tagging sensor. Many DT neutron generators do not have an alpha-tagging sensor because they do not utilize the associated alpha particle method. The Thermo Fisher Scientific API-120 neutron generator uses a circular 50 mm diameter by 0.5 mm thick YAP:Ce crystal scintillator as an alpha-tagging sensor with a pixelated readout on the photomultiplier tube. The alpha-tagging sensor is mounted 57 mm from the neutron generation spot. The neutron generation spot size is 5 mm, and the angular resolution (sometimes stated as uncertainty) of neutrons is about 5° [11, 13]. The light guide on the alpha-tagging scintillator detector is segmented into pixels that are 1.5×1.5 mm^2. These neutron generators were operated at about 4×10^7 neutrons per second, but this is emitted into 4π, so the incident rate of alpha-particles on the scintillator, and the rate used for interrogation is much less due to geometric efficiency. The average detector count rate is about 700 events per second.
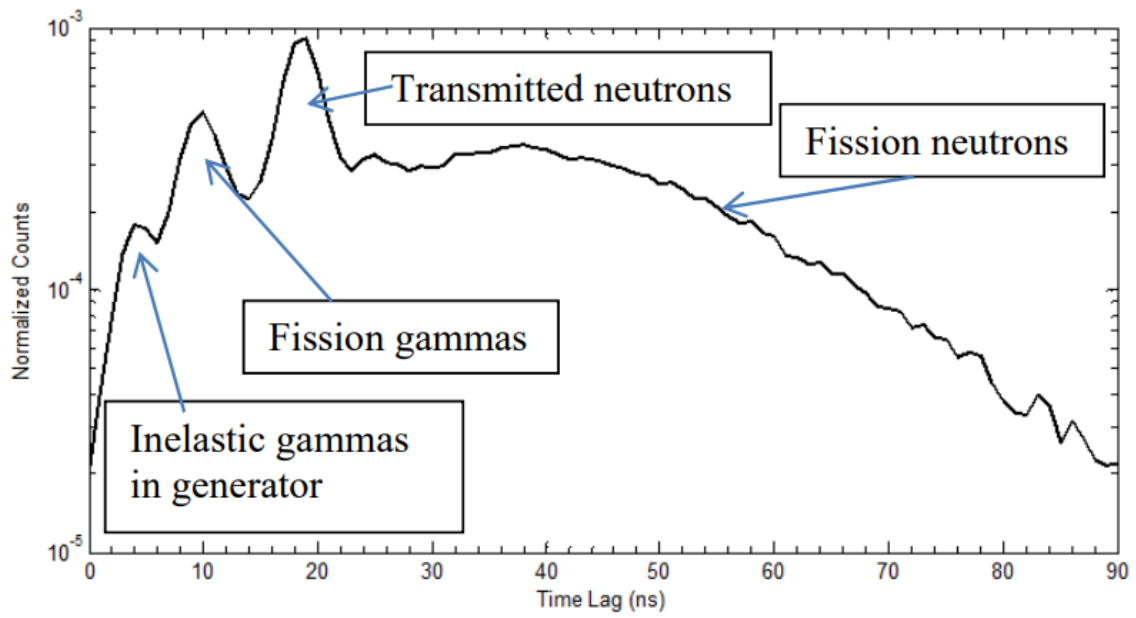
Figure 3: Typical time response of DT neutrons traversing a Y-12 NSC standard 18 kg, annular 161 storage casting [4].

These systems were deployed in the latest Nuclear Materials Identification Systems (NMIS) and the Advanced Portable Neutron Imaging Systems (APNIS). A different model was able to improve the angular resolution of the emitted neutrons to 4º by reducing the spot size to 3 mm and using a pixelated silicon semiconductor detector as an alpha-tagging sensor, but it is not clear if this system was ever deployed in NMIS or APNIS.

In these modern systems, the time of arrival of neutrons at the array of plastic scintillators is used to identify interactions due to transmitted (un-interacted) 14.1 MeV neutrons. The time window for transmitted neutrons in NMIS and APNIS are ± 2 ns and ± 1 ns respectively [4]. These time windows are the expected arrival time of a 14.1 MeV neutron at the detector array, or the time-of-flight. The expected arrival time is known because the detector array to neutron source distance is known. These time windows are very precise when compared to the range in the distribution of arrival times shown in Figure 3, which removes a lot of error associated with background/scattered neutrons arriving near the transmitted neutron time window. Corrections for attenuation/scattering are made to remove scattering contributions to further separate transmitted neutrons from scattered neutrons. This is important because the probability of scattering versus transmission are directly related to the scatter cross sections of the materials present and material locations. Measurements are taken at different rotations of the item under interrogation and two image reconstruction algorithms are used (filtered back-projection and maximum likelihood expectation maximization). When transmitted neutrons are successfully isolated, materials are correctly identified. This includes identification of aluminum, polyethylene, graphite, explosives, lead, steel, uranium metal, and tungsten. Figure 4 shows examples of tomographic and image reconstructions of two uranium metal annuli [11]. The tomographic reconstructions (b) are done with multiple orientations (gaps between each annulus), while the image reconstruction (bottom) was completed with a gap of 3 mm between each annulus. The object is symmetric, so only one measurement was taken for 30 minutes (with asymmetric objects, measurements at various rotations would be taken). As you can see, the 3 mm gap can be seen in the image reconstruction, demonstrating the capability of discrimination between features on the millimeter scale.

There are key takeaways that include how to reduce error in the reconstructions shown in Figure 4. Decreasing statistical errors can be done with either longer measurement times, larger neutron fluxes, or both. Systematic error can be decreased by better resolving the neutron emission angles, improving timing resolution, and improving the accuracy of scattering subtractions/corrections.

To further demonstrate the capabilities of APNIS, also utilizing the API-120 neutron generator, Figure 5 shows the experimental setup and results of measurements of a steel block, a lead block, and a depleted uranium (DU) cylinder next to one another [13]. Again, this method uses the associated alpha particle method, neutrons detected at the array can be correlated to a specific path or position that the DT neutron traveled as it passed through the object being interrogated. Each neutron detected at the array may be measured as a transmission neutron or as an induced neutron, and the distinction is made using timing information. Transmission neutrons and induced-fission neutrons were used to perform reconstructions. 36 measurements were performed while rotating the objects 10 degrees between each of the measurements (objects stationary during each measurement).
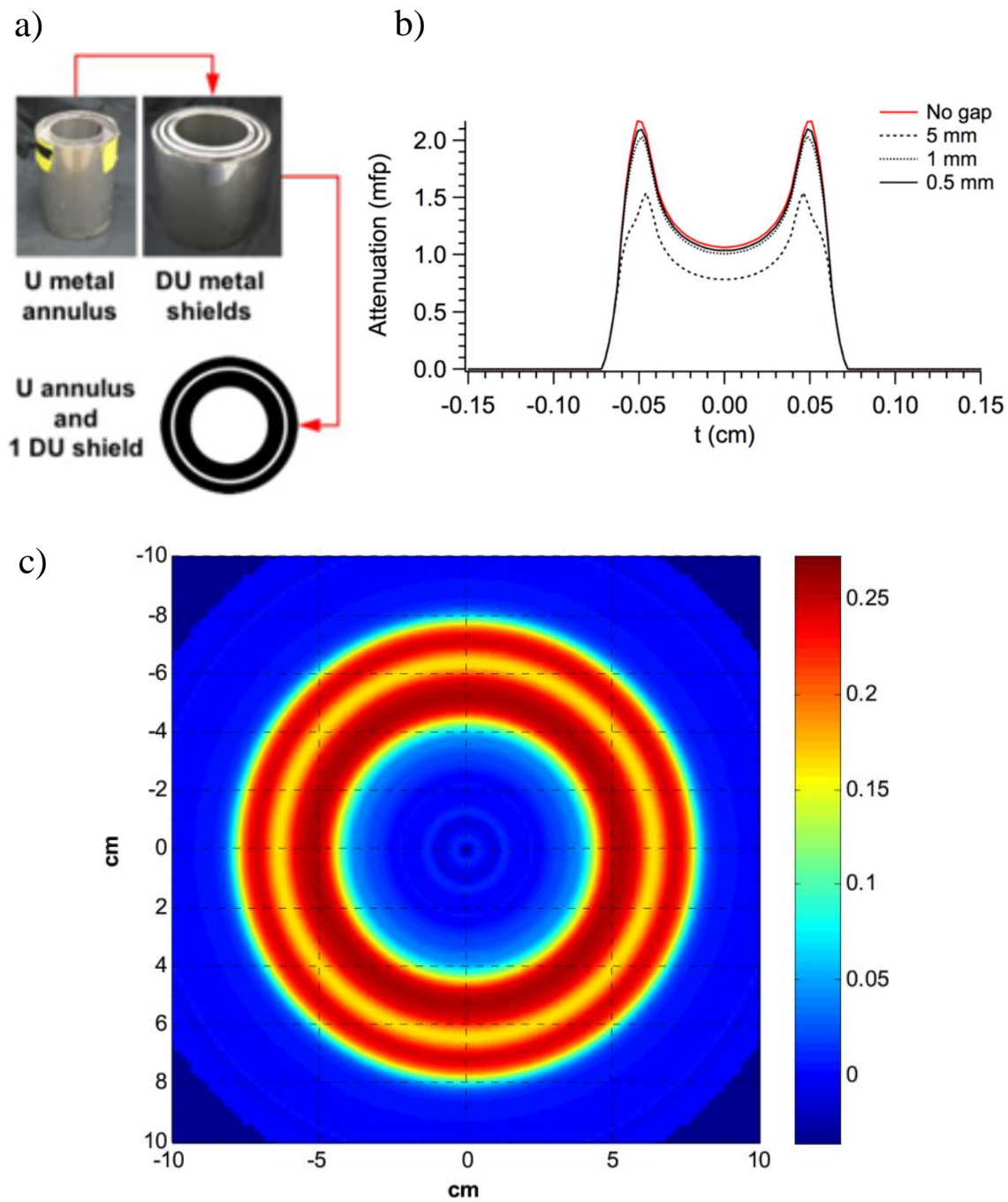
Figure 4: The two uranium metal annuli (a), the tomographic reconstruction (b) and an image reconstruction (c), the scale is the attenuation coefficient (cm^{-1}) [11].

11

a)

b)

c)

Transmission **Singles (unconstrained)** **Singles (constrained)**

d)

Measured Sinogram **Reconstructed Sinogram** **Reconstructed Image**
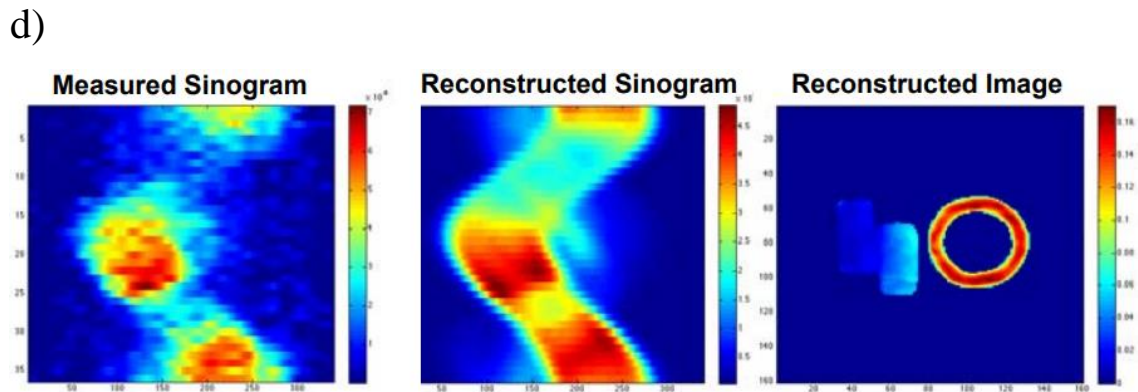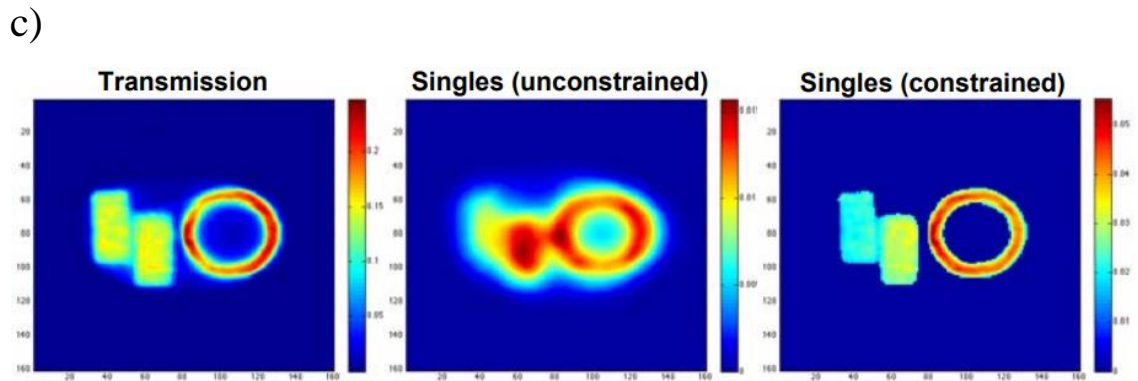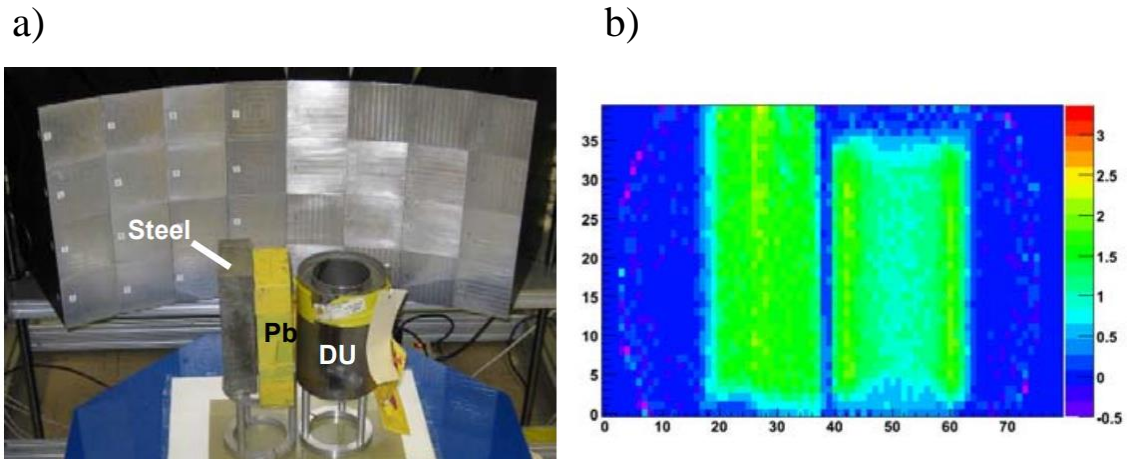
Figure 5: Experimental setup for image reconstructions using simultaneous transmission and induced fission measurements with APNIS [13]. The experimental setup (a) and single transmission projection (b) are shown, the transmission and neutron singles image reconstructions are shown in the middle row (c), and the neutron doubles reconstructions are shown at the bottom row (d).

Each measurement was taken for 2.5 minutes at a DT neutron generation rate of 8.6×10^6 neutrons per second in 4π. Figure 5a shows the experimental setup paired with a single transmission projection of one rotational position (Figure 5b). Figure 5c shows three image reconstructions, made by first using all 36 measurements to assemble a sinogram. The sinogram was then used to reconstruct the attenuation coefficients of cross sections of the objects. The reconstructed images are plots of attenuation coefficients. Excuse the poor resolution on the axes and scale in the figure. The important thing to note is that the color scale is the attenuation coefficient. The transmission image reconstruction was made using only data from transmitted neutrons. Transmission appears to show DU as most attenuating, with steel and lead being very similar. Induced fission reconstructions were completed in two different methods. One method is called the induced neutron singles reconstruction. This method only requires one induced neutron to be detected in the array for it to be included in the data set. There are two versions of this, unconstrained and constrained. Constrained means that the origins of induced neutrons are constrained to areas that have neutron attenuation. As you can see, the image reconstruction of the constrained singles is far better than unconstrained. Unlike the unconstrained reconstruction, constrained shows strong contrast between DU and lead, and some contrast between lead and steel. The second induced fission method is called the induced neutron doubles reconstruction. Image reconstructions for doubles reconstruction are shown in Figure 5d. As the name suggests, this method requires that two induced fission neutrons are detected at the array. Like the singles constrained reconstruction, it uses the reconstructed transmission image to identify where fission is allowed, while additionally using the transmission image to determine attenuation of neutrons through each volume element in the object. This is used to calculate the probability that an induced fission event in the object results in two neutrons being detected at the array, for each volume element in the object (determined by the transmission reconstruction). The measured sinogram, reconstructed sinogram, and reconstructed image using the doubles method are all shown in Figure 5d. This method exhibits better contrast between DU and lead/steel. Note that even though DU does exhibit fission, a 93% ^{235}U cylinder would be expected to have five times the doubles events as DU, leading to even greater contrast with enriched uranium. The capabilities of this system and further examples of image reconstructions have been well documented [4].

4. Key Mechanisms and Challenges in Associated Particle Imaging

As the previous section alluded to, one of the main challenges is API is determining the source of each neutron that is detected by the detector array (DT fusion, induced fission, or spontaneous fission). Excellent timing resolution is necessary for effective discrimination between the different neutron sources [6]. The elevated background associated with the object and neutron source can further the challenge of doing so. Pulse-shape-discrimination (PSD) may be used to discriminate between neutrons and high energy X-rays/gamma rays, but if the photon intensity is high enough, detectors may become overwhelmed by them. These challenges are largely in regard to the array of detectors outside of the DT neutron generator, which are often organic scintillators [6, 7, 9, 13, 14].

Once the neutrons are detected, induced fission neutrons may be identified using energy spectroscopy, because fission neutrons follow the Watt spectrum, whereas DT fusion neutrons (moderated or not) do not. Further classification can be made by time correlating the neutron count rates. Depleted uranium or low enriched uranium would still undergo induced fission from the DT source neutrons, however, the cross section for induced fission is different for different isotopes. Neutron count rates will decay differently depending on the isotopes present, the mass of fissile material, and the geometric orientations. Neutron die-away and/or multiplication measurements can be made to characterize fissile materials [14-16]. This has been demonstrated to work for discrimination between highly enriched uranium (HEU), moderated HEU, non-fissile hoax materials in place of HEU, and different enrichments of SNM [7, 14].

API has an advantage over other active interrogation techniques because of the added information of neutron direction. Using both data from timing and the path of the interrogation DT neutron, induced fission neutrons can be correlated to path lines of DT neutrons [13]. This data can be used for image reconstruction by determining the induced fission probability per unit length through the material. Furthermore, transmitted neutrons (neutrons that do not interact) can be used to determine the probability of interacting per unit length. Correlating the induced fission neutrons to path lines of DT neutrons requires that you can discriminate between transmitted neutrons and induced fission neutrons, and that you know the path of the interrogating DT neutrons. The systematic uncertainty in determining the path of the neutrons is largely determined by the position resolution of the alpha-tagging sensor and the neutron production spot size in the DT neutron generator. Separation of DT neutrons from induced fission neutrons can be done if the detector array and alpha-tagging sensor have adequate timing resolution such that the birth time of interrogating neutrons and the arrival time of each neutron at the detector array are precisely known. In other words, time-of-flight is used to separate transmission neutrons from prompt fission neutrons and other reaction products. However, the 14.1 MeV DT neutrons may scatter, without inducing fission, and then arrive at the detector array with timing and energy consistent with induced fission neutrons. The relative magnitude of these occurrences can be estimated by summing the cross sections of significant energy reducing reactions. Since cross sections are nuclide specific, the amount of lower energy neutrons that you would expect to see in the time window after transmission is different for different materials and thicknesses, which further complicate things [13]. In addition to neutrons slowing down due to scattering, neutrons may scatter from a non-fissile material into a fissile material, followed by an induced fission. This could lead to misclassification in the specific location of the fissile material due to the fact that the location would be determined by the initial path length of the incident DT neutron. With these challenges, classification and image reconstructions can still improve with better timing and position resolution of the alpha-tagging sensor. Our work is primarily concerned with the alpha-tagging sensor, so we will focus on the mechanisms and challenges associated with it. These include position resolution of the sensor to determine neutron direction, and the timing resolution of the sensor to determine neutron birth time. It also includes the detector sensitivity to photons and neutrons, which can lead to misclassifying neutron/photon events in the detector as alpha-particle events. Furthermore, sensitivity to neutrons and photons can

result in overwhelming the detector and induced radiation damage. Reducing the sensitivity to non-alpha particles can increase count rate capabilities to enable operation at higher neutron flux. Additionally, radiation hardness is important for maintained performance over longer operating times.

5. *Development of Alpha-Tagging Sensors*

An early associated particle method (roughly the year 1990) was for the Single Pixel Explosive Detection System (SPED), and used a single pixel ZnS alpha detector with no position sensing [1]. The early development was focused on detectors that had some level of two-dimensional spatial resolution, good timing resolution (< 1 ns), compatibility in vacuum/hydrogen environment, and survivability of baking (350°C). Of the early models, a ZnO (WL-1201 powder) [17] phosphor scintillator alpha detector was chosen due to its fast risetime, fast decay time, and high light output. This phosphor system had a 1.3 mm FWHM spatial resolution while measuring ^{210}Po alpha particles. For good timing resolution, BaF_2 and CsI are candidates at 700 ps and 900 ps timing resolution (FWHM), respectively. A limit to the timing resolution is the distance between the deuterium beam spot (neutron generation spot) and the alpha detector. As this distance increases, so does straggling. In this system, the spread in the arrival time of alpha particles was calculated to be about 100 ps at a 10 cm distance. It is not clear what vacuum pressure the system is operating under for this amount of straggling. The beam spot size serves a limitation in the spatial resolution of the alpha detector. In this system, the beam spot size is 1 mm (FWHM). For this combination of detector spatial resolution (1.3 mm) and beam spot size, the overall spatial resolution of the system is 1.6 mm [1].

Early alpha particle sensors for the more recent NMIS were gallium doped zinc oxide inorganic scintillators (ZnO:Ga) [2, 5]. These have sub nanosecond timing resolution, a high melting point, and 90% detection efficiency for 3.5 MeV alpha particles. Literature around these developments (roughly the year 2005), still express struggles with detector "ruggedness and cleanliness to survive the high temperature preparation of the tube" [2]. This detector had a geometric efficiency of 4% (the detector could see about 4% of 4π) which results in a maximum alpha particle rate of 4×10^6 s^{-1}, given the max neutron output of the generator is 10^8 neutrons per second. One downside to this detector is that it is made from an aggregate of small grains, which results in variations of light collection. To still count alpha particle detections that result in very low pulse height and thereby increase efficiency, the threshold on the alpha detector is set very low. This makes it more difficult to detect only alpha particles, especially when considering neutron, gamma, and background can all trigger over the threshold.

More recent studies (year 2009) utilize the same ZnO:Ga scintillators, but with the distance between the alpha detector to deuterium beam spot of 5 cm [5]. During operation during this study, the typical beam spot size was 2.1 mm, although like the previous study, a 1 mm spot size was achievable. This recent study also measured the timing resolution of the alpha detector to be about 0.5 ns (reported as standard deviation, not FWHM). The measurements were taken by measuring the time-of-flight between the alpha detector and a plastic scintillator. The conclusions of this study were that the sub-nanosecond timing

resolution could be taken advantage of by triggering on multiple prompt fission gamma rays that are in coincidence with tagged alpha particles for imaging of SNM [5].

There is significant interest in YAP:Ce scintillators due to their higher light yield, which results in higher signal-to-noise ratio than the ZnO:Ga scintillators. YAP:Ce also has better timing performance when compared to ZnO:Ga scintillators [4, 18]. The API-120 neutron generator has been used with a YAP:Ce alpha tagging sensor, a Schott 75C fiber optic faceplate, and an optically coupled Hamamatsu H9500 photomultiplier tube (PMT) [11]. Cerium doped Yttrium Aluminum Perovskite (YAP:Ce) has excellent timing performance (sub 200 ps FWHM timing resolution) with fast decay time (~25 ns) [19-21]. The primary downside to these scintillators is their sensitivity to X-rays. Approximately 60% or more of the X-rays incident on a 1 mm YAP scintillator will interact, which negatively effects the ability to detect alpha-particles [22]. Reducing the thickness of the scintillator can reduce its sensitivity to X-rays while maintaining high alpha-particle detection efficiency [18], however, the scintillator may become too brittle [19, 23]. Alternatively, diffusing cerium into only the first 10 µm of the surface can result in a thicker and more robust sensor that is not as sensitive to X-rays in the bulk. The cerium doped surface, and most sensitive region, would be extending just beyond the range of a 3.5 MeV alpha-particle [19]. In these designs, the diffusion and annealing procedures appear to heavily influence performance, which results in inconsistent alpha-response in terms of count rates and pulse-height spectra. However, the issues with doping the YAP crystals at higher concentrations near the surface do not appear to be impossible to overcome. More research into the diffusion and annealing procedures would need to be completed to achieve the cerium concentration profiles and performance desired. It is suggested that higher purity materials might also be required for cerium diffused YAP for API based research [19]. There have also been issues of high failure rates of the glass/metal fritting and fiber optic window used with YAP:Ce [24]. These components are required to withstand bakeout at 300ºC for over 24 hours without loss of a vacuum seal. The sapphire window used to mount YAP scintillators must also be thicker (3-5 mm) to withstand the vacuum/atmosphere surface, but thicker windows contribute to more light spreading, which may further worsen the position resolution [25].

Up until this point, API has been addressed and summarized from the standpoint of detection, characterization, and localization of SNM. For completeness, we should address that API does have useful applications outside of the realm of SNM identification. API may be used in many cases for identifying isotopes and/or imaging of materials where X-rays are weakly penetrating. This can be used to fine elemental and isotopic compositions in many materials. For example; identifying explosives buried in soil. More specifically, ^{12}C distributions in soil can be correlated to neutron interactions using API [26]. Like studies on SNM, these can demonstrate the usefulness of API while providing insight into the challenges of implementation in the field. For this application, the alpha-tagging detector is a YAP scintillator mounted to a position sensitive PMT with 16×16 output signals. The readouts were reduced to 4 channels by connecting the output signals through a resistive readout, so that only 4 channels are required to determine alpha particle interaction position. The system achieved a better than 1 mm spatial resolution (FWHM) with this design. While interrogating the ground with DT neutrons, you cannot do

16

transmission imaging, however, you can detect reaction products that leave the soil using isotopic signatures, such as gamma rays from neutron inelastic scattering events. Carbon concentrations in soil may be measured at depths up to 30 cm into the soil and at position resolutions of a few centimeters. Key challenges associated with measurements included measuring two alpha particle events for single gamma ray event. If single alpha events could not be assigned to specific gamma ray events, then the events could not be used to localize the event in the soil. Other challenges that introduce error include background gamma occurring in the time window expected from a ^{12}C inelastic scatter gamma from the soil. If an alpha detector can operate at a higher count rate, then you may be able to run the neutron generator at a higher rate because you can identify single events, however, operating at too high of a rate causes too many alpha particle events to occur in the time window expected for gamma events, making it difficult to correlate a single neutron event to its corresponding alpha particle. This puts a limit on the neutron production rate. An MCNP simulation of a soil interrogation measurement was performed. In order for a gamma event to be correlated to an alpha particle event, the two have to occur between 7 and 16 ns apart. If two or more gamma events occur within this time frame, then they cannot be correlated. For the setup geometry, they found that the percentage of gamma/alpha matches starts to drop off severely at neutron production rates of 2×10^8 neutrons per second. The basic setup is shown in Figure 6a, with the percentage of gamma/alpha matches vs. neutron production rate in Figure 6b. As you can see, if the neutron production rate is increased, then the number of ^{12}C inelastic scatter gammas that you may correlate to a single alpha particle will increase. However, once you approach a production rate of 2×10^8 neutrons per second, one has to expect the number of single event correlations to decline.

They tested the position resolution of the YAP:Ce alpha detector with resistive PMT readout. Recall that the 256 pixels were connected through a resistive readout to reduce the number of readouts to 4. The reason for this is to reduce the complexity and processing power/time of analysis. Figure 7 shows the resistive layout of the PMT readout (a) and what typical pulses look like (b). The resistors were chosen to achieve a linear response with respect to interaction location. The magnitude of pulses is distributed between the 4 corners of the readout. The ratios of these pulses can be used to determine interaction location [26]. The position resolution with ^{241}Am alpha particles was demonstrated to be 0.8 mm (FWHM), which is better than their 1 mm goal [25, 26]. While the application and challenges are different from characterizing SNM, it demonstrates that YAP:Ce can achieve good position resolution with the correct readout scheme.

To test this design, the alpha sensor was implemented into an API system for soil interrogation [25]. To reduce the flux of photons and secondary charged particles, helping prevent the alpha detector from being overwhelmed by background in the neutron generator, a 400 nm thick reflective aluminum coating is put on the front of the alpha detector [18, 25]. This coating will prevent some photons from interacting in the detector but allow the passage of alpha particles. One major limitation to this design compared to other designs is the alpha rate that the detector can handle. Neutron production rates were limited to about 5×10^6 neutrons per second, which increases the measurement time needed.

a)

b)
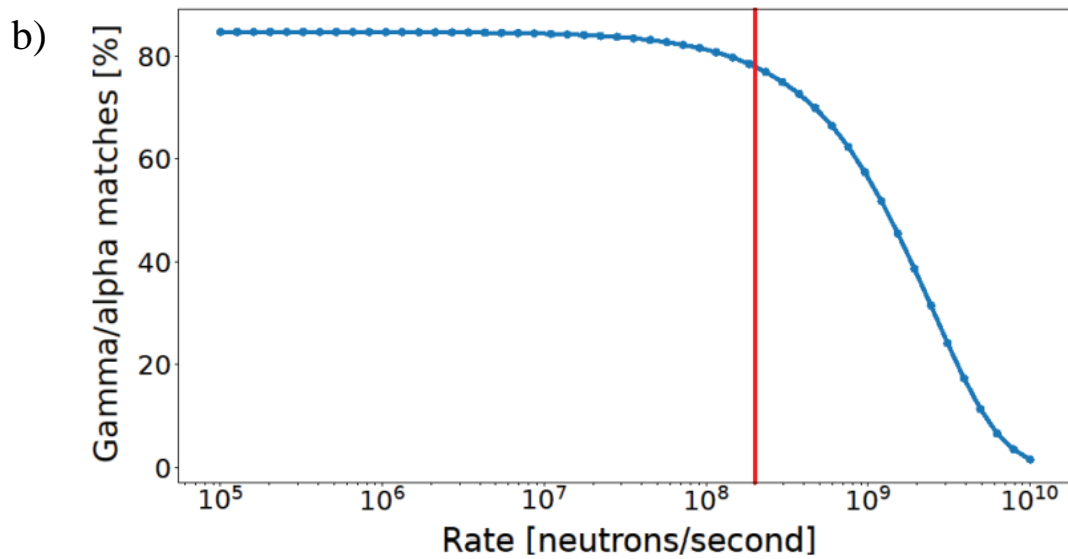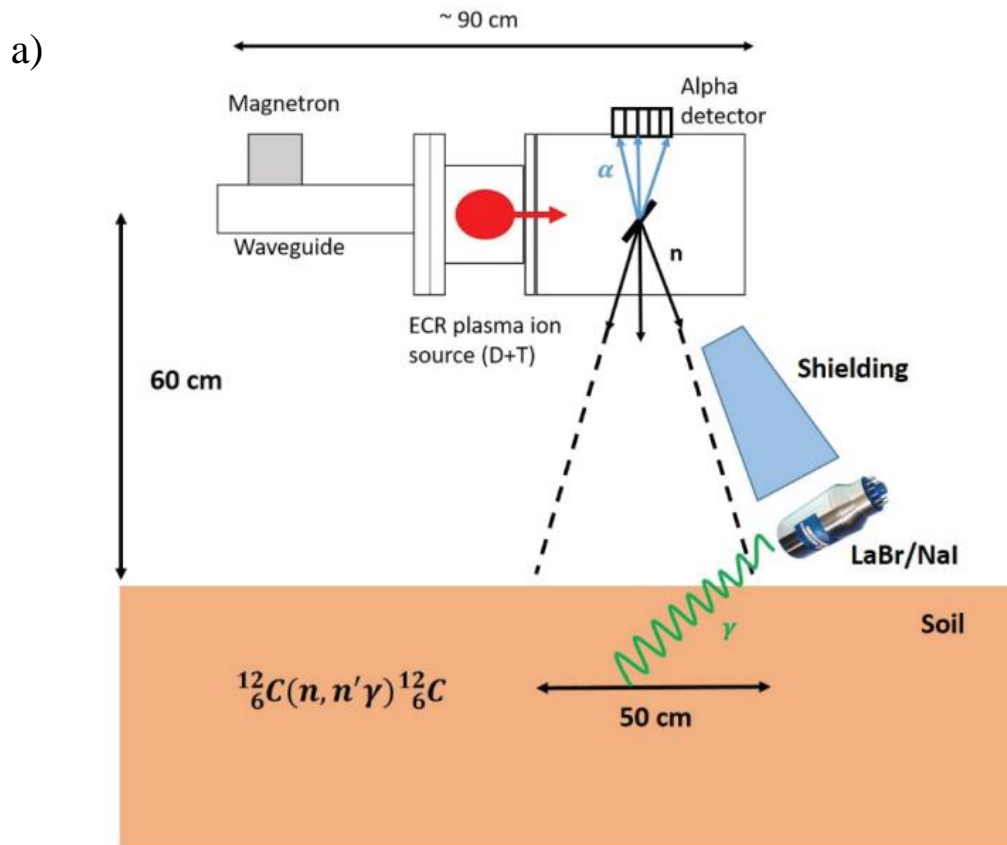
Figure 6: The soil interrogation setup (a) and the percentage of gamma/alpha matches vs. the neutron production rate (b) [26].
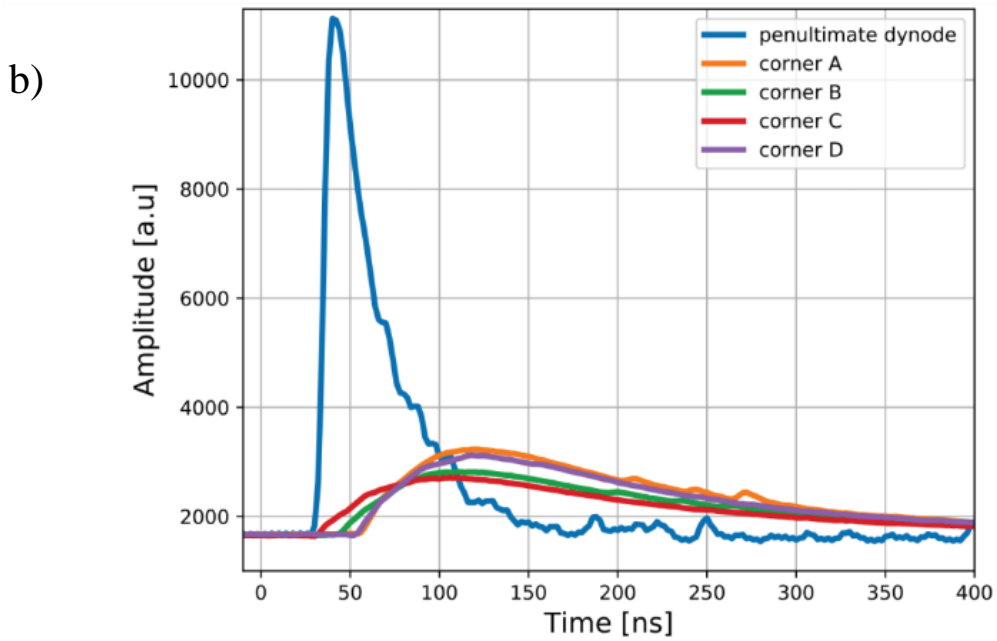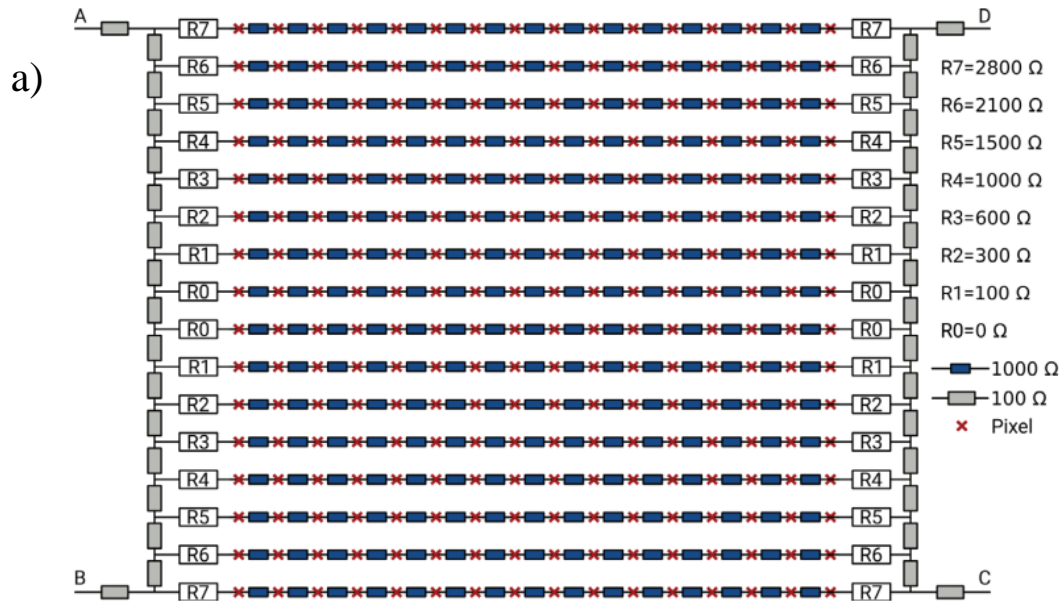
Figure 7: The resistive PMT readout with 256 pixels (16 ×16) reduced to 4 readouts labeled A-D (a), and example traces from a single readout PMT compared to the implemented 4-readout PMT (b) [26].

Reducing the neutron flux is accomplished by reducing the operating voltage, which also increases the neutron generation spot size. This negatively impacts the angular resolution. Neutron flux limits are also due to pile up of events in the readout. Increasing flux to over 10^7 neutrons per second may be achievable if RC delay is reduced, and a pile-up rejection may be possible if it does not degrade position resolution. RC delay broadens the PMT signal, as you can see in Figure 7b. As long as digitizing all 256 channels remains too computationally expensive, it would be beneficial to modify the readout to keep the number of channels reduced while further reducing the RC delay (RC constant). These improvements could introduce higher flux (operating voltage) capabilities, reducing the necessary measurement times while reducing the spot size, which consequently improves angular resolution. Additionally, a more precise determination of the carbon location depth is preferred, and this could be achieved by improving the timing resolution of the alpha detector [25]. Other studies have shown that the position resolution of YAP:Ce can as good as 0.5 mm or better [18, 27].

B. Diamond Semiconductors for API

Semiconductor detectors are attractive for API for a number of reasons. They require no optical readout and have a low X-ray sensitivity, eliminating multiple challenges associated with scintillator detectors. Semiconductors may also offer a higher spatial resolution than scintillators. Silicon semiconductor detectors have been explored for alpha tagging for planetary surface missions, which is an application that has its own unique challenges [28, 29]. Other than Silicon, diamond semiconductors present a number of characteristics that make it a suitable candidate for alpha tagging in API. The properties of diamond semiconductors have been widely documented. Diamond has a wide band gap of 5.47 eV, high charge carrier mobility that has been measured in excess of 3000 $cm^2V^{-1}s^{-1}$ for both electrons and holes, high breakdown voltage of 10^7 V/cm, high heat conductivity of 20 W/cm·K, high radiation hardness, and overall robustness in extreme environments [30-33]. Development of chemical vapor deposition (CVD) diamond growth has led to consistency in materials that natural materials do not offer, opening up the applications for radiation detection. Both single crystal (scCVD) and polycrystalline (pcCVD) diamond have been tested as radiation detectors, having similar electronic and material properties. However, pcCVD diamonds often have worse energy resolution, charge collection efficiency (CCE), and charge carrier lifetime. Charge trapping at grain boundaries and defect sites may cause polarization, which worsens over time during a measurement due to charges building up in the bulk or at the surface of the detector [31, 32, 34]. Measurement times may be kept short to eliminate some effects of polarization.

Diamond detectors have become common choices for high energy physics experiments due to its excellent timing resolution, high detection efficiency, good energy resolution, and radiation hardness. Although diamond does have excellent electronic properties for radiation detection, there are challenges associated with growing high quality CVD diamonds. Compared to other materials, like silicon, the price per unit area of diamond detectors is high, with the largest single crystal diamonds available only being less than $10{\times}10$ mm^2 [35]. Polycrystalline diamond wafers can be grown much larger and cheaper than single crystal, although their performance may be limited and inconsistent.

1. Diamond detector Performance

While single crystal and polycrystalline diamond have similar performance in many instances, there are some differences. For the sake of conciseness, I will report the general performance of diamond (which is usually single crystal), while specifying polycrystalline performance when necessary and relevant.

The timing resolution of diamond has been measured in multiple studies and shown to be very fast. One study found a 28 ps timing resolution (FWHM) using the transient current technique measuring relativistic ^{27}Al ions in single crystal diamond [36]. A second study, which measured the time-of-flight of 32 MeV alpha particles between a polycrystalline diamond and a scintillator measured a 27 ps timing resolution (σ) [37]. In this study, the diamond was connected to a Cividec broadband amplifier for the readout. Studies show that poorer CCE in polycrystalline diamond compared to single crystal diamond does not hinder timing performance significantly as long as the charge deposited in the diamond is sufficiently high [38].

i. Polycrystalline diamond

The major performance downgrade from single crystal to polycrystalline diamond is the charge carrier lifetime and mobility. Unlike single-crystal diamond, polycrystalline contains multiple crystal grains at varying orientations. Due to grain boundaries in polycrystalline diamond, there are more defects resulting in shallow traps. The trapped charge may de-trap at room temperature (thermal emission) with time scales on the order of 1-10 μs [39, 40]. The result is poorer charge collection efficiency and a slow component to the rise due to hole trapping and de-trapping. The activation energy of the hole traps in polycrystalline diamond was estimated to be about 0.3 eV [40]. The same slow rise component due to trapping was not observed for electrons. Deeper traps are not seen through this slow component of the rise time because once trapped, charge carriers will not de-trap at room temperature, but priming may be used to observe the deep traps [40]. Some polycrystalline material is better than others, so some studies show that the rise time of polycrystalline and single crystal diamonds are nearly identical [31]. With that said, even these polycrystalline devices show effects of polarization which results in degradation of charge collection efficiency over time during a measurement. This behavior is detrimental to alpha spectroscopy, but the effect can be alleviated if measurement times are kept short.

ii. Radiation Hardness of Diamond Semiconductor Detectors

The radiation hardness of diamond semiconductors under irradiation of high energy charge particles and neutrons has been extensively studied. Some studies on radiation hardness have been propelled by applications in high energy physics experiments, some by neutron measurement applications, and even some for associated particle imaging [29]. For applications in associated particle imaging, most radiation hardness studies have been comparing diamond to silicon under alpha particle irradiation. For this reason, a significant portion of this summary will use silicon as a material of comparison with diamond. This is because like diamond, silicon semiconductors have fast rise times which result in good timing resolution, can survive high temperature bake-out of the neutron generators, can be manufactured with pixelated readouts to provide different levels of interaction position

information, and are being considered for alpha tagging in API [29]. The radiation hardness of both diamond and silicon is an ongoing subject of study. Silicon detectors exposed to a 300 μCi ^{241}Am source (5.5 MeV alphas) induced damage in the silicon such that the alpha peak shifted to lower channels as damage occurred in the sensor. However, when analyzing the damage due to alpha particles, the silicon sensors are expected to last the duration of the desired lifetime (1000 hours) in the DT neutron generator. It should be noted that these studies evaluate radiation hardness to alpha fluence, but in a DT neutron generator the sensor will also be exposed to high energy neutron fluence and gamma rays. A detector should have a radiation hardness to neutrons and alpha particles that allows the detector to maintain large enough alpha pulses for discrimination between neutron/gamma/alpha interactions for the desired operational time.

Thermal neutrons do not have a significant effect on diamond, but nuclear reactions with carbon can become significant above 5 MeV, leading to damage [41]. As stated, DT neutrons in neutron generators for API are 14.1 MeV. Under 14 MeV neutron irradiation, fluences on the order of 10^{14} n/cm^2 have been shown to result in radiation damage that causes polarization effects in 100 μm thick diamond [42]. Cutting that thickness in half is expected to increase the fluence capabilities by an order of magnitude, emphasizing that the thickness of the diamond being used in a neutron flux is of high importance for radiation hardness. Other studies have shown that diamond of the same thickness was mostly unaffected under similar conditions. The FWHM of an ^{241}Am alpha peak was only reduced after irradiation with 14 MeV neutrons with a fluence on the order of 10^{14} n/cm^2 [41]. Other studies show that reducing the detector thickness results in detectors that can handle lower energy neutrons at fluences larger than 10^{14} n/cm^2, with some reduction in pulse height (CCE) that is often recoverable with detector priming or "pumping" [43-45]. However, it is important to reiterate that these fluences are higher than the expected fluences that an alpha-tagging sensor is expected to withstand. At the neutron production rates that API operates (10^7 n/s), the alpha-detector to neutron production spot distance (5-6 cm), and the expected operational lifetime (1000 hours), the fluence on the alpha detector is expected to be on the order of 10^{12} n/cm^2 [5, 29]. The main takeaways from these studies are that both single crystal and polycrystalline diamond detectors have been shown to withstand the neutron fluences experienced in API, and that the detector thickness plays a large role in its radiation hardness, with thinner sensors being preferred.

For completeness, we will discuss radiation hardness for high energy physics experiments, even though our application concern is for relatively low energy (3.5 MeV) alpha particles from DT fusion. It is well known that silicon detectors do not last long under the irradiation of heavy charged particles [46]. For silicon detectors, radiation damage causes increase in dark current, which results in increased temperature which requires cooling. In diamond, radiation damage does not increase dark current so sensors may be kept at room temperature. Damage does result in a decrease in signal magnitude in both. The level of damage is proportional to the non-ionizing energy loss cross section (NIEL), while the energy loss of incoming radiation that causes ionization is used for detection [46]. At low energies, where DT alpha particles exist (3.5 MeV), NIEL is dominated by elastic long-range Rutherford scattering and creates small lattice displacements. At higher energies (100 MeV and higher), inelastic cross sections in carbon (diamond) are smaller

than silicon, so diamond is an order of magnitude more radiation resistant in these scenarios. However, 100 MeV is higher energy than seen in API. For high energy physics applications, both single crystal and polycrystalline diamond have the same "damage constant" for high energy proton irradiation [47].

MATERIALS AND METHODS

A. Charge Division Readout

The diamond double-sided strip detector (DSSD) has a strip electrode design with a charge division readout. The detector has 11 strips on each side, with the strips on one side being perpendicular to the other. Together, the two-sided readout provides 2-dimensions of spatial resolution. The strips are 250 µm wide with a 350 µm pitch. Instead of a readout on each strip, there are only two readouts on each side of the detector, making four readouts in total. This keeps the power demand lower and data acquisition less intensive. To accomplish position sensitivity with the four readouts, there are resistors between each strip in the circuit. Figure 8 shows a diagram of the design. The figure shows an ^{2}H beam striking a tritiated target, which produces the 14.1 MeV neutron and anti-coincident 3.5 MeV alpha particle through DT fusion. It shows the strips on the device, as well as the four readouts (channels A-D). It also shows how the resistors are connected in the circuit between each strip. All resistors are the same impedance. Each readout is connected to a Cividec C6 charge amplifier (not shown). The diagram shows five strips on each side of the device, but the actual DSSD has 11 strips on each side.

When the alpha particle strikes the detector, it produces free charge carriers (electrons and holes), that move toward the strip electrodes. Because the range of the alpha particle in diamond is very short (< 20 µm from SRIM simulations of 10,000 alpha particles at 3.5 MeV and 5.5 MeV), the charge will be generated very close to the top strips, which are connected to readout channels A & B. Depending on the bias applied to the detector (the direction of the electric field), either the electrons or holes will move across the device to the bottom strips (readouts channels C & D). Since we operate our DSSD with a positive bias on the bottom side of the device and the top side grounded, we will approach the rest of this explanation based on that configuration. Keep in mind that one could change the bias if they wish, according to which charge carrier has the better transport properties (greater lifetime and CCE). Our device exhibited poor hole charge transport properties leading to poor charge collection efficiency when applying a negative bias to the bottom side (channels C & D). Only while applying a positive bias to the bottom side resulted in enough charge collection to see pulses consistently. With the bias configuration established, we know that electrons will move across the bulk of the device due to the alpha particle interactions near the top strips.

During transport, signal will be induced on the strip electrodes. Transport and signal formation in semiconductor detectors is addressed in greater detail in Chapter II. We assume that all charge is either collected by a single strip or shared between two neighboring strips. When the charge is being induced on the strip electrodes, the signal travels through the resistors on its way to the readout. A single interaction results in a pulse at both readouts C & D with positive polarity, and a pulse at both readouts A & B with negative polarity (the Cividec C6 charge amplifiers are inverting).
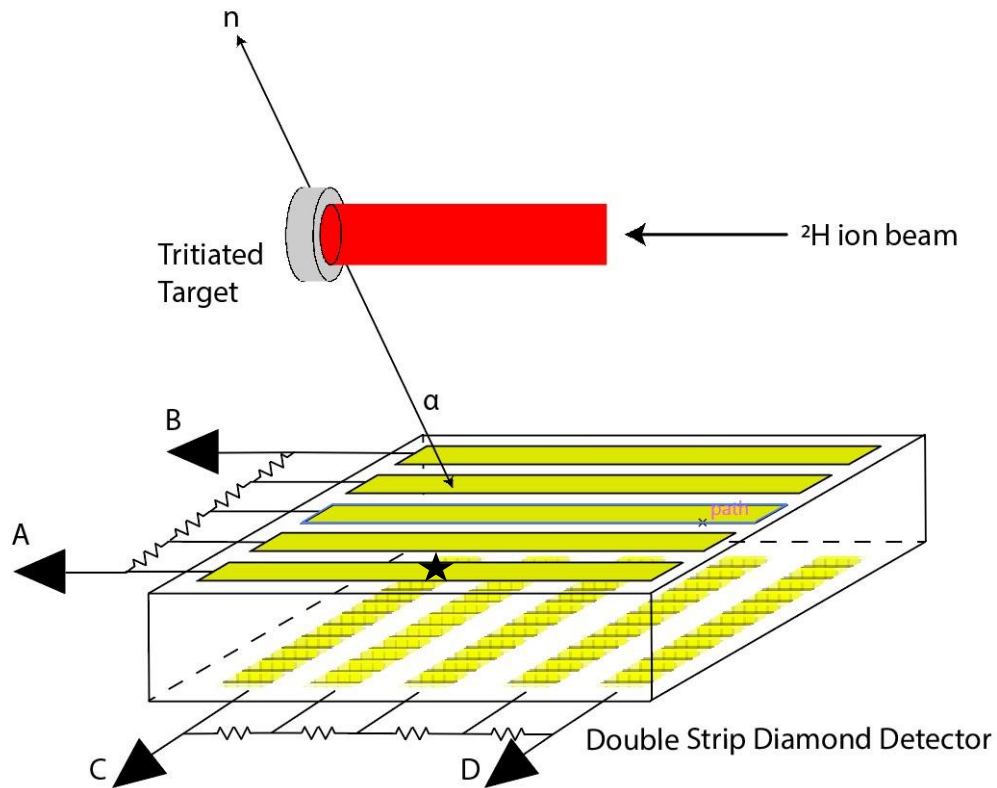
Figure 8: The DSSD design with charge division readout for associated particle imaging.

The number of resistors that the charge passes through before reaching each readout is determined by which strip collected the charge (i.e., where the interaction occurred). This results in different pulse-heights at each readout. The ratio of the pulse-heights can be used to determine where an interaction occurred. For example, consider an interaction that occurs just below the strip closest to readout A on the top, but just above the center strip on the bottom (half-way between readout C & D). The interaction location is denoted by the black star on Figure 8. The signal shared between readouts A & B will result in different pulse heights at readouts A & B because the charge will move through no resistors on its way to readout A, but 10 resistors on its way to readout B. Readout A will have a larger pulse height than readout B. The relationship between the pulse-height-ratio and which strip collected the charge is determined by a calibration that is further explained in the next section, Charge Division Readout Calibration. Since this interaction happened half-way between readouts C & D, the signal that travels to readout C will move through the same number of resistors as the signal that travels to readout D, meaning the pulse-heights at readouts C & D will be the same, and the pulse-height-ratio should be equal to one. Interactions will also occur between strips, which would result in charge being shared by at least two strips, however, the calibration accounts for these instances.

1. *Charge Division Readout Calibration*

We fabricated a PCB for calibrating the charge division readout. This PCB has an identical charge division readout as the DSSD device. It was designed and manufactured using the same methods as the DSSD device (see Materials and Methods: B. DSSD Fabrication, 2. PCB Design and Assembly). Instead of a diamond sensor, there are pin connectors that take the place for each strip in the circuit. The pin connectors are used for injecting charge into the circuit. Figure 9 shows the calibration PCB. Each signal pin is analogous to one strip on the DSSD. By injecting charge into one pin connector, we are imitating an occurrence of a radiation interaction at a specific strip on the DSSD. By injecting charge into two neighboring pin connectors simultaneously, we are imitating an occurrence of a radiation interaction occurring between two strips on the DSSD. We used a pulse generator to inject a square voltage pulse through a capacitor, followed by injection of that charge into the pin connector(s). Once charge is injected, it moves through the circuit to the SMA connectors and into the Cividec C6 charge amplifiers. Lastly, the charge amplifier output is plugged into a CAEN DT5730 digitizer to collect the traces using CAENs COMPASS software. The amount of charge injected into the circuit during calibration was calculated according to Equation 1, where V is the magnitude of the voltage pulse being injected into capacitor, C is the capacitance of the capacitor, and Q is the amount of charge injected into the pin connector.

We want the charge injected during calibration to be similar to that which would be generated from an alpha particle interaction in diamond. Using the average energy to produce an ion pair in diamond of 13.2 eV (W-value), and the capacitor used in the circuit (1.11 pF), we can calculate the magnitude of the pulse that we should inject using the pulse generator. To mimic a 3.5 MeV energy deposition, the pulse height is 38 mV in magnitude.
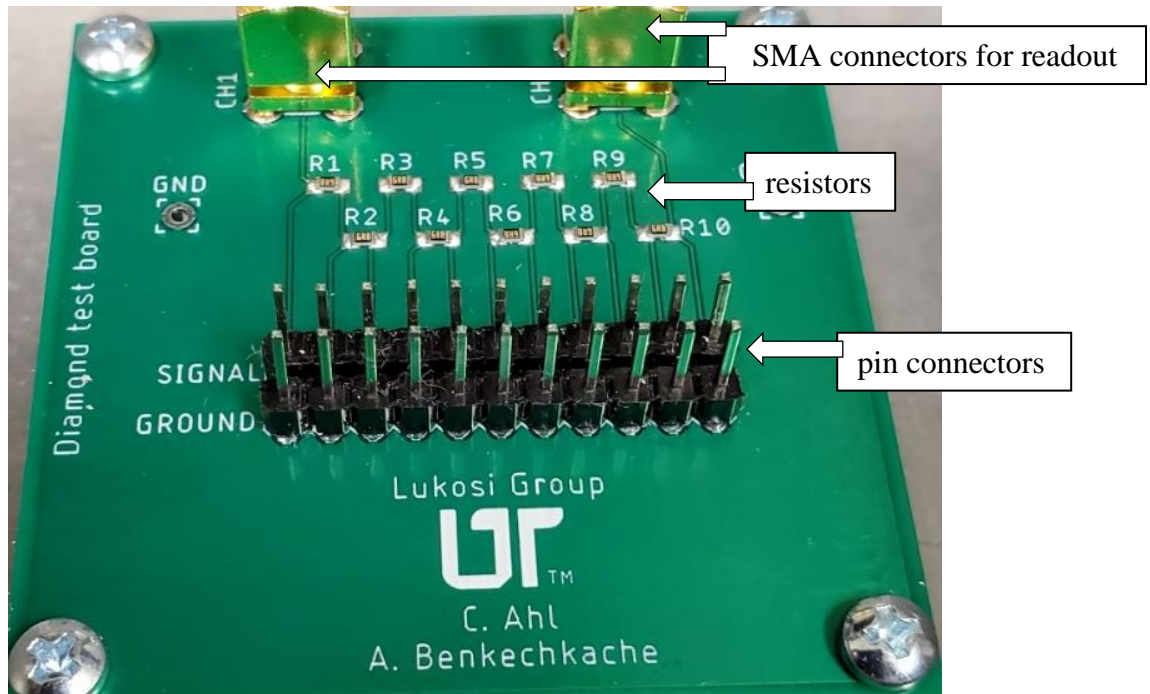
Figure 9: The readout calibration PCB, with an identical charge division readout as the DSSD PCB, with pin connectors in place of a diamond detector.

$$Q = CV \tag{1}$$

$$Q_{injected} = \frac{3.5 \times 10^6 \ eV}{13.2 \ {eV}/{ion \ pair}} \times \frac{1.602 \times 10^{-19} \ C}{ion \ pair} = 4.25 \times 10^{-14} \ C$$

$$C = 1.11 \ pF$$

$$V = \frac{4.25 \times 10^{-14} \ C}{1.11 \ pF} = 0.038 \ V$$

38 mV square pulses from a Siglent SDG1025 waveform generator were injected into a 1.11 pF capacitor and then into the charge division readout through the pin connectors. The calibration PCB only has two readouts, so it calibrates one "side" of the DSSD at a time. The DSSD has four readouts, so it utilizes four Cividec C6 charge amplifiers. To determine which charge amplifiers should be paired on each side, different combinations were tested together in the calibration. This was necessary because we found that each Cividec C6 has a slightly different gain. We determined that pairing them such that the charge amplifiers with the closest gain were paired. The two with the largest gain would be used on the side of the device that has the weakest signal due to charge loss (the bottom side). The two with the smallest gain will be used on the top side of the device. The Cividec C6 were labeled as they were paired, and they would be oriented in the readout consistently through calibration and DSSD measurements. We injected pulses into each pin separately to simulate charge collection on each strip. We also injected pulses into neighboring pins to simulate charge collection shared between two neighboring strips. For charge sharing, charge was split 50/50 between pins 1 & 2, then 2 & 3, and so on until reaching 10 & 11. The digitizer collects the output traces from each channel and then we use the pulse heights at each readout to calibrate the readout. The data was analyzed using Python®. We time correlate the output traces to pair them with a single input pulse, then we find the pulse-height-ratio between the output traces. The pulse-height-ratios are defined in Equation 2. The pulse-height-ratio of the top side readout (PHR_{AB}) is the pulse-height at readout A (PH_A) divided by the pulse-height at readout B (PH_B). The pulse-height-ratio for the bottom side (PHR_{CD}) is the pulse-height at readout C (PH_C) divided by the pulse-height at readout D (PH_D). Once the pulse-height-ratio of every event was found, we could find the mean pulse-height-ratio and standard deviation for each pin (or strip) of charge injection, and for each shared pin combination. A 2nd order least squares polynomial fit on the pulse-height-ratio vs. strip of charge injection was found for readouts A & B, and readouts C & D separately. The 2nd order best fit polynomial for mean pulse-height-ratio versus strip of injection is the calibration, or conversion used to find the interaction location of each alpha particle.

$$PHR_{AB,CD} = {PH_{A,B}}/{PH_{C,D}} \tag{2}$$

B. DSSD Fabrication

 1. *Sensor Fabrication*

The diamond sensor being used is an electronic grade polycrystalline CVD diamond manufactured by ElementSix™. Single crystal CVD diamonds tend to have better charge carrier lifetime, and consequentially better mobility-lifetime product ($\mu\tau$) and charge collection efficiency (CCE). Polycrystalline is being used due to its lower cost, especially when considering larger crystal sizes. This design is using a $5\times5\times0.5$ mm^3 sensor as a proof of concept as an alpha-tagging sensor, but an employed alpha-tagging sensor would be larger for better geometric efficiency when considering distance between the neutron spot size and alpha detector in API neutron generators. This would require the utilization of multiple diamonds sensors, which would result in more significant cost benefits if cheaper and larger polycrystalline diamonds can be used instead of single crystal CVD diamonds.

The sensor has 11 strips on each side. Each strip is 0.25 mm wide with a 0.35 mm pitch (0.1 mm between strips). The strips are 3.8 mm long, which makes the entire strip area 3.8×3.8 mm^2. A more specific description of the readout is in the Materials and Methods: A. Charge Division Readout section of this chapter. For now, we will focus on the strip fabrication. To prepare the sensor before depositing the strips, the sensor was cleaned in an HCl and HNO_3 acid solution, then rinsed in deionized water. Following the acid bath, the sensor was soaked in chromium etchant and rinsed with deionized water again. The acid and chromium etchant steps are typically necessary for removal of gold and chromium contacts that are on a sensor when re-metallization is necessary. In our case, we went through two different metallization procedures during some trial and error, so this was necessary for the final metallization. Following the acid bath, the sensor was placed in a base piranha (NH_4OH and H_2O_2 solution), then acid piranha (H_2SO_4 and H_2O_2 solution), then rinsed in isopropyl alcohol. Lastly for the cleaning process, the diamond was soaked in a UV ozone environment to remove any leftover organic material and help create an oxygen terminated surface to ensure better contact adhesion and a successful formation of ohmic contacts. Materials and processes for contacts on diamond are well documented [48, 49].

We metallized the sensor at the University of Tennessee Institute for Advanced Materials and Manufacturing (IAMM) Micro-Processing Research Facility (MPRF) clean room. The instrument used is an AJA International ATC Orion-5 confocal magnetron sputtering system. To get the strip design, a shadow mask was placed on the diamond before sputtering. A 50 nm base layer of chromium was sputtered first, which forms the ohmic contact. The chromium layer is followed by a thin platinum diffusion barrier of roughly 10 nm. Finally, a gold top layer protects the lower layers from oxidation and creates a surface for which wire bonding can be completed. The platinum layer serves as a diffusion barrier between the chromium and gold. The gold layer on the bottom side of the diamond only needs to be thick enough to protect the base layer from oxidation, so it is only 75 nm thick. The gold on the top side of the diamond is a much thicker 1 μm for wire bonding. Following metallization, the contacts were annealed in an argon environment at 600°C for 15 minutes to achieve good contact adhesion and ohmic behavior. The diamond sensor with strip electrodes is shown in Figure 10.
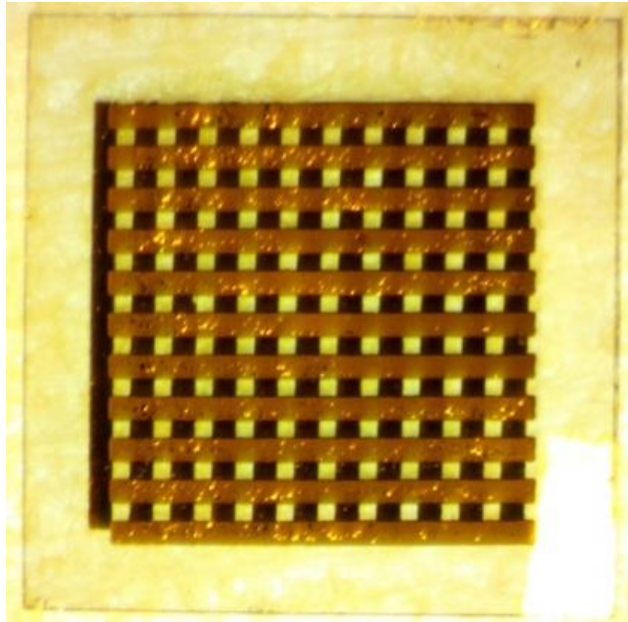
Figure 10: The $5 \times 5 \times 0.5$ mm^3 polycrystalline CVD diamond sensor with strips metallized and annealed.

2. PCB Design and Assembly

Once the sensor was fabricated it needed to be mounted to a PCB with electrical connections established. In addition to the PCB for the DSSD, the calibration PCB had to be fabricated. For now, we will focus on the former. With input from Dr. Lorenzo Fabris and Dr. Seth McConchie of Oak Ridge National Laboratory, and collaboration with the post-graduate in our research group, Dr. Amine Benkechkache, we were able to come up with a PCB design to accomplish all of our goals. Dr. Amine Benkechkache used AUTODESKS's EAGLE to design the PCB, and the designs were sent to Sunstone Circuits for manufacturing. The most significant challenge was establishing the ability to mount the sensor and make electrical connections between the strips on the sensor and the PCB. We also needed to mount resistors to the PCB that are placed in the circuit between each strip. The traces on the PCB should also be designed such that capacitance between traces is minimized for noise reduction. Lastly, there had to be SMA connectors so that the Cividec C6 charge amplifiers could be connected easily and with minimal noise.

The resistors that are placed between each strip in the circuit were 12.7 Ω impedance surface mounted resistors (SMD). SMD resistors were chosen because they could be mounted via reflow soldering and take up less space in comparison to through-hole resistors, which require hand-soldering and more space on the PCB. Our experience with various designs for the calibration PCB helped us make these decisions. For example, hand soldering of through-hole resistors was more inconsistent, took up more space, limited our options for routing traces in the PCB, and resulted in higher noise levels than the design with SMD resistors. SMA connectors were chosen because the Cividec C6 charge amplifiers have SMA connectors, so we could easily mount the amplifiers directly to the PCB. This further minimizes noise because it eliminates the need for a cable between the sensor and charge amplifier. During the design and testing phases of the calibration PCB, we went through a few different resistor impedances. We settled on the 12.7 Ω resistors as they provided sufficient separation between pulse-height-ratios while still maintaining a good signal-to-noise ratio. Larger impedance could result in better spatial resolution due to more separation in the pulse-height-ratios between strips, but further separation is at the cost of signal degradation due to larger impedance in the circuit. Since we are using a polycrystalline sensor with often less than perfect charge collection efficiency, we aired on the side of caution by using a relatively low impedance.

To mount the sensor to the PCB and establish connections between the strips on the bottom of the detector and the contacts on the PCB, we used 3M™ ACF 5363. This anisotropic conductive film utilizes conductive beads embedded in epoxy, enabling connections in a strip design without shorting between strips. The 5363 model has gold-coated nickel beads that are 10 µm in diameter and an adhesive thickness of 40 µm. The minimum space between connectors recommended is 100 µm with a minimum pitch of 200 µm (meaning the minimum strip size is also 100 µm). While the bead size might imply that a smaller pitch is achievable without shorting between the conductors, this is the minimum to achieve the reported interconnection resistance of <20 mOhms. That is because the number of conductive beads that come into contact with the conductor (strip electrode), decreases as the pitch decreases, which could increase the interconnection resistance. 3M™ also reports that interconnection resistance remains <100 mOhms and the

30

strength of the bond is unaffected after heating and cooling cycles as low as -40°C and has high as 125°C.

The ACF bonding procedure required a custom bonder to be designed to mount the diamond. One can purchase an ACF bonding machine, but they are on the order of thousands of dollars. The PCB and the custom heat press for bonding are shown in Figure 11. The bonding procedure requires ≈200°C for 10-20 seconds at a pressure of roughly 40 kg/cm². Both heat and pressure must be applied simultaneously because the pressure ensures that the sensor and PCB become electrically connected, while the heat cures the epoxy and creates the bond. This is a challenge because the strips need to remain aligned throughout the bonding process. Any movement nearing 100 µm would be unacceptable because it would result in a misalignment so severe that strips would be unintentionally crossed or disconnected. Getting the sensor to align, and then keeping it aligned while applying pressure is key. The heat being applied also needs to be stable so that the appropriate heat can be maintained throughout the bonding time. We designed a heat press that utilized a drill press. We used a drill press because it can apply pressure vertically downward, and it is robust so that there will be minimal flexing that could cause movement when applying pressure. We used an OMEGA™ PID temperature controller and connected a 250W cartridge heater to it. The temperature controller contains a built-in relay and an input for a thermocouple to control the temperature. We machined an aluminum head for the heat press which could be mounted into the drill press. The aluminum head has two holes in it, one large hole for the heater cartridge and one small hole at the bottom surface for a thermocouple to be inserted. The aluminum head has a flat, and smooth bottom to apply even pressure and heat to the sensor. The aluminum head touches the sensor directly during bonding.

The more specific procedure is as follows. First, one must peel the protective backing off of one side of the ACF. Next, the ACF should be applied to the contacts on the PCB with the exposed side of the ACF facing down, and the side still with protective backing facing up. Very light pressure should be applied with the heat press at ~100°C, which makes the ACF tacky so that it sticks to the PCB. Next, the protective backing on the top side of the ACF can be removed. If the ACF is uniformly stuck to the PCB, then the sensor can be placed onto the ACF. The ACF is mostly transparent before the epoxy is cured, so you can see if the strips on the diamond sensor are aligned with the contacts on the PCB through a microscope. Once aligned, the PCB and diamond sensor should be placed directly underneath the heat press, as shown in Figure 11. The cartridge heater is able to heat the relatively small block of aluminum quickly. When the temperature of the press is being heated to 200°C, it will overshoot the target temperature on initial heating and oscillate around the target temperature before stabilizing. This is because the cartridge heater is able to heat up the small block of aluminum very quickly, and the aluminum cools down very quickly once heater turns off after overshooting the target temperature. Replacing the aluminum with a larger steel block would help alleviate this issue. After a few oscillations, the temperature will stabilize. Once the heater has stabilized at the target temperature, heat and pressure need to be applied to the sensor and ACF simultaneously. Plenty of practice was conducted with square pieces of glass the same size as the diamond and copper tape while testing bond strength and electrical conductivity.
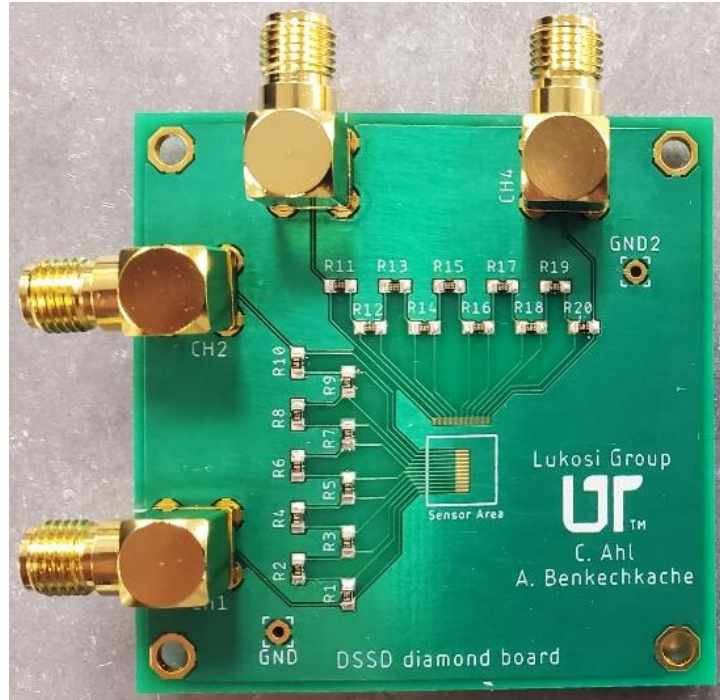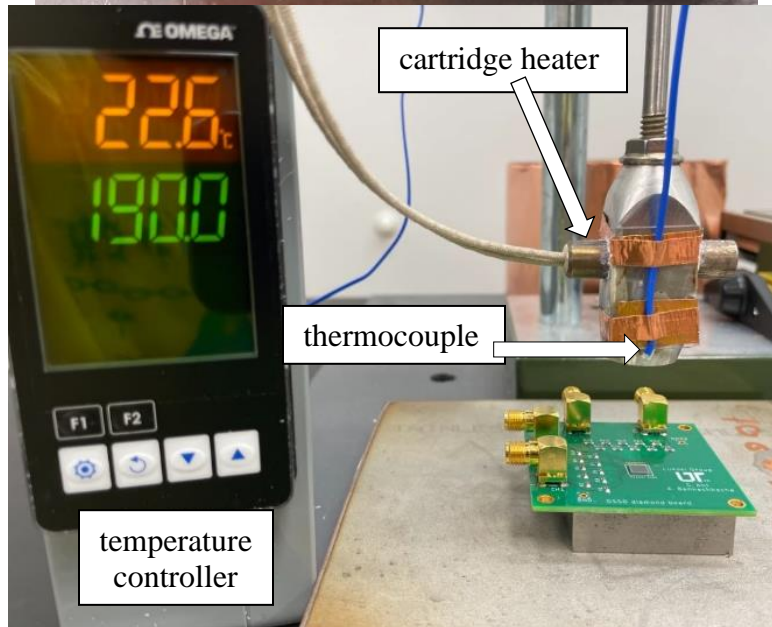
Figure 11: The PCB before mounting of the diamond detector (a), and the heat press designed for mounting the diamond to the PCB using ACF with the diamond in place (b).

Through practice, I discovered a weight that I could hang from the lever on the heat press that would apply enough pressure to form a bond, removing a considerable amount of room for error. The appropriate weight was found through trial and error. It was important to apply enough pressure to allow the conductive beads in the ACF to come into contact with the sensor and PCB to form a connection, but not too much pressure to squeeze the epoxy in the ACF out from the edges of the sensor or break the sensor. Plenty of time was spent practicing with glass cut into small squares to imitate the sensor and copper tape to test for electrical connection. Once the sensor was bonded to the PCB, it was shipped to the Princeton Institute for the Science and Technology of Materials (PRISM) for wire bonding. Figure 12 shows the mounted sensor and the finished wire bonds.

The ACF bonding and wire bond combination was the last and final attempt at fabricating the DSSD. Before this, we went through multiple fabrication/assembly combinations that failed that are simply worth mentioning. The first design had the sensor attached to a PCB with apiezon wax. The PCB had a hole in it and the apiezon wax would hold the sensor steady in the center of the hole. This left both sides of the sensor exposed so that wire bonding could be done on both sides of the sensor. Questions about robustness and difficulty in establishing wire bonds resulted a change of design, where instead of apiezon wax, we used a 3D printed mount, but still employed wire bonding on both sides. This resulted in a better looking and more robust mount, however, the space for the 3D printed mount to hold the diamond without interfering with strips was quite small (roughly 1 mm perimeter). Additionally, the depth of the mount made wire bonding more difficult than it already is. To fix this issue, we decided to employ a completely new PCB design, where the sensor attaches directly to electrodes on the PCB and wire bonding is only necessary on one side. Having the sensor on top of the PCB provides a completely open top side and a sturdy connection for robustness during wire bonding and handling. The first attempts at mounting the sensor to the PCB using this new method was reflow soldering. We struggled to get a strong bond, so the diamond would be very easily disconnected from the PCB. After failing at reflow soldering, we attempted and settled on ACF bonding after finding success.

3. Final packaging

The final packaging of the devices involves placing it in a container which could serve as a protective housing for general handling, as well as shielding from light and background radiation. The packaging had to accomplish the protection from the aforementioned variables, but also had to provide a way to place a source close to the detector face without touching the wire bonds. It also needed room for placement of a "knife-edge" for testing the spatial resolution. The PCB was mounted to posts so that it would stand off of the bottom of the container it is placed in. Additional shorter posts were connected on top of the PCB to mount a source holder. The source holder is an aluminum platform has a hole drilled in it large enough to allow alpha particles to pass through with no collimation, but small enough so that the source will not fall through and touch the detector face and wire bonds. The assembly was placed inside of a metal enclosure with dimensions $14 \times 12 \times 5$ cm^3, and holes were drilled in the side of the enclosure so that the Cividec C6 charge amplifiers could be connected from the outside.
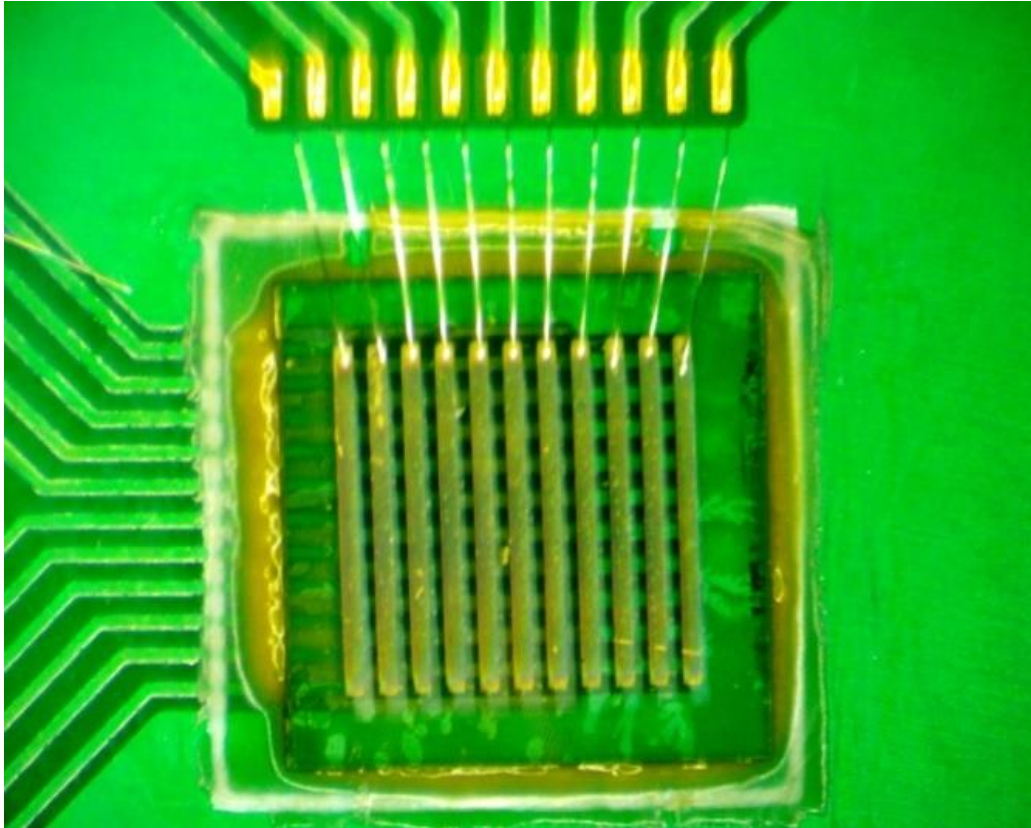
Figure 12: The sensor mounted to the PCB with ACF and wire bonding.

Figure 13a shows the detector inside of the steel enclosure with the Cividec C6 charge amplifiers attached. There is a second view looking downward at the top of the DSSD in the enclosure (b), and a diagram of the side view of the PCB assembly with the posts, and source holder (c). The distance between the source and the diamond is 3 mm, but this measurement does not account for the depth of the source.

C. DSSD Measurements

1. Open face detector

To test the initial response of the detector and get a baseline to compare with the knife edge test, we performed alpha particle measurements with the detector face completely open so that alpha particles strike the entire face of the detector. In these measurements, an ^{241}Am alpha source was placed directly on the source holder and measurements were taken in 40 second intervals. The detector bias is +300 V at the bottom of the device at readouts C & D with the top of the device at ground. Measurement intervals were kept short because polarization in the detector led to a severe reduction in count rate over time. We anticipated some level of polarization, but it was more severe than expected. After 40 seconds, the detector bias would be reversed to reverse the polarization. The detector would then be placed back at +300 V before the next measurement was started. A total of 36 measurements were taken for a total counting time of 24 minutes. To determine the position of an interaction, a pulse has to be triggered in the CAEN DT5730 digitizer at all channels (A-D) at the same time. Once the data was collected, the interaction locations were calculated using the charge division readout calibration to convert from pulse-height-ratio to interaction location. The interaction positions of each alpha particle event and the interaction position distributions were plotted to compare against the knife edge test.

Pulses can also be correlated in 2 channels at a time instead of 4, which will only reveal one-dimension of the interaction position instead of two-dimensions. This is useful in our analysis because of the poor charge collection efficiency. Far more pulses are correlated at A & B than at C & D due to charge being lost by the time electrons traverse through the 0.5 mm thick detector to readouts C & D. Furthermore, poor charge collection efficiency leads to pulses being more difficult to detect at edge strips. Pulses are further weakened at edge strips due to the fact that the charge has to move through more resistors to get to one of the readouts. This means that while one of the readouts may have quite a large pulse, another will have a weak pulse that may not trigger, making it impossible to get an interaction location. For this reason, it is important to have good charge collection efficiency. Low noise helps alleviate this issue so that the trigger level can be reduced. Plotting the pulse-height distributions shows that pulses at readouts A & B are consistently larger than those at C & D. Plotting the distribution of pulses over time also shows that the pulse rate drops to nearly zero over the course of a 40 second measurement, demonstrating the severity of polarization in the polycrystalline CVD diamond sensor. These results are demonstrated in *Results and Discussion*. Having alluded to this previously, smaller impedance resistors in the charge division readout would have made it easier to detect a single interaction at all four readouts due to an increase in signal-to-noise ratio, however, the cost is a reduction in spatial resolution. When dealing with polycrystalline diamond, this is a delicate balance.
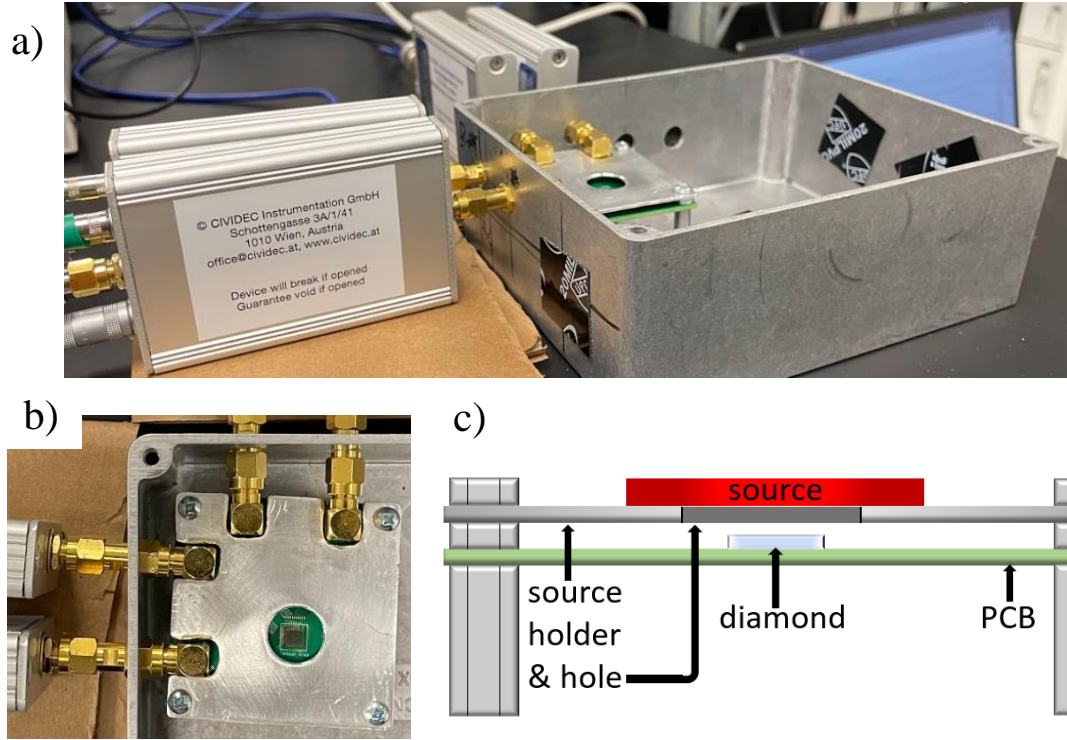
Figure 13: The DSSD in the enclosure with amplifiers connected (a) with a second view (b), and a diagram of the side view of the PCB assembly (c).

2. Knife edge test

To show that the device can determine the position of an interaction, we performed a knife edge test by placing a piece of paper over a portion of the detector to block alpha-particles. The piece of paper was placed so that the top strips 1-5 were blocked. Figure 14 shows the position of the paper during the knife edge test. The paper could not be placed on top of the wire bonds, leaving some of the strips open. The region covered by the paper is shown as the black shaded region over the sensor. The region that we could not cover due to the wire bonds is shown by the red shaded region. The interactions that occurred in the red shaded region were removed from the data during the analysis. The same alpha source was used for the knife edge test as the open face measurements. Like the open face measurements, the time interval for each of the measurements during the knife edge test was also 40 seconds. The same procedure was used to de-polarize the detector between measurements. Since nearly half of the detector is covered, a total of 72 measurements were taken (twice as many as the open face measurements) to obtain a similar number of counts in the data set. This adds to 48 minutes of total counting time. The interaction locations were calculated using the calibration information. Once the interaction positions were calculated, distributions of interaction position were plotted for the top readouts (A & B) and the bottom readouts (C & D). If the device can determine interaction location, then readouts C & D should show roughly equal distribution of interactions across all strips, while readouts A & B should show a sharp drop in counts to the left of strip 5.

The interaction position distribution across the knife edge can be fit by the edge spread function. The edge spread function (ESF) is expressed as the error function (the integral of the gaussian normal distribution), and it describes how sharply the counts drop across the knife edge (i.e., the contrast). The derivative of the ESF is the line spread function (LSF). The LSF is a gaussian normal distribution, where sigma (σ) is the standard deviation and the FWHM (2.35σ) is the spatial resolution. The FWHM spatial resolution describes how far apart two features must be in order to distinguish them apart from one another. The ESF is shown in Equation 3. The mean (μ) and standard deviation (σ) in the ESF are equivalent to that which is in the LSF, shown in Equation 4. The variables A, B, and C are fitting parameters, which transform the ESF and LSF to fit the data. The mean and standard deviation are also used as fitting parameters. The fitting method used is the least-squares method, where the independent variable (x) is the position of interaction (center of bin positions), and the bin heights of the distribution are the dependent data.

$$ESF(z) = A + B \cdot erf(z) = A + B \cdot \frac{2}{\pi} \int_0^z e^{-t^2} dt \qquad (3)$$

$$where: z = \frac{x - \mu}{\sigma\sqrt{2}}$$

$$LSF(x) = \frac{d(ESF)}{dz} = \frac{C}{\sigma\sqrt{2}} e^{-z^2} = \frac{C}{\sigma\sqrt{2\pi}} e^{-\frac{(x-\mu)^2}{2\sigma^2}} \qquad (4)$$

37
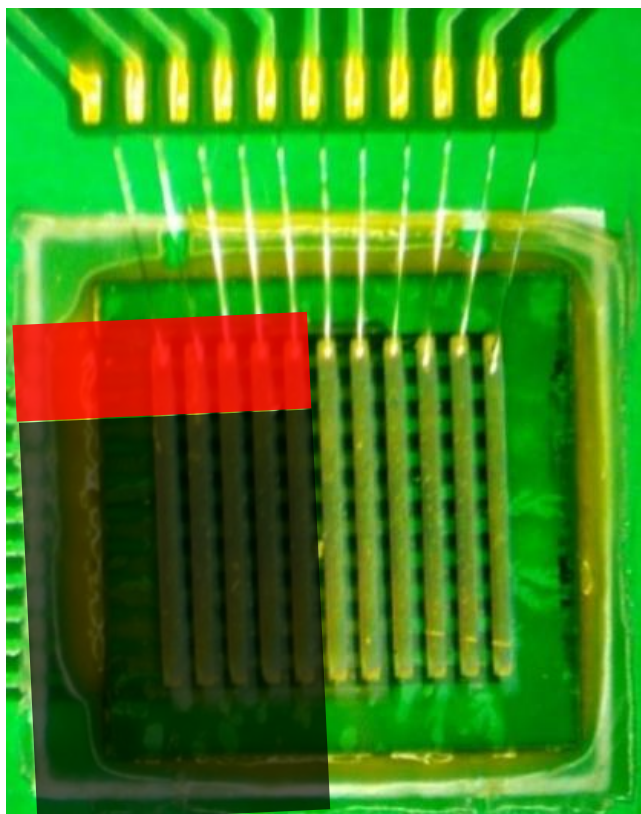
Figure 14: The position of the paper on the detector during the knife edge test, shown by the black shaded region. The region where interactions were removed from the dataset shown by the red shaded region.

D. Timing Resolution Measurements

The timing resolution of diamond has been well documented to be better than the 700 picosecond (ps) goal of the DSSD for API, but the timing resolution of a diamond detector with the Cividec C6 readout we are employing is not documented for the alpha particle energies we are interested in. For this reason, we wanted to be sure that the charge amplifiers we are using would not limit the timing resolution to something greater than 700 ps. To conduct the timing resolution measurements, we collaborated with Dr. Cordell Delzer and Dr. Xianfei Wen of Dr. Jason Hayward's research group (at the University of Tennessee Knoxville). We measured the time-of-flight of 5.48 MeV ^{241}Am alpha-particles between a thin plastic scintillator and diamond. The thin plastic scintillator used is one of a pair, which was designed strategically so that a 5.48 MeV alpha particle would pass through one scintillator, depositing on average half of its energy, before passing to the second scintillator to deposit the rest of its energy. Since our experiment involves the alpha particle passing through the scintillator before passing through the diamond, the alpha particle should deposit roughly equal energy into the scintillator and diamond, however, the experiment was conducted in air so there are energy losses which affect this. Simulations and models were used to correct for the effects of time-walk ($\sigma_{time\text{-}walk}$) and straggling ($\sigma_{straggling}$), which is further explained in the next section; *Time-Walk and Energy Straggling Corrections*. Equation 5 shows the relationship between the time-of-flight distribution and its contributing components. In the equation, sigma (σ) is one standard deviation. The timing resolution of the diamond ($\sigma_{diamond}$) is the unknown we are solving for. The timing resolution of the scintillator ($\sigma_{scintillator}$) is a known quantity. We report timing resolution as FWHM (2.35$\sigma_{diamond}$).

$$\sigma_{TOF,measured} = \sqrt{\sigma_{diamond}{}^2 + \sigma_{scintillator}{}^2 + \sigma_{time-walk}{}^2 + \sigma_{straggling}{}^2} \qquad (5)$$

A diagram of the positioning of the detectors during the timing resolution measurement is shown in Figure 15. It is also a geometric representation of the Geant4 simulations used to determine the effect of straggling and time-walk on the time-of-flight. The plastic scintillator is 20 µm thick EJ-214 produced by Eljen. It is sandwiched between two light guides that are 1.5 mm thick each [50]. The scintillator was mounted to a silicon photomultiplier (SiPM) that is not shown in the diagram. The diamond is an ElementSix™ electronic grade single crystal CVD diamond that is 5×5×0.5 mm^3. The diamond was prepared using the same cleaning and sputtering procedure as the DSSD diamond, except the contact structure varies. The contacts are planar, with a 50 nm chromium base layer and 150 nm thick gold cap layer. The contacts were also annealed in an argon environment at 600°C for 15 minutes. The diamond was mounted to the PCB using silver paste, and the PCB had a 3 mm diameter hole for passage of alpha particles. The PCB is 2 mm thick, which adds to the air that the alpha particle must pass through, increasing energy/time straggling. The other side of the diamond is electrically connected to the PCB using a spring-pin system. The spring-pin would block the face of the diamond from alpha particles and require more space between components, so the PCB had to be turned this way to allow alpha particles to pass through the hole.
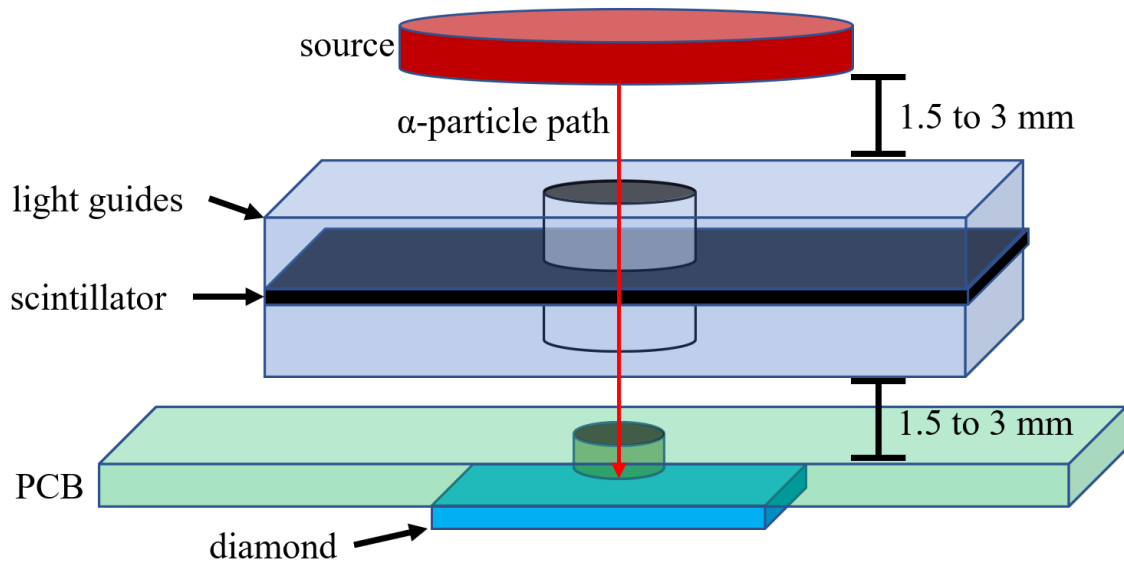
Figure 15: Diagram of the timing resolution measurement.

It was difficult to measure the distance between the source and first light guide, as well as the distance between the second light guide and PCB because we simply placed them as close as we could. We estimated these distances as between 1.5-3 mm each. These dimensions are reflected in Figure 15. This equates to the alpha particle passing through 3-4.5 mm of air before reaching the scintillator, then another 5-6.5 mm of air before striking the diamond. Lastly, the timing resolution measurements were completed while collecting electrons and holes separately using +200 V and -200 V biases, respectively. The diamond was connected to a Cividec C6 charge amplifier. Both the diamond and scintillator readouts were plugged into a Paul Scherrer Institut (PSI) DRS4 digitizer with a 5 GHz sampling rate.

1. Time-Walk and Energy Straggling Corrections

In order to capture the timing resolution of the diamond detector with the Cividec C6 readout, we measured the time-of-flight (TOF) of an [241]Am alpha particle between a thin plastic scintillator with a known timing resolution and the diamond detector. While doing this, we create a TOF distribution, which is gaussian in shape. The width of this distribution describes the timing resolution of our system. As alluded to previously, we have energy straggling due to energy losses in the air, negatively effecting the TOF measurement. This results in fluctuations in the TOF and a widening of the TOF distribution that is not contributed to the timing resolution of the detectors themselves. Furthermore, the alpha particles pass through the thin plastic scintillator before passing through more air on their way to the diamond. While the scintillator thickness is designed such that half of the energy of the alpha particle is typically deposited in each detector, there are fluctuations in this. These fluctuations also lead to variations in the energy of the alpha particle as it travels between the sensors, and thus, fluctuations in the TOF. We used Geant4 to model our measurement setup and quantify the contribution that energy straggling had in widening the TOF distribution. Using the simulation, we could better estimate the timing resolution of the diamond with Cividec C6 readout. The Geant4 simulation contained the scintillator and light guides, the PCB, the diamond sensor, the alpha source, and the air around it (see Figure 15). By collecting the TOF in Geant4, we were able to generate a TOF distribution due primarily to straggling. The straggling TOF distribution was fitted with a gaussian, and the standard deviation ($\sigma_{straggling}$) was found. This was used to remove the effect of straggling according to Equation 5.

Energy straggling also contributes to time-walk. Time-walk is caused by the Cividec C6 shaping amplifier having a fixed rise time. Since it has a fixed rise time, fluctuations in energy depositions will result in fluctuations in the time for which an event pulse is triggered relative to when the event occurred. This is because of variations in the slope of the leading edge of the pulse. This negatively effects the timing resolution in any case where the alpha particles striking the detector are not mono-energetic. The timing resolution experiment was in air and the alpha particles had to pass through a scintillator before reaching the diamond, so energy straggling has a role in the timing resolution measurement. By quantifying the time-walk in our experiment, we could better estimate what the timing resolution of a diamond detector with a Cividec C6 readout would be in a neutron generator. The Geant4 simulation also models the energy deposition in the

41

diamond detector. After modeling the fluctuations in the energy depositions, we had to model Cividec C6 pulses with varying heights according to the energy depositions. To do this, an exponentially modified gaussian (EMG) was used to accurately capture the leading edge and height of the Cividec C6 pulses. The EMG is shown in Equation 5, where the independent variable is time (t), the height of the pulse (h) will vary depending on the energy deposited, the shape of the pulse is fixed (described by both σ and τ), and the peak is centered around μ.

$$f(t, h, \mu, \sigma, \tau) = \frac{h\sigma}{\tau} \sqrt{\frac{\pi}{2}} exp\left(\frac{1}{2}\left(\frac{\sigma}{\tau}\right)^2 - \frac{t-\mu}{\tau}\right) \cdot erfc\left(\frac{1}{\sqrt{2}}\left(\frac{\sigma}{\tau} - \frac{t-\mu}{\sigma}\right)\right) \qquad (6)$$

An example of a Cividec C6 pulse next to the EMG model are shown in Figure 16. It models the pulse accurate at the leading edge and through the first part of the tailing edge. We are primarily concerned with the leading edge in our model, so slight inaccuracies in the tail are not a cause for concern. We chose a trigger level in the model that is consistent with the trigger level we used for the experiment. More specifically, the ratio between the trigger level and the average pulse-height during the experiment is equal to the ratio between the trigger level and the average pulse-height in the model. At that trigger level, we determined the time for which for which every model pulse reached the trigger level. The mean trigger time and standard deviation ($\sigma_{time-walk}$) were calculated. The standard deviation was plugged into Equation 5 to calculate the timing resolution of the diamond detector with Cividec C6 readout.

RESULTS AND DISCUSSION

In this chapter, the results of our models, experiments, and calculations will be summarized. These include the results from the charge division readout calibration, the DSSD open face and knife edge measurements, the timing resolution measurements, and results from the time-walk and energy straggling corrections.

A. Charge Division Readout Calibration

The charge division readout calibration includes two subsections. One section for the calibration of readout channels A & B, and one for readout channels C & D. The calibrations are used directly for conversion of pulse-height-ratio to interaction location. Each readout side provides the alpha particle interaction position in one dimension. The top side of the detector has channels A & B, and the bottom side as C & D. Both combined provide two-dimensions of spatial resolution.

1. *Channels A & B*

The distribution of pulse-height-ratios after injecting charge into each strip of the charge division readout, and charge into neighboring strips, are shown in Figure 17 and Figure 18, respectively. There are a few notable features in Figure 17. When we inject charge into strip 1, we get the largest pulse-height-ratios. That is because the charge goes through zero resistors on its way to readout A.
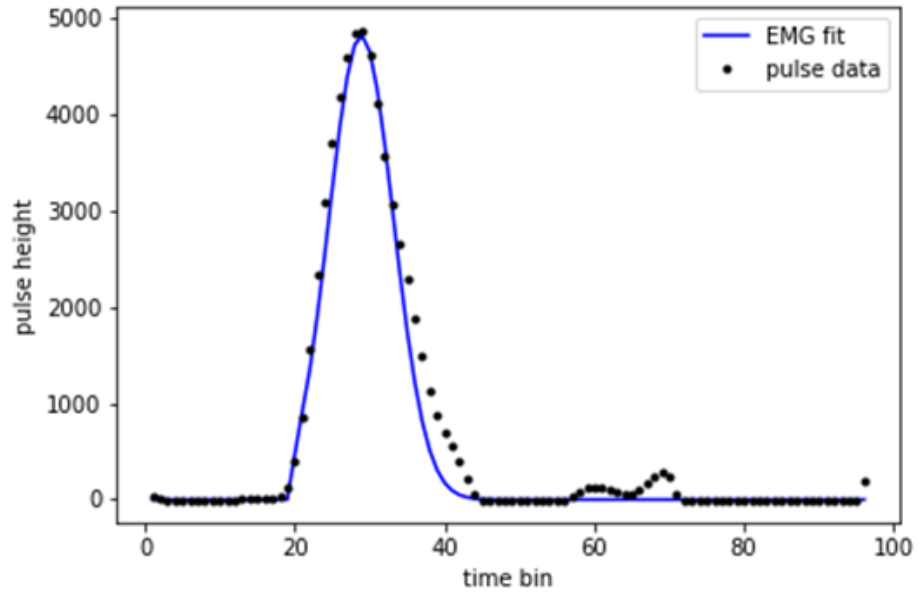
Figure 16: The EMG pulse model with a measured Cividec C6 alpha pulse.
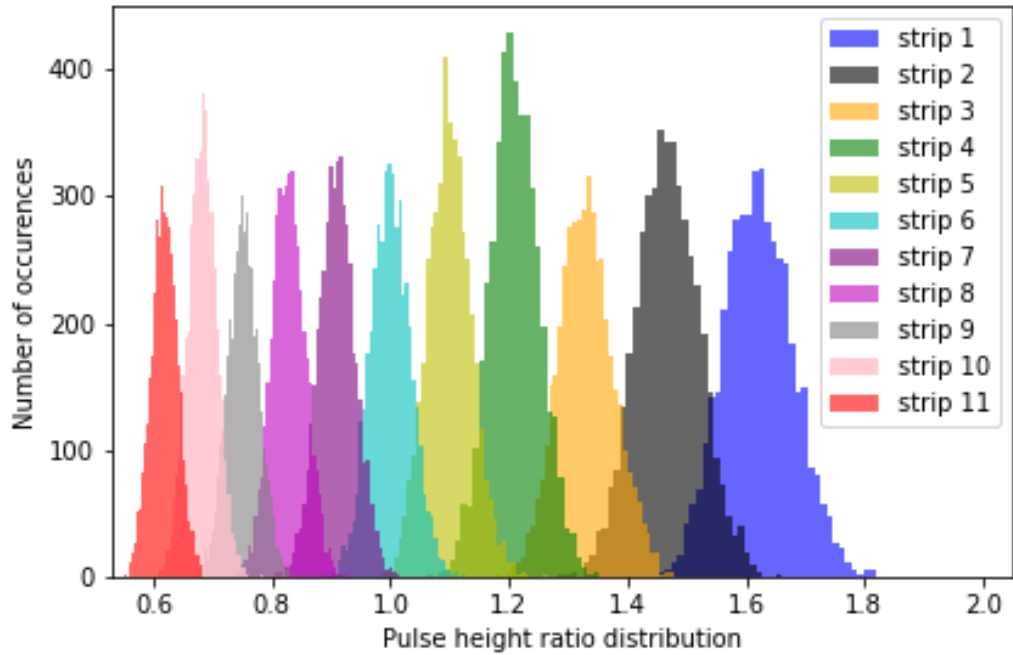
Figure 17: The pulse-height-ratio distributions of injecting charge into each strip of the charge division readout for the top of the detector at channels A & B.
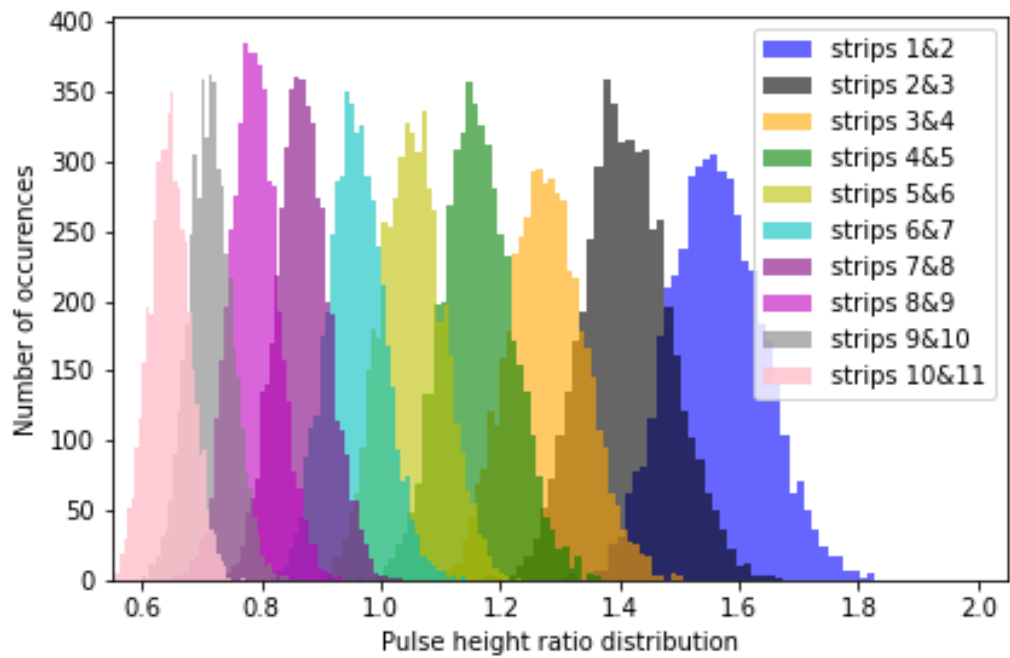
Figure 18: The pulse-height-ratio distributions of injecting charge into neighboring strips in the charge division readout for the top of the detector at channels A & B.

Comparatively, strip 11 has the smallest pulse-height-ratios. In between strips 1 and 11, we see a consistent decrease in the pulse-height-ratios. Notice that there is some overlap between the pulse-height-ratio distributions at neighboring strips. This means that there is possibility for misclassification of one strip over. There is very little overlap between the pulse-height-ratio distributions at strips that are two positions over (for example, strips 1 and 3 have very little overlap). This means that we are unlikely to have a misclassification of 2 strips over. Another notable feature is that the distributions get wider from strip 11 to strip 1. This is expected, because as the pulse-height-ratio gets larger, then the distribution should get wider to maintain the same "resolution" across the device. To focus on instances of charge sharing between strips, see Figure 18. Notice that these distributions follow the same pattern. One key difference is that the distributions are wider when sharing charge, leading to more uncertainty. The mean pulse-height-ratio was found for each scenario (charge into each strip and sharing charge between neighboring strips). The relationship of pulse-height-ratio versus strip of injection was plotted and a 2nd order best fit was found using least squares method. The results are shown in Figure 19. The data points are the mean pulse-height-ratios for each position of charge injection in the readout. The error bars are the standard deviation. The data points between integer values (i.e., 1.5, 2.5, 3.5, etc.) are positions where charge is shared between strips, so it is modeled as an interaction directly between the strips. The 2nd order best fit equation is used as a direct conversion from pulse-height-ratio of an alpha detection to strip position of the interaction.

2. *Channels C & D*

The calibration process of readout channels C & D is identical to that of A & B. The only differences in the results are the resulting mean pulse-height-ratios and 2nd order best fit coefficients. The results are slightly different from A & B due to the slight variations in gain between different Cividec C6 charge amplifiers. The distribution of pulse-height-ratios after injecting charge into each strip of the charge division readout is shown in Figure 20. As you can see, the same patterns are seen in C & D as were seen in A & B. The mean pulse-height-ratio was found for each scenario with a best fit in the same manner as channels A & B. The results are shown in Figure 21.

B. DSSD Measurements

The DSSD measurement results will be split into two subsections. One subsection for the open face detector and one for the knife edge test.

1. *Open face detector*

In the open face measurements, the source was placed 3 mm from the surface of the diamond with nothing obstructing the path of the alpha particles. This means that alpha particles were striking the entire face of the detector. After collecting the data, the calibration information was used to calculate the interaction location of each event in the detector. The positions of the interactions are plotted in Figure 22. The position distributions are plotted in Figure 23, which simply illustrate the same data in a different way. This also illustrates that the center of the crystal is where most events are detected. Even though the detector face is open, there are regions with no counts or few counts.
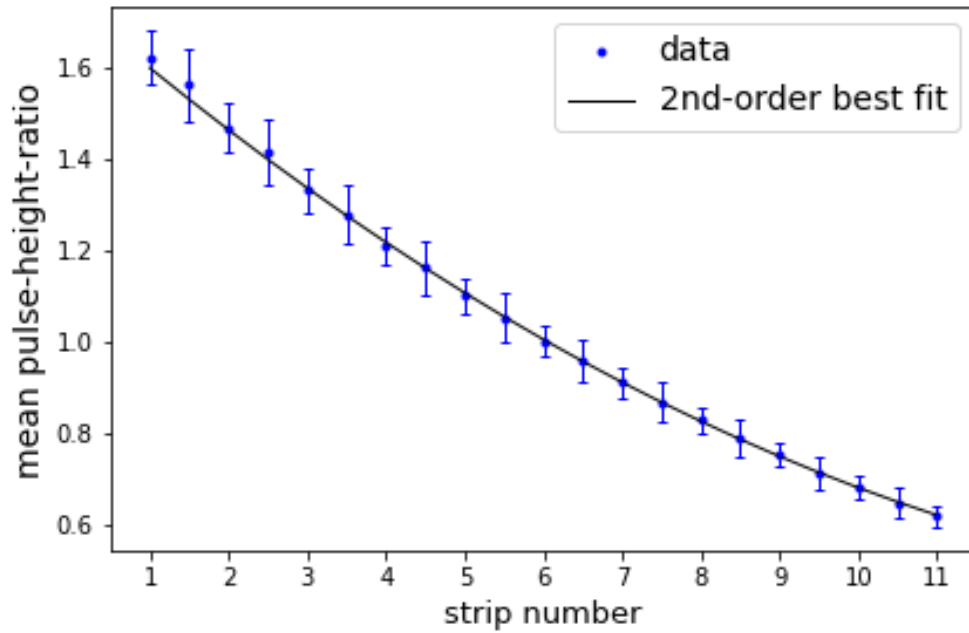
Figure 19: Channels A & B pulse-height-ratio versus strip of charge injection.
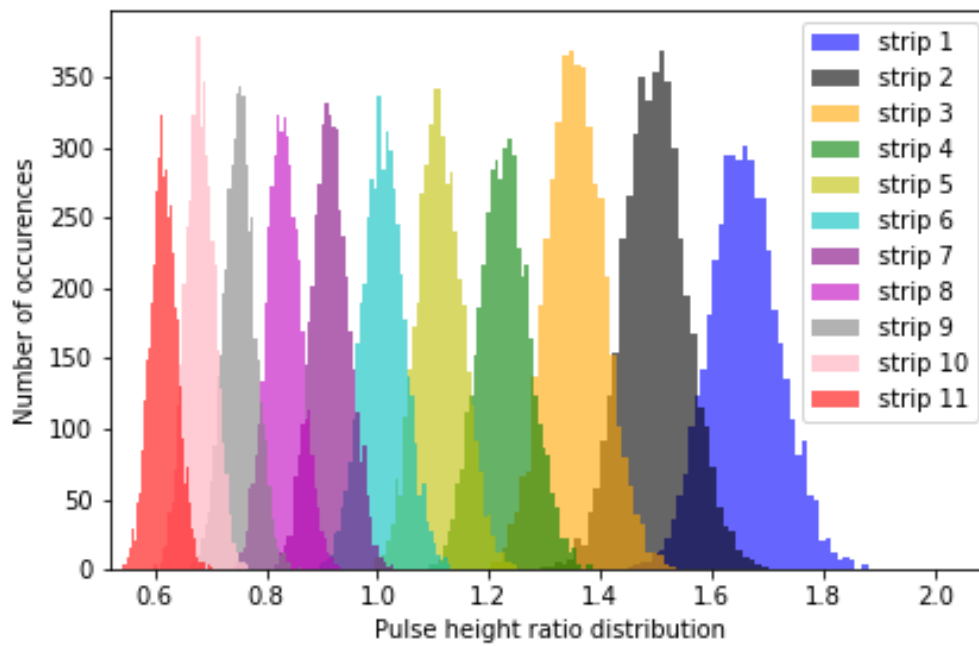
Figure 20: The pulse-height-ratio distributions of injecting charge into each strip of the charge division readout for the bottom of the detector at channels C & D.
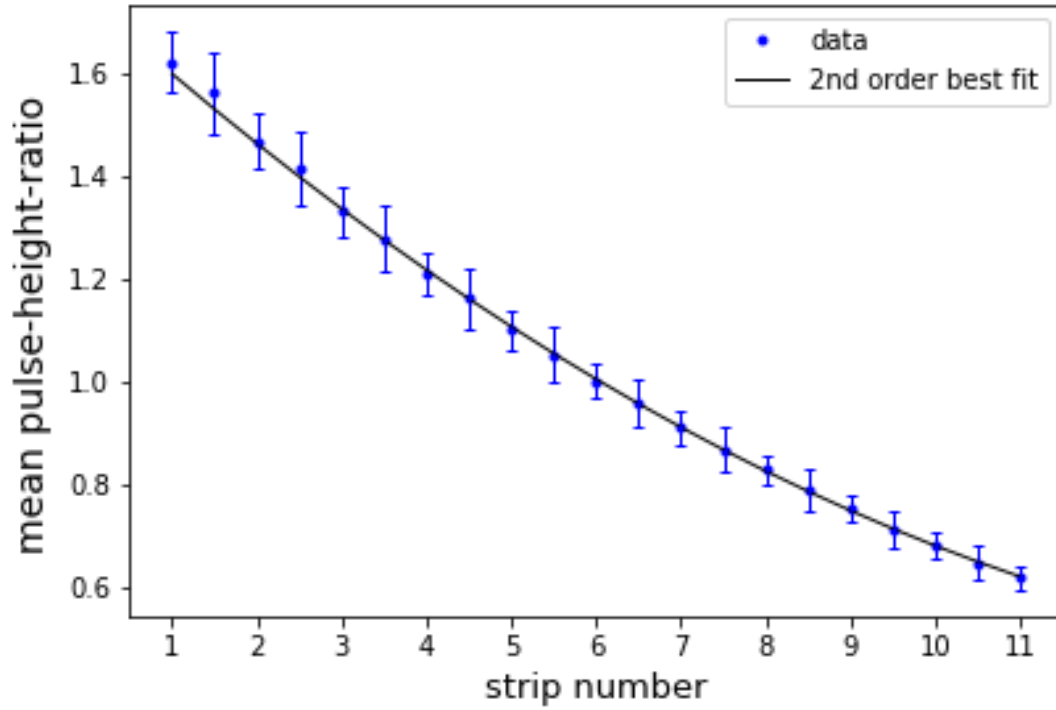
Figure 21: Channels C & D pulse-height-ratio versus strip of charge injection.
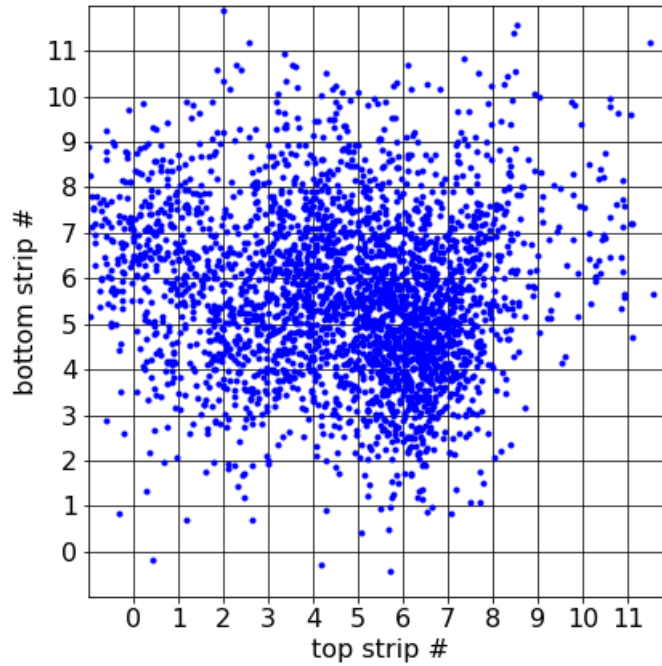
Figure 22: Alpha particle interaction positions during the open face detector measurements.
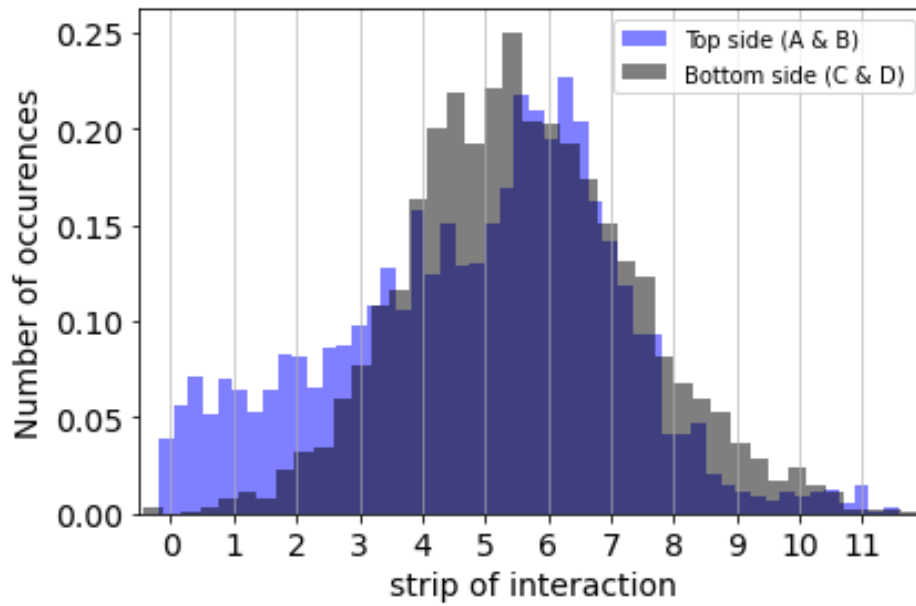
Figure 23: Alpha particle interaction position distributions during the open face detector measurements.

We observed this consistently in our open face measurements. Since the regions with few and no counts were consistently in the same areas of the detector face, we contribute this to specific regions of the crystal being either dead or having very poor charge collection efficiency due to grain boundaries and traps. This is not uncommon for polycrystalline CVD diamond. Figure 24 also illustrates another issue with polycrystalline diamond. Notice that the pulse heights at readouts C & D are much smaller than those at readouts A & B. This is due to poor charge collection efficiency because charge is lost as it travels the ~0.5 mm from the top side of the detector to the bottom side readout. This makes it more difficult to trigger pulses at readouts C & D because the signal-to-noise ratio is worse. This leads us to another explanation of "dead" regions, primarily around the edges of the device. Around the edges of the detector, the charge has to move through more resistors to reach one of the readouts. This leads to degradation in the pulse height at that readout. If charge collection efficiency is weak, and the magnitude of the pulse is further weakened by the path through the resistors, then it is even more difficult to trigger the pulse at one readout. Even if the other readouts successfully trigger the pulse, the system requires all four readouts to trigger in order to get an interaction location in two-dimensions. However, we can analyze the data in one dimension at a time to test and compare the performance of each dimension. We predicted that the top side readouts (channels A & B) will have much better performance due to the charge losses associated with the bottom side readout (channels C & D). When comparing the two, this is exactly what we saw. Of all of the events that triggered at both channels C & D, 99.5% of those also led to triggers at channels A & B. However, of all of the events that triggered at both channels A & B, only 9% of those also led to triggers at channels C & D. This has very significant implications on how many events lead to triggers in all four channels. While a better signal-to-noise ratio would certainly help with pulse-heights being more precise, variations in the energy deposited or the charge collected should have very little effect on the pulse-height ratio itself. This means that if both readouts see enough charge collection to simply trigger, then an interaction location can be determined regardless of poor CCE. With that said, the interaction position will become more accurate as the signal-to-noise ratio increases.

2. *Knife edge test*

The open face measurements aided us in setting up the knife edge test in the following ways. First, it was important to block off a region that we know is active and regularly receives counts. Blocking off a portion of the detector that does not receive counts would negate the purpose of the knife edge test. This is why the top side (vertical) strips 1-5 were blocked by the piece of paper placed in the knife edge test. This also means that we are essentially testing the position resolution in one dimension, which is the dimension that the top side (channels A & B) takes care of. This gives us a better idea of what the design is capable of with a device that has good charge collection efficiency. Lastly, horizontal knife edge tests to determine the spatial resolution in the second dimension (taken care of by channels C & D at the bottom side) were unsuccessful. It became impossible to get events to trigger enough to obtain the data necessary for a horizontally oriented knife edge test. Figure 25 shows the alpha particle interactions during the knife edge test. The shaded region demonstrates what area of the detector was covered by the piece of paper.
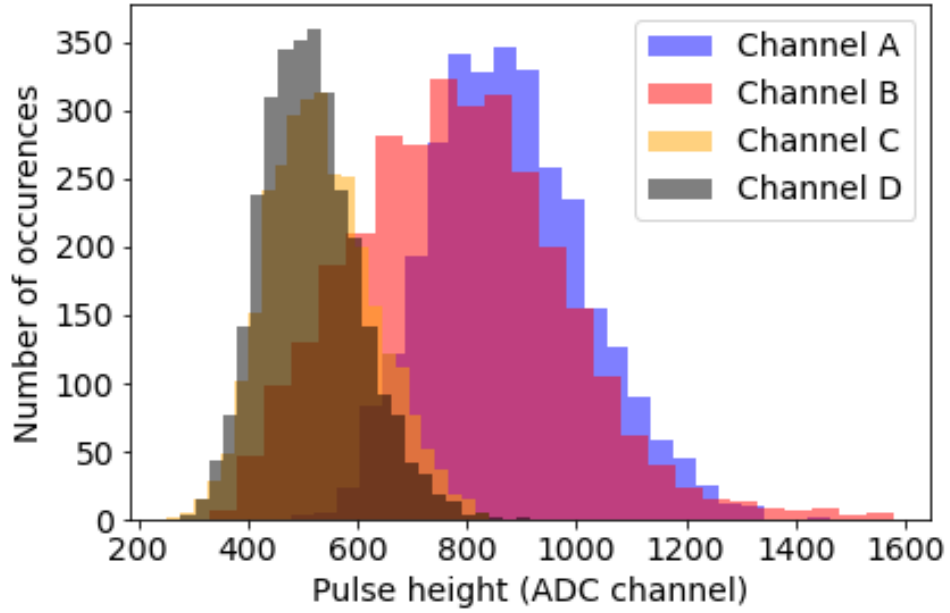
Figure 24: Pulse height distributions from each channel in the charge division readout.
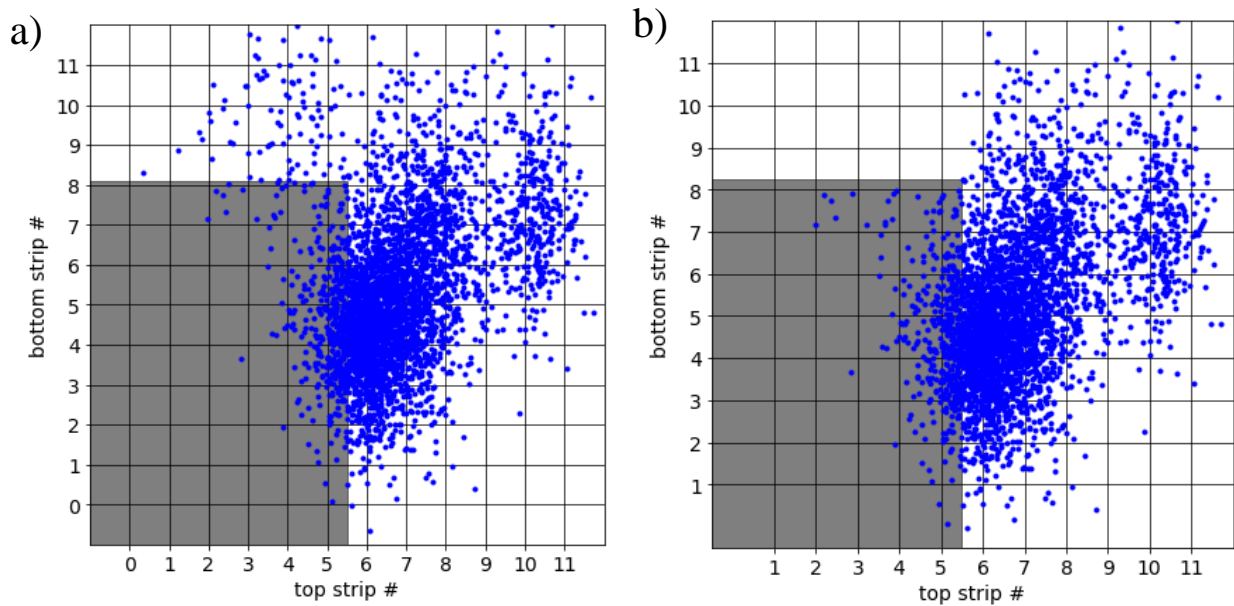
Figure 25: The alpha particle interaction positions during the knife edge test before filtering (a) and after filtering out the region that could not be blocked by the knife edge (b). The shaded regions shows where the piece of paper was blocking the detector.

The region above the shaded region is where the piece of paper could not be placed because of wire bonds being in the way. For that reason, we removed the interactions that occurred in that region for our analysis. Figure 25a shows all of the interactions before removing any data. Figure 25b shows what interactions were used after removing data, which is what we use for the rest of the analysis.

Interaction position distributions from the top side (A & B) and the bottom side (C & D) are shown in Figure 26. As you can see, the counts on strips 1-5 drop dramatically at the top readout because of the piece of paper, or knife edge. Since the bottom side readout did not have any strips blocked off completely by the knife edge, the distribution is centered mostly around the middle of the detector (strip 6), although dead regions and poor charge collection efficiency do shift that distribution slightly. Analysis of the top side distribution can tell use the position sensitivity, and the spatial resolution in the dimension that is taken care by readout channels A & B. After fitting the ESF to the distribution, then finding the LSF, we could calculate the spatial resolution. The spatial resolution was measured at 388 µm (FWHM), which is better than the 500 µm goal. The channel A & B position distribution with the ESF and LSF are shown in Figure 27. If the charge collection efficiency was better such that channels C & D performed identically to channels A & B, then the spatial resolution in C & D would be the same. If the charge collection efficiency was nearing 100% as it does in many single crystal CVD diamond sensors, then signal-to-noise ratio would be much larger, and the spatial resolution could be significantly improved. The resistor impedances in the charge division readout could also be increased, leading to more separation in the pulse-height-ratios with respect to strip of charge collection. This would even further improve the spatial resolution.

Lastly, the polarization in our detector caused the count rate to decrease over the 40 second counting interval of each measurement. This required resetting the detector between measurements. Figure 28 shows the decrease in count rate during the counting time. The counting time starts almost immediately after bias is applied. By the end of the 40 second counting time, you can see that there are almost no detection events due to the severe polarization within the crystal.

C. Timing Resolution Measurements

Like the previous sections of results, the timing resolution measurements will be split into subsections. First, we will talk about the energy straggling corrections and time-walk corrections. This will be followed by the time-of-flight measurements and the determined timing resolution of the diamond detector with Cividec C6 readout.

1. Time-Walk and Energy Straggling Corrections

To correct for energy straggling which contributes to spreading out the time-of-flight distribution, we modeled the system in Geant4. We did two different simulations with two different spacings to come up with a range for which our system operated. One simulation had short spacing between components, and one had larger spacing. The Geant4 simulation with short spacing had 1.5 mm between the source and scintillator, and 1.5 mm between the scintillator and diamond. The Geant4 simulation with large spacing had 3 mm between the source and scintillator, and 3 mm between the scintillator and diamond.
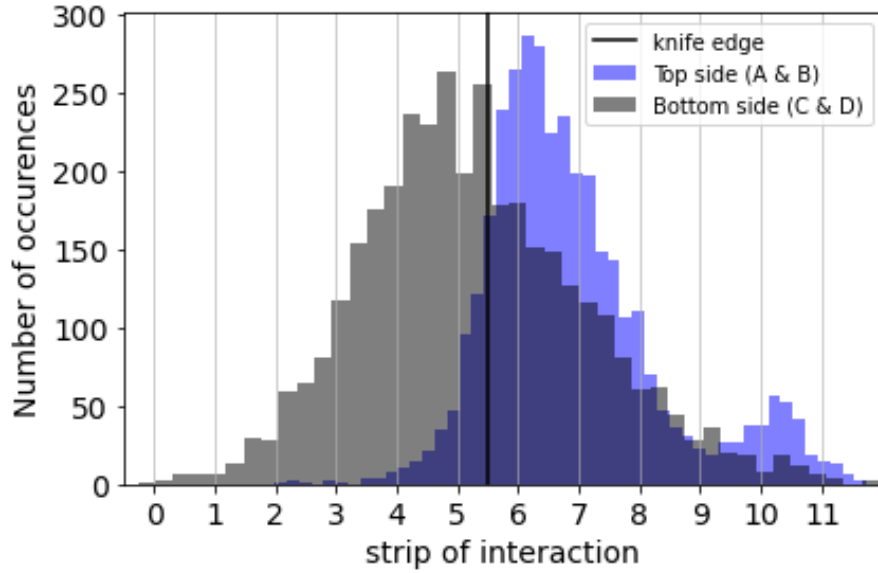
Figure 26: The alpha particle interaction position distributions for the top side and bottom side. The position of the knife edge which blocked strips 1-5 on the top side is shown.
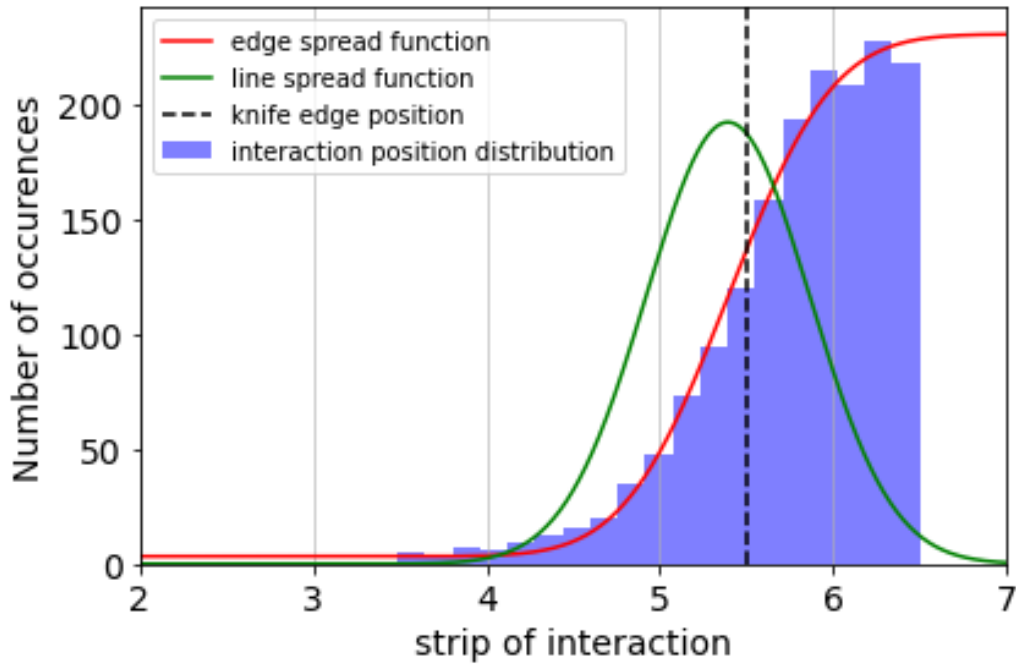
Figure 27: The position distribution of the top side readout (channels A & B) during the knife edge test, plotted with the edge spread function (ESF), the line spread function (LSF), and the position of the edge of the knife edge.
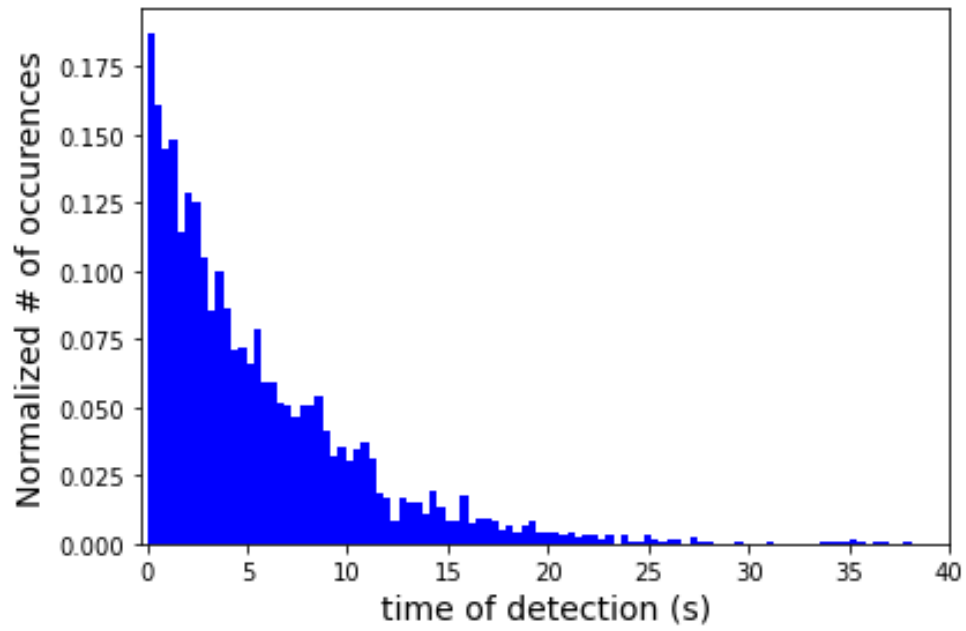
Figure 28: The time distribution detected events during the 40 second counting interval.

These spacings were chosen for our simulation because we estimate that the spacing between each component was between 1.5-3 mm. These spacing differences yield significantly different results in the time-walk and energy straggling corrections. Consequentially, they lead to significantly different calculations of the timing resolution of the diamond. Realistically, the timing resolution falls somewhere in between the two calculations. The time-of-flight distribution for each of the two simulations is shown in Figure 29. Two plots are in the figure, one of the smaller 1.5 mm spacing (a), and one of the larger 3 mm spacing (b). Each plot has the distribution of simulation data, with the shaded region representing one standard deviation around the mean. The gaussian normal distribution is plotted with it to show how well the simulation data matches the normal distribution. The mean (μ) and standard deviation (σ) with the shorter spacing is 0.459 ns and 0.00502 ns, respectively. The mean (μ) and standard deviation (σ) with the larger spacing is 0.686 ns and 0.0136 ns, respectively. This gives us two bounds on the possible values for $\sigma_{straggling}$ in Equation 5. So, 0.00502 ns $\leq \sigma_{straggling} \leq$ 0.0136 ns. The energy deposited distributions in the scintillator and diamond are shown in Figure 30. These were also generated using the Geant4 simulation. The air contributes significantly to energy losses and energy straggling, which widens the time-of-flight distribution significantly. Making these corrections means that we will more accurately capture the timing resolution of the diamond sensor.

To model the effect of time-walk due to the Cividec C6 charge amplifier having a fixed rise time, we used the energy deposition data from Geant4 simulations as inputs for the pulse model. Each alpha particle deposition in the Geant4 simulation was used to model a Cividec C6 pulse. We modeled each pulse shape with the exponentially modified gaussian. After modeling every energy deposition from the simulation, we found the mean trigger time (the time when the pulses cross the trigger value). To calculate the time-walk distribution, the time that each pulse crossed the trigger was evaluated relative to the mean trigger time. This was also completed for both the short and long spacing. Figure 31 shows the time walk distribution from the model with short spacing on top and large spacing on bottom. Notice that the distributions do not have a gaussian shape. We are relying on gaussian statistics in the rest of our experimental and simulation data because the rest of the data follows a normal distribution. Each component of our time-of-flight distribution (i.e., $\sigma_{diamond}$, $\sigma_{scintillator}$, $\sigma_{time\text{-}walk}$, $\sigma_{straggling}$) is expressed as one standard deviation in the normal distribution. The standard deviation defines the width of the region for which 68% of the data lies. Meaning 34% of the data lies one standard deviation to the right of the mean, and 34% of the data lies one standard deviation to the left of the mean. To calculate $\sigma_{time\text{-}walk}$ with a statistical certainty of 68%, we found the mean time walk. We then moved left of the mean until 34% of the data was included. We followed by moving right of the mean until another 34% of the data was included. Of course, because our data is skewed (not normal), the amount that we must move left, and right are not equal. However, the sum of the two expresses the total width of the region around the mean which covers 68% of the data. This total width is shown by the shaded regions in Figure 31, and is labeled as the "1-sigma confidence interval". Half of the width of this shaded region is equal to our definition of one standard deviation in the time walk distribution ($\sigma_{time\text{-}walk}$).

54
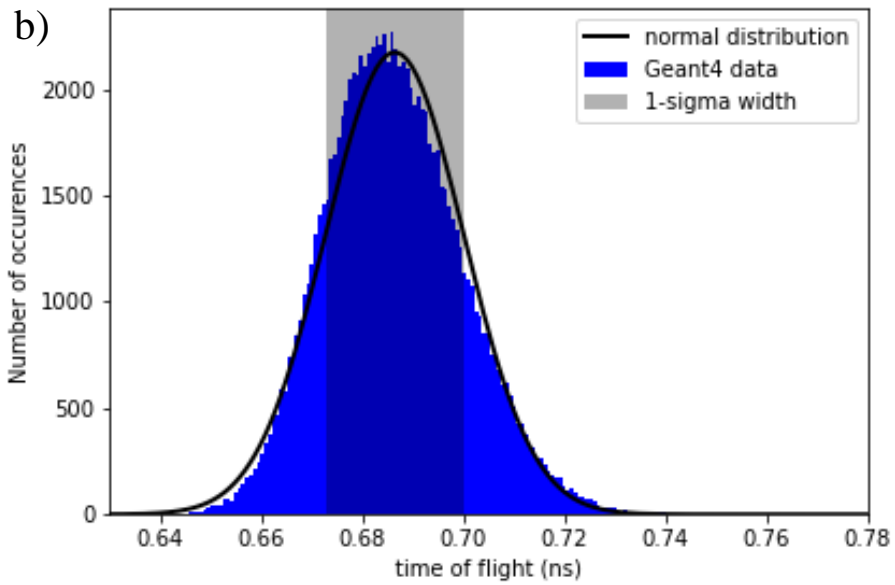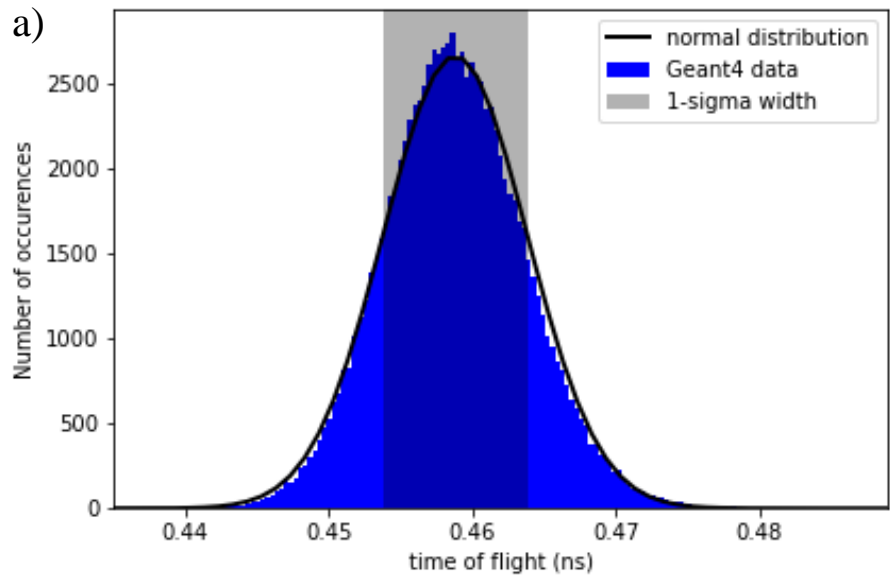
Figure 29: The time-of-flight distributions due to energy straggling of alpha particles in the plastic scintillator and air. Showing the results of the simulation with the shorter spacing (a), and with the larger spacing (b).
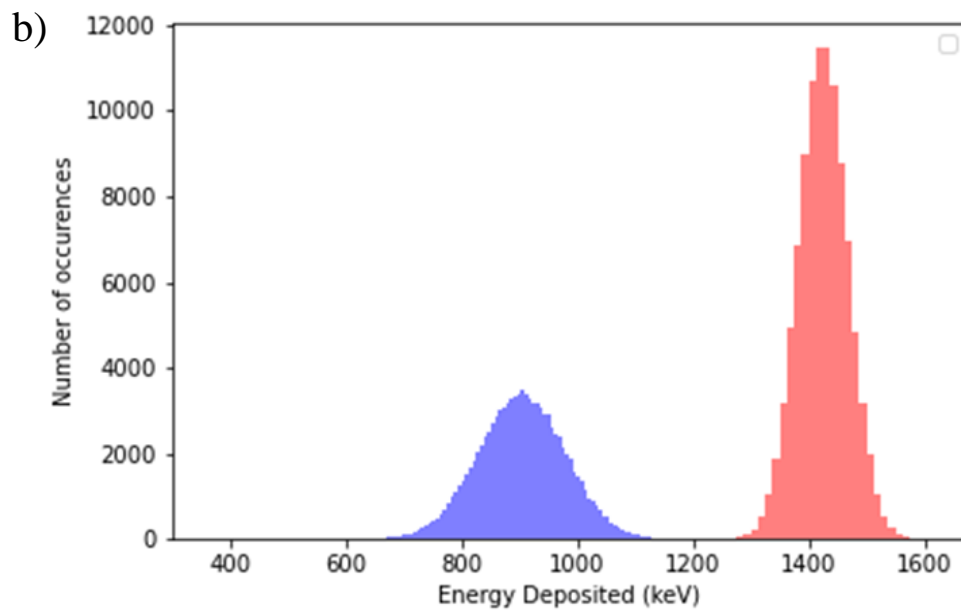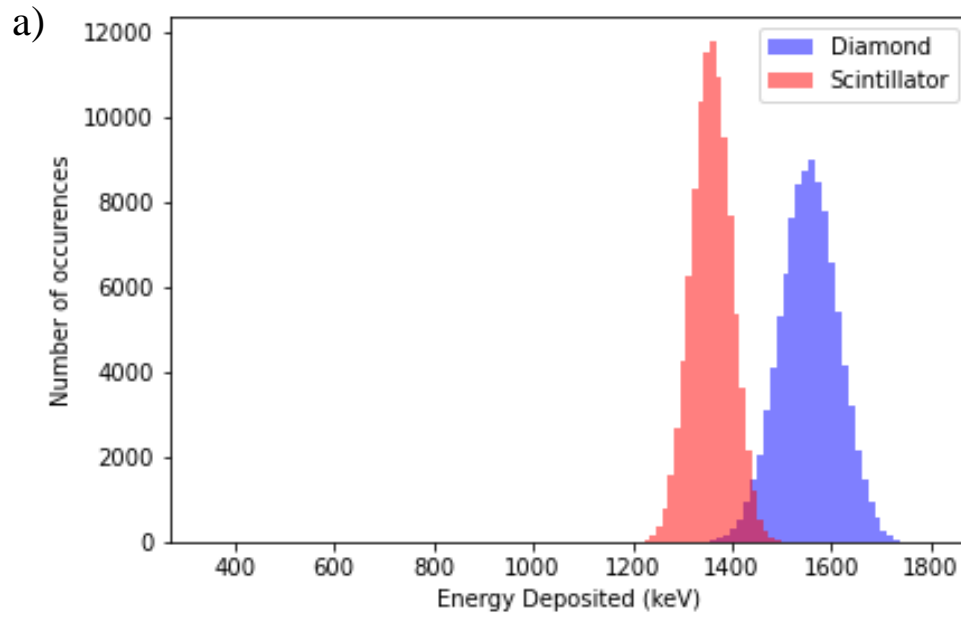
Figure 30: The energy deposited distributions in the scintillator and diamond from the Geant4 simulation with two different spacings. Showing the shorter 1.5 mm spacing (a) and the larger 3 mm spacing (b).
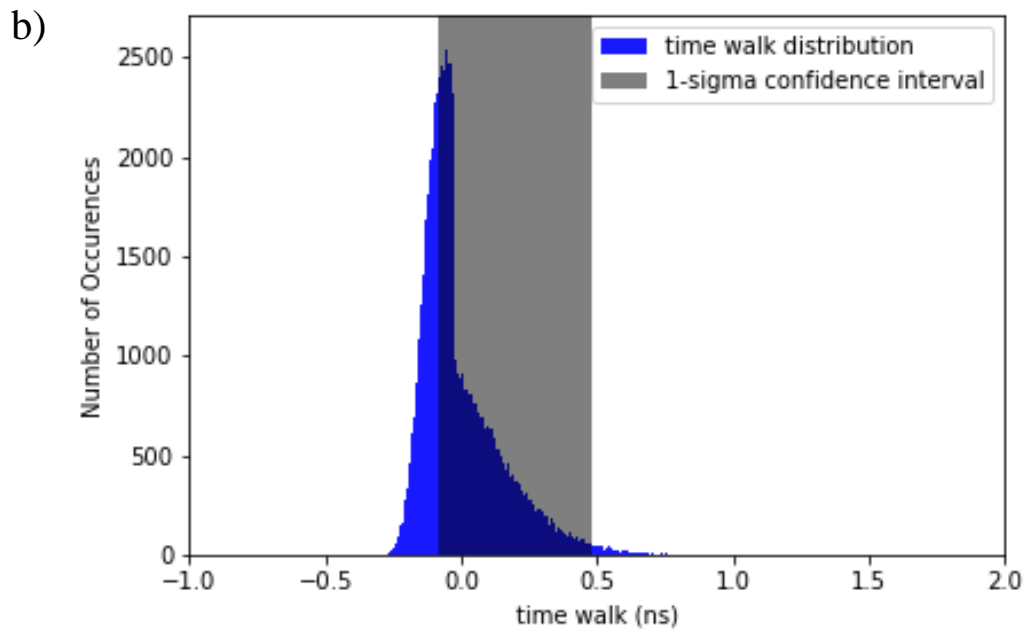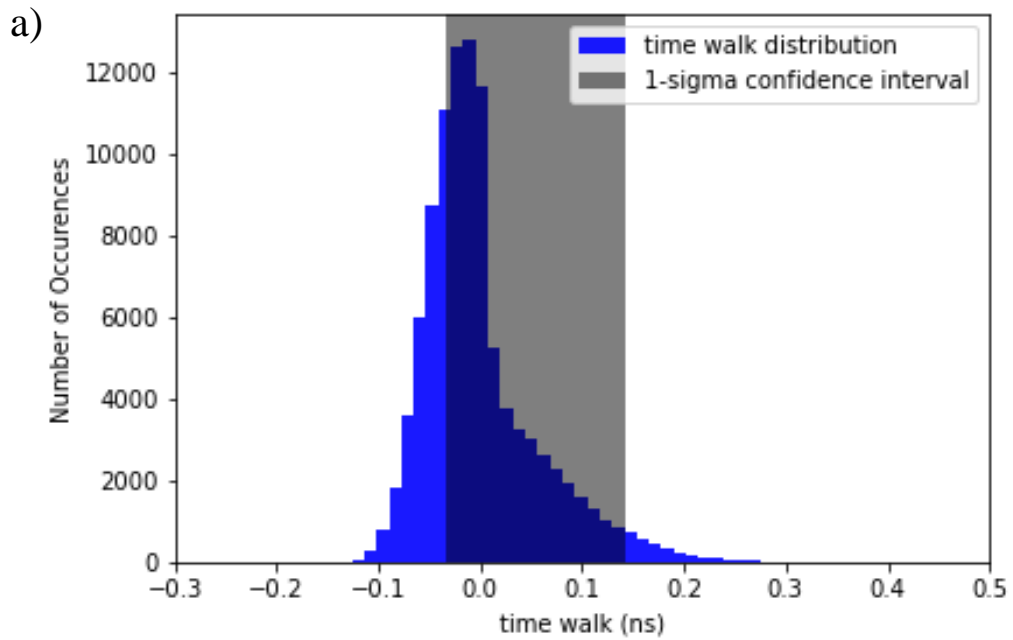
Figure 31: The modeled time walk distribution modeled using short spacing in the Geant4 simulation (a) and larger spacing (b).

To illustrate what the distribution of pulses looks like due to the time walk in our system, Figure 32 shows all of the pulses modeled on top of one another, with the trigger level illustrated by the dashed line, and a single pulse which represents that of a mean energy deposition (labeled average pulse). Observing the pulses reveals that the higher the trigger level, the more the trigger time will deviate, resulting in even larger $\sigma_{time\text{-}walk}$. The magnitude of $\sigma_{time-walk}$ is 0.0874 ns and 0.284 ns for 1.5 mm and 3 mm spacing, respectively. To summarize the experimentally measured data and modeling data, all values with the short spacing and large spacing are listed in Table 1 (provided in the next section: *Time-of-flight measurements*).

2. *Time-of-flight measurements*

We measured the time-of-flight of alpha particles between the scintillator and diamond in order to measure the timing resolution of the diamond. We measured the timing resolution of the diamond while collecting both electrons and holes. The time-of-flight distribution while collecting electrons is shown in Figure 33. The time-of-flight distribution while collecting holes is shown in Figure 34. The standard deviation in the time-of-flight distributions ($\sigma_{TOF,\ measured}$) for electrons and holes are 0.303 ns and 0.325 ns, respectively. These values are plugged into Equation 5 with the known scintillator timing resolution ($\sigma_{scintillator} = 0.0728$ ns), and the values found using Geant4 simulations and pulse modeling ($\sigma_{time\text{-}walk}$ and $\sigma_{straggling}$). After solving for the timing resolution of diamond, we found that sigma lies in the range 0.177 ns $\leq \sigma_{diamond} \leq$ 0.660 ns, while collecting electrons. While collecting holes, sigma lies in the range 0.328 ns $\leq \sigma_{diamond} \leq$ 0.715 ns. This means that the FWHM timing resolution of our diamond detector with the Cividec C6 readout is likely better than the 700 ps goal. The higher end of our range is slightly above the goal while collecting holes, but not electrons. The modeling shows that the spacing between our source and detectors had a large influence on energy straggling. Since we estimate our spacing somewhere in the middle of these two values, we can estimate the timing resolution of the diamond as being somewhere close to the middle of these values as well. If we split the difference, that gives us 419 ps and 522 ps while collecting electrons and holes, respectively.

CONCLUSIONS AND FUTURE WORK

The DSSD was fabricated and tested for its spatial resolution, and the timing resolution of a diamond detector with a Cividec C6 charge division readout was measured. We were only able to measure the one-dimensional spatial resolution of the DSSD; however, it did fall within the 500 µm goal at 388 µm. The timing resolution measurements were better than the 700 ps goal after correcting for energy straggling, and time-walk in our system. Polycrystalline diamond often suffers from poorer charge collection efficiency than single crystal, and our DSSD was no exception to this. Lower than expected charge collection efficiency resulted in low pulse-heights and low signal-to-noise ratio, making it difficult to trigger pulses above noise. This was especially true at the bottom readout (C & D). Determining interaction location of an alpha particle relies on the calibration data, which in turn relies on pulse-heights with good signal-to-noise ratio.
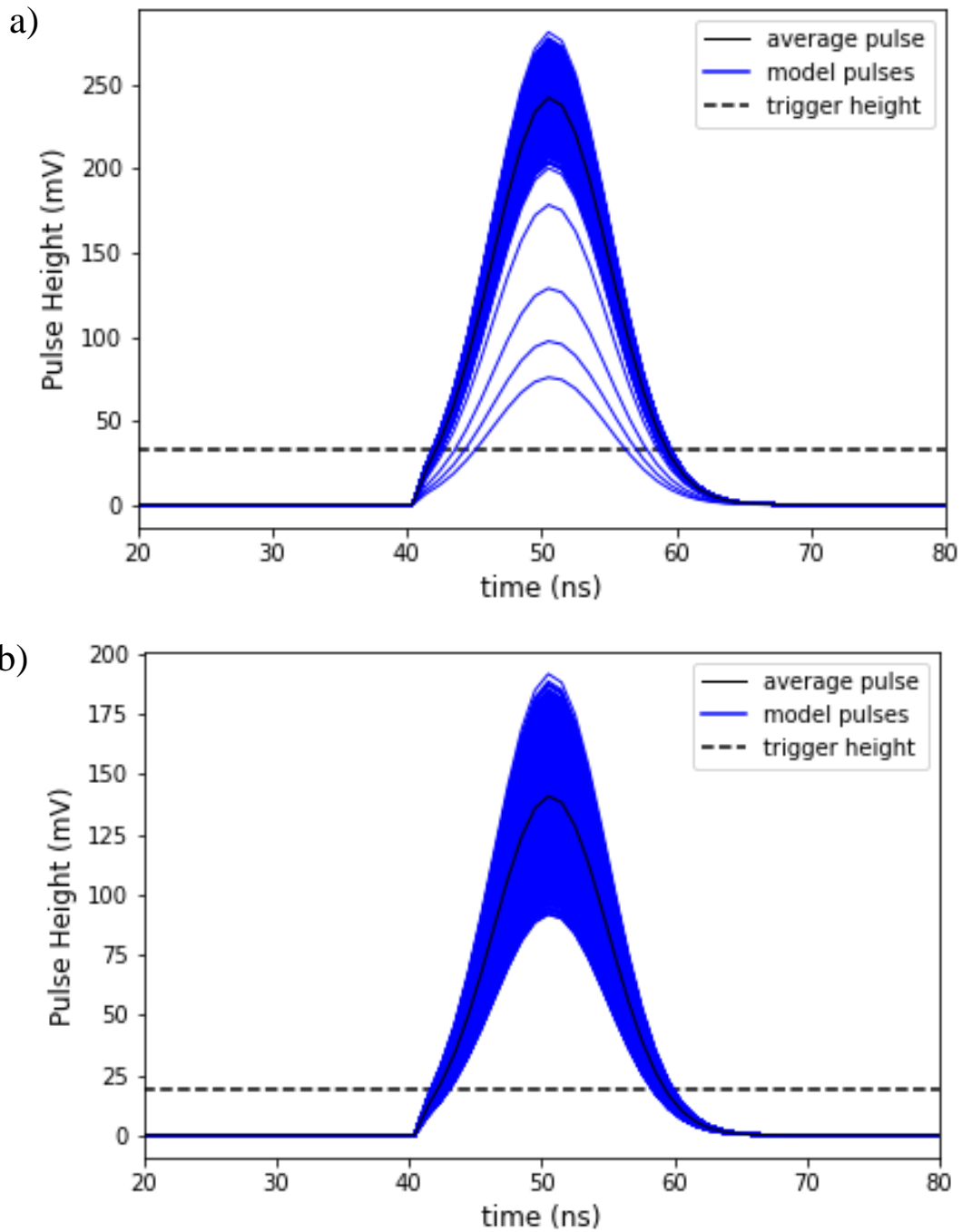
Figure 32: The distribution of pulses from our Cividec C6 pulse model and Geant4 energy deposition data. Showing the distribution of pulses from the simulation with shorter spacing (a), and with the larger spacing (b).

Table 1: The standard deviation values used to calculate the timing resolution of the diamond sensor, found both experimentally and using simulations/modeling.

Experimentally measured data		
$\sigma_{scintillator}$	0.0728 ns	
$\sigma_{TOF, measured}$ (electrons)	0.303 ns	
$\sigma_{TOF, measured}$ (holes)	0.325 ns	
Model and simulation data		
	Short spacing (1.5 mm)	Large spacing (3 mm)
$\sigma_{straggling}$	0.00502 ns	0.0136 ns
$\sigma_{time\ walk}$	0.0874 ns	0.284 ns
Timing resolution values		
$\sigma_{diamond}$ (electrons)	0.281 ns (0.660 ns FWHM)	0.0753 ns (0.177 ns FWHM)
$\sigma_{diamond}$ (holes)	0.304 ns (0.715 ns FWHM)	0.140 ns (0.328 ns FWHM)
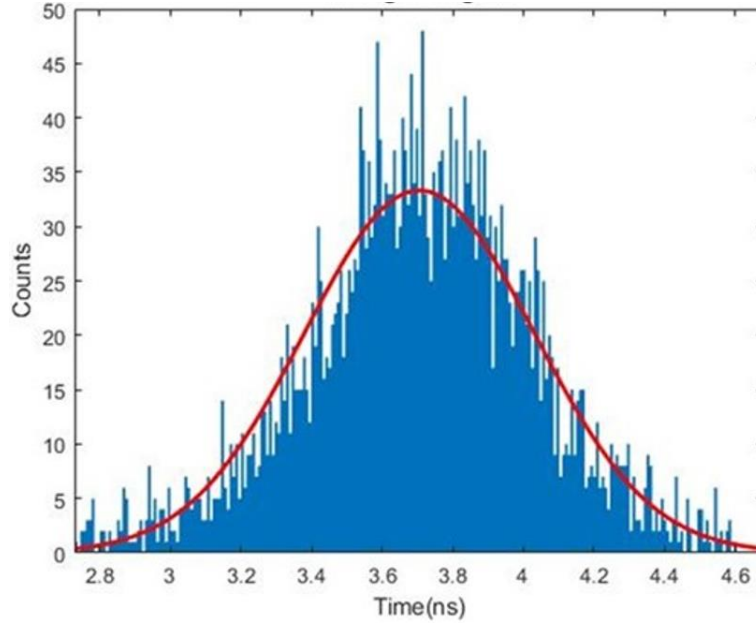
Figure 33: The measured time-of-flight distribution of ^{241}Am alpha particles between a thin plastic scintillator and diamond detector while collecting electrons.
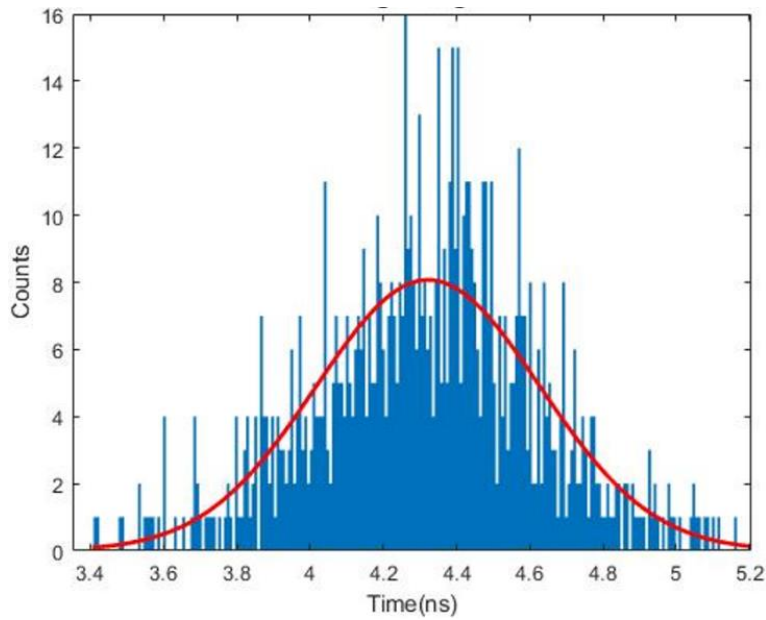
Figure 34: The measured time-of-flight distribution of ^{241}Am alpha particles between a thin plastic scintillator and diamond detector while collecting holes.

While the performance could be improved with a better sensor, the results show that a diamond DSSD with charge division readout can meet the spatial resolution and timing resolution requirements for API.

While polycrystalline diamond would be preferred in many cases because of the availability of larger and less expensive crystals, a single crystal sensor would almost definitely yield better performance. A single crystal sensor with nearly 100% charge collection efficiency would make it easier to trigger pulses at all four readouts, while opening up the option to increase the resistor impedance or add more strips (and resistors) with a finer pitch for better spatial resolution. The performance could also be improved with a thinner polycrystalline diamond. A thinner diamond would decrease the distance for which charge carriers must travel, improving the charge collection efficiency. In fact, we originally had a thinner sensor (310 µm thick compared to 500 µm), but the sensor was broken during metallization when applying pressure to the shadow mask. This was due to user error/mistake, and not necessarily due to excessive fragility of the sensor. A thinner sensor would be preferred regardless of it being single or polycrystalline. Benefits of sensor would be higher charge collection efficiency, less sensitivity to neutrons and photons, improved radiation hardness, and lower bias voltage. The downsides to using a thinner sensor are its reduced robustness during detector fabrication, but this can be overcome.

One last notable aspect of the design was showing that ACF could be used to bond a diamond strip detector to a PCB. The ACF formed a robust bond while establishing an electrical connection between the strips on the detector and PCB. This sensor packaging technique could be repeated and more extensively tested with different strip widths/pitches and different detector materials.

Future work of this device should include fabrication of a DSSD with thinner crystals that have a larger active area. In addition, DSSDs with identical dimensions/readouts could be constructed with both single crystal and polycrystalline CVD diamond to compare the performance. Single crystal CVD diamonds have charge collection efficiencies approaching 100%, and are free from polarization effects, which would allow testing of the capabilities of the design with an ideal sensor. There is still value in testing with different polycrystalline CVD diamonds, primarily thinner ones, due to their lower cost and larger active area. A major benefit proposed by diamond sensors in API is the capability of high-count rates. The charge division readout should be tested with high-count rates to determine if and how much the resistive readout effects the count rate capabilities. The resistive readout may contribute to broadening of pulses such that the count rate capabilities are reduced. Lastly, the impedances could be better optimized to optimize spatial resolution with a sensor that has better charge collection efficiency and/or lack of polarization effects.

CHAPTER II
A HIGH PURITY GERMANIUM DETECTOR RESPONSE FUNCTION FOR THE LOS ALAMOS NATIONAL LABORATORY DETECTOR RESPONSE FUNCTION TOOLKIT

ABSTRACT

Los Alamos National Laboratory is currently developing a detector response function toolkit (DRiFT) intended to post-process MCNP output and provide realistic nuclear instrumentation response. We are developing an HPGe semiconductor detector response function for DRiFT to complement the gas detector and scintillator detector response functions already included. In order to generate a detector response function, MCNP is used to model the specific measurement scenario. Particle interactions from the MCNP ptrac file are used as inputs for a custom charge transport code and electronics readout model written in Python and C++. The electric field and weighting potential in the HPGe crystal are modeled using Silvaco. The charge transport code takes in the ptrac file from MCNP and outputs the detector signal seen by the input terminals of the readout electronics. Modeling the readout electronics consists of a charge sensitive preamplifier and trapezoidal shaping amplifier model that includes effects from ballistic deficit, pile-up, and noise. The readout model outputs a full energy spectrum that can be compared to measurement datasets. The DRF will provide a higher fidelity pulse-height-spectrum than MCNP provides by accounting for variables in the charge transport and readout that contribute to spectral distortions. Furthermore, the model may be easily adapted to different semiconductor radiation detectors. We have demonstrated the functionality of the different components of the detector response function and their effect on the modeled pulse-height spectrum.

INTRODUCTION AND GENERAL INFORMATION

A. Overview

       High-purity germanium (HPGe) radiation detectors are widely used in gamma spectroscopy due to their excellent energy resolution and detection efficiency. Many applications require excellent energy resolution for source identification and characterization. In some applications, it is useful to be able to predict and/or verify what is seen on a detector by using a detector response function (DRF). A DRF models a detectors response in order to provide information on what a detector would see given a certain measurement scenario/orientation. For our purposes, we wish to predict and/or verify the gamma energy spectrum of an ORTEC GEM140P-S HPGe detector. To make it applicable to a broad range of measurement scenarios, the DRF will take input from MCNP ptrac data so that different sources and environments may be modelled using Monte-Carlo radiation transport. Many DRFs can successfully model a spectrum, but a single DRF is typically only accurate for a specific geometry. By importing interaction data from the MCNP ptrac file, we can model any environment that is built in MCNP around the detector volume. By inputting that data into a charge transport code and readout model to build detector response functions, features of the spectrum can be modeled at a higher fidelity compared to the MCNP F8 tally. The F8 tally is a pulse-height tally, which records the pulse-height distribution in a defined region (typically the detector region or cell). However, in the most general sense, it is a simple recording of the energy deposited in the cell, and not necessarily an accurate representation of an experimentally measured pulse-height spectrum.

       The project can be broken up into 4 main sections to make it more digestible. These sections can most broadly be called: MCNP, Silvaco, charge transport, and readout. The purpose of each section will be briefly introduced in this overview.

       The MCNP model contains the geometry of the detector and the environment in which the detector sits. This can be changed depending on what source and environment the user wants to model. Building a precise detector model is important so that radiation interactions within the detector and its housing are accurate. Modeling the radiation interactions that occur in the crystal and materials around the crystal are the first step to an accurate DRF. This dictates the attenuation and scattering of radiation between the source and detector, any interactions that occur in the detector housing, and what scatters into the detector active volume. It also allows accurate modeling of what escapes the detector by either passing directly through it without interacting or scattering out. The interactions that occur in the detector will dictate how much charge is generated, and where. This is very important for the relative intensities of Compton scattering regions, full energy peaks, escape peaks, etc. Once an MCNP simulation of the specific environment is complete, the ptrac data is filtered to collect energy depositions and their locations in the crystal volume.

       Silvaco is used to model the electric field and weighting potential in the crystal. The crystal is a coaxial design p-type HPGe, with a boron implanted p++ inner surface and a lithium diffused n++ outer surface. It is important to accurately model the shape of the crystal, the different doping regions in the crystal, and the bias. The electric field will be used to determine the charge carrier transport kinematics in the crystal. The weighting

potential is used to determine the charge induced on the readout electrode due to the moving charge carriers.

The charge transport portion of the DRF reads the MCNP ptrac data and the Silvaco data to generate charge in the crystal, transport that charge, and calculate the charge induced on the electrode for each radiation interaction. Shockley-Ramo theorem is used to model the induced charge during charge transport. The charge induced on the electrode over time from each radiation interaction is used as the input into the readout model. The charge transport itself plays a significant role in the shape of the pulse-height spectrum due to variations in interaction location, charge loss due to trapping, and statistical variations in the amount of charge generated by energy depositions. A pulse-height spectrum may be build from the charge induced on the electrode alone if a user wishes to ignore the effects of the readout electronics.

The readout portion of the code models the preamplifier and amplifier stages of the detector system. It generates both preamplifier and amplifier pulses resulting from each gamma event. The readout also models electronic noise, peak pileup, and ballistic deficit. The magnitude of the noise, pile-up, and ballistic deficit depends on what values the user assigns to various input parameters. The readout model output is used to build a pulse-height spectrum based on the magnitude of each amplifier output pulse. This is analogous to an MCA or digitizer processing the amplifier output.

Lastly, this project was started in collaboration with Los Alamos National Laboratory (LANL) for their Detector Response Function Toolkit (DRiFT). DRiFT contains different DRF modules, such as gas detectors and scintillators, all of which take input from MCNP ptrac files to generate higher fidelity pulse-height-spectra. The HPGe semiconductor will be just one module in DRiFT. The charge transport and readout models in the detector response function were built locally in Python and in C++. While we are modeling a specific model of HPGe, the program can be adapted to different detector shapes and materials. This would require different MCNP and Silvaco models, but the charge transport code is "universal" in this sense. Furthermore, it is not necessary for Silvaco to be used to model the electrostatics in the detector, and it is not necessary for MCNP to complete the Monte-Carlo radiation transport. The importance lies in the information gathered from the models and the format that it must be in for the charge transport portion of the program to read.

LITERATURE REVIEW

In this literature review, I will summarize the properties of HPGe detectors. We are modeling a coaxial design HPGe detector, so the design factors of the coaxial design will be the main focus of the HPGe semiconductor detector summary. I will address why each detail of the coaxial design is chosen and its advantages to other designs. A review of Shockley-Ramo theorem and charge transport provides the relevant information regarding our methods for charge transport. The literature review extends to the readout, which has sections to address preamplifiers, shaping amplifiers, electronic noise, pile-up, and other aspects of the readout that are necessary to cover for our readout model. Lastly, the literature review closes with a review on detector response functions, and the benefits and drawbacks of the different methods for building detector response functions.

A. HPGe Semiconductor Detectors

HPGe semiconductors are used for gamma ray spectroscopy due to their excellent energy resolution and detection efficiency. The relatively high-Z (Z=32) of germanium and growth of large crystals make it more efficient than other semiconductors, like silicon (Z=14). HPGe production became more reliable in the 1980s, so a shift from Ge(Li) to HPGe occurred. Ge(Li) detectors required lithium drifting throughout the crystal which could take weeks, and they needed to be kept cool at 77 K at all times. HPGe detectors may be stored at room temperature without significant lithium drift, however HPGe does have a very low band gap of 0.67 eV, so detectors must be operated a liquid nitrogen temperatures (77 K) to keep leakage current low during operation [51, 52]. The energy resolution of an HPGe detector at 1.33 MeV is typically less than 2 keV full-width-half-maximum (FWHM). A good estimation of the energy resolution as a function of energy is provided by ORTEC (Equation 7), where N is the noise line width, E is the energy, and R is the FWHM resolution [53].

$$R(FWHM) = \sqrt{N^2 + 2E} \qquad (7)$$

1. Applications of HPGe

HPGe is a useful tool in non-destructive assay and passive methods of characterization in non-proliferation and nuclear forensics. In comparison to other detector types, such as sodium iodide (NaI), HPGe simplifies characterization techniques such as uranium enrichment [54]. For example, in uranium enrichment measurements, the relative count rates in the full energy peaks from different isotopes can be used to measure the relative abundance of each isotope. When there are many sources present, or when there is significant background, the broadening and convolution of different peaks will make it more difficult to determine the area of each peak, for example, the 186 keV peak in ^{235}U. In HPGe, peaks are thinner due to better energy resolution, and better separated from neighboring peaks. Furthermore, even when peaks are well separated, thinner peaks make it less complicated to define a peak region for analysis while making a linear approximation to the underlying Compton background more appropriate. Paired with neutron detectors, gamma ray and neutron count rates may be used together to better estimate uranium enrichment [55]. This is especially effective because the 186 keV gamma rays are easily self-attenuated by the uranium itself or the container. In measurements of uranium metal, or UF$_6$ containers, this phenomenon can cause errors in a measurement or be used to shield information about a material. Neutrons can provide insight into the enrichment deeper into the material, although the 186 keV enrichment meter is generally more accurate, so neutron enrichment meters may best serve as a confirmation [55].

HPGe has also been used for environmental surveying to detect and identify contaminated areas and airborne radionuclides [56, 57]. These have been deployed on land, water, and aerial vehicles, and could be used to detect the products of a disaster/accident, or a nuclear weapons treaty violation. Some of the major challenges with deploying these systems in a mobile environment are caused by the requirement to cool the HPGe crystal. This requires a large apparatus filled with liquid nitrogen, limiting the construction of the apparatus, the space required, and the time available for a measurement. Furthermore, in a

mobile environment, moving the detector and liquid nitrogen causes vibrations that effect the measurement. Not completely unrelated to environmental surveying is background characterization and analysis. Background often consists of many isotopes covering a broad range of energies and intensities. It can originate from both the environment around the detector (external), and in the detector itself (internal).

In rare event studies, such as double beta decay, high resolution, ultra-low background, and background characterization is necessary. HPGe is often used for the detection of rare events, especially in the case of double-beta decay, as ^{76}Ge can provide an internal source of the rare event [58, 59]. Here, two-neutrino double-beta decay (2νββ) or neutrino-less double-beta decay (0νββ) may occur. In these events, two neutrons in the nucleus are converted into two protons and two electrons. In 2νββ, two antineutrinos are also emitted. The 0νββ event has no emission of neutrinos. This decay mode is forbidden by the Standard Model of Particle Physics, and its detection would confirm that massive neutrinos are Majorana fermions [60, 61]. The 2νββ event occurs at a higher rate with a similar Q-value, which results in a background that would make identifying 0νββ events difficult. The excellent energy resolution of HPGe can be used to separate these two events. Here, HPGe serves as an excellent background discriminator, an identifier and characterizer of the 0νββ event, and the source of the event. These experiments are often placed underground within additional shielding to eliminate further background.

2. *Fano-factor and energy resolution*

HPGe has a mean electron-hole pair production energy (W-value) of 2.96 eV at 77 K. The operating temperature of the crystal is typically 85-100 K due to limitations in the cryostat/detector assembly. The W-value varies by 2.53×10^{-4} eV/K, meaning in the operational temperature range, the W-value is 2.962-2.965 eV [53].

The Fano factor (*F*) describes the statistical variance in the number of charge carriers generated. If we expect a mean number of free charge carriers will be produced for a given energy deposition (based on the W-value), and the number of charge carriers produced is random, then for a given energy deposition we might be expect the number of charge carriers produced to follow a Poisson distribution centered around the W-value. In semiconductors, the variance in the number of charge carriers produced is smaller than this due to the limited number of ways ionization may occur. This requires further explanation.

To help explain this, it is useful to think of ionizations as analogous to radioactive decay, because decay follows Poisson statistics. In radioactive decay, events happen discretely (there will never be a fraction of a decay). Decays also occur randomly in time and are independent of one another. If you were to measure the time interval between many decay events, then the distribution of the time interval between decays would follow a Poisson distribution centered around the average time interval. Events do have some probability of occurring, which causes some isotopes to have a higher specific activity than others. Most importantly for our analogy, there is no limitation on the time interval between any two decays, and the time interval does not follow discrete values.

Now, let's compare the Poisson statistics of decay to the production of charge carriers. Instead of a decay event, we consider an ionization event (generation of an electron-hole pair). Instead of a time interval between decays, we consider the energy to

produce an electron-hole pair. The average time interval between decays is analogous to the W-value. The actual number of decays observed within some larger time frame is analogous to the actual number of electron-hole pairs produced for some energy deposited. Recall that there is no limitation on the time interval between any two decay events. Decay events occur randomly in time. If ionizations were random, and there was no limitation on the number of ways an ionization event might happen (or no limitation on the amount of energy used to create an ionization), then the number of ionizations per unit energy would follow a Poisson distribution. However, the possible variations in the amount of energy required to generate an electron-hole pair is limited by the electron shells. This limitation causes the distribution in the number of charge carriers produced to have a smaller variance than the Poisson distribution.

In other words, there are limitations in the energy required to create electron-hole pairs due to the dependence on the electron shells in the material. This limitation results in the variance of the number of electrons generated to be reduced relative to the variance in a Poisson distribution. The Fano-factor is a correction factor for the variance. If the Fano factor equals zero, then the variance in charge pairs produced is zero. If the Fano factor equals one, then distribution follows Poisson statistics precisely.

For HPGe, the Fano-factor is reported between 0.08-0.13 [52], but commonly 0.1-0.105 [51, 62]. ORTEC reports that the best estimate of the Fano factor is 0.1. The low Fano factor plays a key role in the excellent energy resolution of HPGe because it means that there is little variance in the number of charge carriers produced for a given amount of deposited energy. Use of the Fano factor is described in Equation 8, where sigma-squared (σ^2) is the variance in the number of charge carriers produced, F is the Fano factor, and the mean number of charge carriers produced is $\bar{N}$ [52, 63, 64]. The probability distribution of the number of charge carriers ($P(N)$) generated follows the normal distribution, also shown.

$$\sigma^2 = F\bar{N} \tag{8}$$

$$\bar{N} = \frac{E_{deposited}}{W}$$

$$P(N) = \frac{1}{\sigma\sqrt{2\pi}} exp\left(-\frac{1}{2}\left(\frac{N-\bar{N}}{\sigma}\right)^2\right)$$

ORTEC provides two equations for estimating the energy resolution of an HPGe detector with a Fano factor of 0.1. The detector resolution (ΔE) can be estimated as a function of energy (E) in units of eV using Equation 9. To account for noise, the detector resolution can be summed in quadrature with the noise (ΔN) to obtain expected measured energy resolution (ΔE_S). The former is shown just below Equation 9 [65].

$$\Delta E = 1.27\sqrt{E} \tag{9}$$

$$\Delta E_s = \sqrt{(\Delta E)^2 + (\Delta N)^2}$$

3. Coaxial HPGe Detector Design

The very basic details of a coaxial design are summarized in ORTEC literature [53, 66]. The coaxial design is a cylindrical detector that has a hole in one end. The hole does not extend all the way through the cylinder. The end opposite of the hole is rounded, or "bulletized". An illustration of a coaxial crystal is shown in Figure 35. The coaxial design offers higher detection efficiency than other designs due to the ability to have a larger active volume at lower voltages. Some common generalizations are a diameter to length ratio of roughly 1:1, rounded corners (bulletized) to remove regions with low electric field, and center hole of approximately 10 mm in diameter. The size of a coaxial design detector is often reported in terms of efficiency instead of dimension. The efficiency is reported as percent detection efficiency of 1.33 MeV ^{60}Co photons relative to a 3×3 in^2 NaI detector [51]. The detector we are modeling is a 140% efficiency detector.

i. Doping and design factors

Like silicon, germanium has four valence electrons which form covalent bonds with neighboring germanium atoms in the crystal. An n-type dopant, or a donor impurity, is able to donate an electron to the conduction band. For example, phosphorus has five valence electrons, leaving one extra that is not used in the four covalent bonds and can be donated to the conduction band. A p-type dopant, or acceptor impurity, leaves a positively charged "hole" in the valence band. For example, boron has three electrons in the valence band (one less than germanium and silicon). This allows an electron to be accepted into that hole to form the four covalent bonds [67]. Common impurities in germanium that serve as n-type dopants are phosphorus and lithium. Common p-type dopants are boron, aluminum, and gallium [51].

We will focus on lithium as the n-type and boron as the p-type because these are the specific dopants used in coaxial design HPGe detectors. The bulk material of HPGe detectors can be either p-type or n-type, depending on which impurity is more dominantly present. The maximum net impurity concentration level viable in an HPGe detector is about 10^{10} cm^{-3}. More specifically, for an HPGe detector with p-type bulk material, the difference between the acceptor concentration (N_A) and donor concentration (N_D) must be $|N_A - N_D| < 10^{10} \ cm^{-3}$. The maximum impurity concentration is due to limitations in the voltage required to deplete the detector. The higher the impurity concentration, the higher the voltage required for depletion. The components around the crystal are limited to roughly 5 kV bias. Higher bias voltages result in arcing and discharges between the detector components. The max net impurity concentration may be 10^{10} cm^{-3}, but the optimum impurity concentration to maintain peak performance is approximately 3×10^9 cm^{-3}. If impurity concentrations are too low, then high enough electric field strength is not achievable. You may increase bias voltage to increase field strength, even after depletion has occurred, but leakage current will be increased and weak field strengths at certain regions of the detector will remain, leading to poor charge collection efficiency in those regions [51]. If an n-type bulk material is used, then the outer surface should be p-type, while if a p-type bulk material is used, the outer surface will be n-type. This maintains the p-n junction being on the outside surface of the crystal to generate high electric field strength on the outside diameter where most interactions take place.

bulletized end
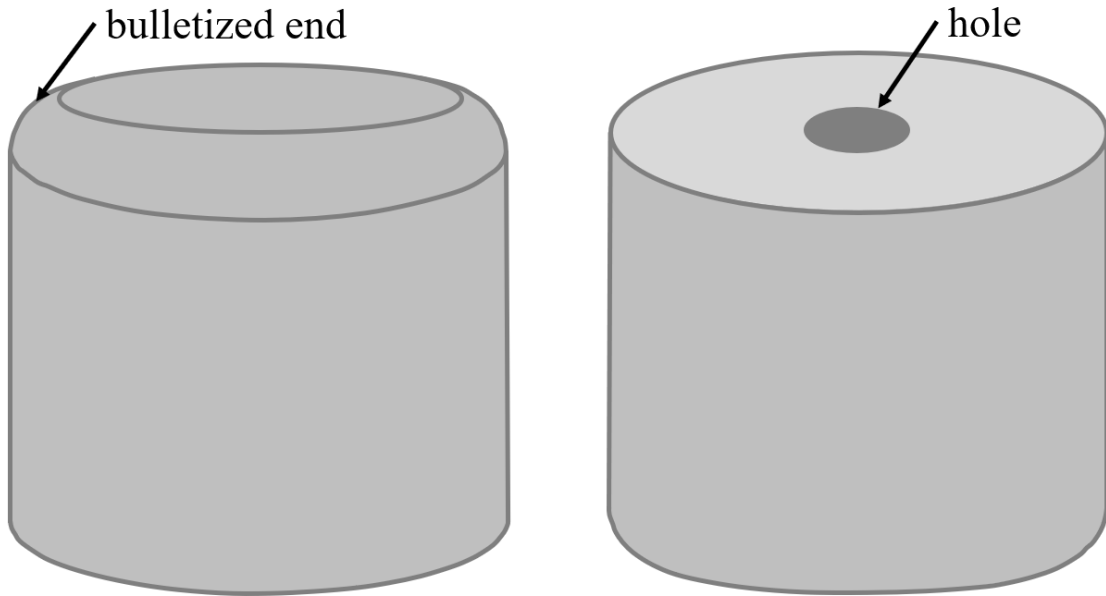
hole

Figure 35: A coaxial HPGe crystal illustration showing the bulletized top side and the flat bottom side with a hole in the center.

The outer surface p-n junction includes the outside of the cylinder and the top of the cylinder (the bulletized end). The p-n junction is not extended to bottom of the crystal (the flat end where the hole is drilled). An n-type outer contact is made by lithium diffusion on the outer surface. The diffusion depth is 700 µm, resulting in a dead layer (non-depleted layer) at the outer surface [53, 66]. This dead layer reduces detection efficiency at lower energies (<40 keV), making them less ideal for detection at those lower energies. N-type HPGe detectors utilize a p-type dopant on the outer surface, which employs boron implantation at a depth of only 0.3 µm, so the thinner dead layer in an n-type detector is suitable for energies as low as 3 keV [51, 68]. However, n-type detectors have a dip in efficiency just above 10 keV due to k-absorption edges. The highly doped (sometimes referred to as n+/n++, or p+/p++) outer surface acts as a contact for which a bias is applied. The second contact is formed inside of the hole that is drilled in the crystal. In a p-type crystal, this contact will be heavily boron doped (p+) using boron implantation (still 0.3 µm depth).

The detector we are modeling is a p-type crystal with n+ outer contact and p+ inner contact. The contacts serve a second purpose by acting as blocking contacts to reduce leakage current. The positively biased n+ layer on the outside of the crystal blocks holes but not electrons, while the grounded p+ layer on the inside of the crystal blocks electrons but not holes. Biasing the outer surface instead of the inner surface also results in a larger depletion region/field strength. The n+ and p+ contacts serve as conductors, but sometimes the surfaces can have metal deposited to further reduce resistance between the contact pin and the boron implanted inner surface, and between the metal housing and lithium diffused outer surface [51]. The impurity level to achieve n+ and p+ contacts (degenerate contacts) is on the order of 10^{19} cm^{-3} [69]. An n+ contact occurs when the impurity concentration reaches a level where donor electrons of the impurities begin to interact with one another, and energy bands split and widen. If this happens enough, then the concentration of electrons will exceed the density of states in the conduction band, which results in a Fermi energy that lies in the conduction band (N_c). For a p+ contact, the same thing occurs when adding acceptor impurities at a high enough concentration such that the acceptor energy states overlap with the valence band, so that the number of holes exceeds the density of states in the valence band (N_v), causing the Fermi energy to shift into the valence band.

The top side of the detector has a rounded edge, also known as the bulletized end. While rounding the top edge lowers the total volume of the crystal, it optimizes the volume that is left by increasing field strength and removing regions of weak field strength. This ensures that a high charge collection efficiency is maintained in the entire active volume, and that saturation velocity of the charge carries may be reached.

B. Charge Transport

Charge transport in semiconductors describes the production and motion of the charge carriers in the crystal, and the resulting charge induced on the readout electrode. When ionizing radiation enters the detector, it generates electron-hole pairs by exciting electrons into the conduction band, leaving a hole behind in the valence band. When the detector has a bias applied, and an internal electric field, the charge carriers (electrons and holes) drift through the detector according to the direction of the electric field. The motion

of the charge carriers induces a signal in the readout that is used to detect the ionizing radiation [70].

The charge carrier mobility expresses the rate at which charge carriers may drift through the material. It is a term that factors in the time between collisions and the effective mass of the charge carrier. Some collisions that slow down charge carriers are due to lattice vibrations (interaction between the charge carriers and vibrating lattice atoms). These collisions can be reduced by lowering the temperature of the material since this reduces lattice vibrations. For this reason, you will often have an increase in mobility at colder/lower temperatures [69]. Collisions between charge carriers and impurities result in a decrease of mobility with increases in impurity concentration. The units of charge carrier mobility are often expressed in terms of $cm^2V^{-1}s^{-1}$. For HPGe detectors, the mobility at 300 K is on the order of 1900 and 3900 $cm^2V^{-1}s^{-1}$ for holes and electrons, respectively. At 77 K (liquid nitrogen temperature), the mobility increases tremendously to 42000 and 36000 $cm^2V^{-1}s^{-1}$ for holes and electrons, respectively [53, 69]. The velocity of the charge carriers is expressed by Equation 10, but that does not assume a saturation velocity [69, 70]. As the charge carriers enter higher electric fields, the relationship is no longer linear, as the charge carriers approach their saturation velocity (v_{sat}). The saturation velocity of the charge carriers is about 5.9×10^6 cm/s at room temperature and 9.6×10^6 cm/s at 77 K [53, 69, 71]. Equation 11 shows the expression used to calculate velocity, which is a slight modification of equation 12 [72]. Some report higher saturation field ($\vec{E}_{sat}$) and velocity ($\vec{v}_{sat}$) for electrons [72], than for holes [69, 71]. However, the saturation velocity for both is reported as equal for each charge carrier by ORTEC and others [53, 71]. Both equations 11 and 12 are equivalent for $\beta = 2$.

$$\vec{v}_{e,h} = \mu_{e,h}\vec{E} \tag{10}$$

$$\vec{v}_{e,h} = \frac{\mu_{e,h}\vec{E}}{\sqrt{1 + \left(\frac{\mu_{e,h}\vec{E}}{v_{sat(e,h)}}\right)^2}} \tag{11}$$

$$\vec{v}_{e,h} = \frac{\mu_{e,h}\vec{E}}{\sqrt[\beta]{1 + \left(\frac{\vec{E}}{\vec{E}_{sat}}\right)^\beta}} \tag{12}$$

As charge carriers drift through the material, with their motion dictated by the electric field, they induce charge on the electrodes. The phenomenon is explained and can

be calculated using Shockley-Ramo theorem [73-75]. The amount of charge induced on the electrode (Q) due to moving charge (q) is determined using an imaginary potential called the weighting potential (φ_0). The weighting potential is related to the electric potential, but there are fundamental differences. All electrodes in a detector system (bias electrodes and ground electrodes) contribute to the electric potential (V) in a given position inside of the detector. The orientation of the electrodes and the materials around/between each electrode determines what shape the electric potential will take (recall that $\vec{E} = \vec{\nabla}V$). There is only one electric potential profile for a configuration. In contrast to electric potential, each electrode has its own weighting potential associated with it. For one given configuration of electrodes and materials, there will be as many weighting potential profiles as there are electrodes. The weighting potential for a given electrode provides the means for calculating the charge induced on that specific electrode. The same moving charge (q) may induce a different amount of charge (Q) on each electrode due to differences in weighting potentials, which results in a different signal on each electrode. In coaxial designed HPGe detectors there are only two electrodes: one bias and one ground electrode. The consequence of a two-electrode design is that the weighting potential takes the same shape as the electric potential. If we consider a two-electrode system with one ground electrode and one bias electrode, and the bias electrode is equal to the unit potential, then the charge induced on the electrode can be calculated using Equation 13 [74]. In other words, the electric potential is normalized such that the weighting potential at some instantaneous position (x) follows Equation 14. Furthermore, the current on the electrode (i) can be calculated using Equation 15. Lastly, the induced charge calculations using Shockley-Ramo theorem are independent of fixed space charge [76] and the magnetic field [74].

$$Q = -q\varphi_0(x) \tag{13}$$

$$\varphi_0(x) = \frac{V(x)}{V_{bias}} \tag{14}$$

$$i = q\vec{v} \cdot \vec{E} \tag{15}$$

1. Modeling Charge Transport

Charge transport and induced signals in semiconductors are modeled using varying methods, including numerical, analytical, and Monte-Carlo type methods. Most methods are similar in that they are an application of Shockley-Ramo theorem. The goals can be to predict detector response, or to evaluate different detector designs during development.

Complex CdZnTe and CdTe detectors have been modeled using similar common assumptions, such as quasi-steady-state, meaning the electric field in the detector is not altered by radiation interactions [67, 71, 74, 77]. In these devices, there is a unique solution for each electrode due to each electrode having a unique weighting potential. Furthermore, there is a unique solution for each location of charge generation in the detector. To reduce

74

the amount of time that it would take to map out the charge signal with respect to interaction location, a new method was used. Using common assumptions and linearization, a series of charge carrier continuity equations that express electron continuity, hole continuity, charge generation, recombination, etc., are used to construct an adjoint continuity equation [77]. Solving this adjoint continuity equation results in a function (Green's function) to express the charge induced on the electrode with respect to interaction position. This method provides a quick and efficient way of calculating pulses [77, 78].

In Silicon strip detectors, charge signal sharing between strips varies depending on the detector material/shape, charge carrier properties, pixel/strip size, depth of interaction, and the electric field [79]. Different charge transport models implement different simplifications to reduce computational time [80-83]. Of the different simplifications, using Monte-Carlo and analytical tools yielded the most accurate results [79]. In strip or pixelated detectors, it was found that charge carrier diffusion played a significant role in how signal is shared between strips, especially when charge is generated far from the electrode. This stresses the importance of carefully choosing modeling methods based on the detector design.

Charge transport is often modeled in organic semiconductor devices for optimizing devices (such as organic light-emitting diodes) [84]. Modeling these devices is often more complicated than inorganic semiconductors due to low charge carrier mobility, static dielectric constants, long recombination times, and disorder within the devices themselves. Monte-Carlo methods [85], numerical methods known as MOLED [86], and the drift-diffusion model [84, 87]. The drift-diffusion models have different input parameters to accommodate different devices, such as voltage, disorder, temperature, and trapping, however, these models are not targeted towards radiation detection applications. While they are relevant in terms of semiconductor charge transport modeling, they are not necessarily directly translatable to radiation detector response functions. However, certain factors modeled, such as charge carrier diffusion, trapping, recombination, mobility, etc., are directly related to semiconductors used in radiation detection. As mentioned earlier, this is especially true when considering devices with complicated readout schemes where charge carrier diffusion is more important, such as strip detectors and pixilated detectors.

There is a common theme between charge transport models. The balance between accuracy and computational time results in compromises. Different semiconductor devices may inhibit and enable different simplifications, so the detector being modeled must be taken into consideration when building a charge transport model. Making bad simplifications may result in unacceptable inaccuracies. In all cases, there are benefits of some simplifying assumptions heavily outweigh a minimal cost in accuracy.

C. Readout

There are multiple options for the readout on an HPGe detector, but all of the options are comprised of the same basic components. These include a preamplifier, amplifier, and MCA. The preamplifiers used for energy spectroscopy are charge sensitive preamplifiers, which integrate the charge collected and output a voltage pulse with a fast rise time, and slow decay. The amplifiers used are shaping amplifiers, which may have a series of differentiation and integration stages that shape the pulse according to the desired

75

outcomes, which may cater to maximizing the energy resolution at high count rates or varying charge collection times. Also included in the readout is pile-up and noise. Pile-up results when two events or pulses occur close enough such that they are not distinguishable, and they are summed as one pulse by the readout electronics. Electronic noise is an unavoidable aspect of radiation detection, and is necessary to include in the model in order to get accurate energy peaks at all energy levels.

1. Preamplifier

The charge generated and collected in a semiconductor is often small in magnitude and collected over a very short time interval. The purpose of the preamplifier in spectroscopy with HPGe detectors is to integrate, amplify, and shape the signal to improve the signal magnitude and it's integrity for further analysis and processing [71]. The preamplifier used is a charge-sensitive type. In basic form, it contains a feedback capacitor (C_f) and feedback resistor (R_f), the product of which is the RC-constant ($R_f \cdot Cf$), sometimes called the decay constant. The rise time of the preamplifier pulse is dictated by the charge collection time of the detector, while the decay is dictated by the RC-constant. As long as the RC-constant is sufficiently larger than the collection time, then the affect that decay has on the rise during charge collection will be negligible. In that case, the magnitude of the preamplifier output pulse (V_{out}) is equal to Equation 16, where charge ($Q_{collected}$) is in coulombs, capacitance (C_f) is in farads, and the resulting output is in volts. The decay of the pulse is modeled using Equation 17, with time (t) in seconds and resistance (R_f) in ohms [71, 88].

$$V_{out} = \frac{Q_{collected}}{C_f} \tag{16}$$

$$V(t) = V_{out} \, exp\left(-{}^{t}/_{R_f C_f}\right) \tag{17}$$

Because the decay of a preamplifier pulse is slow, it is difficult or impossible to avoid charge collection from radiation interactions from occurring before the preamplifier signal has decayed back to baseline. When pulses occur in quick succession, this is known as pulse pile-up. At high count rates or high energy depositions that generate vast amounts of charge (or both simultaneously), the preamplifier can become saturated due to the building up of charge in the preamplifier. The maximum rate that a preamplifier can handle before saturation is expressed in terms of energy deposition rate (*MeV/s*). To increase the maximum energy deposition rate, the RC-constant can be decreased to increase the rate of decay, but this comes at the price of increased noise. In general, it is best to keep count rates low enough to avoid saturation. Some readout systems also have reset techniques, which inhibit the processing of signals when saturation is met until the signal has decayed sufficiently.

Interactions may occur close enough in time such that the rise of each is indistinguishable from one another. In this case, there is not much that can be done to separate them, and they will be seen as one pulse by the readout and are consequentially summed. In other cases, where a second pulse occurs during the decay of the first pulse,

76

and the rise of each is distinguishable, then the readout electronics can process them as separate events even though they are piled-up in the preamplifier. The distinction between these successive pulses mostly done at the amplifier stage. An illustration of successive preamplifier pulses is shown in Figure 36, which demonstrates the shape of a pulse with a fast rise and slow decay, as well as the pile-up of pulses [89]. In this illustration, there are five pulses that would be distinguishable from one another.

2. *Amplifier*

Amplifiers are in place to process the preamplifier output pulses by shaping them and increasing magnitude through amplification. The result of the pulse shaping is a large pulse that should have a slower rise than the preamplifier, but a much faster decay back to baseline. Ideally, the preamplifier pulse that is being input to the amplifier will have fast enough rise that it essentially appears as a step voltage to the amplifier. The faster decay allows for higher count rates and better separation between successive pulses. Even if pulses are piled up at the preamplifier stage, they can be seen as completely separate pulses by the amplifier. They will not result in pile-up in the amplifier as long as the shorter amplifier pulse has had time to decay to baseline before the rise of the next pulse. The specific shape of the amplifier output pulse, its rise time, fall time, and width may all be tailored to the application. For coaxial HPGe detectors, there are a few things to consider when selecting an amplifier type and which settings to use. We will introduce CR-RC shaping as a background on what the CR (differentiating) and RC (integrating) stages in a shaping circuit accomplish. However, CR-$(RC)^n$ and trapezoidal shaping are the main focus, as they are the preferred types for spectroscopy with coaxial HPGe detectors.

i. *CR-RC shaping*

In CR-RC shaping, there are two primary stages; the differentiating stage (CR) and the integrating stage (RC). The result of CR-RC shaping is a quick rise with a sharp peak, and a much faster fall time in comparison to the preamplifier output pulse. The CR-differentiator acts as a high-pass filter, which means that the fast-leading edge of the preamplifier pulse is not differentiated by this stage (as long as the differentiating time constant is sufficiently large such that the preamplifier rise appears as a step voltage). The RC-integrator acts as a low-pass filter, and it will integrate the input signal (as long as the integration time constant is large compared to the duration of the input) [71]. The two stages could act as a noise filter if the time constants are selected to do so, however, they must usually be selected such that high frequency noise is allowed to pass through with the fast rise. Usually, the differentiating and integrating time constants are equal in a CR-RC shaping circuit. Shorter time constants result in quicker return to base line and less opportunity for pile-up at higher count rates. If the time constant is too short, then the input rise no longer acts as a step voltage and some of the amplitude may be lost during shaping (ballistic deficit). In summary, time constants should be chosen to limit of both ballistic deficit and pulse pile-up, as well as noise if possible. A common case of CR-RC shaping which has one differentiating stage followed by multiple (n) integration stages, is denoted as CR-$(RC)^n$ [71]. In general, this makes the shaper return to baseline quicker than a simpler CR-RC shaper, which is better for high count rates [64].
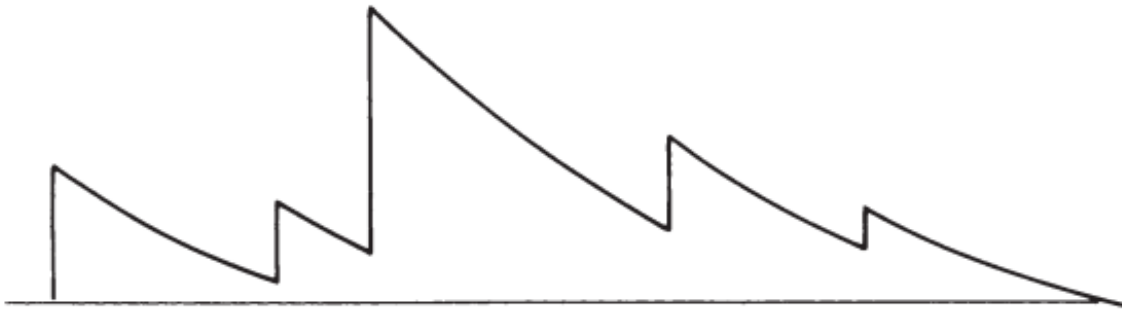
Figure 36: An example of successive charge sensitive (resistive-feedback) preamplifier pulses, with fast rise time and slow decay [89].

The result of CR-(RC)^n is a semi-gaussian shaping, with 4 stages (n=4) being sufficient to reach near gaussian pulse shape [71]. In practice, the circuitry of shapers is more complicated, but in a case where the differentiating and integrating time constants are the same, then the output can be simply expressed by Equation 18. In the equation, τ is both the differentiating and the integrating time constant. Note that for n=1, the solution is equivalent to a simpler CR-RC shaper [64, 71].

$$V_{out} = \frac{V}{n!}\left(\frac{t}{\tau}\right)^n exp\left(-\frac{t}{\tau}\right) \tag{18}$$

For n=4, and all equal time constants, the rise time is four times that of a CR-RC shaping circuit with the same time constants. However, by changing the different time constants, the rise time can be made equivalent to the CR-RC with a faster return to baseline and better signal-to-noise ratio. This combination of fast rise and decay make CR-(RC)^n shaping ideal for spectroscopy at high count rates [71]. However, longer and equal integrator and differentiator time constants yield optimum signal-to-noise ratio [64]. A common case of CR-(RC)^n shaping in practice is with two integration stages (n=2).

ii. *Trapezoidal shaping*

One of the challenges in pulse shaping is picking a large enough time constant such that ballistic deficit does not occur, but short enough such that the count rate capabilities are not limited too drastically. This is especially true in detectors with largely varying collection times because the ideal shaping time varies with collection time. The flat top of trapezoidal shaping makes it ideal for limiting ballistic deficit in detectors with largely varying collection times, such as large coaxial HPGe detectors [71]. The rise time, and flat top duration can all be adjusted in trapezoidal shaping, but the key is to have the duration of the flat top longer than the variation in the rise time of incoming preamplifier pulses (or collection time). Trapezoidal shaping is usually implemented by digital pulse processing systems, which are able to accomplish the symmetric rise, flat-top, and fall with varying widths. This limits ballistic deficit and keeps shaping constants short to improve energy resolution at high count rates [89].

The ORTEC DigiDART portable HPGe MCA is an example of a digital readout that utilizes trapezoidal shaping [90]. This will be referred to later in the *Methods* section, as it is the readout system that we are emulating in the DRF toolkit. The trapezoidal shaping has rise time settings in the range of 0.2 to 23 μs. The fall time is equivalent to the rise time, resulting in symmetric pulse shapes. The flat top duration setting ranges from 0.3 to 2.4 μs. The large range and fine tuning of these settings allow for user control to optimize energy resolution and throughput. There is also a specified dead time per pulse that varies with the settings, making it possible to estimate the true event rate (or true count rate) in the detector after a measurement. The DigiDART system does calculate the dead time percent automatically using the Gedcke-Hale method. The dead time and count rate shown on the MCA can be used in conjunction with the Gedcke-Hale correction method to calculate the dead time corrected count rate (event rate) in the detector. This is explained further in *Methods: D. Modeling Readout*.

3.   Pulse pile-up

The concept of pile-up in the preamplifier has already been introduced. Pile-up occurs when a second pulse occurs before the original pulse has had time to return to baseline. If the second pulse arrives before the tail of the first pulse has reached baseline, then the second pulse will be slightly elevated from baseline. In this case, it is still possible to distinguish the two pulses from one another. This is especially true with pulses that have a slow decay, and it is called *tail pile-up*. It is possible for two or more pulses to occur in quick enough succession that they cannot be distinguished from one another. This results in the two pulses being treated as one, in which case they are summed. This is called *peak pile-up* [71]. Pile-up can be mitigated in the amplifier by reducing shaping times of pulses so that pulses are shorter in duration, reducing the probability of overlap. However, this introduces higher signal-to-noise ratios and increases ballistic deficit. Pile-up can also be eliminated by keeping count rates low, but that is not always possible. Many shaping amplifiers have pile-up rejectors. The effect of pile-up can be estimated using the event rate in the detector volume, the collection time, and the different shaping time constants in the readout components.

i.   Pile-up at the preamplifier

In a semiconductor, pile-up can occur before/during the preamplifier stage because the detector does not become dead itself. Furthermore, the decay of preamplifier pulses is very slow, which makes tail pile up almost inevitable (refer to Figure 36). If a second event occurs in the detector before the first event has finished being collected then both events will be combined into one because the preamplifier sees it as one event [91]. In this case, the pile-up cannot be mitigated by the readout electronics because the two pulses are indistinguishable. The probability of this occurring depends on the charge collection time, or rise time of the preamplifier, and the event rate in the detector volume. Longer collection times and rise times increase the probability of peak pile-up in the preamplifier, which means that the severity can vary widely between different detectors. To reiterate, when a second event happens within the collection time of the first event, the rise time from both events is combined into one rise time, and they are combined into one event by the preamplifier. Once this type of pile-up occurs, it cannot be mitigated by the readout electronics later on. However, tail pile-up at the preamplifier stage can be mitigated. If tail pile-up occurs at the preamplifier stage, then it doesn't necessarily affect the energy spectrum because the rise of each event will be distinguishable. This results in the two pulses being distinguishable from one another by the amplifier/digitizer. This is true because the amplifier sees relative amplitude (or change in amplitude) coming from the preamplifier, not total amplitude (from baseline). Even though tail pile-up in the preamplifier may not be detrimental to energy resolution, it is still preferable to keep count rates low enough such that tail pile-up does not result in saturation of the preamplifier [71].

ii.   Pile-up at the amplifier/digitizer/multichannel analyzer

Depending on the type of amplifier or digitizer used, pile-up can be treated in different ways. It is also important to have settings on the amplifier/digitizer appropriately

adjusted to minimize both pile-up and ballistic deficit. Similar to peak pile-up at the preamplifier, peak pile-up can also occur at the amplifier. If two preamplifier pulses arrive at the amplifier in a short enough time interval compared to the shaping time, then the two pulses will be summed as one pulse in the amplifier, with no discrimination between the two. Tail pile-up in the amplifier varies from the preamplifier because the multichannel analyzer (MCA) sees total amplitude coming from the amplifier pulses, not relative amplitude. If the tail of the first pulse is still above baseline when the second pulse begins, then the second pulse will be seen as larger than actual because it will be elevated from baseline. If this occurs enough, then there will be high energy tailing on the full energy peak in the pulse height spectrum. If the tail of the first pulse falls below baseline (undershoot) and the second pulse begins during the undershoot, then the second pulse will be seen as smaller than actual by the MCA. In this case, low energy tailing on the full energy peak occurs in the pulse-height-spectrum [71]. This makes choosing amplifier shaping types, settings, and pole-zero adjustments crucial for limiting tail pile-up at the amplifier stage of the readout.

iii.   Pile-up rejection

Some readout systems have methods for rejecting pulses that may be piled up. Pile-up rejection occurs at the amplifier or digitizer. In some systems, the amplifier will process an incoming preamplifier pulse with two separate shapers. One shaping process is the semi-gaussian shaper that we have already discussed ($CR-(RC)^n$). The semi-gaussian shaper is a slower shaper that produces pulses that are used to build the pulse-height-spectrum. The slower shaper maintains good signal-to-noise ratio and linear amplification, as discussed previously. The second shaping process is a very fast shaper that sacrifices signal integrity for speed. This faster shaper produces an inhibit pulse, which initiates a time period for which no new events will be processed. The length of this time period is equal to the duration of the slower semi-gaussian shaper pulse used for spectroscopy. This ensures that no new event is processed until the amplifier output has reached baseline. While this prevents tail pile-up from effecting the pulse-height-spectrum, it does introduce an extending dead time in the electronics. At high count rates, the extending dead time can severely limit throughput. An extending time (paralyzation) also requires a different method for dead time correction. Lastly, if pile-up rejection is being used, it is still possible for pile-up to occur if a second pulse shows up before the inhibit pulse has been able to trigger the waiting period [71, 89].

The portable ORTEC DigiDART readout system that we are modeling has an automatic pile-up rejector feature, which uses a variable threshold that is automatically set. The threshold ensures that the pile-up rejector will reject pulses that are too close together to be detected separately by the fast channel. The range of the threshold is from 250 nanoseconds to 6 microseconds [90].

iv.   Pile-up statistics

The Poisson distribution in Equation 19 tells us the probability of some number of randomly distributed events (x) occurring in some time frame (τ_{pu}). There is a third variable involved, which is the average event rate (n). The average event rate is found by calculating

81

the dead time corrected count rate, which is discussed in the section preceding Equation 21. The pile-up time window (τ_{pu}) is the time window for which if multiple events occur, they will be indistinguishable by the readout electronics and thus piled up. The time window is initiated by an event itself, which means that for $x=0$, a regular detector count is recorded with no pile-up. For $x=1$, one event happens in the time window after the original event, so two events are added together to form a pile-up. For $x=2$, two events occur in the time window, so three events are added together in the pile-up… and so on [71].

$$P_x = \frac{\left(n\tau_{pu}\right)^x e^{-n\tau_{pu}}}{x!} \tag{19}$$

It should be noted that Equation 19 is for the specific case of a non-paralyzable system, which would be the case for the detector and preamplifier output as long as the count rate is kept low enough not to saturate the preamplifier. In a paralyzable system, such as a system with pile-up rejection activated, then two events may occur within the time window without resulting in a pile-up being recorded. In order for a pile-up to occur in paralyzable conditions, there must be a specific series of event free periods of time that follow a series of events. The probability of some number of events (x) piling up in a paralyzable system is shown in Equation 20 [71].

$$P_x = e^{-n\tau_{pu}}(1 - e^{-n\tau_{pu}})^x \tag{20}$$

Both the non-paralyzable and paralyzable model require knowing the true event rate (n) in the detector, which is calculated using dead time correction of the measured count rate (m). The dead time correction method also depends on if the system is non-paralyzable, or paralyzable.

4. Dead time corrections
Detector systems are usually referred to as paralyzable and non-paralyzable. A paralyzable system refers to a system that remains dead for some resolving time (τ) after an event. The resolving time expresses how long it takes for the system to recover after an event. In a paralyzable system, another event cannot be detected until the resolving time passes without another event occurring. If a second event occurs within the resolving time, then the recovery restarts. The consequence of this is a detector that can be paralyzed for time frames much longer than the resolving time in high count rate situations. A non-paralyzable system also has a resolving time, however, if a second event occurs during the resolving time, the "clock" does not restart. The system is only dead for a fixed time after each event. Equation 21 is the idealized non-paralyzable expression for the true number of events in the detector (n) related to the count rate (m) and the dead time (τ) [71, 91]. It is often referred to as the Gedcke-Hale method. Although paralyzable and non-paralyzable models have been derived, data often shows that the relationship between count rate and true event rate in a detector lie somewhere between the two [92]. Hybrid models have been

derived; however, they are system specific and thus require tailoring to the specific system being modeled [93, 94]. Lastly, the accuracy of the Gedcke-Hale method only comes into question at very high count rates. The detector readout systems we are interested in utilize this method [90]. If an amplifier is being used that has a pile-up rejection feature utilizing an extending dead time, it may necessary to use the paralyzable dead time correction model instead of the non-paralyzable model. This is common for CR-(RC)^2 shaping amplifiers, but only necessary when the pile-up rejection feature is being used [89]. In this case, the dead time correction method follows the paralyzable model of Equation 22, where the time constant (τ) is the dead time, or waiting time triggered by each incoming pulse due to the pile-up rejection feature [71, 89]. The DigiDART system has an automatic pile-up rejector, but still uses the Gedcke-Hale method. Lastly, it is important to distinguish the difference between the dead time that we are referring to as the resolving time (τ), and the commonly referred to dead time that is communicated as a percentage value on an MCA. As you can see by the relationships just below Equation 21, the two are related. The percent dead time communicates the fraction of time that the detector spent waiting in the resolving time, and is calculated using the resolving time, but both are often referred to as "dead time".

$$n = \frac{m}{1 - m\tau} \tag{21}$$

$$\frac{MCA\ live\ time}{MCA\ real\ time} = (1 - m\tau)$$

$$m\tau \cdot (100\%) = dead\ time\ percent\ as\ read\ on\ an\ MCA = \frac{MCA\ dead\ time}{MCA\ real\ time}$$

$$m = n \cdot \exp(-n\tau) \tag{22}$$

5. *Electronic noise*
In spectroscopy, the effect of noise on the pulse-height spectrum is a broadening of energy peaks due to variation of the pulse-height at the output. This broadening occurs on both sides (low energy and high energy) of the full energy peak. For detector response functions, our primary concern is the nature of the sum of all noise sources at the output of the shaping amplifier. The output of the amplifier is the primary concern because the amplifier output is what the multichannel analyzer (MCA) or digitizer uses to build a pulse-height spectrum. For this reason, we could concern ourselves solely with the amplifier output, but it serves us to understand the basics of different noise sources in semiconductor detector systems. Electronic noise in semiconductor detectors can be broken up by a few major and minor distinctions, separated by their origins. First, we will make the distinction between intrinsic and extrinsic noise sources. Intrinsic noise sources come from within the detector circuit. In short, these would include current/voltage noise originating in the sensor material, resistances, and capacitances in the readout circuit, etc. Extrinsic noise sources are those originating outside of the detector and readout circuit. Extrinsic noise sources

could include microphonics or mechanical vibration, cross-talk between different electronics near the circuit, or ground noise [71]. Due to the nature of extrinsic noise, it will vary widely between experimental setups and environments, so our focus will be on intrinsic noise.

    i.   Noise sources

        Three main types of intrinsic noise are shot noise, thermal noise, and low frequency ($1/f$) noise [64, 71]. Shot noise is characterized as carriers being injected independently of one another. The spectral distribution of shot noise depends on the transit time of charge carriers from cathode to anode, or the recombination time. Typically, this time if very short, so shot noise pulses can be considered a sequence of delta pulses. Sources of shot noise are the trapping and detrapping of charge carriers, which introduce fluctuations in dark current in the detector. Shot noise is commonly referred to as a source of "current" or "parallel" noise. Even if dark current is zero, charge carriers are still moving in the device with a root mean square velocity greater than zero at a given moment (Brownian thermal motion). The velocity fluctuations of charge carriers cause thermal noise, or Johnson noise. The spectral distribution of thermal noise depends on the velocity distribution of the charge carriers. Thermal noise can be considered a source of current/parallel noise or voltage/series noise. Thermal noise from resistors in parallel with the input (i.e., bias resistor) are considered current noise, while thermal noise from resistors in series with the input act as a voltage noise. Lastly, $1/f$ noise is white noise with power inversely proportional to frequency (f). This means that $1/f$ noise is not uniformly distributed, which is caused by noise fluctuations that are not purely random. An example of this is carriers being trapped and detrapped in resistors, dielectrics, and semiconductors with a time constant [64].

    ii.   Quantifying noise

        Probably the most useful way of quantifying noise is using equivalent noise charge (ENC). There are a couple of useful definitions of ENC that point to the same outcome, but provide a full explanation while paired. ENC is the amount of charge that if injected into the input terminals of the readout, results in an output voltage equal to the root mean squared (RMS_{noise}) level at the output due to noise [71]. The second useful definition of ENC is the signal charge that results in a signal-to-noise (SNR) ratio of one [64]. ENC is most often expressed in units of coulombs or number of electrons, however, it is sometimes expressed in units of energy. When observing noise, the fluctuations in output voltage are what we see when we plug the output into an oscilloscope. The fluctuation in voltage is also what the digitizer or MCA sees when it builds the pulse-height spectrum. Although the fluctuations of voltage observed do correlate to an ENC, charge injected into the input terminals may not actually contribute to fluctuations in the output voltage. This is because band-pass filters in different components are designed to prevent the passage of certain frequencies, which effectively reduce noise at those frequencies [64]. Furthermore, charges may be injected into the readout by components at any point in the readout, meaning some signals may be injected after amplification has already occurred. This reality is important when considering the definition and usage of ENC to model and quantify noise.

        While noise can be measured using a spectrum analyzer, a simple and intuitive way of analyzing noise is using a simple oscilloscope exercise to help understand the

relationship between RMS$_{noise}$, the spectral distribution of noise, and ENC. This review is not meant to be experimental instructions, however, going over the steps of a simple RMS$_{noise}$ measurement helps with understanding what it means to quantify noise in this way. This starts by plugging the amplifier output into two different channels on an oscilloscope, and setting the baseline offset of one channel such that the two signals are distinguishable from one another. The time scale should be set long enough such that the noise appears as a wide, continuous band. Next, the baseline offset between the two channels should be decreased until the wide bands of the two channels are touching and barely indistinguishable. At this point, the difference between the baseline of the two channels is equal to twice the RMS$_{noise}$ (baseline offset = 2·RMS$_{noise}$ = 2·σ$_{noise}$). This exercise stems from two simple principles. First, that the distribution of the noise is gaussian. Second, two identical gaussians are indistinguishable in their sum when the means of the gaussians are within 2σ. Using this method, the RMS$_{noise}$ will be in units of voltage. Estimating ENC can be done using a pulser and an oscilloscope. This is done by injecting a known amount of signal charge (Q_s) into the readout circuit and measuring the voltage amplitude of the output pulse (V_{so}) and the voltage amplitude of the noise (V_{no}). The ENC for a capacitive sensor is expressed by Equation 23, where ENC is equal to the equivalent noise charge (ENC = Q_n) and V_{so}/V_{no} is equivalent to the signal-to-noise ratio (S/N).

The ENC is convenient due to it being a direct relationship between charge injected at the input, and the resulting output noise. The relationship between RMS$_{noise}$, ENC, and FWHM are shown in the equations following Equation 23. As you can see, the RMS$_{noise}$ is equivalent to ENC if we decide to express the two in the same units. The FWHM broadening in terms of energy (eV) is especially useful, as it gives an even more intuitive relationship between noise and the energy resolution, or the minimum energy that is distinguishable from noise. W is the average energy to generate an electron-hole pair in the semiconductor (sometimes referred to as W-value or ϵ in the corresponding text), and ENC is no longer in units of charge, but number of electrons [64, 71].

While these equations provide some intuitive understand of ENC, it is important to understand a distinction. The ENC here is considering the amount of charge that would need to be injected into the input terminals of the readout to result in the noise seen at the output of the readout. It does not tell you how much charge was actually being injected into the input terminals, but tells you the equivalent noise charge that would be injected at the input terminals. As alluded to previously, all charge injected at the input terminals does not make it through the readout due to band-pass filters. Additionally, noise can be injected at any point in the readout, not only the input terminals. What we see at the output of the readout is a summation of charge injected at the input terminals, minus the charges that did not pass through various band-pass filters, plus any other noise charge injected throughout the readout circuit. Depending on how much charge was injected into the terminals, made it through band-pass filters, and was injected at various stages of the readout, different sources will be multiplied by the effects of gain differently. With that made clear, ENC is still an effective way of quantifying noise, as is RMS$_{noise}$ in units of voltage. However, in a model using ENC, we are defining the noise as the equivalent charge at the input

terminals. This requires that we treat the charge as if it went through the readout, being affected by the gain of the preamplifier and amplifier.

$$ENC = Q_n = \frac{V_{no}}{V_{so}} Q_s = \frac{Q_s}{S/N} \qquad (23)$$

$$FWHM_{noise}[volts] = 2.35 \cdot RMS_{noise}[volts]$$

$$FWHM_{noise}[electrons] = 2.35 \cdot ENC[electrons]$$

$$FWHM[eV] = 2.35 \cdot ENC[electrons] \cdot W[eV/pair]$$

ENC and noise in general is important because it determines the minimum detectable signal by the combination of your detector and readout electronics. ENC also limits the energy resolution at low energy, and the lowest energy for which a distinguishable peak may form in the pulse-height-spectrum. Noise also plays an important role for choosing shaping times and/or time constants in shapers. Since shaping is often accomplished using different CR-RC or CR-RC^n networks, the networks chosen may contribute to noise or filter noise in the system differently. At short shaping times (high bandwidth), "voltage noise" dominates ENC, while "current noise" dominates ENC at long shaping times (long integration). The minimum ENC is achieved when current and voltage noise sources are equal. At this level, the $1/f$ noise dominates and is the limiting factor in the ENC. Furthermore the $1/f$ noise is independent of shaping times. There are methods for estimating or predicting the ENC and the minimum ENC based on the individual components of the readout system. The terms included are shaping factors (F_i and F_v) which are calculated using the weighting function ($W(t)$), the sum of capacitances shunting the input (C), the spectral noise density of shot noise (i_n^2), and others [64]. The weighting function is the shaper output when delivered a step function at the input. While these estimations can be made, for modeling noise in a detector response function, it is convenient for users best to be able to assign an ENC or RMS$_{noise}$ value as an input parameter, as it correlates directly to spectral broadening across the energy spectrum and can be changed according to different measurement systems and environments with varying internal and external noise sources.

D. HPGe Detector Response Functions

A primary purpose of a detector response function (DRF) is to predict or verify the output of a radiation measurement. More specifically, to predict the pulse-height spectrum, or energy spectrum resulting from a radiation measurement. For HPGe detectors, this means the gamma spectrum. In a basic sense, building a DRF requires knowledge of the energy of the radiation incident on the detector and the amount of energy deposited during different interactions in the detector. When building a DRF, it is necessary to take

information about the radiation source and the detector, and calculate the energy deposited in the detector. Radiation from a source can be scattered and attenuated on its way to the detector, creating differences between the source spectrum and the spectrum incident on the detector. Once radiation enters the detector, different reactions can occur that result in varying energies being deposited in the detector volume. These include photoelectric effect, Compton scattering, and pair production. The photoelectrons and X-rays from photoelectric absorption may remain in the detector and deposit all of their energy or escape the detector volume (unlikely unless the detector is very thin). In Compton scattering, scattered photons can deposit varying energies between varying numbers of scatters. All of the incident photon energy may be absorbed or only a portion of the energy, depending on the amount of scatter events and the energy deposited in each scatter event. In pair production, the positron from the electron-positron pair will annihilate and produce two 511 keV photons. Each of these photons may deposit all of their energy in the detector, a portion of their energy, or escape while depositing no energy. The process is further complicated considering that any of these interactions may occur outside of the detector volume, with the products of the interactions (like a 511 keV photon) entering the detector to deposit energy [71, 95]. The process of source radiation reaching the detector and undergoing the various reactions is what generates the pulse-height spectrum. The relative probabilities of each of these interactions will play a major role in the shape of the pulse-height spectrum from a radiation measurement or the DRF. Other factors will also play a major role in the shape of the spectrum, such as the properties of the detector and the behavior of the readout electronics. For HPGe detectors, energy to create an electron-hole pair (W-value), charge carrier mobility and lifetime, detector size, collection efficiency, and Fano-factor will all play a role in the shape of the pulse-height spectrum. Noise from the detector and the readout electronics should be considered, too. The behavior of the detector and readout electronics will also influence different types of spectral distortions, such as pile-up or ballistic deficit.

There are multiple approaches to estimating the energy spectrum deposited in the detector volume for building a DRF. Some ways include using Monte-Carlo particle transport to simulate radiation transport/interactions in the environment and detector volume. These methods are ideal for accuracy in determining the detection efficiencies and radiation interactions that will occur in the detector volume. These methods can also enable a user to build DRFs of varying environments by changing the environment in the simulation. The benefits of using Monte-Carlo methods are the accuracy in the interactions that occur in the detector and the flexibility in the environments or measurement scenarios for which a DRF can be build. The drawbacks of Monte-Carlo methods are the time and computational power that it takes to run the simulation with enough particles to build the DRF with prominent and distinguishable spectral features. Monte-Carlo simulations can also generate large datasets that take more time to process. To save time and computational power, empirical methods may be used to calculate the probabilities of different interaction types and the shape of a pulse-height spectrum. This can include calculating the positions of full energy peaks, escape peaks, Compton edges/continuum, and the relative efficiencies of the reactions that generate those features in a spectrum. The benefits of empirical methods are the speed for which you can generate a DRF. While empirical methods can

generate sufficiently accurate DRFs, accuracy is usually limited to a highly specific environment. This is because different environments will vary in the attenuation and scattering of particles as they travel to the detector, resulting in large variance in the relative efficiency of different interaction types, and significant differences in the pulse-height spectrum as a result. Empirical methods are limited in modeling different detector types and sizes for the same reasons that they are limited in modeling different environments around a detector.

Once either empirical or Monte-Carlo methods are used to determine the nature of the energies deposited in the detector, the signal that the detector will produce must be modeled. The pulse-height spectrum of two different detectors in the same radiation environment can be tremendously different depending on the properties of the detector. Statistics of charge carrier generation, like the Fano-factor will vary between detectors and result in different levels of spectral broadening of spectral features like the full energy peaks. Differences in collection efficiency in different detectors will result in variations in low energy tailing of full energy peaks. Furthermore, the charge collection efficiency and charge trapping rely largely on the charge carrier mobility and the size of the detector due to their influence on charge collection time. Similar to the energies deposited in the detector, the amount of peak broadening and low energy tailing can be estimated using empirical methods. A DRF that utilizes empirical methods may produce a very accurate peak profile for a given detector but lack the versatility to generate accurate peak profiles for a detector with a very different size, charge collection efficiency, or charge carrier mobility. Parameters may be included to estimate these variations, but if a high accuracy is desired in a multitude of detectors with different materials, sizes, and physical properties, simulation of charge transport is a more guaranteed approach. Just like Monte-Carlo particle transport, simulating charge transport also takes time and computation power compared to empirical methods. Simulating charge transport also requires having additional data that isn't required for empirical methods. If one uses Monte-Carlo to model particle transport, then the data required to simulate the charge transport of individual reactions will be available, however, if one uses empirical methods to estimate energy depositions in the detector volume, there may not be sufficient data available.

Depending on the desired versatility and time afforded to the program, empirical methods, simulation, or a combination of the two may be best for generating DRFs. The next sections will go through examples of different DRFs, which brief explanations of their methods with strengths and drawbacks.

1. GADRAS

Sandia National Laboratories (SNL) has developed the Gamma Detector Response and Analysis Software (GADRAS) for gamma-ray and neutron detectors. There are two versions of this software, one full version (GADRAS) [95], and one public version with some radiation transport and analysis features removed (GADRAS-DRF) [96]. Unless specified otherwise, the focus of this review will be on gamma response in the full version. GADRAS was developed in 1986 as a sodium iodide (NaI) response function and has since had additional scintillators and semiconductor detectors added, including HPGe. To estimate radiation transport and calculate the probabilities of different interactions,

GADRAS uses a combination of first-principle calculations, empirical models, pre-computed tables, and approximate solutions [95, 97, 98]. Since GADRAS does not utilize Monte-Carlo, it can generate a DRF quickly (in seconds or minutes), which is one of the major benefits [95, 98].

In GADRAS, a detector is modeled as a rectangular shape, with parameters for length (thickness perpendicular to the side facing the source), width (relating to area seen by the source), and the height to width ratio (also relating the area seen by the source). While this is a rectangular shape, its primary purpose is related to geometric efficiency and the path length of source particles through the detector (called chord length in GADRAS user manuals). The length can be considered analogous to the intrinsic efficiency of the detector, while the width and height to width ratio can be considered analogous to geometric efficiency. Together, these parameters are used to calculate the probability of an interaction occurring. Even though these point to a rectangular shaped object, there are ways of estimating the changes in path length of a particle if the object is not rectangular, most notably in the case of a cylindrical detector turned sideways such that the source still "sees" the cross section of a rectangle, but the length changes depending on the path length. This is done using shape factors. These corrections can estimate certain geometries, but may not be as accurate when considering sources around coaxial HPGe detectors due to the bulletized end, drilled out central hole, contact pin, and possible orientations of the source relative to the detector.

The probability of an unscattered photon interacting in the detector is calculated based on the detector distance from the source and detector size parameters. Once a photon strikes the detector, the probability of a photon depositing all of its energy in the first interaction in the detector depends on the ratio between the photoelectric cross section to total cross section. If a photon does not deposit all of its energy in the first interaction then it may undergo Compton scattering. If so, the probability of the photon scattering outside of the detector after depositing some amount of energy is calculated using the energy of the incident photon. Electrons generated from Compton scattering and photoelectric absorption do have some probability of escaping, which is a relatively small probability and calculated empirically [95].

The probability of photons scattering into the detector volume depends on the distance and materials between the source and the detector. GADRAS uses first-principals and empirical calculations to estimate the scattering of radiation between the source and the detector [95, 98]. Scattering is controlled by several scattering parameters. There are scattering terms for attenuation that also reduce the probability of low energy gamma ray interactions in the detector. The user can choose between attenuators that are either in contact with the detector (to estimate the effect of a detector housing), or attenuators that are outside of the immediate vicinity of the detector. The presence of these attenuators can reduce low energy gamma and increase scattering. Shielding can also be estimated. Shielding refers to materials being directly around the sides or back of the detector to shield the detector from radiation coming from the sides and back of a detector and/or collimate the source. Following the same principles, air attenuation is also estimated based on air pressure [95]. All of the scattering parameters work in the same way, in the sense that they add scattering or attenuation as the parameter is increased.

Pile up can be estimated by GADRAS by including a shaping time parameter, which refers specifically to a preamplifier shaping time. For pile up rejection, the shaping time parameter can be set to a negative value. Positron annihilation photons, X-rays generated from shielding materials, trapping of holes, and dead layers are other parameters that can be used to adjust the DRF.

GADRAS can estimate the effects of scattering in relatively simple cases that align well with benchmarks, but complex scattering environments require an external transport code. Monte-Carlo radiation transport can be used to calculate the radiation incident on the detector in a more complex environment. GADRAS-DRF has a feature which allows the user to use MCNP to model the environment and tally the energy-dependent current on each surface of the detector. The tally output can then be converted to a file format compatible with GADRAS-DRF. Following this, the scattering calculations that would normally be completed within GADRAS-DRF should be "disabled" by setting the scattering parameters to zero. It should be noted that this method will model the radiation scattering between the source and the detector more accurately, but GADRAS-DRF only accepts the energy-dependent current into the surface of the detector. As a consequence, anything that occurs inside of the detector volume is calculated using the same empirical methods as usual. Furthermore, the detector needs to be cylindrical in the Monte-Carlo transport such that the current density is on three surfaces, the back, front, and sides [96].

2. *Other detector response functions*

Other HPGe detector response functions use semi-empirical models, which utilize first principles to calculate the positions of the full energy peaks, Compton edges, and escape peaks [99]. The shape of the features is then determined empirically, for example, the width of a full energy peak can be determined by assuming a gaussian shape with a width determined by the W-value, Fano factor, and energy position. Peak tailing, electronic noise, and the shape of the Compton continuum are also determined using a combination of first principles and empirical methods. This method produces accurate peak profiles and positions with only a few input parameters, however, there is not a method to account for the scattering and attenuation that will occur in a complex environment.

For low energy spectroscopy, the approach to obtaining an accurate detector response function changes in comparison to high energy gamma spectroscopy with coaxial HPGe detectors. Changes in the detector design must be made due to the attenuation of low energy photons in the contacts (dead layers) and housing of large coaxial HPGe detectors. HPGe detectors designed for low energy spectroscopy are smaller and have thin metal electrode contacts. Response functions have been used to analyze low energy X-ray spectroscopy data [100]. For low energy applications, several factors are important in the pulse-height spectrum that are not as important in high energy applications. The escape of photoelectrons and Auger electrons that are generated in the crystal will have a prominent impact on the spectrum, as well as the penetration of these electrons into the crystal when they are generated in the contact electrode. The K-shell photoelectrons and K photons from nickel contacts are often seen in the spectrum. Detector response functions can be used to better understand these spectra, especially when considering the large implications that the contact materials, thickness, and detector properties will have on the spectrum.

Some methods combine empirical methods with Monte-Carlo (MCNP) to simulate radiation transport in the environment and detector volume. Using a simple F8 tally (pulse-height tally), the basic response is built, and then gaussian energy broadening is added to generate a more accurate pulse-height spectrum [101]. Gaussian energy broadening is a feature included in MCNP. Measurements are taken with a specific detector, and the FWHM of the measured peaks are used to determine the input parameters for gaussian energy broadening in the MCNP F8 tally. This results in an accurate radiation transport model, followed by a quick empirical model for peak broadening that adds little time commitment to building the response function. While these can be used to make the F8 tally appear more accurate, they lack the detail to account for all properties that result in peak broadening and tailing because they rely on a simple gaussian model with uniform broadening on both the low energy and high energy side of a peak.

Detector response solely from Monte-Carlo simulations have also been used to obtain better characterization of HPGe crystals [102]. A user might find some information about the HPGe crystal difficult to obtain. Things like specific crystal dimensions and dead layer thickness may not be known precisely, especially if a detector has aged significantly. Explicitly measuring these could sacrifice the HPGe crystal. Various analysis techniques, including Monte-Carlo based detector response functions can be combined to learn about the condition of a specific crystal. Like other examples, these methods may provide accurate radiation transport in and around the detector, greatly improving the accuracy of the detector response function. However, fully accurate spectra are rarely obtained without modeling charge transport and readout effects.

3. General response function conclusions

When building detector response functions, there is a balance between time and accuracy. Some methods include using solely empirical methods, which will generate a response function within seconds or minutes. Methods that utilize first-principles and empirical methods (GADRAS for example) can estimate scattering and shielding in the environment to some level, but there is a sacrifice for accuracy that becomes greater in more complex environments. This sacrifice comes at the benefit of reduced computational time and power. Even if MCNP energy current tallies are used as an input to GADRAS-DRF, the interaction probabilities inside of the detector volume are still determined empirically. This also sacrifices some level of accuracy for the benefit of time. For quick acquisition time and accuracy in simple environments, GADRAS could be ideal. If the user is willing to sacrifice time for accuracy, or requires accuracy in a complex environment, then Monte-Carlo will be necessary for accuracy. It should be noted that Monte-Carlo does not guarantee accuracy. The model is limited by the accuracy of the detector dimensions, dead layers, housing materials and construction, and surrounding environment. Oftentimes, Monte-Carlo radiation transport methods are followed by empirical methods to estimate the effects that detector properties (i.e., charge collection efficiency, collection time, mobility-lifetime product, fano factor, etc.) have on the pulse-height spectrum. Doing this empirically results in the same sacrifices as modeling radiation transport empirically. It can be done quickly, but generally less accurately. The same follows for modeling the effects of the readout on the pulse-height spectrum. If accuracy is the main concern across a broad

range of conditions, and computation time and power are available, then the most accurate detector response functions would use analytical and/or numerical methods with first principles to model all aspects of the detector system. This could look like using Monte-Carlo to model radiation transport, followed by explicitly modeling charge transport in the detector according to individual reactions in the detector volume. This would be followed by a readout model that separates noise, ballistic deficit, and pile-up. Having each modeled separately would allow users to model a wide variety of detectors, readouts, and environments.

METHODS

Building the detector response function requires multiple elements. DRiFT starts by using MCNP and its corresponding ptrac file to model an environment and particle tracking within a detector volume. The particle interactions in the ptrac file are used as an input into a charge transport code, which models charge generation, charge transport through the detector volume, and detector response for each interaction. The detector response is fed into a readout model, which models the preamplifier, shaping amplifier, noise, and pile-up. The output of the readout model is used to build a pulse-height-spectrum, or DRF. The basic form of the workflow used to build the DRF is shown in Figure 37. It is a simple schematic for how each component of the DRF fits together and the general purpose of each item. In the following sections, the purpose of each component and the methods within each will be explained in detail.

A. Modeling the Electric Field and Potential in Silvaco

Silvaco was used to model the electric field and electric potential inside of the HPGe crystal. Silvaco is often used for modeling these things in microelectronics. It can account for different materials, shapes, multiple electrodes, n-type, and p-type dopants at different concentrations, and more. It is an excellent tool to model the crystal accurately. Modeling the detector required knowing the details of the crystal precisely, and that starts with the specific detector type. Recall the details of the detector that we are modeling (ORTEC GEM140P-S coaxial design). The bulk of the material is p-type HPGe. The outer surface is a 700 µm lithium diffused (n+ type) outer contact that serves as both the outer electrode and a blocking contact (blocking holes but not electrons). The inner surface of the hole is a 0.3 µm boron implanted (p+ type) contact that serves as the inner electrode and blocking contact (blocking electrons but not holes). Having crystal size and shape, the dopant types/concentrations/regions, and detector bias accurate in the Silvaco model is necessary for getting accurate field and potential profiles.

1. Building the mesh

Silvaco starts by building 2 or 3-dimension mesh based on the geometry and mesh size that the user specifies. However, it is a 32-bit program so memory issues arise if you try to generate a mesh that is too fine in a large object. We took advantage of symmetry in the coaxial design of the HPGe crystal and modeled it in 2-D using cylindrical coordinates. This reduces the number of mesh points so that we can make the mesh much finer than if it was a 3-D mesh.
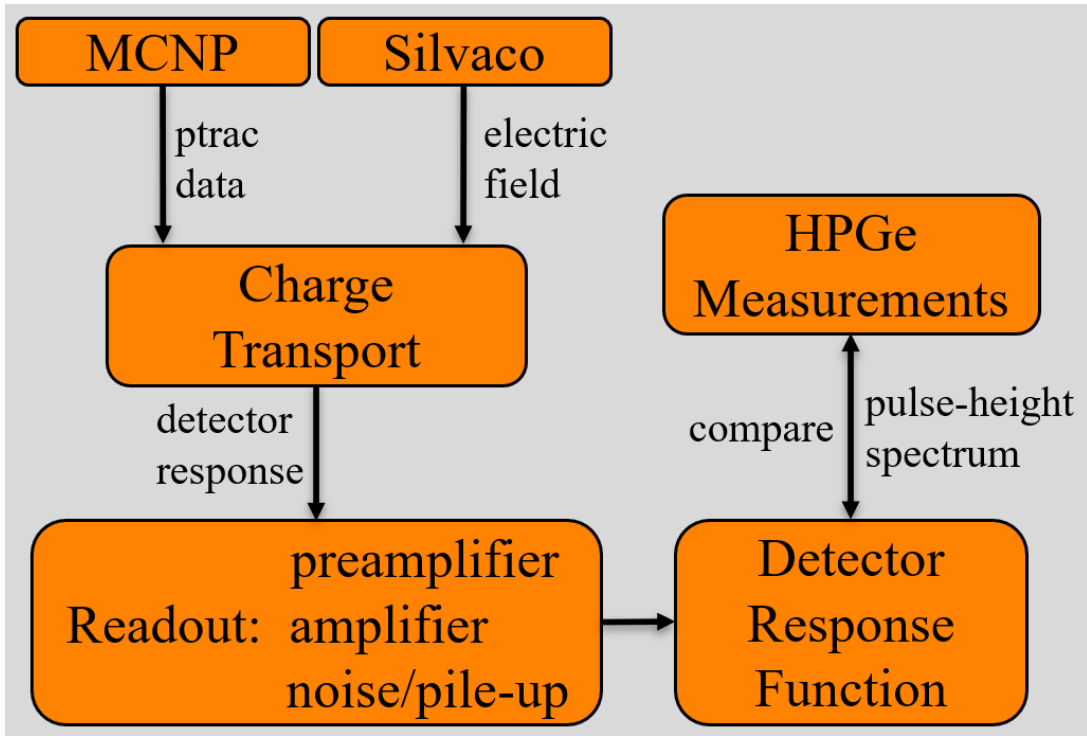
Figure 37: The workflow of the HPGe detector response function for DRiFT.

We also made the mesh finer near boundaries and places with large electric field and electric potential gradients. This is important when considering the geometry of the coaxial design and the thin n+ and p+ contact layers on the surface of the crystal. Through trial and error, we found a satisfactory mesh solution that allowed us to capture the features of the electric field and potential without running into memory issues. Mesh is built in Silvaco by using an input deck that has a single line of code for each region. Curved regions of the crystal, such as the end of the hole and bulletized end need to be constructed by generating multiple rectangular regions of different sizes. This requires that many regions be defined to capture the curved surfaces precisely. A Python script was written solely for generating the many lines of code needed to build the mesh. We oriented the coordinate system such that the origin is at the center of the base of the crystal, with the positive y-axis pointing straight through the central axis of the cylindrical shape of the crystal. In other words, the positive y-axis follows the center of the hole in the crystal. This is a subtle but important point, because the orientation is consistent with the crystal orientation in MCNP. Otherwise, a translation of the radiation interaction coordinates generated by MCNP would be required.

2. *Simulating the electric field and electric potential*

Once the mesh was built, the user defines dopant concentrations in different regions, defines the electrodes, and the bias on each electrode. This device has a +4500 V bias on the outer electrode (n+ lithium diffused layer) with a donor concentration of 10^{19} cm^{-3}. The inner electrode (p+ boron implanted layer) is grounded and has an acceptor concentration of 10^{19} cm^{-3}. The bulk of the HPGe material has an acceptor concentration of 3×10^9 cm^{-3}. Silvaco runs the simulation and outputs a mesh-grid of coordinates and corresponding electric field and electric potential values. Since we used cylindrical coordinates reduced to a 2-dimensional mesh, the values are output in radius and height (r, y). Figure 38 shows the electric field and electric potential gradients generated by Silvaco (the data and the figures were generated by Silvaco). Also refer to Figure 39 for plots generated by Python which show the magnitude of each electric field vector instead of the scalar magnitude. If we plot the electric field and electric potential, then we can see the gradient in different places in the crystal. To do this, we plot them as a function of radius (r) at different y-values, or different places along the height of the crystal. Figure 40a shows the electric field versus r-coordinate at different y-positions in the crystal (y=40, 70, 93, and 100 mm). Figure 40b shows the electric potential versus r-coordinate at the same y-positions. Each electric field plot contains the magnitude of each vector and the scalar magnitude. In the legends, *Er* denotes the electric field vector in the r-direction, *Ey* denotes the electric field in the y-direction, while *E* denotes the overall scalar magnitude of the electric field ($E = \sqrt{E_r^2 + E_y^2}$). Notice the behavior of *Ey*, where it is mostly zero in the bulk of the cylindrical crystal until we approach the top of the crystal where the hole terminates and the bulletized end begins. The values at 93 mm are roughly where the rounded end of the hole begins. From here, the electric field vector in the r-direction (*Er*) starts to become less dominant compared to (*Ey*). The electric potential follows a more linear relationship but behaves less linearly as it approaches the bulletized end.

a)

center hole

b)

rounded end

Figure 38: The electric field (a) and electric potential (b) gradients generated by Silvaco.

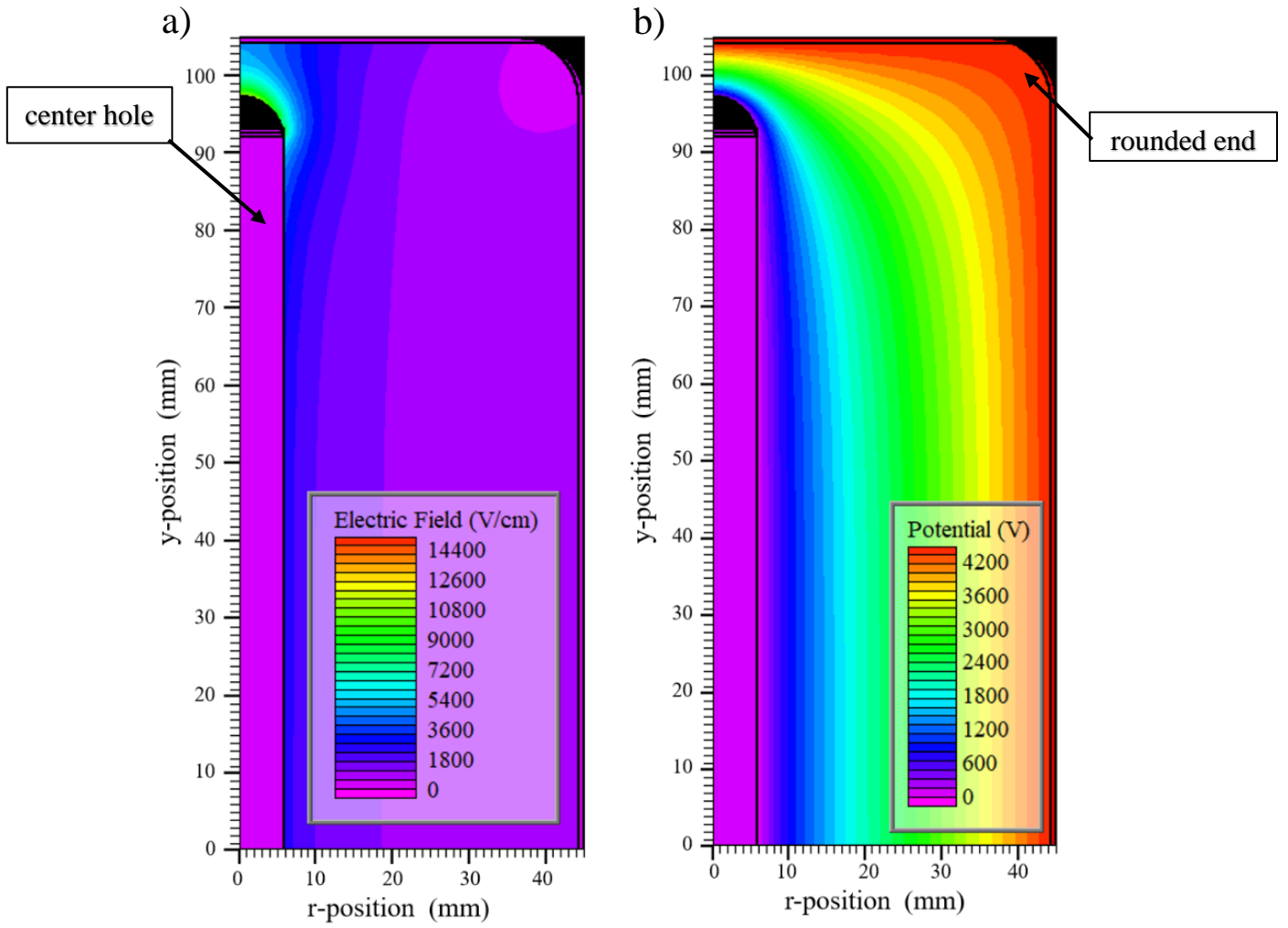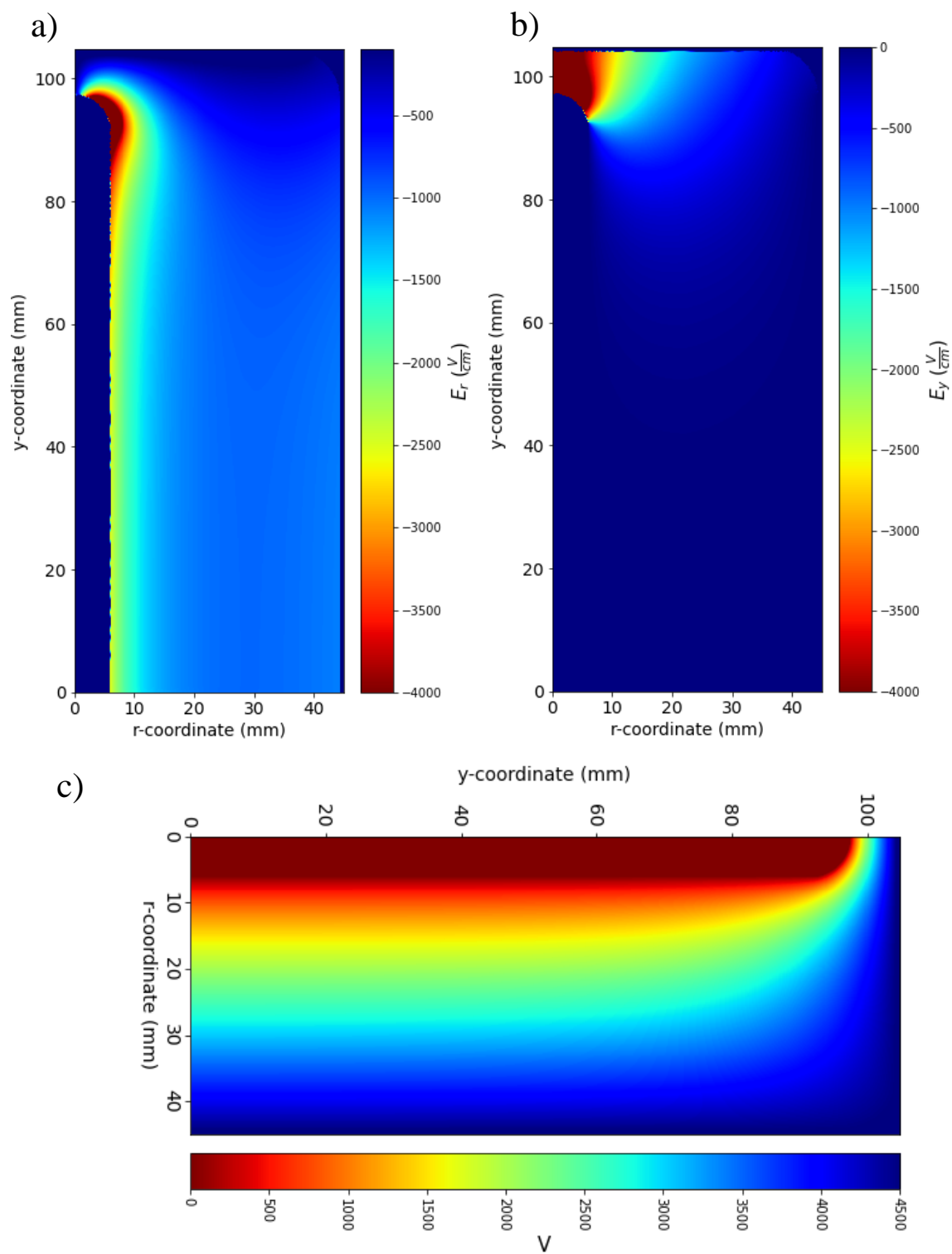Figure 39: The electric field r-vector (a), the electric field y-vector (b), and electric potential (c) generated by Silvaco but plotted in Python.
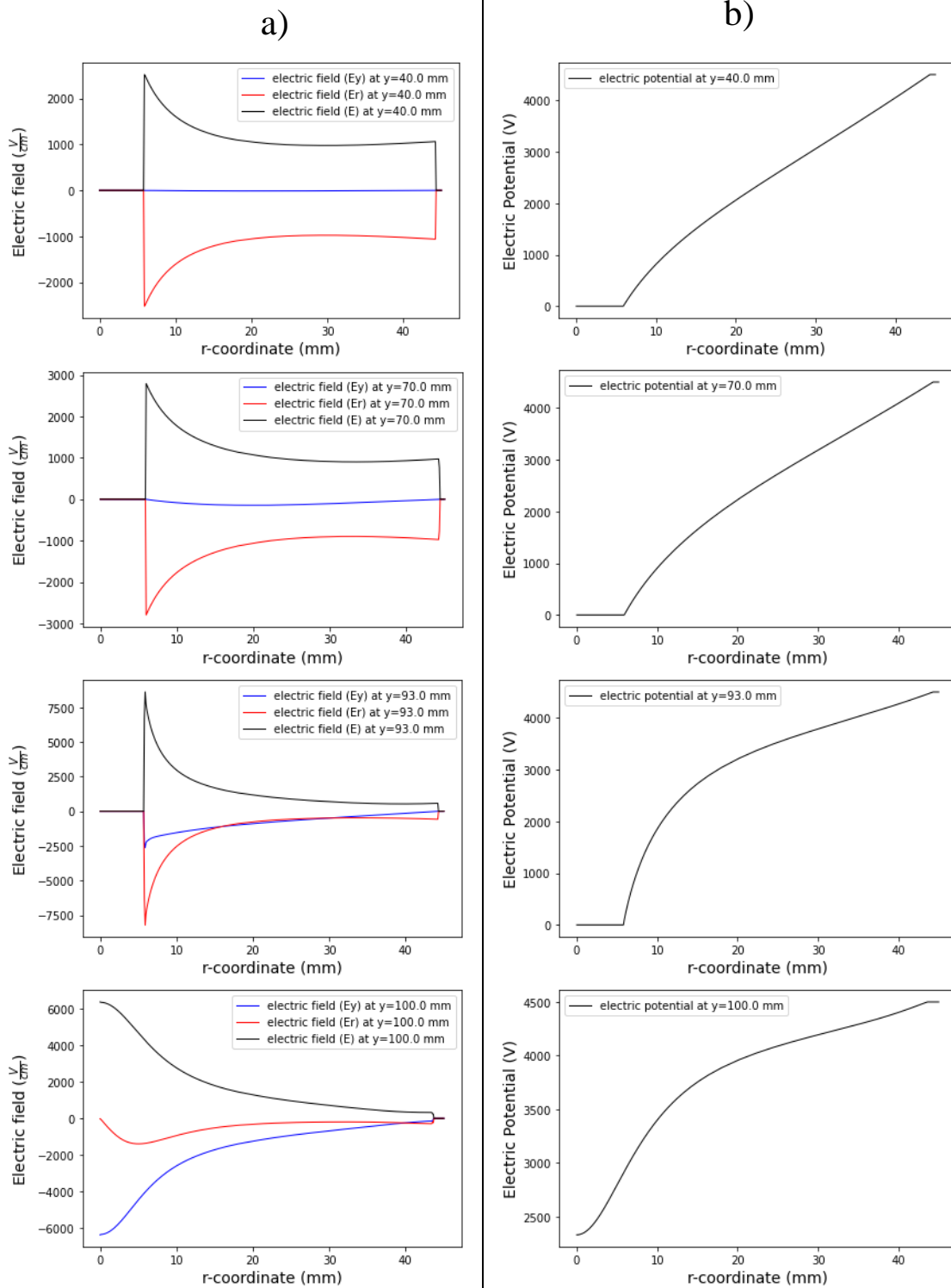
Figure 40: The electric field (a) and electric potential (b) as a function of radius (r-coordinate) in the crystal at different y-coordinates.

97

B. Modeling the Detector in MCNP

Our DRF, and DRiFT rely on ptrac data from MCNP simulations, so a detailed MCNP model is needed for accurate particle tracking in the detector volume. This starts with the detector geometry, around which an environment can be built to generate DRFs in a broad range of scenarios. To model the detector, we started with information provided by the manufacturer (ORTEC) and openly available documentation online [53, 66]. Upon request from ORTEC, we were provided a specification sheet which contains more precise detector and assembly dimensions that are specific to the detector being modeled. There is a lot of important information that ORTEC will not disclose. From here, we turn to the literature for information about the internal construction of coaxial ORTEC HPGe detectors. We also disassembled a coaxial ORTEC HPGe detector to determine materials and dimensions not able to be disclosed.

1. Reviewing the literature

Several studies have looked into the internal geometry specifically for the purpose of creating accurate models. Radiographs of these detectors have been made to learn about the crystal dimensions and overall construction [102, 103]. Figure 41 shows an example of a radiograph, however, it is not known exactly what brand/model of detector this is. The radiograph does not reveal what materials are present; we can only see shapes and relative densities. The density of the crystal shields details of the contact pin and central hole. Other radiographs are similar due to the limitations of X-ray imaging.

Maybe the most important detail that ORTEC will not disclose is size of the central contact pin that goes into the hole of the crystal. The diameter and length of the contact pin make a significant difference in detection efficiency. Analysis of CT scan, and comparisons of experimental data and simulations (Geant3 and Geant4) suggest that the copper contact pin of an ORTEC 140% efficiency HPGe detector had a diameter of 6.9 ± 0.5 mm [103], while another study suggests that the copper contact pin in a larger ORTEC GEM150P4 (150% efficiency) is between 1-3.5 mm [104]. The latter concludes that the copper pin diameter range they studied causes a change in detection efficiency of up to 2% at photon energies of about 1.4 MeV and a source to detector distance of 20 cm. However, they also discovered that the changes in detection efficiency for different contact pin diameters become more drastic at larger source to detector distances and higher photon energies. Over a broad range of measurement scenarios, the error in detection efficiency at high energies due to an incorrect contact pin diameter could be far beyond 2%.

ORTEC was able to provide more specific measurements than what is found in the open documentation and literature online. Given a serial number, they provided a specifications sheet, or Quality Assurance Data (QAD) sheet. This information is privately provided by ORTEC when requested, and the dimensions within the sheet are specific to the detector of the serial number given. These are dimensions of the crystal that vary between detectors, even of the same model. To avoid releasing sensitive information, we omit these specific dimensions and diagrams, however, they include crystal diameter, height, hole diameter, radius, metal component thickness, relevant spacing between components, and more.

98
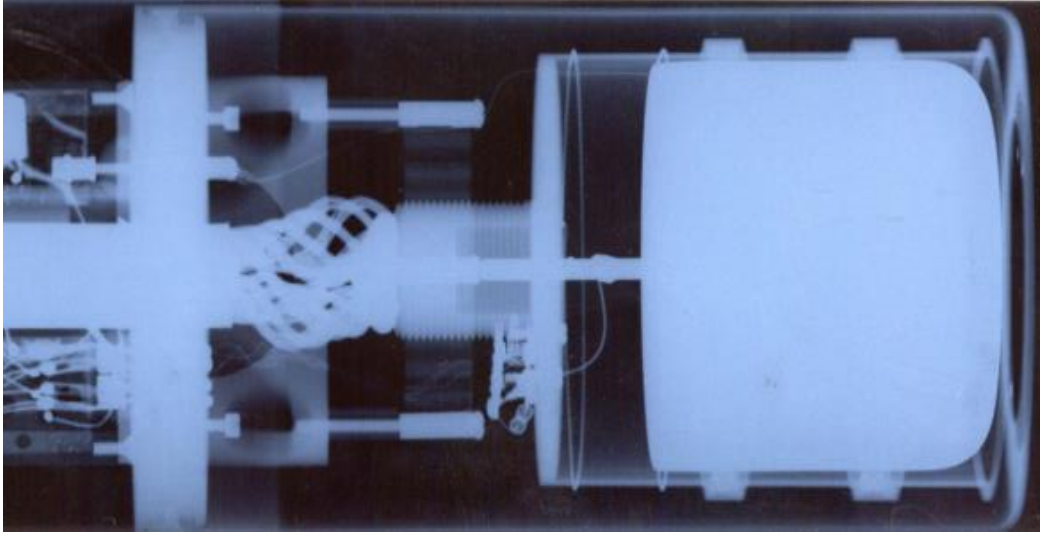
Figure 41: An X-ray image of a coaxial design HPGe, revealing information about the internal construction [102].

2. *Disassembly of an ORTEC HPGe detector*

Since our DRF is expected to generate accurate DRFs over a broad range of measurement scenarios, we decided to disassemble an ORTEC GEM-10185 HPGe detector and inspect the internal construction. This will give us a chance to measure the dimensions of the central copper contact pin directly and inspect the structure and materials inside of the detector housing. While the detector we disassembled is a different size, it is still the same design (ORTEC GEM p-type coaxial) with a similar central hole diameter. The central hole diameter in the detector we are modeling is just over 11 mm, while the hole in the detector we disassembled has a diameter of 10 mm. That is just barely smaller despite the fact that the crystal is half the size in diameter and height. Furthermore, the general hole diameter has been referenced as roughly 10 mm for coaxial designs [51]. Knowing this, hole diameters and contact pin sizes are expected to be similar across crystal sizes. The copper contact pin during disassembly was measured to be 3 mm in diameter, so we went forward with that measurement for the MCNP model of the larger detector.

Several detector components missing from the ORTEC documentation were found during disassembly of the detector, and many of them were added to the MCNP geometry. These include ceramic materials, wires, plastics, metals, and refining of interfaces where components go together. Some components were added more precisely than others, and the following will summarize what has been added. We refrain from adding detailed figures of the internal components after considering that ORTEC does not openly communicate the information due to is proprietarity. Disassembly showed us that there is an aluminum mounting cup, as described by ORTEC, but there is also a ceramic spacer in the mounting cup, not disclosed by ORTEC. There is also a plastic spacer with channels in it for different wires. The mylar/aluminized mylar is now known to be two separate sheets of mylar and aluminum foil that are held on by a plastic sleeve on the end of the detector mounting cup. Lastly, the mounting cup has an accompanied aluminum mounting post that inserts into a copper slot, which is connected to the copper cooling rod for keeping the detector close to liquid nitrogen temperature.

Removing the HPGe crystal and taking a look inside of the mounting cup revealed that the crystal sits on the contact pin with a negligible amount of contact paste. Disassembly also showed a small square of contact paste or tape on the outer surface of the crystal, revealing that there is not a paste or glue surrounding the entire crystal (a question of concern that we had while building the model).

The MCNP model takes a lot of the mounting cup features into consideration. These include the aluminum/mylar foils, the main cylindrical shape of the mounting cup and its mounting post, the contact pin, the ceramic spacer, the plastic spacer, and some basic wires. The model does not take into consideration the complexity of the bends in wires or the small gaps in the plastic spacers where wires feed through. In the model, the included wires do have a sheath around the central copper wire. Concerning the crystal itself, the MCNP model mimics the bulletized coaxial design and includes the 700 µm contact layer (dead layer). This ensures that interactions that occur within this dead layer are not recorded as detected events, which is important for low energy photons. The MCNP model of the detector housing is shown in Figure 42. The figure was creating using the MCNP VISED application. This view is the YZ plane cutting through the center of the crystal.
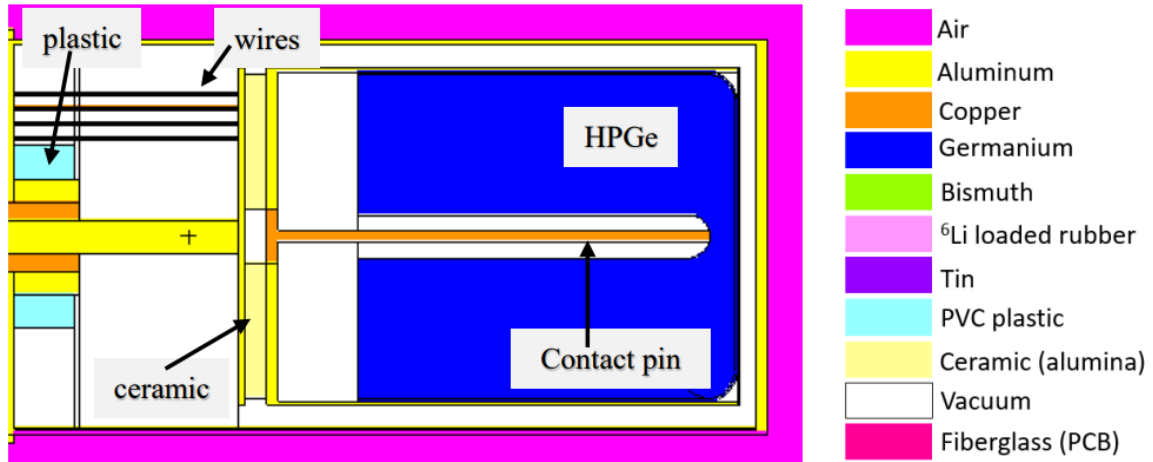
Figure 42: The MCNP model of the detector housing and materials color legend.

It shows the rounded or bulletized end, the hole, the contact pin, and other components. VISED is limited in its resolution so certain areas where components are too small are not captured at this scale. Most notably, smaller components such as the wires, mylar, and the dead layer are not properly represented in the figure. Since mylar layers are so thin and invisible in any images, it is left out of the legend. Furthermore, some materials listed in the legend are only in components not shown in the figure (^{6}Li loaded rubber, tin, bismuth).

The electronics housing is easily accessible without any extensive disassembly because it is not kept under vacuum like the detector housing. The electronics housing includes a PCB that has many components mounted to it, and a power supply line (Figure 43). To model this in MCNP, we included a shielded power supply cable, meaning it has a central copper line, outer copper sheath, and shielding between the copper layers and the outside. To model the PCB in a simple way, we used a simple sheet of copper sandwiched between two layers of fiberglass. This ignores the plastic and metals in the components on top of the PCB but captures the bulk of the component. We also modeled the copper cooling rod which runs up the center of the electronics housing. Figure 44 shows the MCNP model of the electronics housing in two views. One in the YZ-plane to show the side view, one in the XZ-plane to better illustrate the shape of the components. There is also a color legend. Like Figure 42, some materials listed in the legend are only in components not shown in the figure (germanium, ^{6}Li loaded rubber, tin, bismuth, ceramic, vacuum). Finally, the entire MCNP model is shown in Figure 45 as a slice in the YZ-plane. The top of Figure 45 only shows the HPGe detector, while the bottom left includes one option for a collimator that has bismuth, ^{6}Li loaded rubber, tin, and an aluminum handle. The collimator materials and dimensions were provided by LANL.

3. *Comparing F8 tallies of different MCNP geometries*

To test how different components changed the efficiency at different photon energies, we compared MCNP F8 tallies of a ^{60}Co source for models with various levels of detail. The source is an isotropic source roughly 10 cm from the front of the crystal in all simulations. For each run, 100,000,000 particles were run. The error is about 2% in the Compton region of each spectrum, however, in bins where counts are low, such as the region between the 1.17 and 1.33 MeV peaks, it is approaching 20% for some energy bins (only a few bins). The peak bins have errors of less than 0.5%. The comparisons are made by plotting F8 tallies from two different models together, and by finding the ratio between the two F8 tallies to show where differences occur. In energy bins where the ratio is equal to one, the two models performed identically. Each F8 tally has 1 keV energy bins. To keep this concise, only a brief description of the geometry that generated each F8 tally will be provided. The collimator is not used for any of these comparisons. The 4 different models are listed as Model A-D, where complexity and accuracy are increased from A to D. Table 2 lists the different MCNP models and briefly explains their differences and levels of detail. Figure 46 shows MCNP Vised images of Models A-C. For an image of Model D, see the top of Figure 45.
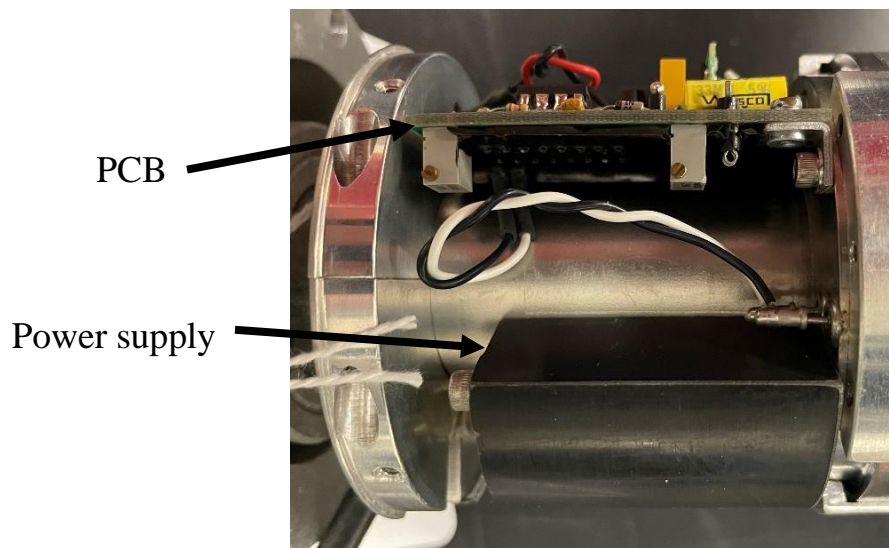
Figure 43: The electronics housing of the HPGe detector.
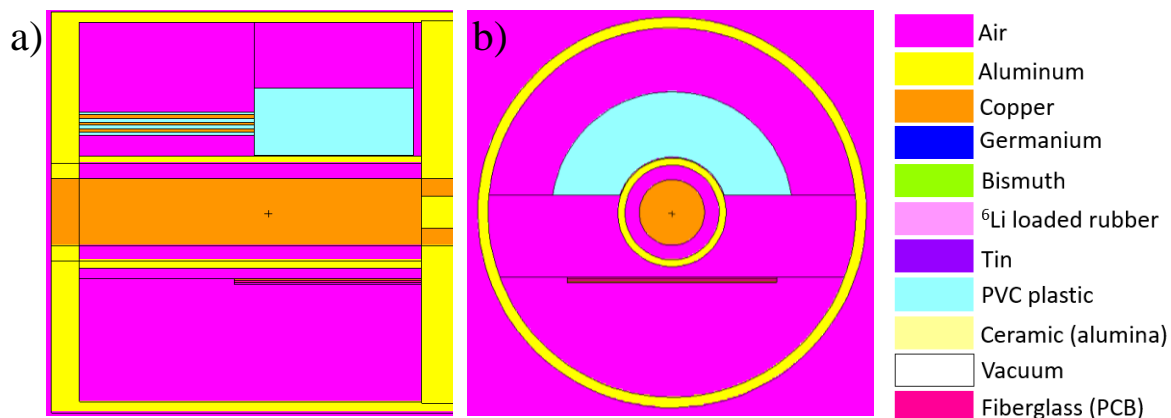
Figure 44: The MCNP model of the electronics housing in the YZ-plane (a), the XY-plane (b), and a materials color legend.
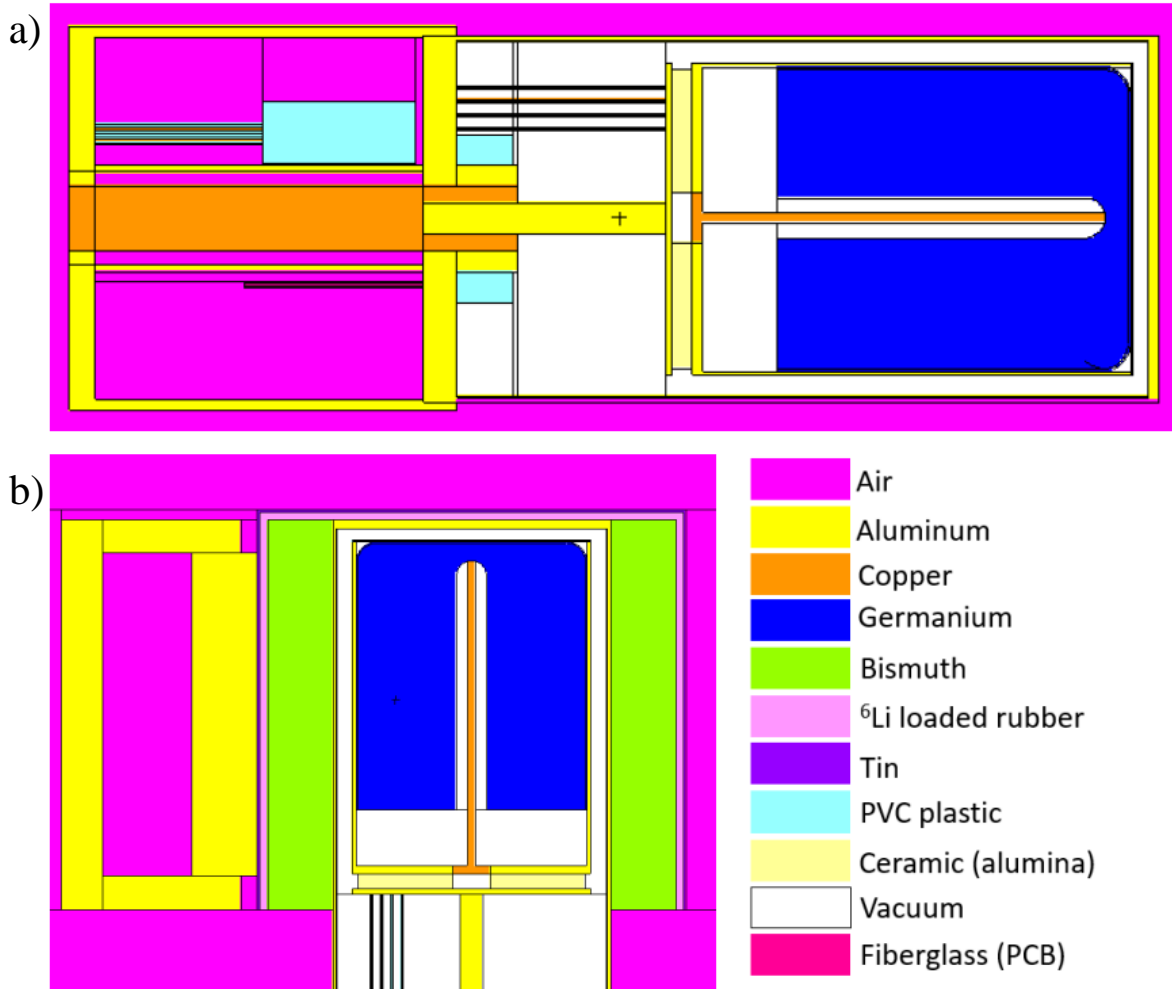
Figure 45: A full view of the HPGe MCNP model (a), with an included collimator option (b), and materials color legend.

Table 2: A list of MCNP models being used to compare the effect of adding components on the F8 tally

Model Name	Details
Model A	The HPGe crystal only.
Model B	Added aluminum crystal mount and detector housing.
Model C	Added a dead layer on outside of crystal, contact pin and cold finger (cooling rod). The contact pin is incorrect by having too large diameter.
Model D	Added components found after disassembly of an HPGe detector, such as: wires, ceramics, plastics, and a circuit board. Also refined the dimensions and interfaces where different components fit together.

For Model D, see the top of Figure 45a

Figure 46: MCNP VISED images of Models A-C.

i. Model A versus Model B

The most basic model includes only a crystal surrounded by air (Model A). The crystal has the coaxial shape with rounded edges but does not have the dead layer or any detector materials around it. The model we will compare this to is one with the same crystal, with an added crystal mount and basic detector housing (Model B). Figure 47 shows a comparison between the F8 tallies of each. Figure 47a shows each F8 tally, while Figure 47b shows the F8 tally of Model A divided by Model B. You can see that adding the housing increased the counts in the Compton region and impacted the counts at higher energies the most. This can be contributed to increased Compton scatters in the housing before photons reach the detector. There is not a drop in counts at low energy because the photons incident on the detector housing are mostly high energy (>1 MeV). If there were more low energy source photons that could be completely shielded by the housing, then we would expect a drop in efficiency in that range after adding the detector housing for Model B.

ii. Model B versus Model C

Next, we will compare the F8 tallies of Model B and Model C. Model C has the addition of a dead layer on the outside of the crystal formed from lithium diffusion, and the addition of a copper contact pin. Figure 48 shows the two F8 tallies and the ratio between the two. The same changes in the spectrum from Model A to B are seen from Model B to C. Again, the difference becomes more drastic at higher energies, as expected from the addition of a contact pin.

iii. Model C versus Model D

Finally, we will compare Model C to Model D. Model D is the most up to date geometry shown in the top of Figure 45. It includes a refined contact pin, refined housing, and added components behind the crystal, such as the wires, ceramics, plastic, interfaces, etc. Figure 49 has both F8 tallies plotted and the ratio between the two F8 tallies. The spectra are mostly the same, but adding the additional components behind the crystal volume resulted in more fluctuation in efficiency at energies greater than about 1 MeV. The differences in components are behind the crystal, which are outside of the direct path of the source photons, which implies that the added components in the electronics and detector housing have a significant effect on backscatter events at high photon energies.

iv. Correct contact pin versus incorrect contact pin

Finally, for the last comparison, we will compare the final HPGe geometry (Model D), to an identical model with a larger contact pin (6 mm instead of 3 mm). The purpose is to demonstrate the importance of having the correct contact pin size by comparing F8 tallies for different contact pin sizes. The comparison shows that the larger 6 mm diameter contact pin increases detection efficiency relative to the 3 mm contact pin at photon energies greater than about 1 MeV. This shows that not only having a contact pin is important, but a correct contact pin for accurate particle tracking across all energies. The comparison is shown in Figure 50.
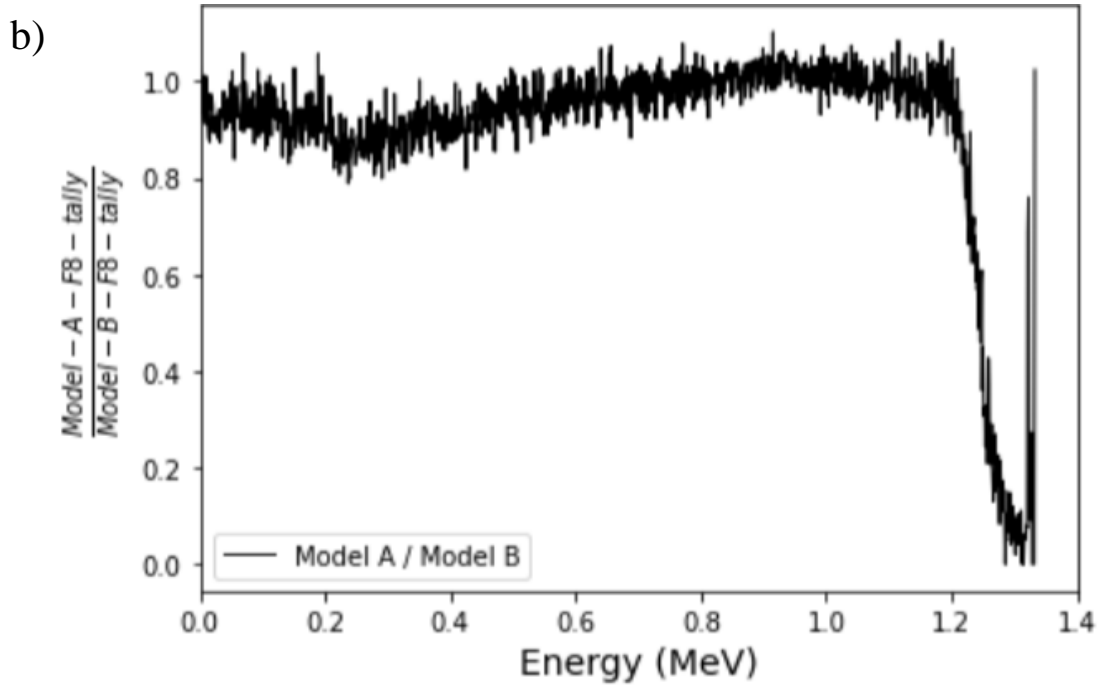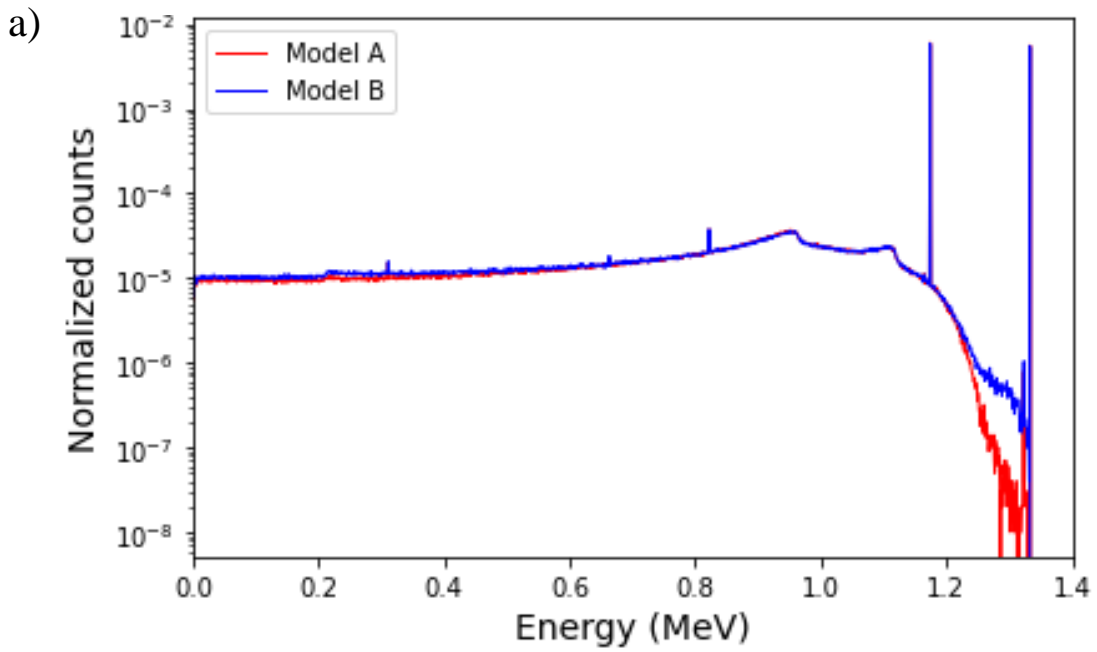
Figure 47: Comparison of F8 tallies between a model with only a crystal, to a model with a crystal and detector housing. Both F8 tallies plotted (a) and the ratio of the two F8 tallies (b).

a)

b)
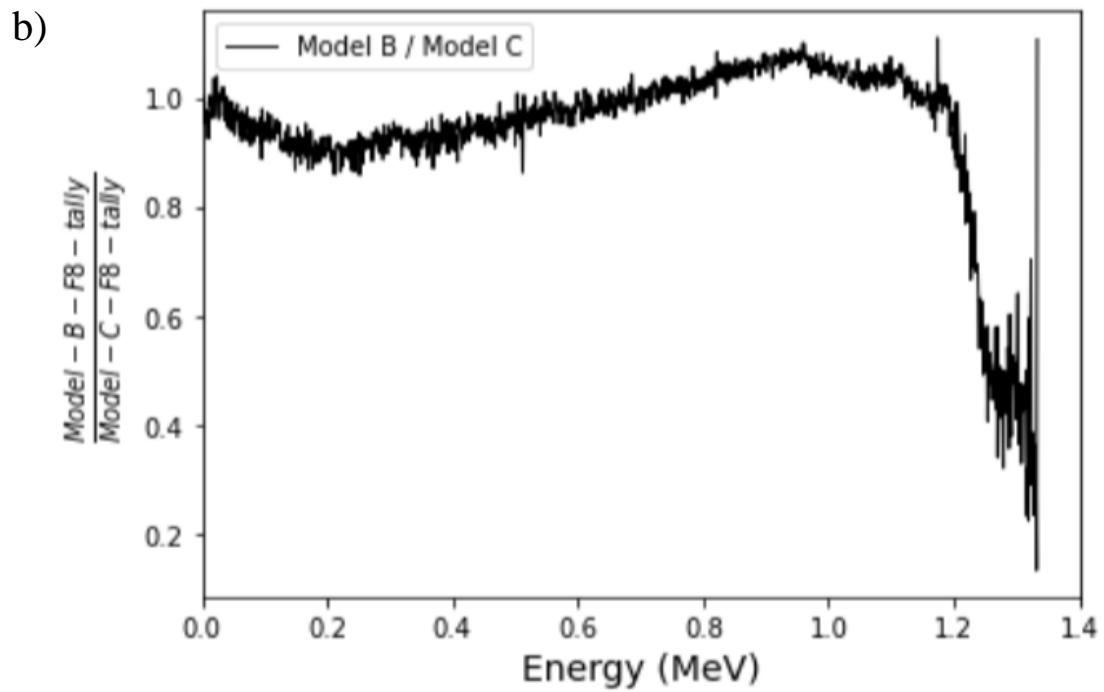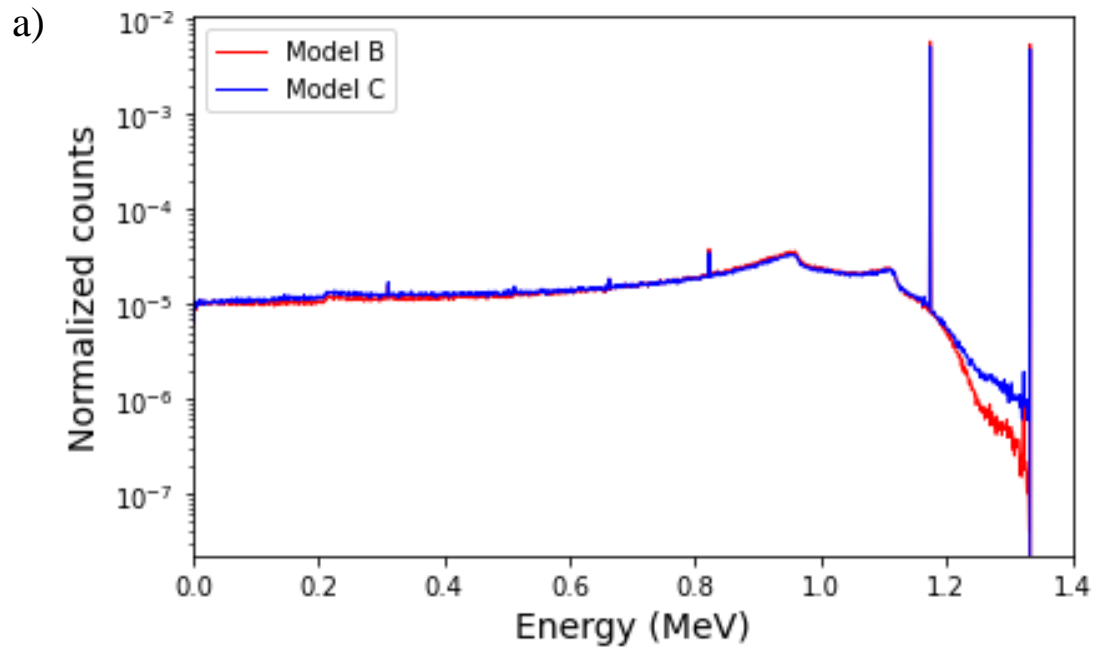
Figure 48: Comparison of F8 tallies between a model with a crystal and detector housing, to a model that also includes a dead layer and contact pin. Both F8 tallies plotted (a) and the ratio of the two F8 tallies (b).
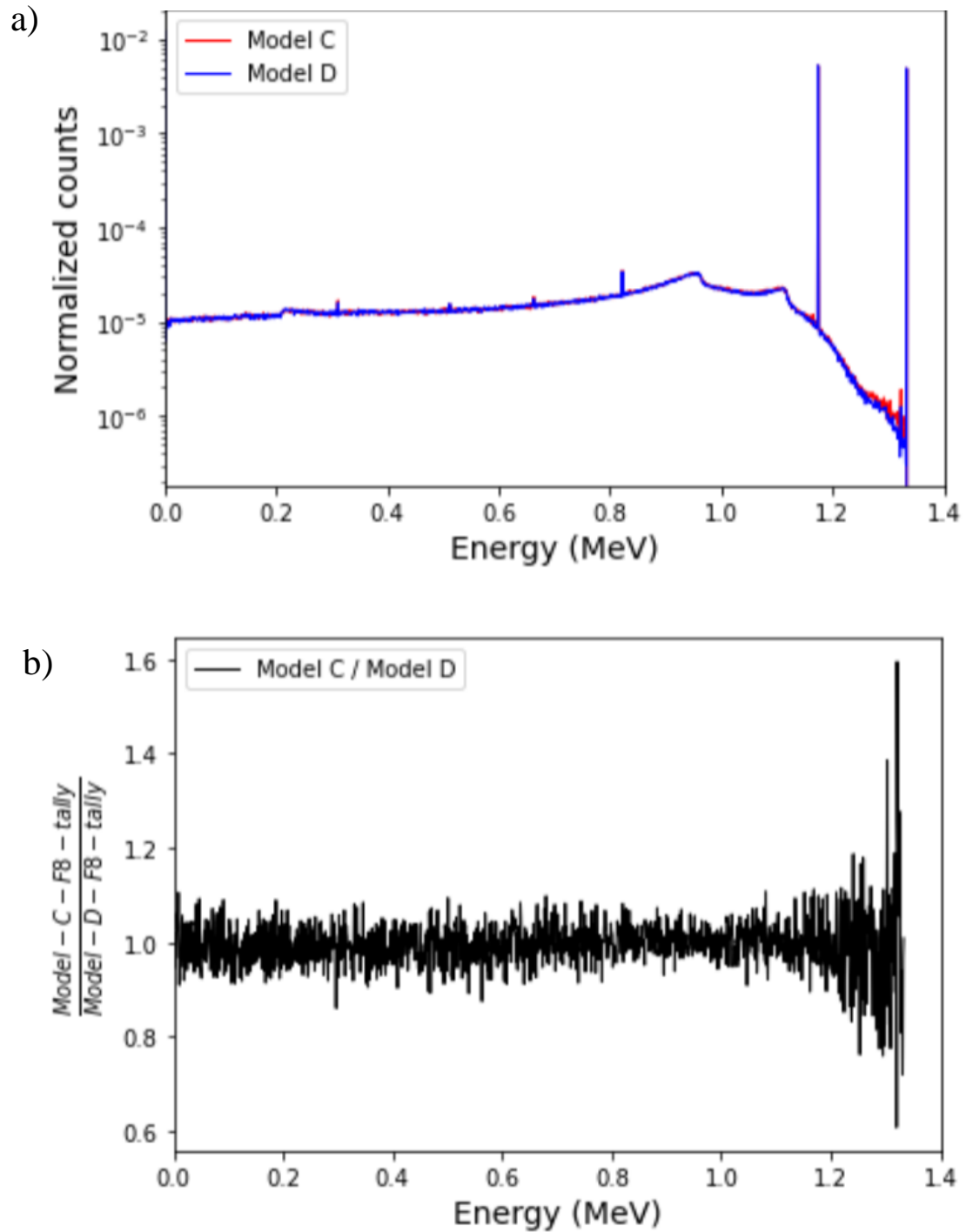
Figure 49: Comparison of F8 tallies between a model with a dead layer and contact pin, and a model with added and refined components. Both F8 tallies plotted (a) and the ratio of the two F8 tallies (b).
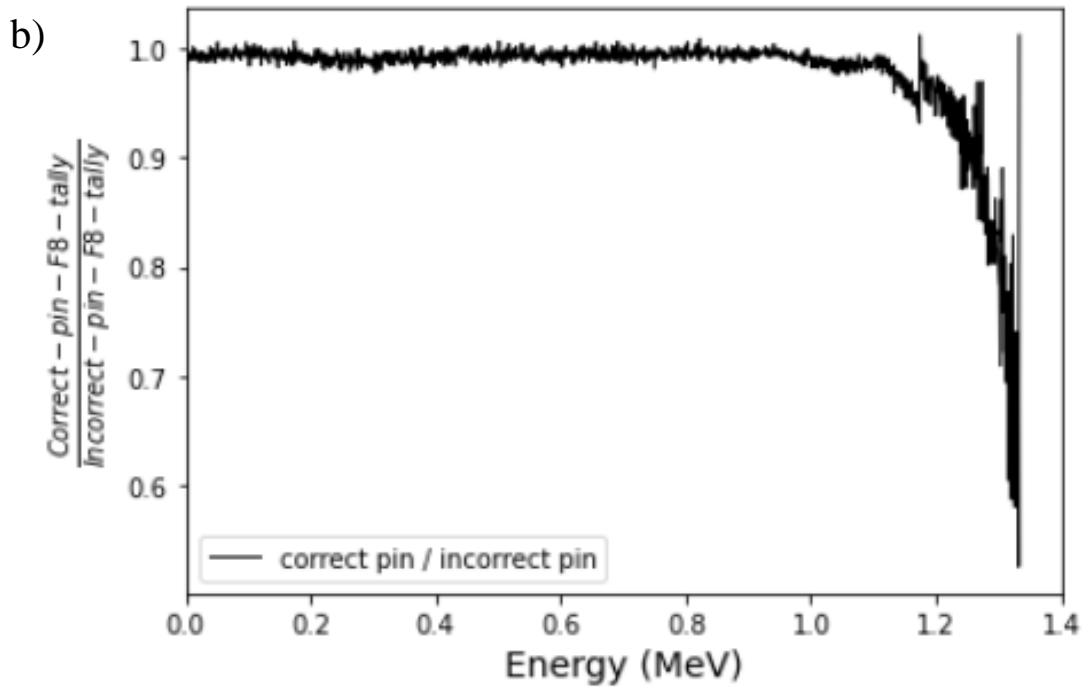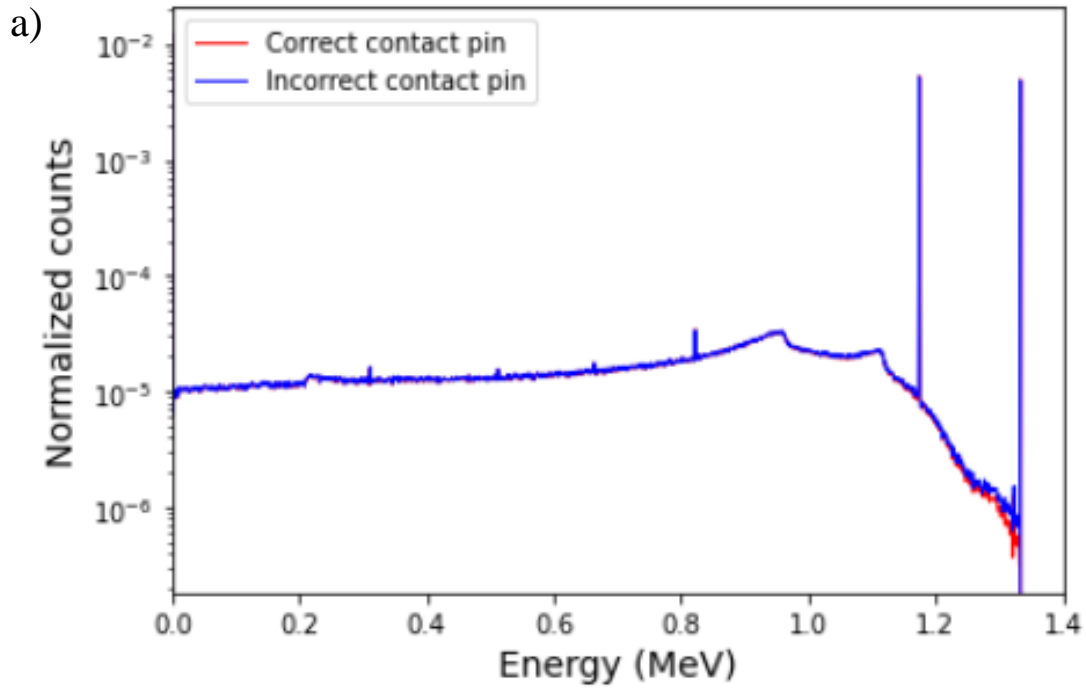
Figure 50: Comparison of F8 tallies from two different contact pin diameters. The two F8 tallies (a) and the ratio between the F8 tallies (b).

v.   MCNP geometry conclusion

We have built a detailed MCNP model of an HPGe detector with a high degree of accuracy. Early MCNP models included the crystal, mounting cup, detector housing, electronics housing, cooling rod, and an incorrect contact pin. By looking in the literature and disassembling an ORTEC HPGe detector, we were able to add components that were previously unknown and make the geometry of several components more accurate. These include wires, ceramic, parts, plastic parts, interfaces where parts join together, and the contact pin diameter. The model also includes an option for adding a collimator described by LANL that goes around the detector housing. Comparing the F8 tallies of different MCNP models shows that varying details results in significant differences in pulse-height-spectra, especially at higher photon energies.

4.   MCNP ptrac data

After running an MCNP simulation, the ptrac file needs to be read and filtered. This starts with writing the MCNP input deck such that the necessary data is written to the ptrac file. Writing all events in the crystal cell (cell 10 in our geometry) is sufficient. For future proofing and ease of filtering, MCNP6.3 is being used on LANLs high performance computing (HPC) so that we can write the ptrac information in the most up to date HDF5 file format. Once an MCNP simulation is finished, MCNPtools is used to parse/extract the ptrac interaction data and write it to a text (.txt) file. This information is put through a secondary filter that reads the text file, makes calculations, and puts the data into a format suitable for the charge transport code to build a DRF.

For now, it helps to skip ahead a few steps and address what the end result of ptrac filtering needs to be. The information that we need for the DRF is a comma separated file (or .csv file) that contains 5 columns in the following order: particle/history number, y-position of interaction, r-position of interaction, energy deposited during the interaction, and the time of the interaction. The units of y-position and r-position should be in μm. It is important to note that MCNP records interactions in the cartesian coordinate system (x, y, z). To obtain the r-position, we simply use the Pythagorean theorem to convert the x and z coordinates to an r-coordinate to be consistent with our cylindrical coordinate system. Simply put, $r = \sqrt{x^2 + z^2}$ in the specific geometry we have set up. Energy should be printed in units of MeV. Time should be printed in units of nanoseconds (ns), but MCNP records time in shakes, so it must be converted (1 shake = 10 ns). Furthermore, when recording interaction information, MCNP does not print energy deposited, but energy of the particle after the collision or interaction. This means that energy deposited for each interaction must be calculated based on the information provided in the ptrac file. This requires an understanding of the file format and a filtering algorithm. The final format of the data, which is used as the input for the charge transport function to build a DRF, should look like Table 3. The two lines of information listed as particle history #42 are just example lines. There should be a line for every interaction that deposits energy. Most of the time, there will be multiple lines for a single particle history because an individual gamma will enter the crystal and scatter multiple times while generating secondary particles that can also deposit energy. For example, consider a situation where particle history #42 is a 1.33 MeV gamma, which enters the crystal, undergoes pair-production,

111

and both 511 keV photons and all remaining energy deposits into the crystal. There will be a list of interactions for particle history #42. Summing all of the energies assigned to nps #42 should equal to 1.33 MeV: no more and no less. Consider that all energy deposits except for one 511 keV photon. A sum of the energies should be 0.819 MeV (1.33 MeV – 0.511 MeV). Understanding how the final format should read, and what information needs to be included, helps with understanding the steps taken to get us there.

Now that we know what the final data format needs to be for building a DRF, let's go back to how we get from a the HDF5 ptrac file to that final format. As mentioned previously, all events in the crystal cell are written to the HDF5 ptrac file. The HDF5 file is read using MCNPtools and a text file is written which contains the following columns: cell, surface, collision #, event type, reaction type (MT), x, y, z, energy, time, nps. The format of this data should appear like Table 4. The data is also comma separated. This format provides the information needed to calculate the energy deposited for every interaction that occurs in the crystal. Remember that energy printed in this file is not energy deposited, but energy of the particle after the event. There are collision events, surface events, termination events, etc. Keep in mind that the example interactions have digits removed so that they fit in the table, however, all digits that MCNP provides are still preserved at this point. In this example, NPS #42 enters the crystal through the top surface of the crystal with an energy of 0.356 MeV. The same particle then undergoes a collision (COL 4000) with a specific reaction type identifier of -1.0. The position, energy, and time are all recorded. All of this data is required to get to the end result, which is in Table 3. There is a secondary filter, which applies an algorithm that takes the information from Table 4, calculates the energy deposited for each interaction, and prints it to a CSV into the format shown in Table 3. Ultimately, the end goal can probably be achieved in multiple ways, however, this is the way that we have found successful.

C. Charge Transport Code

The charge transport code, written in Python, reads the filtered MCNP ptrac data and outputs the charge induced on the electrode. The transport code generates the appropriate amount of charge at point locations in the crystal volume. Then, the Silvaco data and Shockley-Ramo theorem are used in the custom charge transport code to move the charge carriers through the detector and calculate the charge induced on the readout. The code organizes the data from the different interactions into arrays that can be plotted or further processed. Each line of the ptrac data (see Table 3) is an interaction that is treated separately by the charge transport code. After the charge induced on the electrode is calculated for each interaction individually, different interactions that belong to the same gamma ray are combined. Each interaction results in both electrons and holes being generated and transported separately, although the contributing signals from each are summed. The output of the charge transport code may be run through a readout model, which is explained later. The charge transport code (as well as the readout model) is duplicated in C++. The primary purpose of the duplication is to make implementation into DRiFT easier later on.

Table 3: The final format of the particle interaction data needed to build a DRF.

Particle History (# or nps)	y-position (μm)	r-position (μm)	Energy (MeV)	Time (ns)
42	98244.44	29566.105	0.017316323	0.3534575
42	98148.87	29620.078	0.09788261	0.35384202

Table 4: Format of the text file generated by reading the HDF5 ptrac file with MCNPtools.

Cell	Surface	Collision #	Event type	Reaction type (MT)	X	Y	Z	Energy	Time	NPS
10.0	3.0	0.0	SUR 3000	n/a	2.09	10.41	-1.84	0.356	0.0333	42
10.0	n/a	1.0	COL 4000	-1.0	2.21	9.82	-1.95	0.338	0.0353	42

1. Generating charge

The amount of charge generated in the crystal depends on the average energy to produce an electron-hole pair (*W*-value), and the variance in the expected number of electron-hole pairs generated (related to the Fano factor in Equation 8. The result is a probability function that determines the amount of charge generated during each interaction. The Fano factor (*F*) determines how much variance there is, and consequently, it contributes to the amount of widening of gamma peaks in the DRF. The Fano factor can be adjusted in the program to add more or less variance, but the default value is *F*=0.1. To determine the amount of charge generated for each individual energy deposition, we find the expected number of charge carriers produced ($\bar{N}$) using the energy deposited and the *W*-value. Then find the variance in the number of charge carriers produced (σ^2) using the Fano factor and $\bar{N}$. While the number of charge carriers produced follows a Poisson distribution for *F*=1, the Poisson distribution can be accurately approximated as a Normal Gaussian distribution for instances where the mean number of occurrences ($\bar{N}$) is large. We are dealing with the generation of charge carriers, which happens on the order of tens of thousands at energy depositions as low as 100 keV. Here, the Gaussian approximation to the Poisson is sufficient. The number of charge carriers generated for the individual energy deposition is then calculated based on a normal distribution with mean equal to $\bar{N}$ and variance equal to σ^2. A random value is taken from the distribution, and charge is generated as a point deposition at the position of the interaction. Figure 51 shows the probability distributions for the number of charge carriers generated during a 1.33 MeV energy deposition. The two distributions show that a larger Fano factor results in a wider distribution. The mean is the same for each distribution ($\mu = \bar{N} = 1.33 \times 10^6 \ eV/W$), and the standard deviation varies with Fano Factor ($\sigma = \sqrt{F\bar{N}}$). The Fano factor causes a limitation in the energy resolution of a detector, which varies with energy deposited. The limitation in the energy resolution due to the Fano factor is illustrated in Figure 52 ($Energy \ resolution = {}^{2.35\sigma}/_{\mu} \times 100\%$). This ignores all other factors that widen the energy resolution, but demonstrates the importance of the Fano factor.

2. Transporting charge

Both electrons and holes must be transported through the crystal. They follow the same basic rules of charge transport, only with different charge carrier properties (mobility, lifetime, and +/- charge). The mobility and lifetime of each charge carrier is a variable that can be changed. For example, if one wishes to negate the effect of charge losses due to trapping, the charge carrier lifetime (τ) can be set very large. The lifetime of a charge carrier in modern HPGe detectors is on the order of 10^{-4} seconds, with the default value in our transport code being exactly that [65]. The velocity of the charge carriers throughout their transport will be comprised of two velocity vectors, one in the y-direction, and one in the r-direction. The velocity in each direction is determined by the corresponding electric field vector in that direction. The velocity of the charge carriers at each step in the transport follows the relationship in Equation 24. The variables are velocity in the r- or y-direction ($v_{r,y}$), the mobility of the charge carrier (μ_i) where *i* denotes electrons or holes, the electric field in the r- or y-direction ($E_{r,y}$), and the saturation velocity of the charge carrier ($v_{sat,i}$).
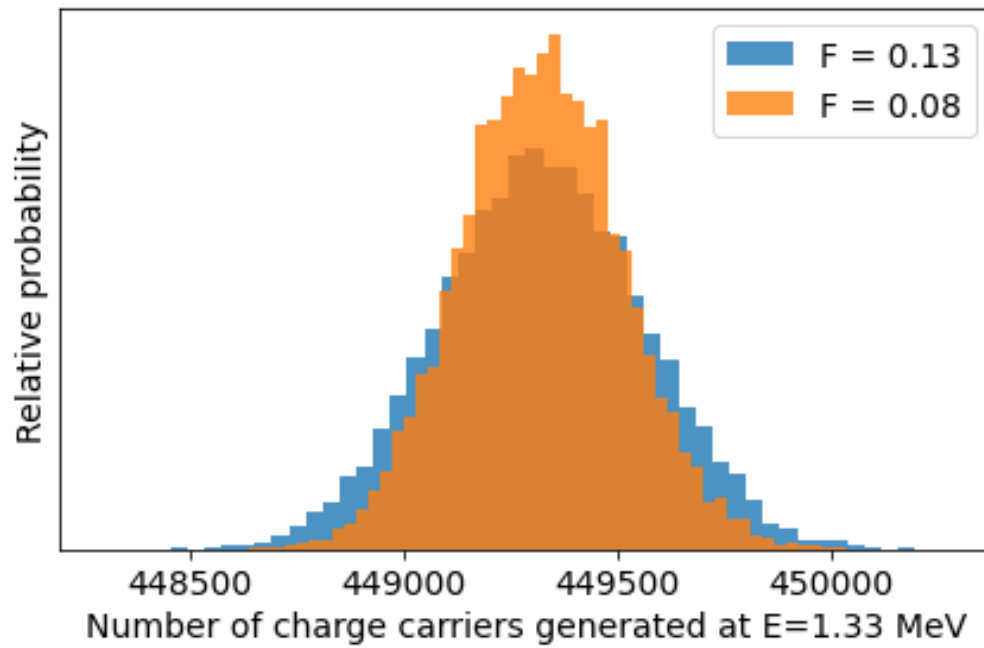
Figure 51: The probability of generating some number of charge carriers during a 1.33 MeV energy deposition for two different Fano factors (F=0.08 and F=0.13).
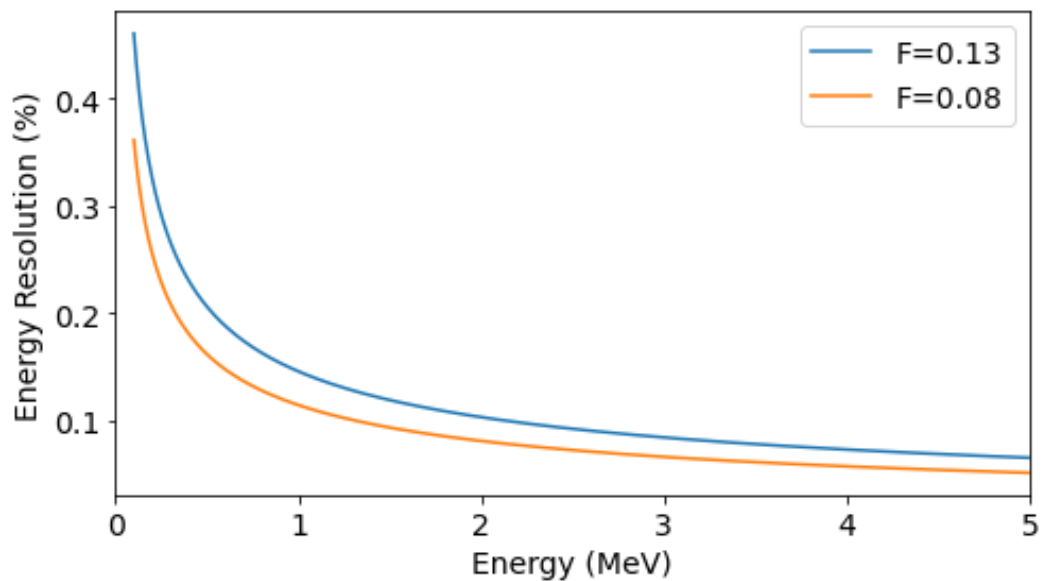
Figure 52: The limitation in the energy resolution (%) due to two different Fano factors (F=0.13 and F=0.08)

$$v_{r,y} = \frac{\mu_i E_{r,y}}{\sqrt{1 + \left(\dfrac{\mu_i E_{r,y}}{v_{sat,i}}\right)^2}} \tag{24}$$

For each step in the charge transport, the electric field is calculated by linearly interpolating the Silvaco electric field mesh data to find the value at the location of the charge. The charge is transported at that velocity for some time period (*dt*). Typically, we use *dt*=1 nanosecond. The new position of the charge is found based on the velocity and *dt*, and the process repeats until the charge reaches the electrode. Through this, we can record the position of the charge over time. The electrons will stop when they reach the outer electrode (see a bias of 4500 V), while the holes will stop when they reach the central electrode (see a bias of 0 V).

3. Charge induced on the electrode

The charge induced on the electrode is calculated using the common method of Shockley-Ramo theorem, which relates the motion of the charge carrier through the weighting potential to the charge induced on the electrode. The signal read by each electrode depends on the specific electrode's weighting potential. A coaxial design HPGe detector is a two-electrode design, with one bias electrode and one ground electrode. This simplifies the weighting potential and calculation of the total charge induced on the electrode. For each step in the transport, the change in the induced charge on the electrode for some charge carrier (*i*), is denoted as dQ_i. This is equal to the amount of charge (*q*) that was transported through the weighting field of the electrode times the difference in the weighting field that the charge passed through (*dV*). The equation to calculate the charge induced on the electrode in our system for one step of the transport is shown in Equation 25. Keep in mind that the amount of charge being transported (q_i) may change during each step of the transport because of charge losses due to trapping. To generate a more accurate charge induced on the electrode over time profile, each step of the charge transport is kept sufficiently small (*dt*=1 ns).

$$dQ_i = -q_i(dV) \tag{25}$$

Figure 53 is taken from the book *Radiation Detection and Measurement* by Glenn F. Knoll (book figure 12.13) shows the expected signal shape resulting from an interaction in the three different regions in a coaxial design HPGe detector [71, 105]. This figure shows the expected signal shape resulting from an interaction in the three different regions in a coaxial design HPGe detector. Region 0 is near the outer edge of the cylinder, Region 1 is about half way between the outer edge and the central hole in the crystal, and Region 2 is nearest to the central hole. Results of the charge transport code are in Figure 54, Figure 55, and Figure 56 for interactions in Regions 0, 1, and 2, respectively. Charge transport paths are in each figure side a. Charge is generated where the electron and hole pathways meet. Each group of charge carriers (electrons and holes) followed the path of the line as they travel to the electrodes. The charge induced on the electrode is in each figure side b, too.

116
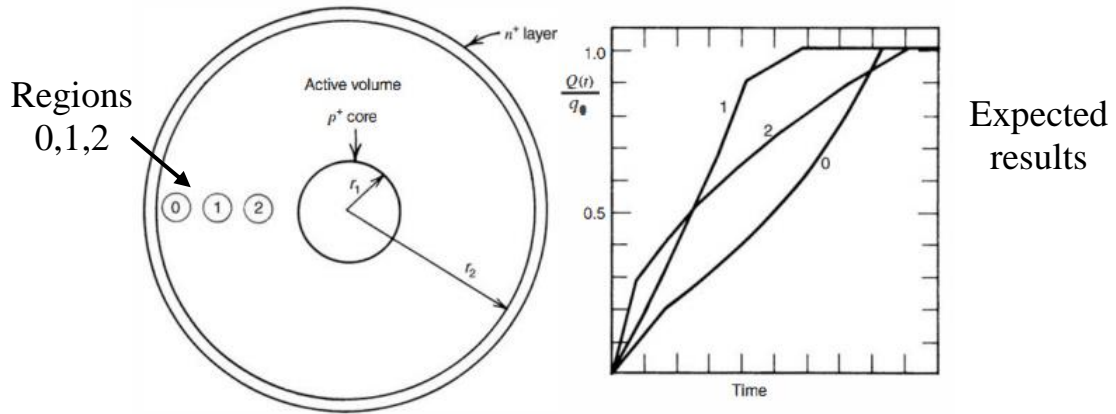
Figure 53: Expected signal shape induced on the readout electrode over time for different interaction regions in a coaxial HPGe crystal [71, 105].

Figure 54: Demonstration of charge transport path and corresponding induced signal in region 0.
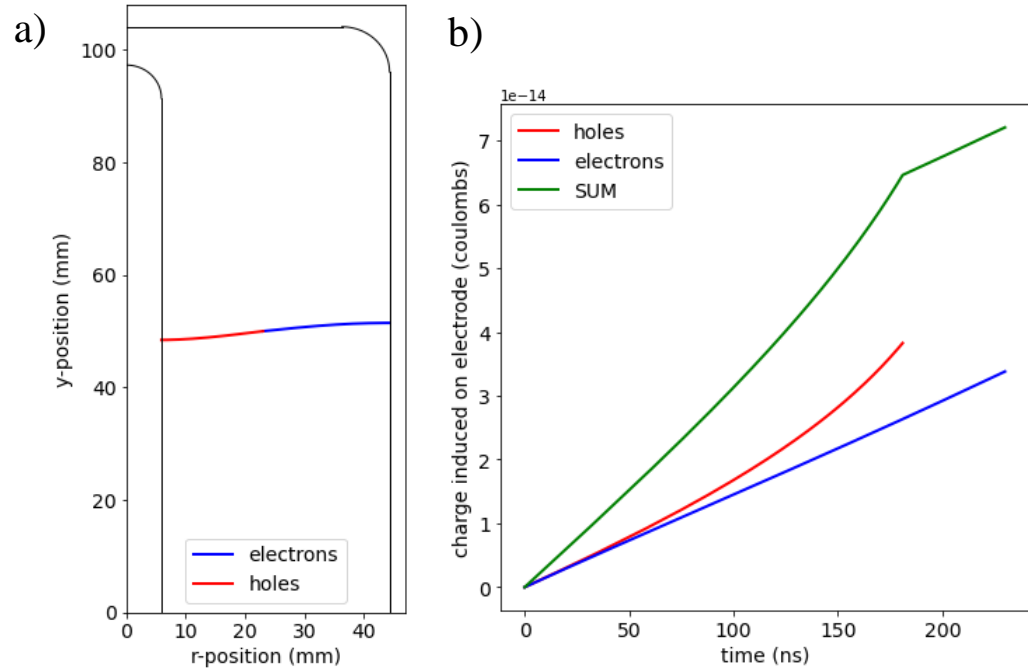
Figure 55: Demonstration of charge transport path and corresponding induced signal in region 1.
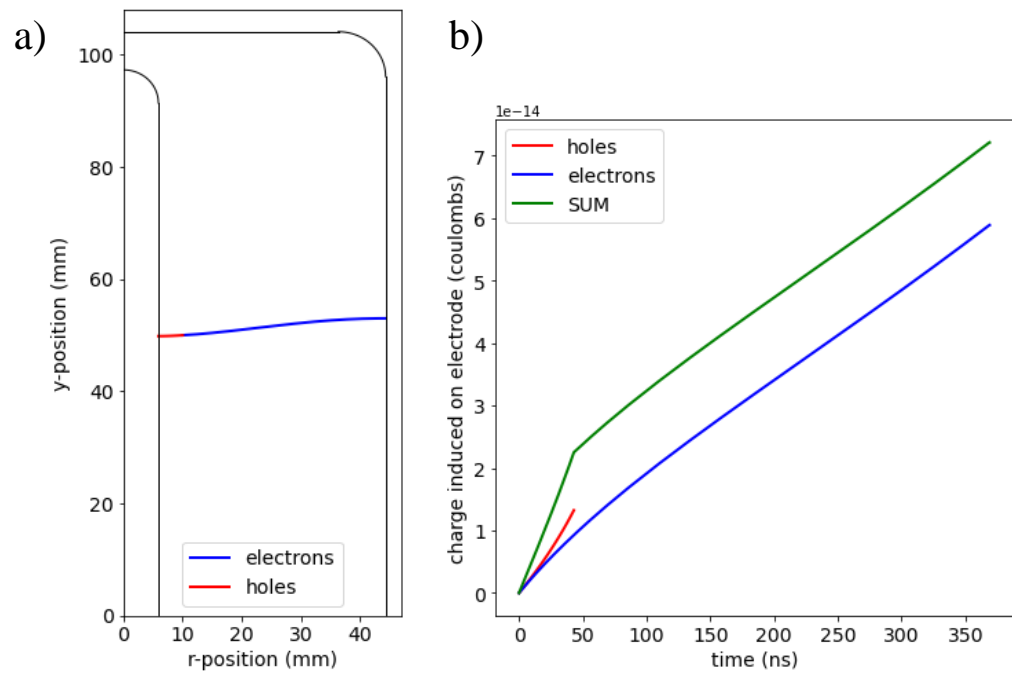
Figure 56: Demonstration of charge transport path and corresponding induced signal in region 2.

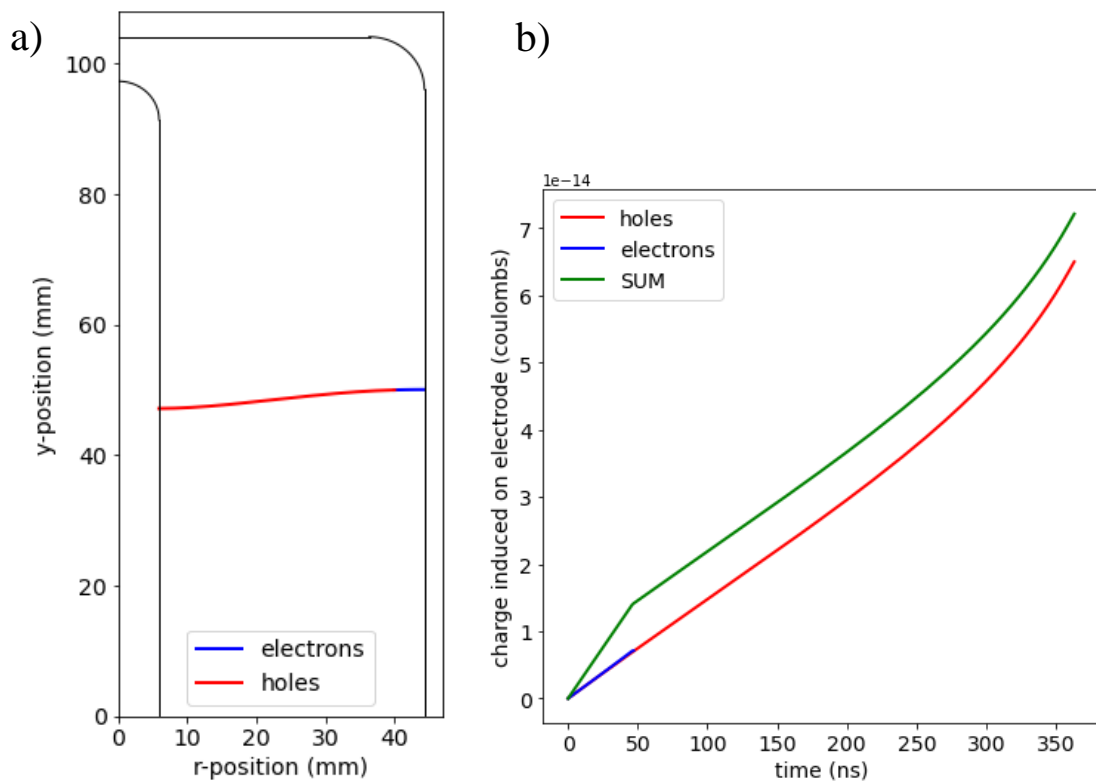The charge induced on the electrode shows both the contributions from electrons and holes separately, and their sum. Comparing the sum in each region shows that there is consistency between the transport code and the expected results.

D. Modeling Readout

The output of the charge transport code is two, 2D arrays of data. One is the charge induced on the electrode, and the other is the corresponding time. Combined, they represent the charge induced over time. Each row is the result of a different gamma interaction. This data set is the input to the readout model. The readout model is a combination of four different readout component models. There is a preamplifier, amplifier, pile-up, and noise model. The effects of ballistic deficit are built into the preamplifier and amplifier models. The output of the readout model is a single array of data, where each value is a pulse-height from the amplifier pulse. Each value is a count in the spectrum, so the output array is the DRF, and building a histogram of this array builds the pulse-height spectrum.

1. Preamplifier

The ORTEC HPGe detector we are modeling uses a combination of an ORTEC 257 charge sensitive preamplifier that has a model 138 high voltage filter. With the standard 2000 MΩ feedback resistor ($R_f = 2 \times 10^9$ Ω), the max energy rate before saturation is 180,000 MeV/s. It also contains a high-count rate indicator, which indicates the energy rate exceeding some level such that saturation occurs. In this event, the preamplifier momentarily shuts off to recover. The feedback capacitor can be anywhere from 0.1 to 5 picofarads, and we assume a 1 picofarad capacitor ($C_f = 1 \times 10^{-12}$ F) [88]. The values for the feedback resistor and capacitor can be changed in the model. The model assumes that saturation in the preamplifier never occurs. This could lead to an inaccuracy in the DRF under some specific circumstances. When saturation of the preamplifier occurs frequently, it represents an extending dead time in the readout. This requires a different dead time correction method. The inaccuracy in not accounting for saturation comes from using the non-extending dead time corrected count rate when we model pile-up. This consequence is that if a preamplifier is saturated frequently during a measurement, pile-up will be underestimated in the model.

We use the charge induced on the electrode over time from the transport model to model the preamplifier pulse from each interaction individually. For each interaction, the charge induced on the electrode (units of coulombs) is converted to a voltage (units of mV) with the preamplifier gain added according to the value of the feedback capacitor. This is done for each step of the rise of the preamplifier pulse to model the building of charge during charge collection. This means that the shape of the rise of the preamplifier pulse will reflect the charge collection, with a minor difference. The charge or voltage being "held" in the preamplifier is constantly decaying according to the decay constant, even as charge continues to build, and the preamplifier pulse rises. This is because some amount of time passes between each step in the rise, allowing charge to "bleed" off. The default time between each step is 1 ns because it follows the charge transport model time step. This is also a changeable variable in the charge transport. Since the preamplifier signal decays according to the decay constant (R_fC_f), there will be some amount of decay in the signal

between each step. This is negligible if the decay constant is large, however, with long collection times and a relatively short decay constant, this can result in an observable level of ballistic deficit. The amount of ballistic deficit is negligible with the default values for the feedback resistor and feedback capacitor, and the collection times considered by the HPGe that we are modeling. The shape rise in charge collection is important for ballistic deficit. For example, if a large portion of the charge is collected early in the rise, this gives more opportunity for a higher degree of ballistic deficit in the preamplifier. Equation 26 is used to calculate the rise in the preamplifier pulse. During the rise of the preamplifier, each step in the rise (i) is calculated by decaying the previous step (i-1) and then adding the voltage of the current step. Time (t) is in seconds, R_f is in ohms, C_f is in farads, charge (Q) is in coulombs, and the resulting voltage is converted from volts to millivolts. Just below Equation 26 shows how the preamplifier output decays over time, once the rise of the pulse is complete. This is essentially equivalent to Equation 26, without the addition of new charge (Q_i) at each iteration (i). The output of the preamplifier model is a preamplifier output pulse for every gamma interaction in the detector. Each pulse will have a quick rise according to the charge collection time, followed by a slow decay.

$$V_i = V_{i-1}\, exp\left(-\frac{(t_i - t_{i-1})}{R_f C_f}\right) + \left(\frac{Q_i - Q_{i-1}}{C_f}\right) \cdot \left(\frac{1000\ mV}{V}\right) \tag{26}$$

$$V_{decay}(t) = V_{peak}\, exp\left(-\frac{t}{R_f C_f}\right)$$

2. *Amplifier*

The output of the preamplifier model is used as the input for the amplifier model. The shaping amplifier and digitizer we are modeling is the portable ORTEC DigiDART MCA specifically for HPGe spectroscopy [90]. It is a digital trapezoidal shaper that has variable rise time and flat top settings. The trapezoid is uniform, so the fall time is equal to the rise time. With this system, ballistic deficit can be more easily avoided than RC-CR^n shaping techniques due to the adjustable length of the flat top. If a short rise time and short flat top are chosen (relative to the collection time of the detector), then ballistic deficit may still occur [71, 90]. A general rule for the DigiDART is that the rise time is twice the shaping time on an analog semi-gaussian shaping amplifier, meaning a rise time of 12 microseconds would be equivalent to a shaping time of 6 microseconds on an analog amplifier. There is an optimization setting that automatically adjusts the tilt (slope of flat top) and pole zero (removing undershoot/overshoot). Optimization of the tilt and pole zero give the best resolution, so we assume that these are properly optimized in a measurement to leave these variables out of the amplifier model. Another general rule of thumb is to set the flat-top time equal to the spread or range in the detector charge collection times. DigiDART specifies that the dead time per pulse (τ) varies with rise time and flat top settings. The dead time per pulse is $\tau = 3 \cdot (rise\ time) + 2 \cdot (flat\ top)$ [90]. This ultimately effects the calculation of the dead time corrected count rate, which has an effect on pile-up calculations later. The dead time correction method used within the system is the Gedcke-Hale method (see Equation 21). DigiDART has a built-in pile-up rejector

(PUR), which is automatically set with a threshold for rejection. The threshold values range between 250 nanoseconds and 6 microseconds. We assume that the pile-up rejector in the DigiDART system is effective at rejecting pulses. This means that pile-up of the output trapezoidal pulses will not occur. This does not mean that pile-up will not affect the spectrum because pulse pile-up that occurs in the preamplifier will still occur and be un-resolvable by the shaper and PUR. The main factors in the trapezoidal shaper model are the rise time setting, flat top setting, gain, and rise time of the preamplifier pulse.

Recall that each gamma event in the detector corresponds to an induced charge, and its own preamplifier pulse. The same follows for the amplifier. Each preamplifier pulse will result in a separate amplifier pulse. From here, we will now refer to the rise time of the preamplifier pulse as collection time. This is to avoid confusion between the rise time of the preamplifier pulse and the rise time setting on the trapezoidal shaper in the amplifier. So, "collection time" is referring to the rise time on the preamplifier pulse, and "rise time" is referring to the rise time setting on the trapezoidal shaper. The shape and height of the trapezoidal output depends on the combination of settings and the collection time of the input pulse. Table 5 lists the different scenarios considered and the calculations made to generate the corresponding trapezoidal pulse.

In scenario 1, the collection time is shorter than the rise time setting. The preamplifier pulse can be considered a step function at the input to the shaper. The result is an output pulse from the shaper that follows the "weighting function" of the trapezoidal shaper.

In scenario 2, the collection time is greater than the rise time but still shorter than the rise time plus the flat top. This means that the output of the shaper will no longer follow the "weighting function" of the shaper. The trapezoid will not be uniform, but the collection time is short enough such that the full rise of the preamplifier pulse can be processed, preventing ballistic deficit. The consequence is a longer rise time on the output trapezoidal pulse, and a shorter flat top. The difference between scenario 1 and 2 is not seen in the final spectrum or DRF, as the height of the trapezoid is unaffected. In fact, this is one of the major benefits of trapezoidal shaping for large coaxial detectors with varying collection times.

In scenario 3, the collection time is greater than the rise time plus the flat top. This means that the shaper has not had time to process the full rise of the preamplifier pulse, causing ballistic deficit. The pulse shape also changes drastically. The height of the pulse is determined by the height of the preamplifier pulse (V_{preamp}) evaluated at the time that the shaper stops processing the pulse (rise time + flat top). Just like the preamplifier, the shape of the rise at the input is an important factor regarding the severity of ballistic deficit. The differences in scenario 3 are seen in the final spectrum. If it happens at a high enough rate, then severe low energy tailing will be observed on the full energy peaks.

Figure 57 shows examples of the resulting pulses that would be seen from the three scenarios. The units of time and pulse-height are arbitrary. The major take away is that scenario 3 results in a relative pulse height shorter than scenarios 1 and 2 due to ballistic deficit.

Table 5: Methods of calculating the shape of the trapezoidal pulse based on different collection time scenarios

Scenario 1: collection time less than or equal to the rise time setting on shaper (preamplifier acts as a step function at the input of the shaper)

$$Trapezoid\ height = \ V_{preamp,peak} \times gain$$

$$Trapezoid\ rise\ slope = \frac{Trapezoid\ height}{rise\ time}$$

$$flat\ top\ length = \ flat\ top\ time$$

Scenario 2: collection time greater than rise time setting, but less than the rise time plus the flat top time (preamplifier peaks in the middle of the flat top)

$$Trapezoid\ height = \ V_{preamp,peak} \times gain$$

$$Trapezoid\ rise\ slope = \frac{Trapezoid\ height}{collection\ time}$$

$$flat\ top\ length = rise\ time + flat\ top\ time - collection\ time$$

Scenario 3: collection time greater than the sum of the rise time setting and flat top time setting (ballistic deficit will occur because the preamplifier pulse is cut off)

$$Trapezoid\ height = \ V_{preamp}(rise\ time + flat\ top)$$

$$Trapezoid\ rise\ slope = \frac{Trapezoid\ height}{rise\ time + flat\ top\ time}$$
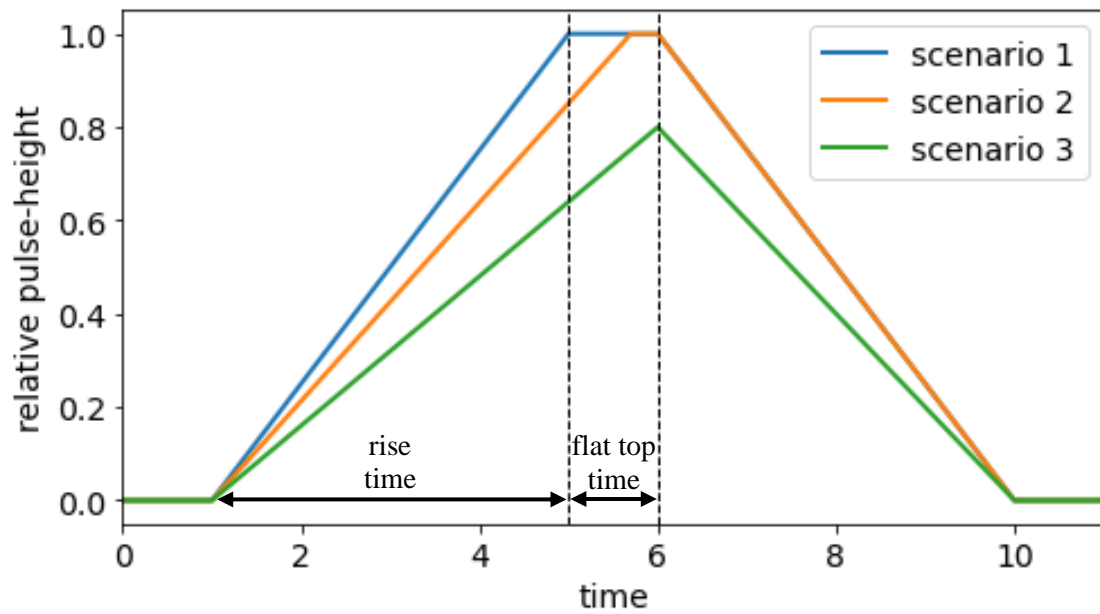
$$flat\ top\ length = 0$$

Figure 57: Examples of trapezoidal amplifier pulse modeling in scenarios 1, 2, and 3

3. Dead time corrections

The idealized non-paralyzable model is being used for dead time corrections in our model. The idealized non-paralyzable model was chosen for its simplicity, generality, and because this is the dead time correction method employed by the ORTEC DigiDART readout system that we are modeling. The dead time corrections start with user inputs of measured count rate (m) and percent dead time, both as they would be seen on the MCA. Given a count rate and percent dead time, the event rate in the detector (n) can be estimated using Equation 21. This leads to a potentially confusing nomenclature, so I will be very specific in the following explanation. The MCA dead time (τ) is equal to the amount of time that the MCA remains dead after the detection of a single count (pulse from the amplifier). It is sometimes referred to as the resolving time. It can be thought of as an MCA dead time per count, with units of time (usually on the order of a couple of microseconds). By multiplying the MCA dead time by the count rate ($m\tau$), you get the fraction of time that the MCA spent being dead during the measurement. If you continue by multiplying that product by 100%, then you get percent dead time ($m\tau \cdot 100\%$). The percent dead time is what a user reads on the MCA during or after a measurement, and it is also the input for the dead time correction when building a detector response function. The true event rate in the detector is calculated so that pile-up statistics can be completed in the pile-up model.

4. Pile-up modeling

Pile-up modeling is applied after the preamplifier and shaping amplifier models in order to save computational time and power. This results in a quicker pile-up calculation but does have negative implications in certain situations. First, we will talk about the pile-up calculations and methods, then the implications of the method chosen.

It was previously stated that the DigiDART readout system we are modeling has an automatic pile-up rejector, and that we assume the pile-up rejector is effectively preventing pile-up from occurring in the shaping amplifier. However, even an effective pile-up rejector will not be able to distinguish between two events that occur in a detector so closely that their charge collection is convolved on top of one another. This results in a single preamplifier pulse that cannot be deconvolved by the readout electronics. The probability of this pile-up occurring is determined by the event rate in the detector and the collection times. Longer collection times and higher event rates result in larger probabilities of pile-up. We consider the average collection time from all of the events in calculating the probability of pile-up. If two or more events occur within the average collection time, then they will be considered to be convolved and indistinguishable by the readout electronics, and thus piled-up.

To calculate the probability of this, the average charge collection time is calculated from the charge transport results. The average charge collection time is used for (τ_{pu}) in Equation 19. The probability of pile-up for $x=0$, 1, 2, and 3 is found by calculating P_0, P_1, P_2, and P_3, respectively. Any remaining probability that could be contributed to $P_{>3}$ is added to P_3. This is done under the assumption that no greater than four events will pile-up within the collection time. The total number of events in the detector (N_{events}) is equal to the number of events recorded in the detector in MCNP. The number of counts recorded after accounting for pile-up (N_{counts}) is calculated based on the number of events and the

124

probability of each pile-up case. In Equation 27, the denominator can be thought of as the average number of true events per count. The number of regular counts (N_0), number of 2 event pile-ups (N_1), number of 3 event pile-ups (N_2), and number of 4 event pile-ups (N_3) are calculated.

To generate pile-up based on the pile up statistics, the pulse-height from each amplifier output pulse is extracted into an array of single values, and the pulse-heights from some events are summed together.

$$N_{counts} = \frac{N_{events}}{\sum_{x=0}^{2}(x+1) \cdot P_x} = \frac{N_{events}}{P_0 + 2P_1 + 3P_2 + 4(1 - P_0 - P_1 - P_2)} \tag{27}$$

$$N_x = N_{counts}P_x$$

It is fair to ask why the pile-up model is being applied after the amplifier model, when we are specifically modeling the pile-up of pulses in the preamplifier. The reason is to avoid generating an additional large dataset and save computational time and power. First, if we apply the pile-up model directly to the charge induced on the electrode arrays, then we will need to generate new arrays for which the charge induced over time from one event is convolved onto the charge induced over time of another event. This could be for 2, 3, or 4 events in total. The charge induced on the electrode over time arrays (output of transport) are the largest datasets generated. Applying pile-up here would require generating another large dataset roughly equal in size. In fact, it would not just be one large dataset, it would be two large datasets. Consider that we record 100,000 events in MCNP. The transport model will generate 100,000 lists of charge induced on the electrode. What we really have is two datasets, each with 100,000 rows. One dataset having the charge induced on the electrode for each event in each row, and the other dataset having the corresponding time data for each event in each row. Each row is a different length due to varying collection times. Now consider that we model pile-up at this point, and we find that $P_1=0.01$ and $P_{2-4}=0$. We will end up with 99010 detector counts ($N_{counts}=99010$), with 990 being pile-ups of two events ($N_1=990$), and 98020 being regular counts ($N_0=98020$) without pile-up. We would take 990×2=1980 of the events, and sum them in pairs to get 990 new events. To have a dataset that represents this in a format prepared for the preamplifier model, in which we account for the decay of the preamplifier pulse during charge collection (accounting for ballistic deficit), then we would require two new datasets. In these two datasets, there would be 99010 rows, with each row being an array that has either the charge induced on the electrode, or time data. Now consider the size of the datasets. 100,000 events is not a lot to build a spectrum from. The charge induced on the electrode datasets easily surpass 2 GB when there are over 500,000 events. The corresponding time dataset will surpass 1.5 GB. We would essentially duplicate that size, generating an addition 3.5 GB of data, which requires lots of time and space in system memory. Compare this to the way pile-up is being applied currently. We generate a dataset that is a 1D list of values. With 500,000 events, the dataset only exceeds a few MB of data. Furthermore, the single values are all that is required to build a pulse-height spectrum.

Now you may ask, if we only need pulse-heights, then why do we generate such large datasets and carry all of that information into the readout model to begin with? The

primary reason for carrying all of the data through the preamplifier model and onto the amplifier model was to account for ballistic deficit as accurately as possible. If we were not accounting for the ballistic deficit of each event, then there would be no reason to carry that much data. If the program was made more efficient in regard to memory consumption and computational speed, it could enable pile-up to be modeled at the charge collection or preamplifier stage while also modeling ballistic deficit accurately. The current methods save us computational time and power while preserving accuracy, but slight inaccuracies may arise in certain situations.

When pile-up is applied in this way, there is an underlying assumption. The assumption is that when events pile-up, they occur at exactly the same time in the detector. This assumption is not obvious, but it comes from the following line of reasoning. If two events occur close enough in time (within the average collection time in our model), then they will pile-up. The second event can occur at either the exact same time as the first event; it can occur as late as the collection time of the first event, or anytime in between. This means that the total collection time of the two events combined will be no less than the collection time of the first event, but probably longer. It may even be much longer. If the average collection time is a few hundred nanoseconds, then the collection time of two piled-up events may be near a microsecond or greater. This has implications in ballistic deficit. Longer collection times require larger decay time constants in readout electronics (R_fC_f). If the decay time constant is short, then ballistic deficit in the preamplifier has the potential to occur on some piled-up pulses more severely than the non-piled up pulses. This follows for ballistic deficit in the shaping amplifier as well. A longer collection time results in a longer preamplifier rise time, which increases the potential for ballistic deficit in the shaping amplifier if the shaping settings are short. It should be noted that non-piled up pulses are unaffected by our methods. The overall consequences of our methods are the following: if the collections times are long compared to the preamplifier decay time constant and amplifier shaping time settings (rise time and flat top), then ballistic deficit will occur more severely on piled-up pulses. The DRF pulse-height spectrum will be affected by having less low energy tailing on pile-up peaks than it should. The non-pile-up portions of the spectrum, such as full energy peaks, will not be affected. Furthermore, if long decay constants, rise time, and flat top settings are chosen, then the method has a negligible effect on the pulse-height spectrum, even in pile-up regions. For these reasons, the benefits of saving computational time and power by applying pile-up after the amplifier model are worth the minimal (and unlikely) cost in accuracy of the detector response function.

5. *Electronic noise*

Electronic noise is applied to the model after pile-up. We employ the equivalent noise charge (ENC) model described previously by Equation 23 and its subsequent sections. This is being chosen for convenience, and the direct correlation between charge at the input and the noise seen by the digitizer or MCA at the output. At this point in the model, we have a single array of data that is comprised of amplifier pulse heights from each detector count, including piled-up reactions. We simply need to add or subtract from each value to emulate the effect of noise on each pulse-height. The user will input a value

for the noise model, which is the ENC in units of number of electrons. The gaussian distribution of noise is a normal distribution with the mean equal to zero and the standard deviation (RMS$_{noise}$) equal to the ENC value. A random value is pulled from the distribution, which will represent the number of electrons added to, or subtracted from, the pulse-height. Since this model represents electrons being added to the input terminals of the readout, they must be treated as if they were processed by the readout. The electrons are converted to charge (using the charge of an electron). The charge is divided by the feedback capacitance value of the preamplifier to convert it to a voltage consistent with the preamplifier gain. This is followed by multiplying by the gain of the amplifier, and finally a conversion from volts to millivolts so that the units are consistent with the output from the amplifier model. It is important to repeat a distinction here. This method implies that all noise charge sources were injected at the input of the readout and processed through the preamplifier and amplifier. This does not reflect the true nature of all noise sources, but the methodology provides an output at the amplifier that is consistent with observed noise at the output. That is because the ENC is the noise that *if* injected into the input terminals of the readout, *will* result in the noise seen at the output. It is *not* defining the ENC as the noise that was injected into the input terminals.

The relationship between ENC in units of electrons and the RMS$_{noise}$ in units of volts at the readout is shown in Equation 28. A random value pulled from the normal distribution is added to each amplifier output value. This value has an equal probability of being less than or greater than zero, so the noise adds a uniform widening to full energy peaks. The noise contribution to the widening of the full energy peak at a given energy (FWHM), or the energy resolution (ΔE), can be estimated using the ENC, W-value, and the energy peak position (E). This is approximated just below Equation 28.

The effect of both noise and the Fano-factor on the energy resolution combined can be estimated. This is shown in Equation 29. It ignores all other factors and is used only to show the relationship between the different variables and energy resolution.

$$\frac{ENC[electrons] \cdot (1.602 \times 10^{-10}\ C) \cdot gain}{C_f[farad]} = RMS_{noise}[volts] \qquad (28)$$

$$FWHM_{noise}[eV] = 2.35\sigma_{noise} = 2.35 \cdot ENC[electrons] \cdot W[eV]$$

$$\frac{\Delta E_{noise}}{E} = \frac{2.35 \cdot ENC \cdot W}{E}$$

$$\sigma_N = \sqrt{F\overline{N}} = \sqrt{\frac{FE}{W}} \qquad \rightarrow \qquad \frac{\Delta E_{fano}}{E} = \frac{2.35 \cdot \sqrt{F\overline{N}} \cdot W}{E} = 2.35\sqrt{\frac{FE}{W}} \cdot \left(\frac{W}{E}\right)$$

$$\frac{\Delta E}{E} = \sqrt{\left(\frac{\Delta E_{noise}}{E}\right)^2 + \left(\frac{\Delta E_{fano}}{E}\right)^2} \qquad (29)$$

E. Building detector response functions

Once the charge transport code goes through all of the interactions in the filtered ptrac file and passes the results through the readout model, the bulk of the modeling is complete. The only thing that is required to build the DRF is to build a histogram (pulse-height spectrum) from the final results. Adjusting the number of bins in the histogram may be necessary. Too little data (counts in the spectrum) may limit the number of bins you can use in the histogram. Bins are analogous to channels in the MCA or digitizer, so the effect of having too many bins is weak statistical certainty in peak analysis and spectral features that lack prominence. However, using too few bins will mask otherwise useful and prominent details of the pulse-height spectrum. The inability to use as many bins or channels as desired is due to either running too few particles in the MCNP simulation or not running all data through charge transport. This could be done on purpose simply to save time and computational space. Luckily, adjusting bin numbers and rebuilding a histogram can be done quickly, so some fine tuning or trial and error is not time or computationally intensive.

There are other options to increase the usability of the program. For instance, the user does not have to run the readout model at all. If the user wishes to ignore the readout, a pulse-height spectrum can be built solely on the charge transport results (charge induced on the readout). This ignores ballistic deficit, noise, and pile-up. It will build a spectrum based on units of charge (coulombs) instead of voltage (mV). Furthermore, a user can import transport results and run them through the readout model. This is useful because transport is by far the most time and computationally expensive portion of the program. Being able to input the results of a previous transport run and only modify the readout parameters is quite useful. Different aspects of the readout may be negated by simply adding parameters that will have no effect on the results. For instance, if one wishes to ignore the effect of noise, then an ENC=0 will do just that. If one wishes to ignore pile-up, a count rate and dead time of zero will accomplish that. Ignoring ballistic deficit is as simple as choosing very large time constants (R_fC_f, rise-time, and flat-top time). These accommodations will not necessarily speed up the program, but they do provide a wide level of adjustment.

1. Sources modeled

Multiple different sources have been modeled to test the DRF. These were modeled to mimic calibration measurements that were taken with the HPGe detector that we are modeling. The radiation sources were modeled in MCNP as point sources placed about 10 cm from the detector face. The DRF built from the MCNP simulations should reproduce the calibration measurements, given the right settings are used in generating the DRF. The Fano-factor and ENC are the same in all DRFs (F=0.13 and ENC=100 electrons). Not every emitting gamma-ray from each isotope was modeled, but the gamma-rays with the largest branching fractions were modeled. The gamma ray energies modeled for each DRF are listed in Table 6. We built a DRF for ^{137}Cs, ^{60}Co, and ^{133}Ba. All gamma ray energies were not modeled, but those with the highest branching ratios and likelihood to have a large impact on the full energy peaks and Compton region were included. Lastly, the collimator shown in Figure 45b was included in the MCNP particle transport for every DRF.

Table 6: A list of the gamma ray energies included in each DRF with their branching ratio. Branching ratios are not necessarily normalized.

Energy (MeV)	Branching Ratio
^{137}Cs	
0.661657	0.913
0.0365	0.0263
0.03219	0.0394
0.031816	0.0213
^{60}Co	
1.332492	0.999826
1.173228	0.9985
0.8261	0.000076
0.34714	0.000075
^{133}Ba	
0.38385	0.0894
0.356	0.6205
0.30285	0.1834
0.2764	0.0716
0.08099	0.329
0.0796	0.0265
0.0532	0.0214
0.0358	0.429
0.0353	0.395
0.03097	0.602
0.0306	0.326
0.0047	0.153

F.   HPGe measurements

HPGe measurements have been taken at LANL, by LANL personnel, with the specific detector we are modeling. While all HPGe measurements were taken at LANL, the analysis was conducted locally at the University of Tennessee. These are being used for baselines of comparison in both situations with and without significant pile-up. HPGe calibration measurements of ^{137}Cs, ^{133}Ba, and ^{60}Co, have been completed. Additionally, ^{133}Ba and ^{60}Co measurements were taken at high count rates and high dead times to evaluate the effect of high dead time and pile-up on the spectra. These include dead times of 10%, 40%, 70%, and 90% for the ^{133}Ba measurements, and 3%, 30%, 60%, and 80% for the ^{60}Co measurements. The dead time versus count rate, and energy resolution versus dead time are shown in Figure 58. Notice that the energy resolution is mostly unaffected when measuring at high dead times and count rates, although some cases show a slightly worsened energy resolution in measurements with very large dead time percentage. We can use the relationship between the count rate and dead time to inform the settings in the readout model. Based on Figure 58a, the count rate versus dead time follows the same relationship, regardless of the energy. This is represented by the fact that ^{60}Co and ^{133}Ba follow the same relationship, even though they are comprised of very different energy gamma-rays. This means that each dead time in Figure 58b should represent roughly the same count rate. To further demonstrate this, the full energy peaks of ^{60}Co and ^{133}Ba are shown from measurements with both low dead time and high dead time (Figure 59). As you can see, there is almost no difference in the shape of the full energy peaks. However, the high dead time measurements are not completely free of extra tailing or broadening near the base of the full energy peak. The tailing that is present could be due to pile-up, as there is visible pile-up in both spectra at high count rates. Another explanation could be some small amount of undershoot and/or overshoot on the shaping amplifier pulse, because the high energy tailing appears slightly worse than low energy tailing. Another explanation is that the DigiDART pile-up rejection system is not 100% efficient at rejecting pulses with overlap, causing a small number of pulses with tail pile-up to be processed. This would normally only result in high energy tailing, but this combined with an undershoot at the tail of the pulse could result in extra tailing at both low and high energy sides of the peaks.

Some measurements were taken with the collimator attached to the HPGe detector, and some were not (see Figure 45b for an illustration of the collimator). The collimator is effective at blocking a significant portion of background. All measurements shown were taken with the collimator to match the DRF which also includes the collimator. Although the collimator does suppress some background, the background still plays a large role in the low energy portion of the Compton region. ^{137}Cs measurements with and without the collimator, and a background measurement are shown in Figure 60. A wide window extending beyond the ^{137}Cs (Figure 60a) shows the extent of background, while a shorter window isolating only the ^{137}Cs spectrum (Figure 60b) gives a closer look at the effect of background.

Lastly, HPGe measurements of the ^{137}Cs source were conducted at a different date, and possibly a different room environment from the ^{60}Co and ^{133}Ba measurements, resulting in different background. The background from the latter are shown in Figure 61. Here, counts are divided by the live counting time to plot count rate per channel.

a)

b)
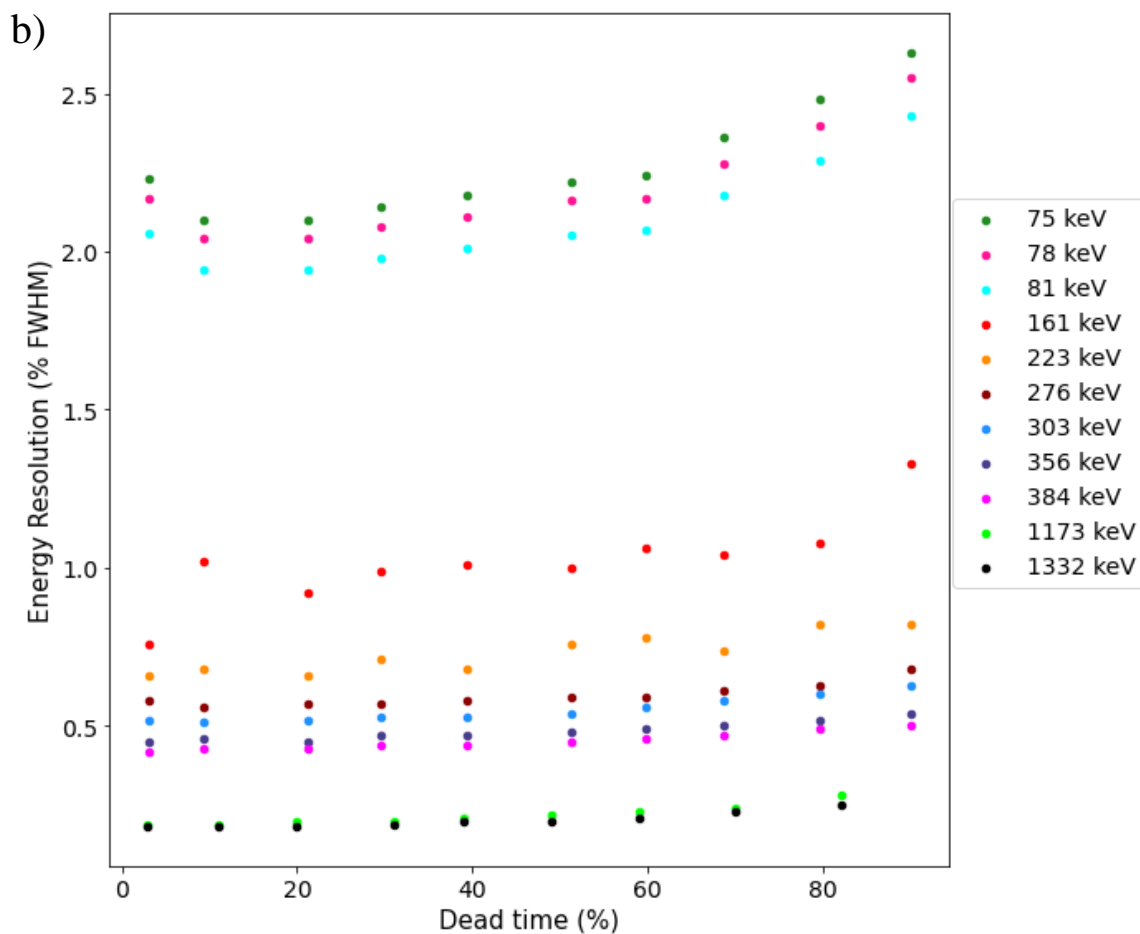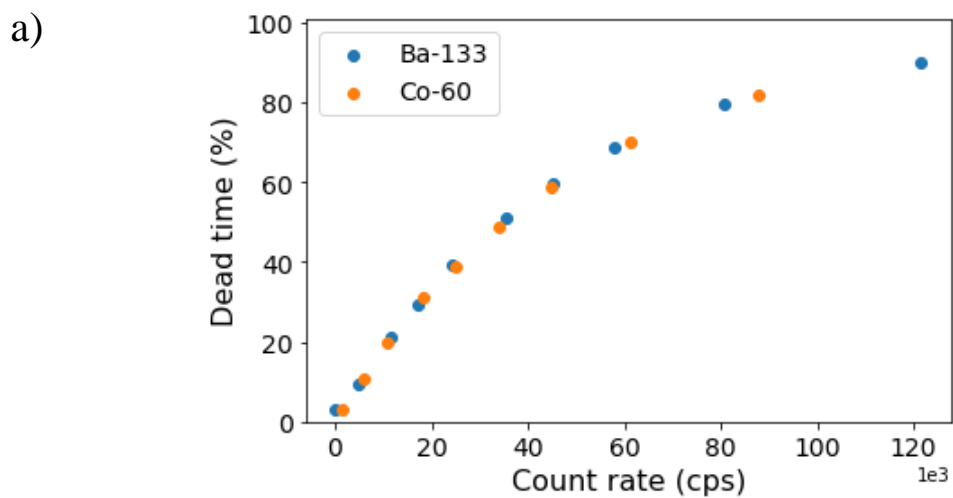
Figure 58: The dead time versus count rate (a) and energy resolution versus dead time at different gamma energies (b), measured with the ORTEC HPGe detector at LANL.

131
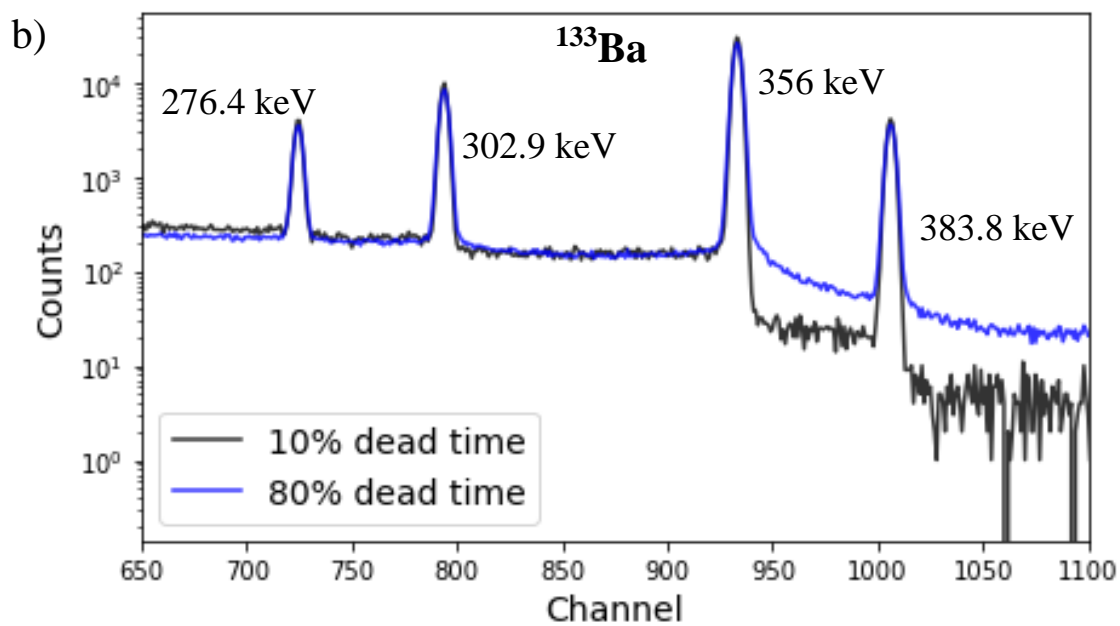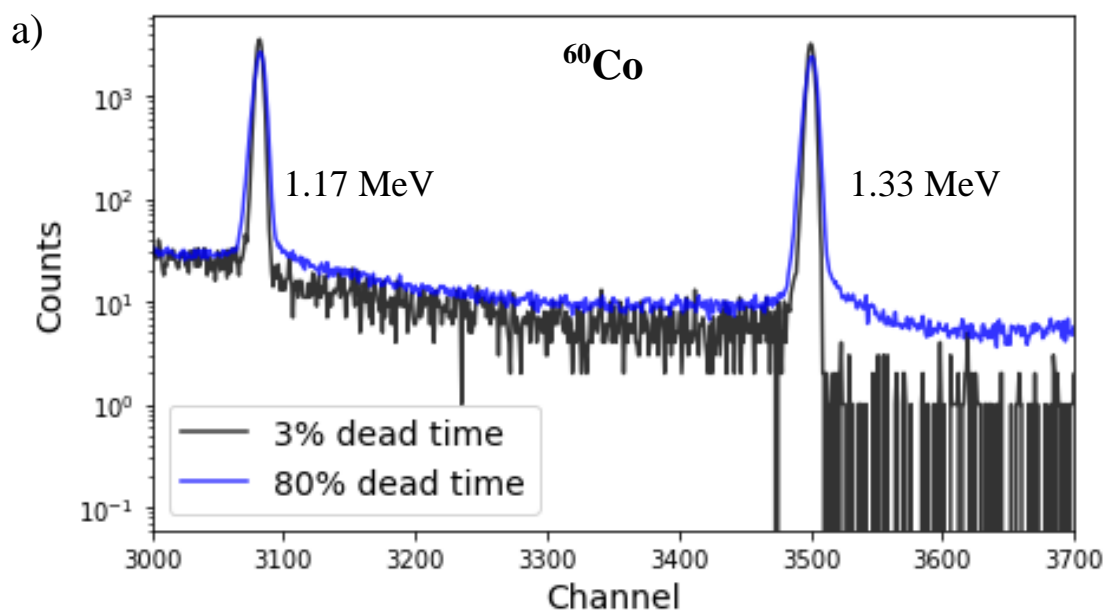
Figure 59: ⁶⁰Co full energy peaks at measurements with 3% and 80% dead time (a), and ¹³³Ba full energy peaks at measurements with 10% and 80% dead time (b).

a)

b)
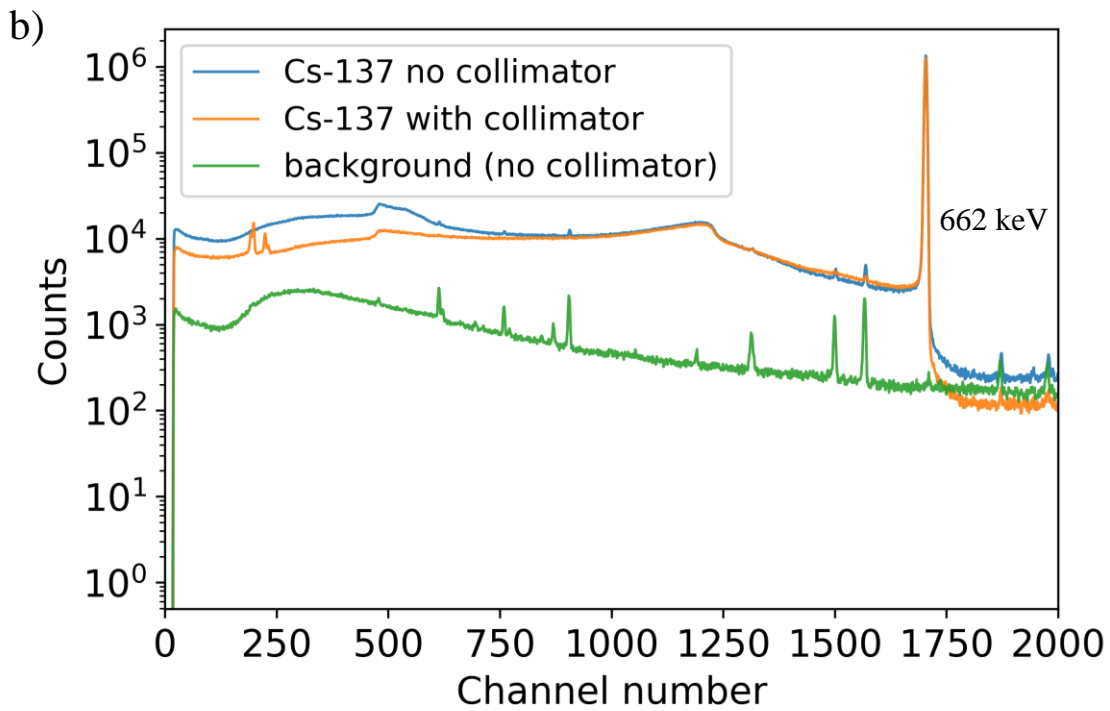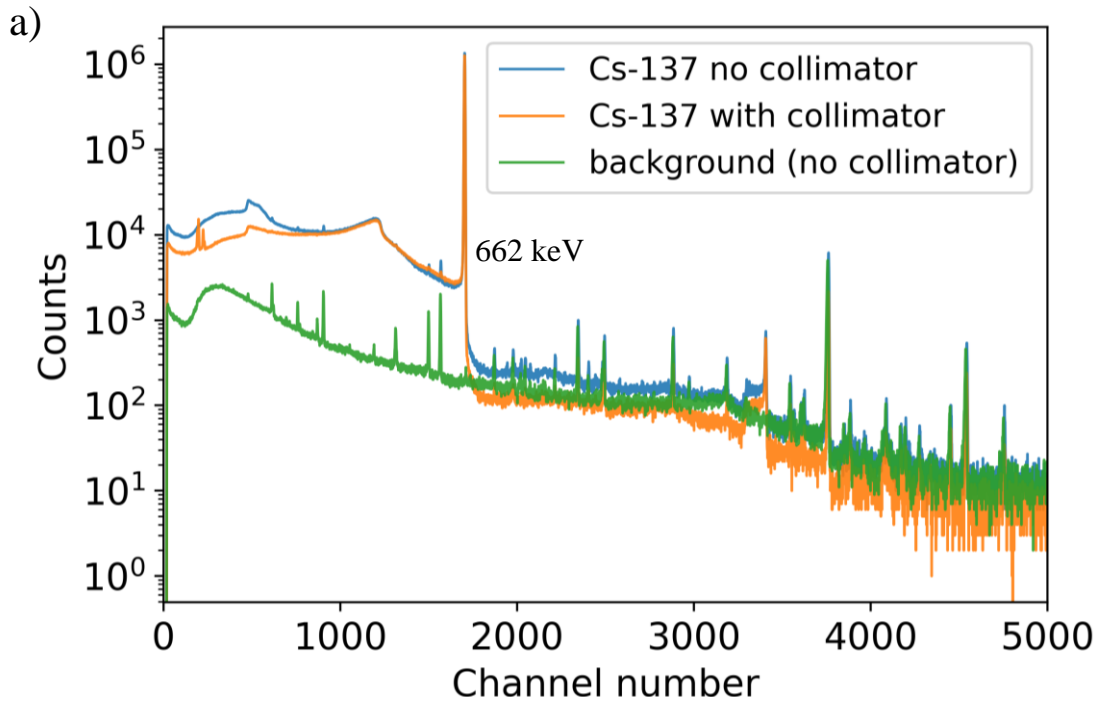
Figure 60: ^{137}Cs measurements taken with and without the collimator, with a background measurement to demonstrate its effect on background suppression. All measurements taken with same live time (3600 seconds).

133
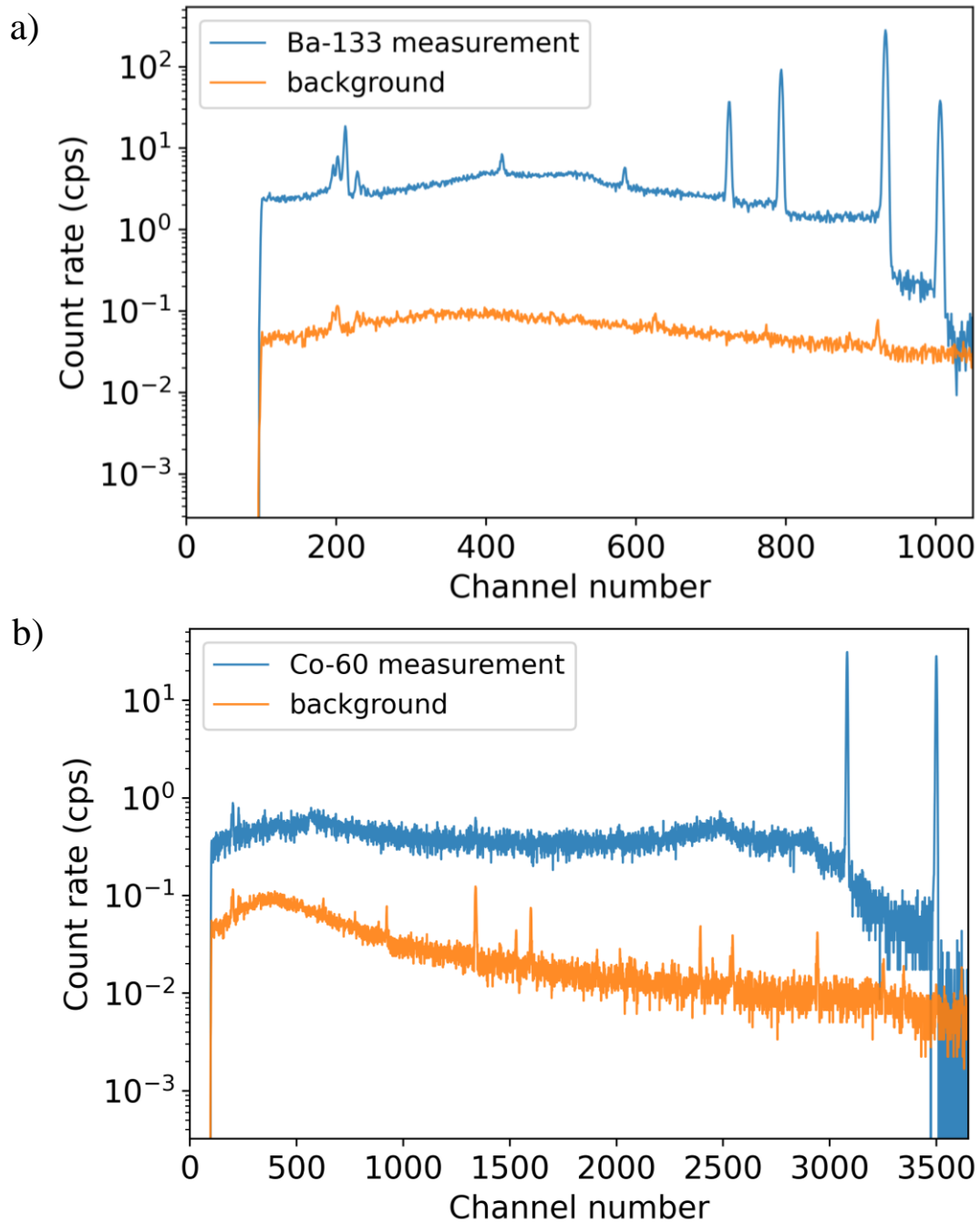
Figure 61: The ^{133}Ba (a) and ^{60}Co (b) measurements with the background included.

RESULTS AND DISCUSSION

The results of the different tools that are used to build a DRF have been addressed already. These include the results of MCNP simulations, Silvaco modeling, charge transport, experimental measurements, etc. Those results show that each component works and help to demonstrate the methodology used. Each of those components come together to build and analyze a DRF. This chapter will be kept solely for results directly regarding DRFs. That includes comparing DRFs to HPGe measurements. In this section, we will review the DRFs of ^{133}Ba, ^{60}Co, and ^{137}Cs point sources. Pile up is also demonstrated with the ^{60}Co measurements/DRFs.

A. Barium-133 detector response functions

Figure 62 shows the DRF of the ^{133}Ba source with a ^{133}Ba measurement. The measurement was taken at a count rate of 4698 cps and dead time of 9.28%. These values were also used for the readout model to be consistent with the measurement. Figure 62a shows the full spectrum. The DRF and the measured spectrum show the various X-ray energies, a similarly shaped Compton continuum, followed by the four largest full energy peaks (276 keV, 302 keV, 356 keV, and 384 keV). The full energy peaks have very similar shape and width. The Compton continuum, the position of the most prominent Compton edge, and the X-ray spectrum are also alike. Perhaps most importantly, the relative positions, widths, and heights of peaks are consistent between the DRF and the measured spectrum.

There are clear differences between the two spectra. The measured spectrum contains two small peaks on the Compton continuum which are not present in the DRF. By conducting a detector calibration, these peaks were determined to be roughly 161 keV and 223 keV. These positions are not consistent with the expected positions of backscatter peaks (148 keV, 156 keV, 168 keV, and 174 keV). ^{133}Ba decays into stable ^{133}Cs, so they are not decay chain emissions. The origins of these remained undetermined until a second look at the chart of the nuclides revealed their origin. These peaks are in fact gamma emissions of ^{133}Ba. While building the MCNP simulations, I had been referring to the IAEA isotope browser mobile application for important gamma ray and X-ray emissions. This application has several energies missing from the library. A look at other web-based isotope browsers (or chart of the nuclides) shows these emissions. The solution here is simple; to ensure that all photon energies from a given source are modeled in the DRF, one should choose a web-based database instead of the mobile application. The difference is in the Compton region in the area around the two missing peaks is most likely due to the Compton scattering of those missing gamma energies. One more major difference is the existence of peaks in the pile up region of the DRF. These are due to X-rays (30-35 keV) piling up on the most prominent full energy peak (356 keV).

Figure 63 shows the DRF and measured spectrum with a high count rate and dead time to demonstrate pile up. The peak positions and widths across the spectrum match well between the DRF and the measurement. The high energy tailing observed in the two larger full energy peaks (Figure 63a) is more severe in the measured spectrum. This is most likely one of two things. The pole zero (or tilt) on the trapezoidal shaper may not be optimized properly, causing overshoot or undershoot of the tail of the amplifier pulse. There may also
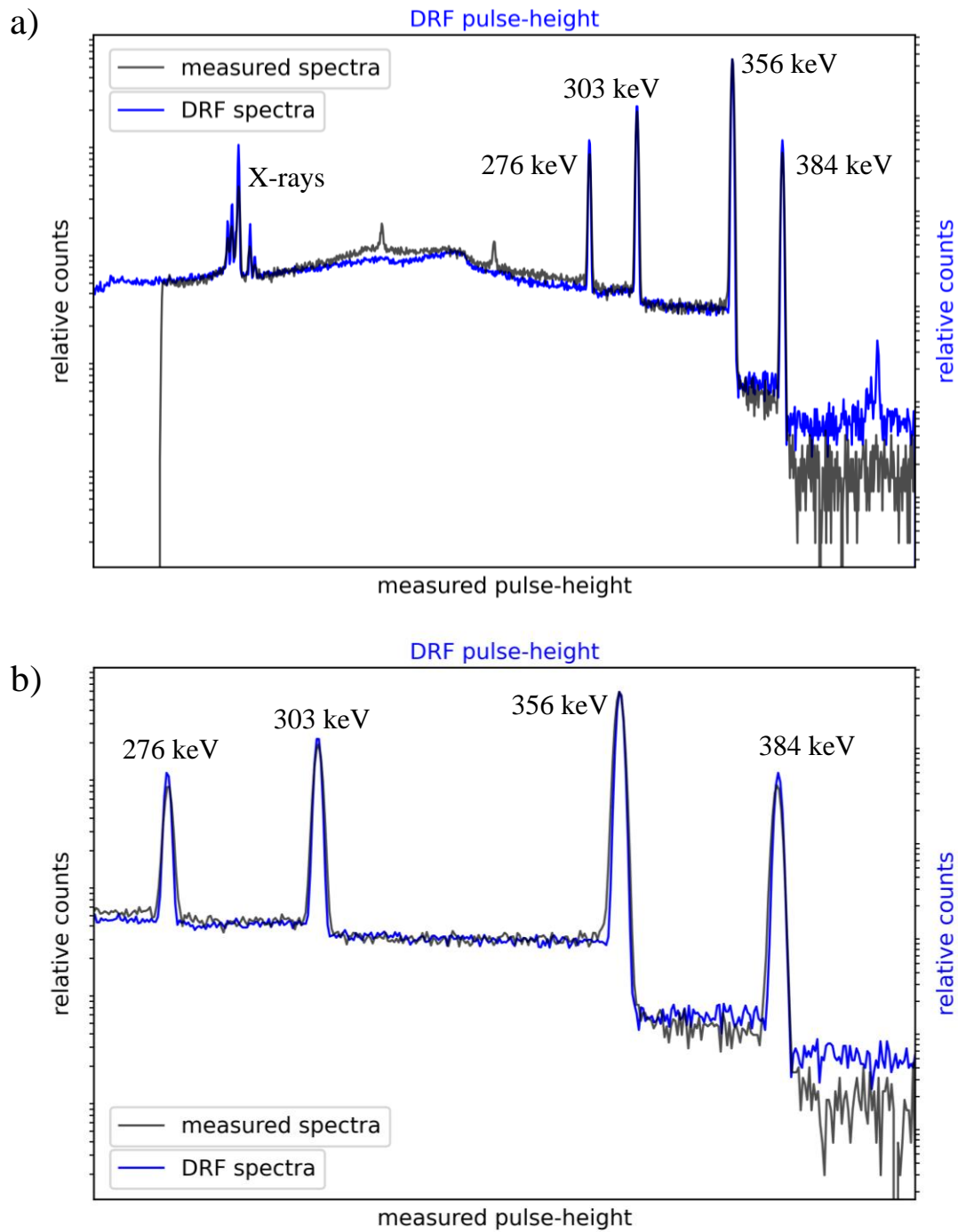
Figure 62: The DRF and measured spectra of a ^{133}Ba source (a), and a close up of the four full energy peaks (b). Both have a 9.28% dead time and count rate of 4698 cps.
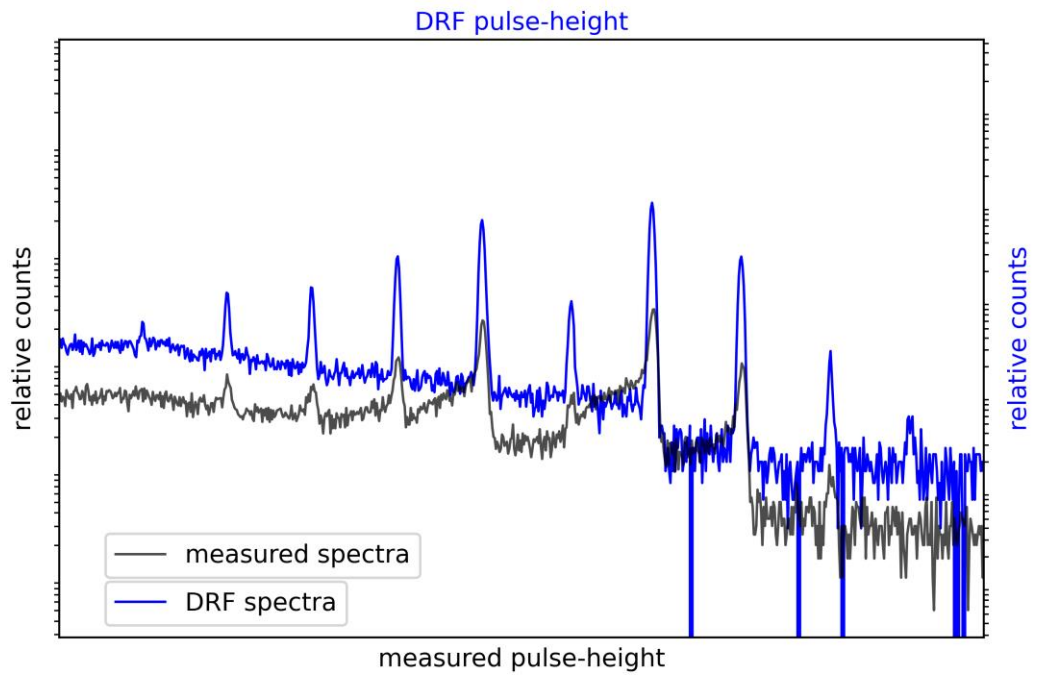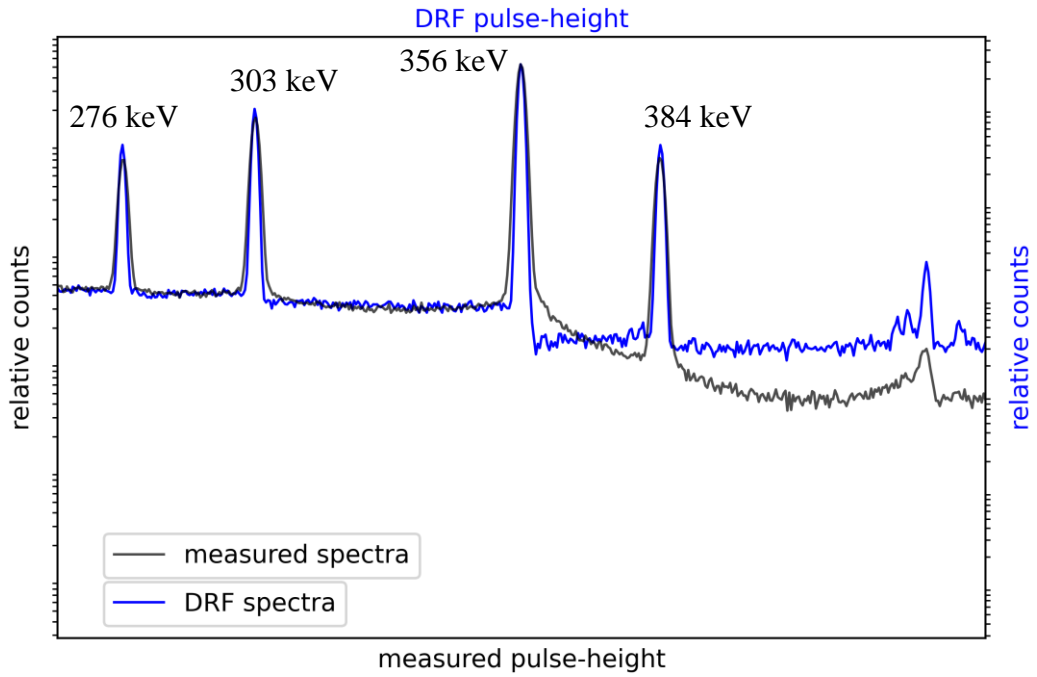
Figure 63: The DRF and measured spectra showing full energy peaks (a) and pile up peaks (b) of a [133]Ba source. Both have a 79.56% dead time and count rate of 80692 cps.

137

be tail pile up in the shaper. The pile up rejection in the DigiDART system is automatic, as well as self-optimizing, but may not be perfect in preventing tail pile-up. At high count rates, tail pile up and/or an incorrect pole-zero (or tilt) can result in high and low energy tailing on full energy peaks. In the pile up region (Figure 63b), the DRF is elevated with relatively more counts in each peak. The reason that pile up is elevated could be due to the fact that there is no background radiation modeled in the DRF. In the measured spectrum, background can take up a large portion of pile up, which may not show up higher in the spectrum because background is usually lower energy. This could also explain why X-rays are more prominently piled up on the 356 keV peak. One other difference is the severe low energy tailing on pile up peaks in the measured spectrum. Due to the way we pile up is modeled, we expect to underestimate low energy tailing on pile up peaks in some measurement scenarios (see Methods: *D. Modeling Readout: 4. Pile-up modeling*). The measurement and DRF has an 80% dead time with an extremely high count rate of 80692 cps. High count rate and dead time meet some criteria for an environment expected for an underestimation in low energy tailing in pile up peaks.

B. Cobalt-60 detector response functions

Figure 64 shows the DRF, measured spectra, and corresponding measured background of a ^{60}Co source. The dead time and count rate used in the DRF is consistent with that of the measurement (3% dead time and 1616 cps). The full ^{60}Co spectrum is shown in Figure 64a, and the peaks are isolated in Figure 64b. This results in very little pile up. As you can see, the 1.17 MeV and 1.33 MeV peak locations and peak profiles are mostly consistent. While the peak widths are the same, there is slightly more low energy tailing on the 1.33 MeV peak than the 1.17 MeV peak. This is most likely due to incomplete charge collection in the measurement. There is also a minor visible difference in the region between the two full energy peaks. Background could be elevating the region just below the 1.33 MeV peak in the measured spectrum. The same background would have less influence on the Compton region to the left of the 1.17 MeV peak because this Compton region has an order of magnitude more counts while background is mostly constant. An artificial constant background was added to quickly test the effect of adding background to the DRF. The results are shown in Figure 65, which shows that adding background to the DRF may help the spectra match better. A more plausible explanation for the difference between the two peaks would be low energy tailing on the 1.33 MeV peak due to incomplete charge collection.

Figure 66 shows the DRF and measured spectra with higher count rates and dead times to demonstrate pile up. The non-pile up portion of the spectrum (everything ≤ 1.33 MeV peak) is mostly similar to Figure 64, with the exception of peak broadening in the measured spectrum. The shape of the pile up spectrum is very similar. Figure 67 shows the pile up peaks. The peak locations and widths match well, but the DRF is slightly elevated with relatively more counts in each pile up peak. Like Figure 63 (^{133}Ba pile up), the reason that pile up is elevated in the DRF could be due to the fact that there are no background counts in the DRF to take up some of the pile up. The low energy tailing in pile up peaks of the measured ^{60}Co spectrum (Figure 67) is similar to that observed in the ^{133}Ba spectrum (Figure 63), but less severe.

138

Figure 64: The DRF and measured spectra of a ^{60}Co source (a), and a close up of the two full energy peaks (b). Both have a 3% dead time and count rate of 1616 cps. Measured background is also shown.
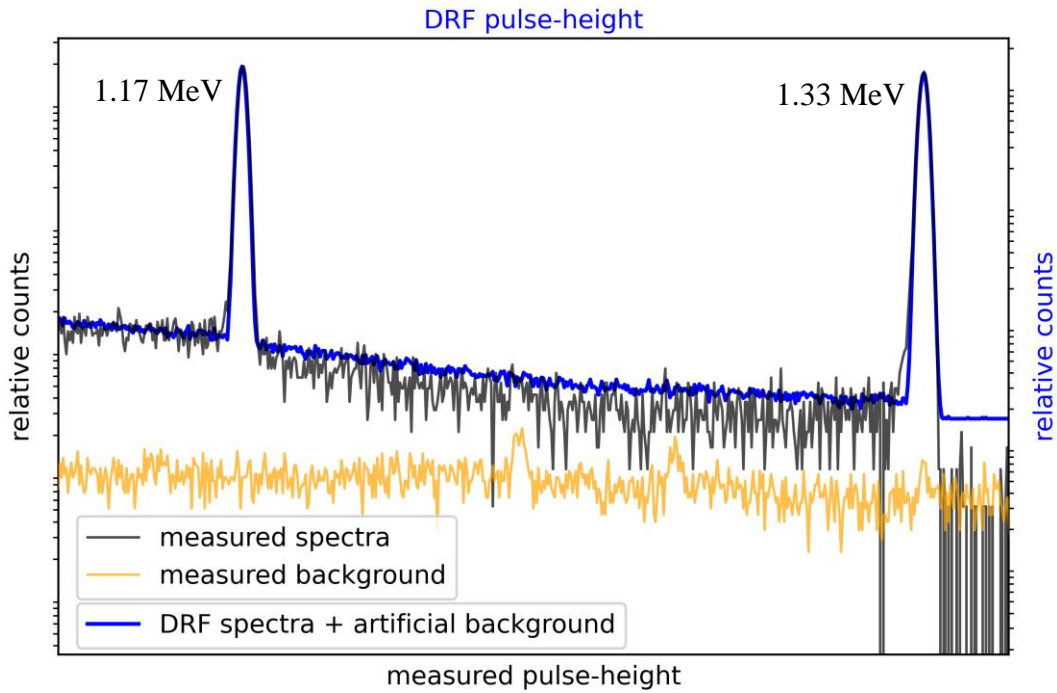
Figure 65: The DRF and measured spectra showing the full energy peaks of a ^{60}Co source. Artificial background is added to the DRF spectra. Both have a 3% dead time and count rate of 1616 cps. Measured background is also shown.
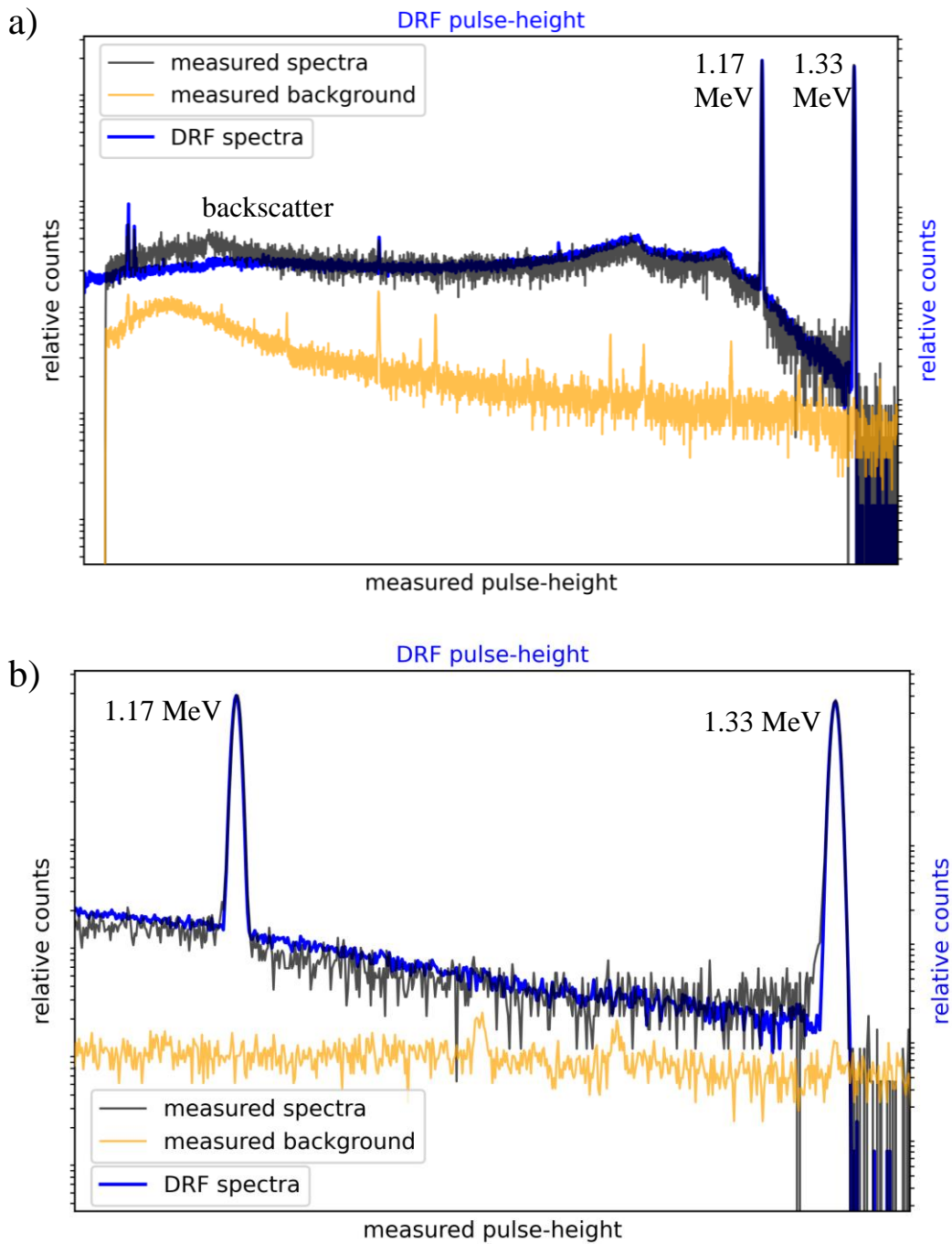
Figure 66: The DRF and measured spectra of a ^{60}Co source (a), and a close up of the two full energy peaks (b). Both have an 82% dead time and count rate of 87851 cps.
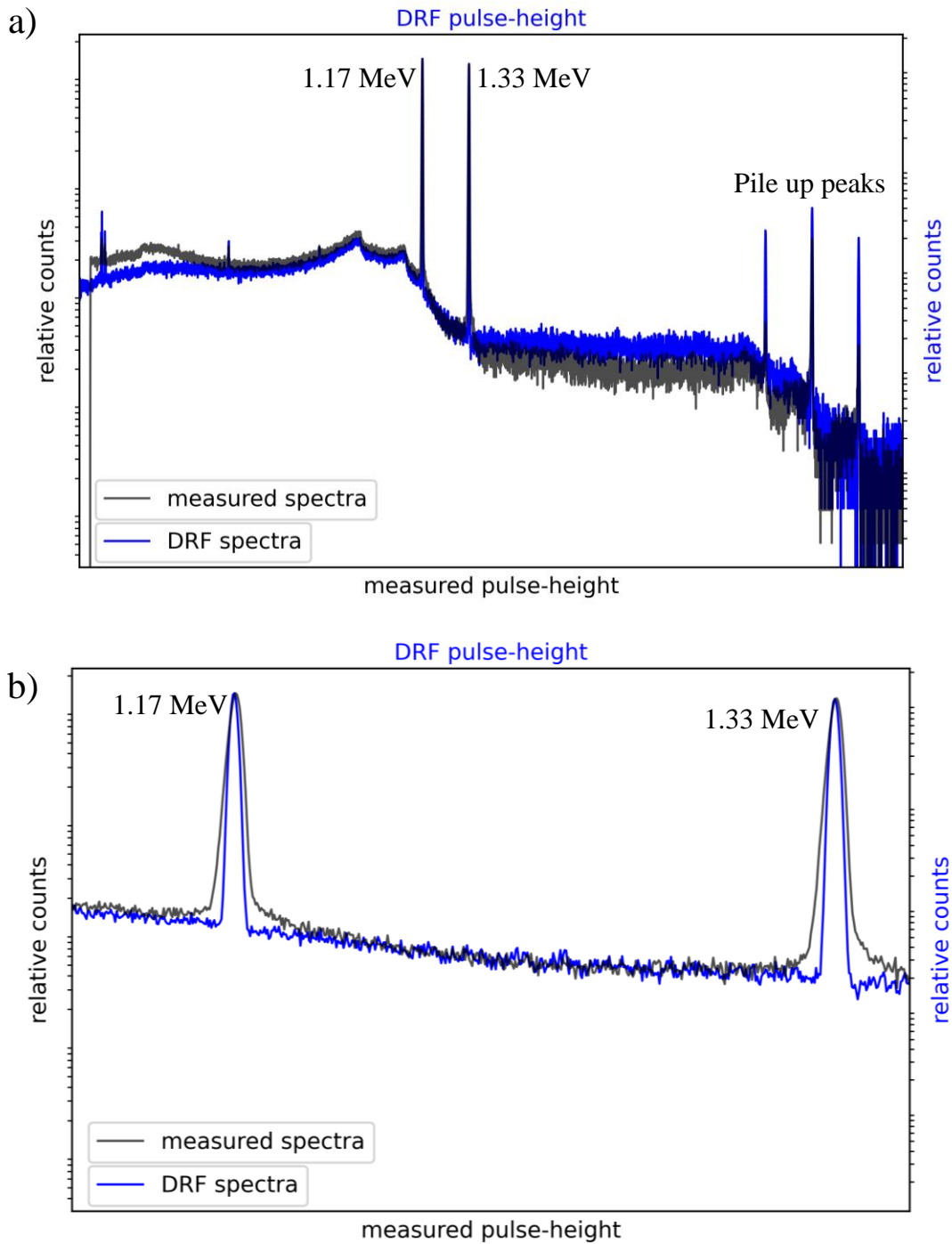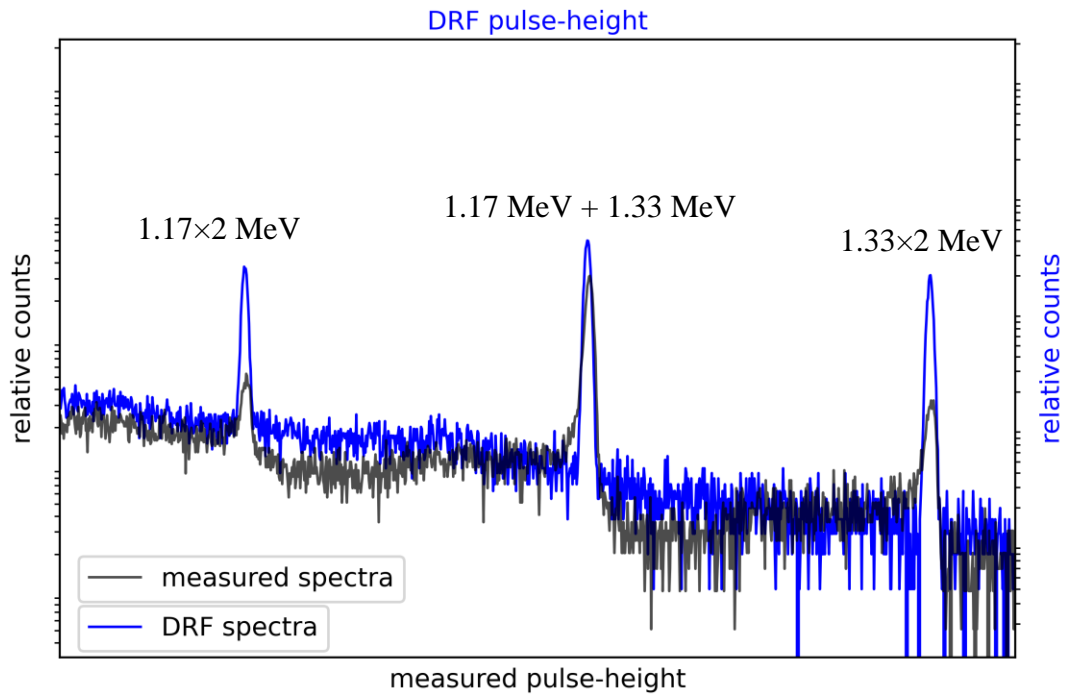
Figure 67: The DRF and measured spectra showing the pile up peaks of a ^{60}Co source. Both have an 82% dead time and count rate of 87851 cps.

The reason low energy tailing is less severe in ^{60}Co could be because ^{133}Ba has lower energy emissions. A majority of the interactions may be occurring in a different region of the HPGe crystal, resulting in longer collection times, which could cause relatively greater ballistic deficit (with low energy tailing), especially in pile up signals.

The backscatter peak and region in the measured spectrum is more prominent than the DRF. This is observable in both Figure 64a and Figure 66a. In these figures, the backscatter is in the low energy region of the Compton continuum (about 200 keV). This is due to the difference between the MCNP simulation and the measurement environment. The MCNP simulation did not contain an extension of the cooling rod, or the cryostat, while the measurement would have backscatter occurring in these large objects. This both stresses the effectiveness and importance of utilizing Monte-Carlo particle transport instead of empirical methods to build DRFs in complex scattering environments. With that said, the accuracy of the DRF is still limited to the accuracy of the geometry in the Monte-Carlo simulation.

To show the difference between a DRF spectrum and the MCNP F8 tally, the two are plotted together in Figure 68. The DRF spectrum is from the 3% dead time and 1616 cps scenario. Since the F8 tally is a simple pulse-height tally, the differences between the two show the effect of modeling charge transport and the readout. There is a drastic difference in the two peak shapes. The most notable difference is in peak width, but one should also keep in mind that the F8 tally does not model pile-up at all. Furthermore, HPGe is arguably the most ideal semiconductor detector, which means that the DRF and measured spectra of an HPGe detector will be more similar to an F8 tally than perhaps any other semiconductor DRF. The extent of the widening also becomes more important when modeling more complicated spectra, especially those which have multiple gamma energies that are close enough to cause overlap between peaks. In a DRF, there are also multiple factors in the widening that can be adjusted individually, which can result in varying degrees of widening at different energies, and non-uniformity. However, because we are modeling HPGe, the peak shapes and widths are very uniform and consistent across the energy spectrum.

Finally, in order to evaluate the relative number of counts in different peaks of the spectra, the peak areas are listed in Table 7. The DRFs have less counts than the measured spectra, so we do not expect identical peak areas. However, we can compare difference in peak areas to the difference in total counts (total area). The difference column in the table shows the difference in the ratio (peak ratio – total ratio). A negative difference indicates that the ratio of measured peak area to DRF peak area decreased compared to the total measured and DRF counts. This negative difference means that the full energy peak in the DRF has more counts than expected. In terms of the full energy peaks (1.17 MeV and 1.33 MeV peaks), there is very little "difference." When looking at the pile-up peaks, there is a larger difference, further supporting the fact that the DRF is overestimating pile-up. The pile-up peak area of 1.17 MeV plus 1.33 MeV is closer to expected than the other two pile-up peak areas, indicating that emission direction of the two gamma rays may be playing a factor in the pile-up probabilities that is not being accounted for in the DRF.

a)

b)
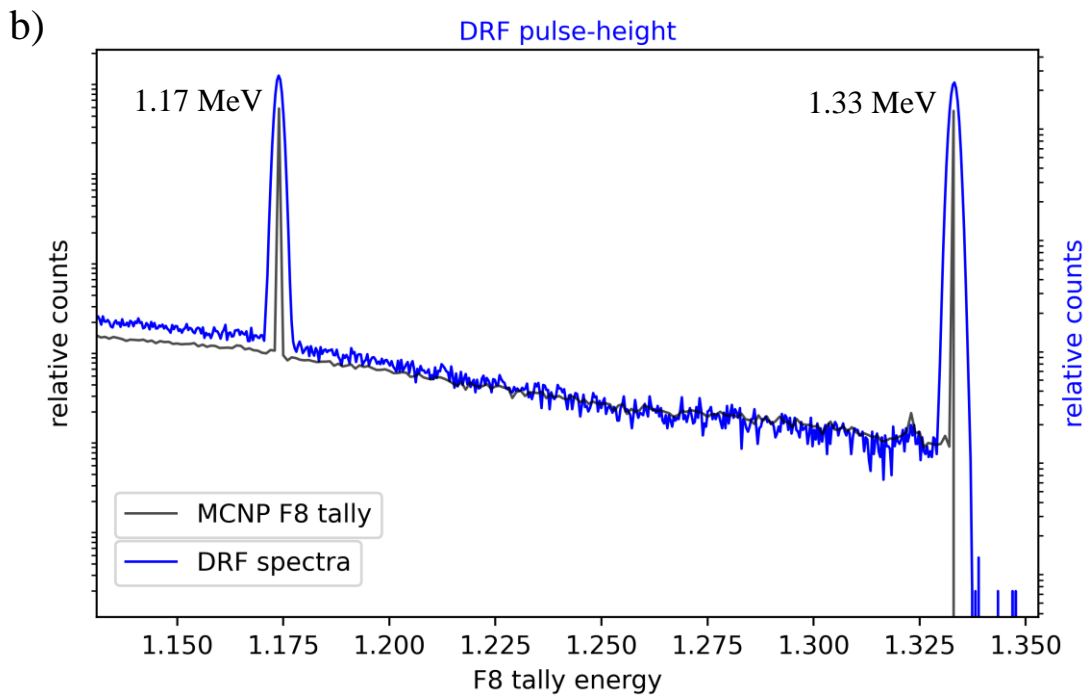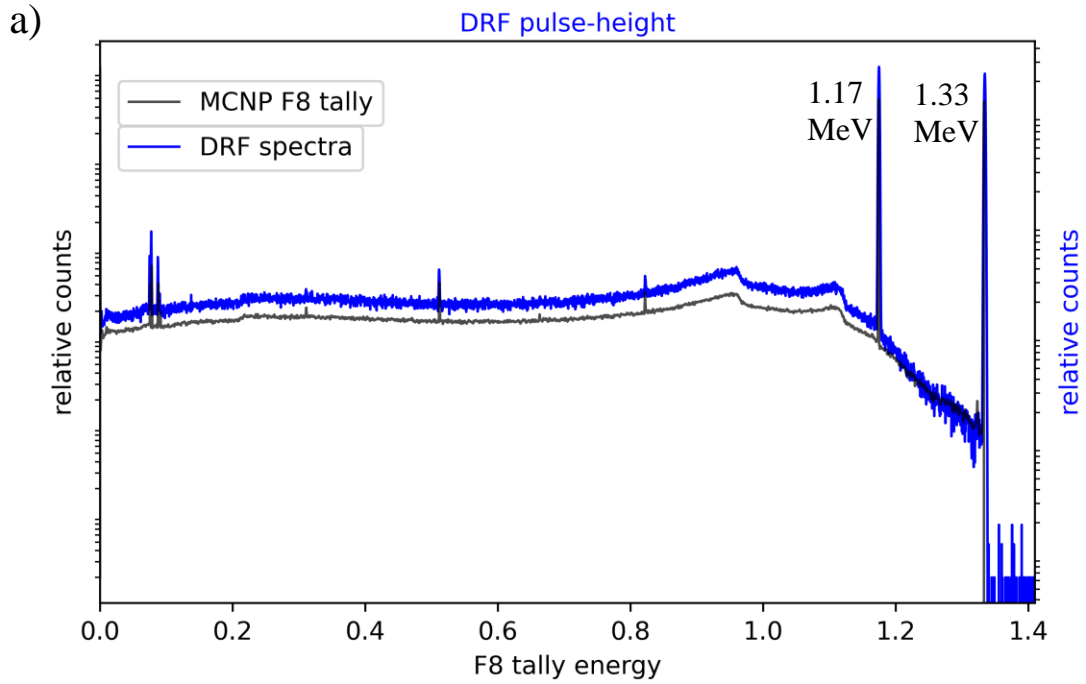
Figure 68: The ^{60}Co DRF at 3% dead time and 1616 cps compared to the MCNP F8 tally. Showing the full spectrum (a) and the full energy peaks (b).

144

Table 7: The peak areas of the DRF and measured spectra.

Energy	$ratio = \dfrac{Measured\ area}{DRF\ area}$	Difference
1616 cps and 3% dead time		
Total spectrum	185,861 / 1,562,679 = 0.12	0
1.17 MeV peak	23,160 / 251,376 = 0.092	-0.028
1.33 MeV peak	21,949 / 234,018 = 0.094	-0.082
87851 cps and 82% dead time		
Total spectrum	1,943,074 / 1,346,914 = 1.4	0
1.17 MeV peak	255,488 / 186,652 = 1.4	0
1.33 MeV peak	235,382 / 174,209 = 1.4	0
1.17+1.17 MeV pile-up peak	1,536 / 5,389 = 0.29	-1.11
1.17+1.33 MeV pile-up peak	7,492 / 8.890 = 0.84	-0.56
1.33+1.33 MeV pile-up peak	1,130 / 4,239 = 0.27	-1.13

C. Cesium-137 detector response functions

The DRF, measured spectrum, and measured background of a ^{137}Cs source are shown in Figure 69. The DRF and measured spectra match up very well across the full energy range, with the exception of a couple of features. Like ^{60}Co, the backscatter peak/region at about 184 keV appears in more prominently in the measured spectrum than the DRF. Again, this is due to other materials associated with the detector system during the measurement, such as the cryostat.

CONCLUSIONS AND FUTURE WORK

We have demonstrated a working DRF which takes MCNP ptrac data as an input to a charge transport code. The charge transport code reads both the ptrac interaction data and Silvaco data to generate charge and transport it through the detector volume to calculate the induced signal. We have demonstrated that the charge transport works and produced the expected signal shape for interactions in different regions of the HPGe crystal. The induced signal is plugged into various sections of an electronic readout model, which include a preamplifier, shaping amplifier, noise, and pile up model. The output of the readout model is a list of pulse-heights that are used to build a pulse-height spectrum, or DRF. By adjusting the input parameters in the DRF, we are able to build spectra that accurately models pulse-height spectra for a specific detector. We built DRFs of ^{133}Ba, ^{60}Co, and ^{137}Cs point sources and compared them to measurements. Settings were kept constant for all DRFs except for count rate and dead time. Count rates and dead time parameters were selected in the DRF to be consistent with measured spectra for comparison. For ^{133}Ba and ^{60}Co, we had measurements at various count rates (and/or dead times) to examine the effect of pulse pile up on the spectrum. We showed that the DRF can accurately reproduce the pulse-height spectrum for cases with little or no pile up, and cases with extensive pile up. While the features of the pulse-height spectra were mostly similar, there were some differences between measured spectra and the DRF. Low energy tailing, high energy tailing, and a small amount of peak broadening occurred in some areas of the measured spectra at very high count rates.

The cause of the low energy tailing and high energy tailing in high count rate scenarios could be an incorrect pole zero on the shaping amplifier, causing undershoot or overshoot. Another cause could be tail pile up of the amplifier pulses, which should be rejected by the pile up rejector, but may not be 100% effective. Low energy tailing in some measured peaks may also be due to ballistic deficit, but the more likely cause is incomplete charge collection. Pile up was often over-estimated in the DRF, but we attribute this to the lack of background in the DRF. Pile up model parameters were adjusted to mirror the count rates and dead times of measurements that had high incidence of background. Without background in the DRF, only source counts were added together for pile up. If background was included in the DRF, a large portion of the counts piled up would have been from background instead of the source. Pile up with background would be less likely to reach higher portions of the spectrum due to the relatively low energy of background. Lastly, backscattering regions in the measured spectra were visibly more prominent than the DRFs. This is due to large components of the measurement setup being missing from the MCNP geometry, such as the cryostat and extensions of the cooling rod.
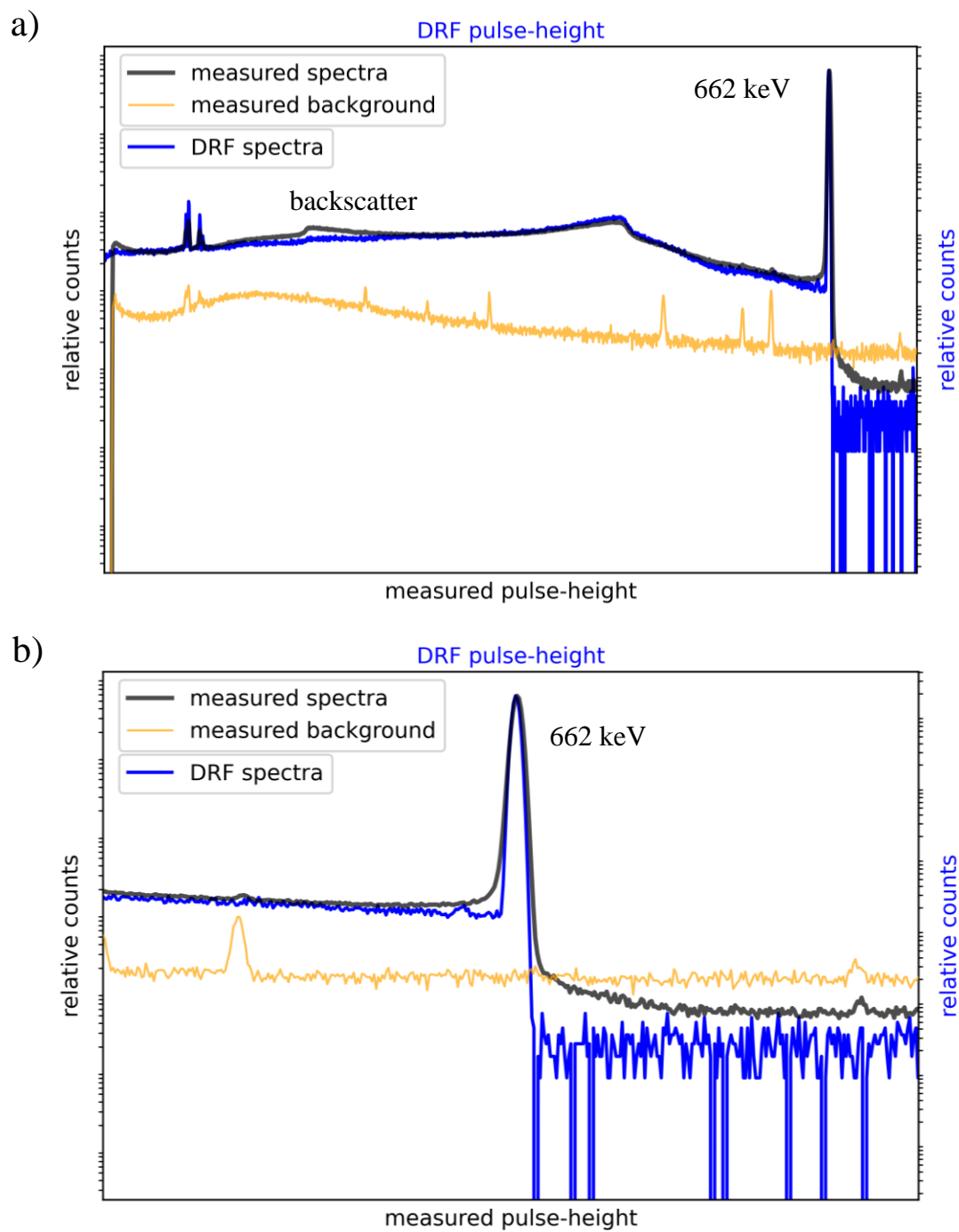
Figure 69: The DRF with measured spectra of a ^{137}Cs source (a) and a close up of the 0.662 MeV full energy peak (b). Both have a 14% dead time and count rate of 7576 cps.

Both the cryostat and cooling rod serve as large scattering centers, but there are probably other components in the measurement environment that have an impact on the spectrum as well. We do not have extensive knowledge of the measurement environment in which the HPGe measurements were taken, but a more accurate MCNP geometry model could resolve those differences.

The focus of future work should be on optimizing the program. The main drawback to the DRFs that we can build is the time and computational expense. HPGe has very good charge carrier properties (mobility, lifetime, saturation velocity). In a semiconductor with poorer charge transport properties or even longer charge collection times, the charge transport would take even longer to simulate. If DRFs could be built more quickly, then there would be many advantages. First, the user could afford to process more detector events, providing more counts for the pulse-height spectrum. While the DRFs and measured spectrum shown did contain the same number of bins or channels, there were fewer counts in the full spectrum of the DRF. If background is modeled, or multiple sources in a more complex environment, then many more particles will need to be run in MCNP and more events will require processing by the charge transport and readout model of the DRF. Currently, the charge transport model takes the bulk of the time. For example, charge transport for the ^{60}Co DRFs shown took roughly 10 hours while generating over 10.5 gigabytes of data. This large dataset was processed by the readout model to generate a DRF with roughly $1.4{\times}10^6$ counts. This was enough to build a DRF with energy bins of the same width as the measured spectrum, but this may not be enough while modeling more complex environments. The readout model can be ran much more quickly, and it generates a much smaller dataset. Once charge transport is completed, the readout model can be ran and adjusted easily, but if one wishes to modify a charge transport parameter, such as the Fano factor, then all of charge transport must be run again.

There are many potential ways to speed up charge transport. One would be parallelization. If possible, this could speed up charge transport by orders of magnitude. Another optimization could be in the methods that data is read and written. It could be faster to read and write data in a different format, such as binary, instead of reading and writing data in a readable format. In fact, MCNP outputs the ptrac data into a binary or HDF5 format. Upon reading and filtering that data for the DRF, it is converted and saved as a readable format. This was useful for troubleshooting, but if the models could be modified to read and write data in a binary format, then it may be less computationally expensive. Being able to build DRFs more quickly would also allow a user to change settings and quickly optimize the parameters for a specific detector.

Lastly, we modeled and generated DRFs for a specific HPGe detector, but the program is not limited to this detector. The program could be used to build DRFs for many semiconductors of different materials, shapes, and sizes. The requirements for modeling a different detector are an electrostatics model (which we used Silvaco for), and a Monte-Carlo transport model (which we used MCNP for). The parameters of charge transport could be modified to reflect different semiconductors. The readout model is not as broad, but feedback capacitance and feedback resistance of the charge sensitive preamplifier could be modified to reflect different preamplifiers. The shaping amplifier may not be as universal, as it is based on the ORTEC DigiDART system.

148

REFERENCES

[1]   A. Beyerle, J. P. Hurley, and L. Tunnell, "Design of an associated particle imaging system," *Nuclear Instruments and Methods in Physics Research, Section A,* vol. 299, no. 1-3, pp. 458-462, 1990.

[2]   P. A. Hausladen, J. S. Neal, and J. T. Mihalczo, "An alpha particle detector for a portable neutron generator for the Nuclear Materials Identification System (NMIS)," *Nuclear Instruments and Methods in Physics Research Section B: Beam Interactions with Materials and Atoms,* vol. 241, no. 1, pp. 835-838, 2005/12/01/ 2005.

[3]   Q. Ji, B. Ludewigt, J. Wallig, W. Waldron, and J. Tinsley, "Development of a Time-tagged Neutron Source for SNM Detection," *Physics Procedia,* vol. 66, pp. 105-110, 2015/01/01/ 2015.

[4]   P. R. B. John T Mihalczo, Matthew A Blackston, Jason M Crye, Brandon R Grogan, Paul A Hausladen, Seth M McConchie, James A Mullens, "Fast-Neutron Imaging with API DT Neutron Generators," presented at the VNIIA, Moscow, Russia, 2012.

[5]   D. S. Koltick, S. Z. Kane, M. Lvovsky, E. K. Mace, S. M. McConchie, and J. T. Mihalczo, "Characterization of an Associated Particle Neutron Generator With ZnO:Ga Alpha-Detector and Active Focusing," *IEEE Transactions on Nuclear Science,* vol. 56, no. 3, pp. 1301-1305, 2009.

[6]   S. D. Clarke, M. C. Hamel, M. M. Bourne, and S. A. Pozzi, "Detectors for Active Interrogation Applications," *Physics Procedia,* vol. 90, pp. 266-270, 2017/01/01/ 2017.

[7]   M. C. Hamel, J. K. Polack, M. L. Ruch, M. J. Marcath, S. D. Clarke, and S. A. Pozzi, "Active neutron and gamma-ray imaging of highly enriched uranium for treaty verification," *Scientific Reports,* vol. 7, no. 1, p. 7997, 2017/08/11 2017.

[8]   J. Bendahan, "Review of active interrogation techniques," *Nuclear Instruments and Methods in Physics Research Section A: Accelerators, Spectrometers, Detectors and Associated Equipment,* vol. 954, p. 161120, 2020/02/21/ 2020.

[9]   S. D. Clarke *et al.*, "Measurement of the energy and multiplicity distributions of neutrons from the photofission of $^{235}\mathrm{U}$," *Physical Review C,* vol. 95, no. 6, p. 064612, 06/20/ 2017.

[10]   Q. Ji, "Tagged Neutron Source for API Inspection Systems with Greatly Enhanced Spatial Resolution," United States, 2012, Research Org.: Nevada Test Site (NTS), Mercury, NV (United States), Sponsor Org.: USDOE NA Office of Nonproliferation and Verification Research and Development (NA-22).

[11]   J. T. Mihalczo, M. C. Wright, S. M. McConchie, D. E. Archer, and B. A. Palles, "Transportable, Low-Dose Active Fast-Neutron Imaging," United States2017-08-01 2017, Available: https://www.osti.gov/biblio/1400208.

[12]   J. T. Mihalczo, J. A. Mullens, J. K. Mattingly, and T. E. Valentine, "Physical description of nuclear materials identification system (NMIS) signatures," *Nuclear Instruments and Methods in Physics Research Section A: Accelerators, Spectrometers, Detectors and Associated Equipment,* vol. 450, no. 2, pp. 531-555, 2000/08/11/ 2000.

[13]   P. Hausladen *et al.*, "Induced-Fission Imaging of Nuclear Material," 01/01 2010.

[14]   A. C. Trahan, "Utilization of the Differential Die-Away Self-Interrogation Technique for Characterization and Verification of Spent Nuclear Fuel," *University of Michigan Library,* Ph.D. Dissertation 2016.

[15]   C. L. Hollas, C. Goulding, and W. Myers, "Determination of neutron multiplication of subcritical HEU systems using delayed neutrons," *Nuclear Instruments and Methods in Physics Research Section A: Accelerators, Spectrometers, Detectors and Associated Equipment,* vol. 543, no. 2, pp. 559-569, 2005/05/11/ 2005.

[16]   C. E. Moss, C. L. Hollas, G. W. Mckinney, and W. L. Myers, "Comparison of Active Interrogation Techniques," *IEEE Transactions on Nuclear Science,* vol. 53, no. 4, pp. 2242-2246, 2006.

[17]   J. S. Neal, L. A. Boatner, N. C. Giles, L. E. Halliburton, S. E. Derenzo, and E. D. Bourret-Courchesne, "Comparative investigation of the performance of ZnO-based scintillators for use as α-particle detectors," *Nuclear Instruments and Methods in Physics Research Section A: Accelerators, Spectrometers, Detectors and Associated Equipment,* vol. 568, no. 2, pp. 803-809, 2006/12/01/ 2006.

[18]   X. Zhang *et al.*, "Benchmarking the Geant4 full system simulation of an associated alpha-particle detector for use in a D–T neutron generator," *Applied Radiation and Isotopes,* vol. 70, no. 8, pp. 1485-1493, 2012/08/01/ 2012.

[19]   M. E. Moore *et al.*, "Studying the effects of thermally diffusing Ce into the surface of YAlO3 for associated particle imaging," *Nuclear Instruments and Methods in Physics Research Section B: Beam Interactions with Materials and Atoms,* vol. 473, pp. 55-61, 2020/06/15/ 2020.

[20]   S. Baccaro *et al.*, "Scintillation properties of YAP:Ce," *Nuclear Instruments and Methods in Physics Research Section A: Accelerators, Spectrometers, Detectors and Associated Equipment,* vol. 361, no. 1, pp. 209-215, 1995/07/01/ 1995.

[21]   M. Korzhik *et al.*, "Timing porperties of Ce-doped YAP and LuYAP scintillation crystals," *Nuclear Instruments and Methods in Physics Research Section A: Accelerators, Spectrometers, Detectors and Associated Equipment,* vol. 927, 02/01 2019.

[22]   R. Pani *et al.*, "Multi-crystal YAP: Ce detector system for position sensitive measurements," *Nuclear Instruments and Methods in Physics Research Section A: Accelerators, Spectrometers, Detectors and Associated Equipment,* vol. 348, no. 2, pp. 551-558, 1994/09/01/ 1994.

[23]   J. W. Cates, J. P. Hayward, and X. Zhang, "Increased light extraction from inorganic scintillators with Laser-Etched microstructures," *IEEE Transactions on Nuclear Science,* vol. 60, no. 2, pp. 1027-1032, 2013, Art. no. 6496306.

[24]   P. H. SBIR, "DOE SBIR/STTR FY 2021 PHASE I RELEASE 2: topic 2b," A personal communication with Paul Hausladen, and provided link to the SBIR call ed. SBIR.gov, 2021.

[25]   M. Ayllon Unzueta, B. Ludewigt, B. Mak, T. Tak, and A. Persaud, "An all-digital associated particle imaging system for the 3D determination of isotopic distributions," *Review of Scientific Instruments,* vol. 92, no. 6, p. 063305, 2021/06/01 2021.

[26]   M. Ayllon Unzueta, W. Mixter, Z. Croft, J. Joseph, B. Ludewigt, and A. Persaud, *Position sensitive alpha detector for an associated particle imaging system.* 2019, p. 050005.

[27]   J. W. Cates, J. P. Hayward, and X. Zhang, "Achievable position resolution of an alpha detector with continuous spatial response for use in associated particle imaging," in *2013 IEEE Nuclear Science Symposium and Medical Imaging Conference (2013 NSS/MIC)*, 2013, pp. 1-3.

[28]   M. L. Litvak *et al.*, "Associated particle imaging instrumentation for future planetary surface missions," *Nuclear Instruments and Methods in Physics Research Section A: Accelerators, Spectrometers, Detectors and Associated Equipment,* vol. 922, pp. 19-27, 2019/04/01 2019.

[29]   G. Giacomini *et al.*, "Evaluation of radiation hardness of semiconductor materials against alpha particles for an API detector," United States, 2020, Research Org.: Brookhaven National Lab. (BNL), Upton, NY (United States), Sponsor Org.: USDOE Office of Science (SC); USDOE National Nuclear Security Administration (NNSA), Office of Nonproliferation and Verification Research and Development (NA-22).

[30]   C. J. H. Wort and R. S. Balmer, "Diamond as an electronic material," *Materials Today,* vol. 11, no. 1, pp. 22-28, 2008/01/01/ 2008.

[31]   J. Liu *et al.*, "Design, fabrication and testing of CVD diamond detectors with high performance," *AIP Advances,* vol. 9, no. 4, p. 045205, 2019/04/01 2019.

[32]   C. Tuvè *et al.*, "Single crystal diamond detectors grown by chemical vapor deposition," *Nuclear Instruments and Methods in Physics Research Section A: Accelerators, Spectrometers, Detectors and Associated Equipment,* vol. 570, no. 2, pp. 299-302, 2007/01/11/ 2007.

[33]   T. Shimaoka, S. Koizumi, H. J, and Kaneko, "Recent progress in diamond radiation detectors," *Functional Diamond,* vol. 1, no. 1, pp. 205-220, 2021/01/02 2021.

[34]   M. Marinelli *et al.*, "Systematic study of pre-irradiation effects in high efficiency CVD diamond nuclear particle detectors," *Nuclear Instruments and Methods in Physics Research Section A: Accelerators, Spectrometers, Detectors and Associated Equipment,* vol. 476, no. 3, pp. 701-705, 2002/01/11/ 2002.

[35]   S. Lagomarsino *et al.*, "Radiation hardness of three-dimensional polycrystalline diamond detectors," *Applied Physics Letters,* vol. 106, no. 19, p. 193509, 2015/05/11 2015.

[36]   M. Pomorski *et al.*, "Development of single-crystal CVD-diamond detectors for spectroscopy and timing," *physica status solidi (a),* https://doi.org/10.1002/pssa.200671127 vol. 203, no. 12, pp. 3152-3160, 2006/09/01 2006.

[37]   S. Michimasa *et al.*, "Development of CVD diamond detector for time-of-flight measurements," *Nuclear Instruments and Methods in Physics Research Section B: Beam Interactions with Materials and Atoms,* vol. 317, pp. 710-713, 2013/12/15/ 2013.

[38]   F. Schirru *et al.*, "Development of large area polycrystalline diamond detectors for fast timing application of high-energy heavy-ion beams," *Journal of Instrumentation,* vol. 7, no. 05, pp. P05005-P05005, 2012/05/09 2012.

[39]   S. Wang, P. Sellin, and A. Lohstroh, "Alpha particle transient response of a polycrystalline diamond detector," *Carbon,* vol. 43, no. 15, pp. 3167-3171, 2005/12/01/ 2005.

[40]   M. Marinelli *et al.*, "Trapping and detrapping effects in high-quality chemical-vapor-deposition diamond films: Pulse shape analysis of diamond particle detectors," *Physical Review B,* vol. 64, no. 19, p. 195205, 10/19/ 2001.

[41]   M. Angelone *et al.*, "Radiation hardness of a polycrystalline chemical-vapor-deposited diamond detector irradiated with 14 MeV neutrons," *Review of Scientific Instruments,* vol. 77, no. 2, p. 023505, 2006/02/01 2006.

[42]   M. Passeri *et al.*, "Assessment of single crystal diamond detector radiation hardness to 14 MeV neutrons," *Nuclear Instruments and Methods in Physics Research Section A: Accelerators, Spectrometers, Detectors and Associated Equipment,* vol. 1010, p. 165574, 2021/09/11/ 2021.

[43]   M. Mikuz *et al.*, "Study of polycrystalline and single crystal diamond detectors irradiated with pions and neutrons up to 3×1015 cm−2," in *2007 IEEE Nuclear Science Symposium Conference Record*, 2007, vol. 3, pp. 2169-2172.

[44]   A. Oh, M. Moll, A. Wagner, and W. Zeuner, "Neutron irradiation studies with detector grade CVD diamond," *Diamond and Related Materials,* vol. 9, no. 11, pp. 1897-1903, 2000/11/01/ 2000.

[45]   L. Allers, A. S. Howard, J. F. Hassard, and A. Mainwood, "Neutron damage of CVD diamond," *Diamond and Related Materials,* vol. 6, no. 2, pp. 353-355, 1997/03/01/ 1997.

[46]   W. de Boer *et al.*, "Radiation hardness of diamond and silicon sensors compared," *physica status solidi (a),* https://doi.org/10.1002/pssa.200776327 vol. 204, no. 9, pp. 3004-3010, 2007/09/01 2007.

[47]   L. Bäni *et al.*, "A study of the radiation tolerance of poly-crystalline and single-crystalline CVD diamond to 800 MeV and 24 GeV protons," *Journal of Physics D: Applied Physics,* vol. 52, no. 46, p. 465103, 2019/08/30 2019.

[48]   D. Doneddu, O. J. Guy, D. Twitchen, A. Tajani, M. Schwitters, and P. Igic, "Schottky Contacts on Single-Crystal CVD Diamond," in *2006 25th International Conference on Microelectronics*, 2006, pp. 179-182.

[49]   S. A. Manifold *et al.*, "Contact resistance of various metallisation schemes to superconducting boron doped diamond between 1.9 and 300 K," *Carbon,* vol. 179, pp. 13-19, 2021/07/01/ 2021.

[50]   C. J. Delzer, "Fabrication of Specialized Scintillators for Nuclear Security App," PhD, Nuclear Engineering, University of Tennessee, Knoxville, TRACE: Tennessee Research and Creative Exchange, 2021.

[51]   R. B. J. T.E. Schlesinger, *Semiconductors for room temperature nuclear detector applications: semiconductors and semimetals*. San Diego: Academic Press, 1995.

[52]   J. Cerny, *Nuclear Spectroscopy and Reactions Part A*. Academic Press, 1974.

[53]   A. ORTEC. *Overview of Semiconductor Photon Detectors*. Available:
https://www.ortec-online.com/-/media/ametekortec/other/overview-of-
semiconductor-photon-detectors

[54]   D. J. Decman, J. Glaser, J. M. Hernandez, and S. J. Luke, "Portable NDA
equipment for enrichment measurements for the HEU transparency program,"
United States1999, Available:
http://inis.iaea.org/search/search.aspx?orig_q=RN:32047974.

[55]   A. T. Greaney, S. K. Smith, R. Venkataraman, J. M. Richards, and G. A. Fugate,
"Applications of HPGe-detected high energy gamma rays toward quantifying
neutron emission rates and 234U enrichment in UF6 cylinders," *Nuclear
Instruments and Methods in Physics Research Section A: Accelerators,
Spectrometers, Detectors and Associated Equipment,* vol. 972, p. 163912,
2020/08/21/ 2020.

[56]   E. A. Lepel, B. D. Geelhood, W. K. Hensley, and W. M. Quam, "A field-
deployable, aircraft-mounted sensor for the environmental survey of
radionuclides," *Journal of Radioanalytical and Nuclear Chemistry,* vol. 233, no.
1, pp. 211b-215, 1998/07/01 1998.

[57]   S. Stave, "Germanium detectors in homeland security at PNNL," (in English), vol.
606, 2015-05-01 2015.

[58]   F. T. Avignone Iii and S. R. Elliott, "The Search for Double Beta Decay With
Germanium Detectors: Past, Present, and Future," *Frontiers in Physics,* Review
vol. 7, 2019.

[59]   W. Xu *et al.*, "Testing the Ge Detectors for the MAJORANA
DEMONSTRATOR," *Physics Procedia,* vol. 61, pp. 807-815, 2015/01/01/ 2015.

[60]   F. Edzards and L. C. for the, "The Future of Neutrinoless Double Beta Decay
Searches with Germanium Detectors," *Journal of Physics: Conference Series,* vol.
1690, no. 1, p. 012180, 2020/12/01 2020.

[61]   H. Päs and W. Rodejohann, "Neutrinoless double beta decay," *New Journal of
Physics,* vol. 17, no. 11, p. 115010, 2015/11/24 2015.

[62]   S. Croft and D. S. Bond, "A determination of the Fano factor for germanium at
774K from measurements of the energy resolution of a 113cm3 HPGe gamma-ray
spectrometer taken over the energy range from 14 to 6129 keV," *Applied
Radiation and Isotopes,* vol. 42, no. 11, pp. 1009-1014, 1991.

[63]   U. Fano, "Ionization Yield of Radiations. II. The Fluctuations of the Number of
Ions," *Physical Review,* vol. 72, no. 1, pp. 26-29, 1947.

[64]   H. Spieler, *Semiconductor Detector Systems*. New York: Oxford University Press,
2005.

[65]   A. ORTEC. *Review of the physics of semiconductor detectors*. Available:
https://www.ortec-online.com/-
/media/ametekortec/other/review_of_the_physics_of_semiconductor_detectors.pd
f?la=en&revision=7b0c40d6-3fcc-4714-a351-a2df530194ce

[66]   A. ORTEC. *GEM Series Coaxial HPGe Detector Product Configuration Guide*.
Available: https://www.ortec-online.com/-

/media/ametekortec/brochures/g/gem.pdf?la=en&revision=85004f52-4b5d-4d62-8e27-e9ab1de89951

[67]   K. K. N. S. M. Sze, "Physics of Semiconductor Devices," in *Physics of Semiconductor Devices*3rd ed. New Jersey: John Wiley & Sons, Inc, Wiley-Interscience, 2007, pp. 5-75.

[68]   Q. Looker, "Fabrication Process Development for High-Purity Germanium Radiation Detectors with Amorphous Semiconductor Contacts," *Ph.D. Dissertation, Nuclear Engineering Department, Univerity of California Berkeley,* 2014.

[69]   D. A. Neamen, *Semiconductor Physics and Devices: Basic Principles*, 3rd ed. McGraw Hill, 2003.

[70]   C. Leroy and P.-G. Rancoita, *Principles of Radiation Interaction in Matter and Detection*. WORLD SCIENTIFIC, 2009, p. 952.

[71]   G. F. Knoll, *Radiation detection and measurement : Glenn F. Knoll*, 4th ed. ed. New York: John Wiley & Sons, Inc., 2010.

[72]   P. W. Cattaneo, "The effect of velocity saturation on the shape of current signals in germanium cylindrical detectors," *Nuclear Instruments and Methods in Physics Research Section A: Accelerators, Spectrometers, Detectors and Associated Equipment,* vol. 343, no. 2, pp. 583-587, 1994/04/11/ 1994.

[73]   S. Ramo, "Currents Induced by Electron Motion," *Proceedings of the IRE,* vol. 27, no. 9, pp. 584-585, 1939.

[74]   Z. He, "Review of the Shockley–Ramo theorem and its application in semiconductor gamma-ray detectors," *Nuclear Instruments and Methods in Physics Research Section A: Accelerators, Spectrometers, Detectors and Associated Equipment,* vol. 463, no. 1, pp. 250-267, 2001/05/01/ 2001.

[75]   W. Shockley, "Currents to Conductors Induced by a Moving Point Charge," *Journal of Applied Physics,* vol. 9, no. 10, pp. 635-636, 1938/10/01 1938.

[76]   G. Cavalleri, E. Gatti, G. Fabri, and V. Svelto, "Extension of Ramo's theorem as applied to induced charge in semiconductor detectors," *Nuclear Instruments and Methods,* vol. 92, no. 1, pp. 137-140, 1971/03/01/ 1971.

[77]   T. H. Prettyman, "Method for mapping charge pulses in semiconductor radiation detectors," *Nuclear Instruments and Methods in Physics Research Section A: Accelerators, Spectrometers, Detectors and Associated Equipment,* vol. 422, no. 1, pp. 232-237, 1999/02/11/ 1999.

[78]   L.-A. Hamel and S. Paquet, "Charge transport and signal generation in CdTe pixel detectors," *Nuclear Instruments and Methods in Physics Research Section A: Accelerators, Spectrometers, Detectors and Associated Equipment,* vol. 380, no. 1, pp. 238-240, 1996/10/01/ 1996.

[79]   Y. Fang, C. Xu, Y. Yao, N. Pelc, M. Danielsson, and A. Badano, "Modeling charge transport in photon-counting detectors," *Nuclear Instruments and Methods in Physics Research Section A: Accelerators, Spectrometers, Detectors and Associated Equipment,* vol. 899, pp. 115-121, 2018/08/11/ 2018.

[80]   H. H. Barrett, J. D. Eskin, and H. B. Barber, "Charge Transport in Arrays of Semiconductor Gamma-Ray Detectors," *Physical Review Letters,* vol. 75, no. 1, pp. 156-159, 07/03/ 1995.

[81]   G. Rossi, M. Sanchez del Rio, P. Fajardo, and J. Morse, "Monte Carlo simulation of the X-ray response of a germanium microstrip detector with energy and position resolution," *Nuclear Instruments and Methods in Physics Research Section A: Accelerators, Spectrometers, Detectors and Associated Equipment,* vol. 432, no. 1, pp. 130-137, 1999/08/01 1999.

[82]   A. G. Kozorezov, J. K. Wigmore, A. Owens, R. den Hartog, and A. Peacock, "Analytic model for the spatial and spectral resolution of pixellated semiconducting detectors of high-energy photons," *Journal of Applied Physics,* vol. 97, no. 7, p. 074502, 2005/04/01 2005.

[83]   J. E. Klaus and H. Christoph, "Simulation of one-dimensionally polarized x-ray semiconductor detectors," in *Proc.SPIE*, 2011, vol. 7961, p. 79610W.

[84]   E. Knapp, R. Häusermann, H. U. Schwarzenbach, and B. Ruhstaller, "Numerical simulation of charge transport in disordered organic semiconductor devices," *Journal of Applied Physics,* vol. 108, no. 5, p. 054504, 2010/09/01 2010.

[85]   H. Bässler, "Charge Transport in Disordered Organic Photoconductors a Monte Carlo Simulation Study," *physica status solidi (b),* https://doi.org/10.1002/pssb.2221750102 vol. 175, no. 1, pp. 15-56, 1993/01/01 1993.

[86]   H. Houili, E. Tutiš, H. Lütjens, M. N. Bussac, and L. Zuppiroli, "MOLED: Simulation of multilayer organic light emitting diodes," *Computer Physics Communications,* vol. 156, no. 1, pp. 108-122, 2003/12/01 2003.

[87]   R. Coehoorn and S. L. M. van Mensfoort, "Effects of disorder on the current density and recombination profile in organic light-emitting diodes," *Physical Review B,* vol. 80, no. 8, p. 085302, 08/05/ 2009.

[88]   ORTEC-AMETEK, "Preamplifier Introduction," Available: https://www.ortec-online.com/-/media/ametekortec/other/amplifier-introduction.pdf

[89]   ORTEC-AMETEK, "Amplifier Introduction," Accessed on: 2023Available: https://www.ortec-online.com/-/media/ametekortec/other/amplifier-introduction.pdf

[90]   ORTEC. *digiDART Portable HPGe MCA Operator Manual*. Available: https://www.ortec-online.com/-/media/ametekortec/manuals/d/digidart-mnl.pdf?la=en&revision=99c91ed8-114d-4b5e-99b1-a88301f346c3

[91]   S. Usman and A. Patil, "Radiation detector deadtime and pile up: A review of the status of science," *Nuclear Engineering and Technology,* vol. 50, 06/01 2018.

[92]   M. Yousaf, T. Akyurek, and S. Usman, "A comparison of traditional and hybrid radiation detector dead-time models and detector behavior," *Progress in Nuclear Energy,* vol. 83, pp. 177-185, 2015.

[93]   S. H. Lee and R. P. Gardner, "A new G–M counter dead time model," *Applied Radiation and Isotopes,* vol. 53, no. 4, pp. 731-737, 2000/11/15/ 2000.

[94]   A. Patil and S. Usman, "Measurement and Application of Paralysis Factor for Improved Detector Dead-Time Characterization," *Nuclear Technology,* vol. 165, no. 2, pp. 249-256, 2009/02/01 2009.

[95]   D. J. Mitchell, L. Harding, G. G. Thoreson, and S. M. Horne, "GADRAS Detector Response Function," United States2014-11-01 2014, Available: https://www.osti.gov/biblio/1163837 https://www.osti.gov/servlets/purl/1163837.

[96]   S. M. Horne, G. G. Thoreson, L. A. Theisen, D. J. Mitchell, L. Harding, and W. A. Amai, "GADRAS-DRF 18.6 User's Manual," Sandia National Laboratories2016-05-01 2016, Available: https://www.osti.gov/servlets/purl/1431293.

[97]   J. Mattingly, D. J. Mitchell, L. T. Harding, E. S. Varley, and N. R. Hilton, "FY2008 Report on GADRAS Radiation Transport Methods," United States2008-10-01 2008, Available: https://www.osti.gov/biblio/1130402 https://www.osti.gov/servlets/purl/1130402.

[98]   G. G. Thoreson, D. J. Mitchell, L. A. Theisen, and L. T. Harding, "Environment scattering in GADRAS," United States2013-09-01 2013, Available: https://www.osti.gov/biblio/1096953 https://www.osti.gov/servlets/purl/1096953.

[99]   J. Zhang, X. Tuo, Q. Wang, Y. Leng, and R. Shi, "Detector response function of a HPGe detector to photon energies between 200 keV and 1.5 MeV for Gamma-ray nondestructive assay instrument," in *2017 IEEE Nuclear Science Symposium and Medical Imaging Conference (NSS/MIC)*, 2017, pp. 1-5.

[100]   M.-C. Lépy, J. Plagnard, and L. Ferreux, "Study of the response function of a HPGe detector for low-energy X-rays," *Nuclear Instruments and Methods in Physics Research Section A: Accelerators, Spectrometers, Detectors and Associated Equipment,* vol. 505, no. 1, pp. 290-293, 2003/06/01/ 2003.

[101]   E. Eftekhari Zadeh, S. A. H. Feghhi, E. Bayat, and G. H. Roshani, "Gaussian Energy Broadening Function of an HPGe Detector in the Range of 40 keV to 1.46 MeV," *Journal of Experimental Physics,* vol. 2014, p. 623683, 2014/10/07 2014.

[102]   N. Lopez-Pino, F. P. Cabral, K. D'Alessandro, N. L. Maidana, V. R. Vanin, and J. Sempau, "Response function of a p type - HPGe detector," in *Meeting on physics 2011 Physics integration in Latin America*, Brazil, 2011.

[103]   S. Carson *et al.*, "Ratio of germanium detector peak efficiencies at photon energies of 4.4 and 11.7MeV: Experiment versus simulation," *Nuclear Instruments and Methods in Physics Research Section A: Accelerators, Spectrometers, Detectors and Associated Equipment,* vol. 618, no. 1, pp. 190-198, 2010/06/01/ 2010.

[104]   E. Uyar, G. Aksoy, H. Ünlü, and M. H. Bölükdemir, "Investigation of the effect of copper contact pin on efficiency in HPGe detectors using Monte Carlo method," *Journal of Instrumentation,* vol. 16, no. 11, p. T11003, 2021/11/01 2021.

[105]   L. L. Gadeken and B. C. Robertson, "The influence of Ge(Li) detector pulse shape variations on constant fraction and snap-off timing discriminators," *Nuclear Instruments and Methods,* vol. 136, no. 2, pp. 255-259, 1976/07/15/ 1976.

VITA

Corey Ahl spent most of his early childhood in Scotia, NY, where he attended Sacandaga Elementary and Middle school. As a child, he fell in love with motocross racing. At 12 years old, Corey's family moved to Greenville, SC. In this new environment, Corey couldn't help but become obsessed with motocross, and his family became seriously deep-rooted in racing as a consequence. Ultimately, Corey ended up leaving high school during November of the 10th grade, giving him the opportunity to become more dedicated to motocross. He would leave high school and never look back as he practiced, trained, and ended up earning a license to compete professionally. Around the age of 23, and after a long pursuit in racing, Corey decided to earn his high school equivalency (GED) and change his path to one in academia. Corey decided to pursue higher education for the challenge and opportunities for growth, but also out of fascination in several subjects. He decided that studying physics would best suit his interests and goals. Due to having limited education, he would have to start by attending Tri-County Technical College in Pendleton, SC. Here, he would take high school level and introductory level college courses that he missed due to leaving high school early. His success there led to his acceptance at Clemson University, where he would experience many firsts. In fact, he would enter the bachelor's in physics program before having ever taken a physics course. Four years later, in 2019, he earned his bachelor's in science degree in physics, with a minor in nuclear engineering and radiological sciences. His fascination with physics did not end here, and his interest in the nuclear sciences grew. He applied for graduate schools and decided on the University of Tennessee, Knoxville. Here he would earn his PhD in nuclear engineering under the teachings, mentorship, and guidance of Dr. Eric Lukosi. Corey is appreciative of the University of Tennessee, Clemson University, partners, collaborators, mentors, friends, family, and everyone else who was present along the way. He has received an immeasurable amount of support and friendship.